THE UNIVERSITY *of* EDINBURGH

Co-located Analysis of Ice Clouds Detected from Space and their Impact on Longwave Energy Transfer

Christopher J Nankervis

Doctor of Philosophy

School of GeoSciences

The University of Edinburgh

2013

Acknowledgements

- This postgraduate course was undertaken in the Institute of Atmospheric and Environmental Sciences within the School of GeoSciences. The studentship was fully funded by the National Environment Research Council (NERC).

- The NASA Microwave Limb Sounding (MLS) science group at the US Jet Propulsion Laboratory (JPL) has been invaluable to the PhD process. In particular, Dr Dong Wu has ensured a high quality version 2 of the cloud ice water content (IWC) product. NASA has provided continued support and open access to data to the wider Earth Observation community to achieve common science objectives.

- Further data analysis was undertaken using MODIS and CERES Aqua satellite instrument data products. Data was accessed via the NASA Langley Research Center Atmospheric Science Data Center. The Goddard Space Flight Center (GSFC) team and its wider calibration and validation teams have provided valuable information for ensuring the highest standard and range of end-user products.

- The Rapid Radiative Transfer Model (RRTM) code and its respective user manual were downloaded from Atmospheric and Environmental Research, Inc. The cloudy-sky component of the model uses the DISORT RT solver and cloud inputs are computed as in Cloud Community Model (CCM) Version 3.

- European Center for Medium-range Weather Forecast (ECMWF) reanalysis data (ERA-Interim) was used in conjunction with MLS cloud profiles to provide a more complete picture of the atmosphere. Data was downloaded from the National Centre for Atmospheric Sciences (NCAS) British Atmospheric Data Centre (BADC) in 2009 at http://badc.nerc.ac.uk/.

Declaration

I declare that this thesis was composed by myself, that the work contained herein is my own except where explicitly stated otherwise in the text, and that this work has not been submitted for any other degree or professional qualification except as specified.

Christopher Nankervis:

April 2013

Abstract

A lack of quality data on high clouds has led to inadequate representations within global weather and climate models. Recent advances in space-borne measurements of the Earth's atmosphere have provided complementary information on the interior of these clouds. This study demonstrate how an array of space-borne measurements can be used and combined, by close co-located comparisons in space and time, to form a more complete representation of high cloud processes and properties.

High clouds are found in the upper atmosphere, where sub-zero temperatures frequently result in the formation of cloud particles that are composed of ice. Weather and climate models characterise the bulk properties of these ice particles to describe the current state of the cloud-sky atmosphere. By directly comparing measurements with simulations undertaken at the same place and time, this study demonstrates how improvements can be made to the representation of cloud properties. The results from this study will assist in the design of future cloud missions to provide a better quality input. These improvements will also help improve weather predictions and lower the uncertainty in cloud feedback response to increasing atmospheric temperature.

Most clouds are difficult to monitor by more than one instrument due to continuous changes in: large-scale and sub-cloud scale circulation features, microphysical properties and processes and characteristic chemical signatures. This study undertakes co-located comparisons of high cloud data with a cloud ice dataset reported from the Microwave Limb Sounder (MLS) instrument onboard the Aura satellite that forms part of the A-train constellation. Data from the MLS science team include vertical profiles of temperature, ice water content (IWC) and the mixing ratios of several trace gases. Their vertical resolutions are 3 to 6 km.

Initial investigations explore the link between cloud-top properties and the longwave radiation budget, developing methods for estimating cloud top heights using; longwave radiative fluxes, and IWC profiles. Synergistic trios of direct and indirect high cloud measurements were used to validate detections from the MLS by direct comparisons with two different A-train instruments; the NASA Moderate-resolution Imaging Spectroradiometer (MODIS) and the Clouds and the Earth's Radiant Energy System (CERES) onboard on the Aqua satellite. This finding focuses later studies on two high cloud scene types that are well detected by the MLS; deep convective plumes that form from moist ascent, and their adjacent outflows that emanate outwards several hundred kilometres.

The second part of the thesis identifies and characterises two different high cloud scenes in the tropics. Direct observational data is used to refine calculations of the climate sensitivity to upper tropospheric humidity and high cloud in different conditions. The data reveals several discernible features of convective outflows are identified using a large sample of MLS data. The key finding, facilitated by the use of co-location, reveals that deep convective plumes exert a large longwave warming effect on the local climate of $52 \pm 28\,\mathrm{W\,m^{-2}}$, with their adjacent outflows presenting a more modest warming of $33 \pm 20\,\mathrm{W\,m^{-2}}$.

Keywords Aura MLS instrument, high clouds, longwave radiation budget, A-train satellite data, cloud ice, tropical convection, co-located analysis, high cloud radiative forcing, stratosphere-troposphere exchange

Acronyms

A-train Afternoon train (EOS satellite constellation)

ADM Angular Distribution Model

AER Atmospheric and Environmental Research

AIRS Atmospheric InfraRed (IR) Sounder

AMSR-E Advanced Microwave Scanning Radiometer - EOS

AMSU Advanced Microwave Sounding Unit

ASR Absorbed Solar Radiation

BADC British Atmospheric Data Centre

CALIOP Cloud-Aerosol light detection and ranging (Lidar) Instrument with Orthogonal Polarisation

CALIPSO Cloud-Aerosol Lidar and Infrared Path-finder Satellite Observations

CCM3 Community Climate Model 3 (number refers to software version)

CERES Clouds and the Earth's Radiant Energy System

CFCs Chlorofluorocarbons

CIRs Cloud Induced Radiances (EOS MLS)

CPR Cloud Profiling Radar

CRF Cloud Radiative Forcing

CTH Cloud Top Height

CTP Cloud Top Pressure (or approximation to CTP)

CTS Cross-Track Scanner

CWC Cloud Water Content

DISORT DIScrete Ordinate Radiative Transfer

ECMWF European Center for Medium-range Weather Forecasts

EM Electro-Magnetic (Spectrum)

ENSO El Niño Southern Oscillation (index)

EO Earth Observation

EOS Earth Observing (System or Satellite)

ERA ECMWF Re-Analysis (data)

ERB Earth's Radiation Budget

ERBE Earth's Radiation Budget Experiment

FM3 Flight Model 3 (number refers to model of scanner)

FoV Field of View

GCM General Circulation Model, or Global Climate Model

GEOS-5 Goddard Earth Observing System (model version 5)

GHz GigaHertz

GhG(s) Greenhouse Gas(es)

GISS Goddard Institute for Space Studies

GMP Gridded Meteorological Product

GSFC Goddard Space Flight Center (NASA)

H Horizontal (polarisation)

HIRDLS HIgh Resolution Dynamics Limb Sounder (UCAR)

HIRS High-resolution InfraRed (IR) Sounder

HITRAN HIgh-resolution TRansmission molecular AbsorptioN

HR (radiative) Heating Rate (local RT unless specified)

HSB Humidity Sounder Brazil

IIR Infrared Imaging Radiometer

IR Infra-Red (EM)

ITCZ Inter-Tropical Convergence Zone

IWC Ice Water Content (or Clouds)

IWP Ice Water Path

JPL Jet Propulsion Laboratory (NASA)

L1 Level (of data processing)

LBLRTM Line-by-line Radiative Transfer Model

LEO Low Earth Orbit (Satellites)

LHS Left Hand Side (of figure)

LIDAR LIght Detection And Ranging

LS Lower Stratosphere (or Stratospheric)

LT Lower Troposphere (or Tropospheric)

LTE Local Thermodynamic Equilibrium

LW Longwave (EM)

LWC Liquid Water Content (or Clouds)

LWP Liquid Water Path

MAF MAjor Frame (of EOS MLS retrieval)

MAS MODIS Airborne Simulator

MCS Mesoscale Convective System

MIF MInor Frame (of EOS MLS retrieval)

MLS Microwave Limb Sounder (EOS unless specified)

MODIS MODerate-resolution Imaging Spectroradiometer

NASA National Aeronautics and Space Administration

NCAR National Center for Atmospheric Research

NH Northern Hemisphere

NOAA National Oceanic and Atmospheric Administration

NWP Numerical Weather Prediction (model)

OLR Outgoing Longwave Radiation

OMI Ozone Monitoring Instrument (EOS Aura)

ppbv parts-per-billion by volume (mixing ratio)

ppmv parts-per-million by volume (mixing ratio)

RADAR RAdio Detection And Ranging

RAP Rotating Azimuth Plane

RB Radiation Budget

RHS Right Hand Side (of figure)

RMSE Root Mean Square Error (statistics)

RRTM Rapid Radiative Transfer Model

RT Radiative Transfer

SH Southern Hemisphere

SSF Single Scanner Footprint

SW Shortwave (EM)

THz TeraHertz

ToA Top of Atmosphere

TTL Tropical Tropopause Layer

UARS Upper Atmospheric Research Satellite

UCAR University Corporation for Atmospheric Research

UT Upper Troposphere (or Tropospheric)

UT-LS Upper Troposphere - Lower Stratosphere

UV Ultra-Violet (EM)

V Vertical (polarisation) or Volume (atmospheric physics)

V2.2x Data version 2 (level 2 un-gridded geophysical product unless specified)

VMR Volume Mixing Ratio (PPMV or PPBV)

WV Water Vapour

WVP Water Vapour Path

List of Figures

Contents

1 Introduction

This thesis examines high clouds and their interaction with the Earth's climate using data reported from several satellite instruments that form a constellation known as the A-train. The A-train is unique, as its satellites follow each other in a polar orbit. This allows co-located comparisons to be made between measurements that are close in both space and time, therefore producing valid comparisons (Froidevaux et al. 2006). This study focuses on cloudy-sky observations from the Microwave Limb Sounder (MLS), a passive instrument onboard the Aura satellite with two radiometers that view mm and sub-mm wave energy that along the edge of the Earth's atmosphere. MLS is a sensitive instrument that can monitor the natural microwave radiation that is transmitted from the atmosphere to space. Its viewing geometry differs from most satellite instruments that usually view downward into the atmosphere.

Different instrument payloads observe the characteristics of one or more designated cloud parameters by monitoring the intensity of Electro-Magnetic (EM) radiation at different wavelength intervals. Many properties of clouds can affect the amount of scattered and emitted EM radiation at certain frequencies known as spectral channels. Whilst some instruments view radiation emerging from cloud tops, others detect radiation that emerges from their interior. As a result, each cloud product that is derived from these received signals is produced using a unique detection algorithm. The uncertainties of each cloud product, and their contrasting spatial and temporal resolutions, makes valid inter-comparisons between cloud parameters challenging. The application of co-location to characterise cloud properties is explored to establish links between ice clouds and the Earth's longwave energy budget in the low latitudes. The study will also demonstrate how to constrain estimates of longwave cooling to space in the presence of different high clouds.

Cloud formation is an essential process in the Earth's hydrological cycle. Clouds are collections of liquid droplets (warm clouds), frozen ice crystals (cold clouds) or a combination of both (mixed phase clouds). They are made of water that is suspended in the atmosphere above our planet's surface. Several processes can lead to the formation of clouds. Convective cloud-types are formed when heating from the Sun provide the thermal energy to drive moister air upward (ascend) into the atmosphere. If these parcels of air are cooled sufficiently,

warm clouds can then form by cooling. Clouds can also form near the surface of the Earth by addition of water vapour through evaporation. Rising air parcels can lead to cloud formation if the air becomes saturated, where at a specified temperature and pressure the air can hold no more water in its gaseous phase. At this point the air begins to condense on particles known as cloud condensation nuclei. These cloud droplets then grow by collision to form larger droplets, until the upward and downward circulation structure within the cloud can no longer hold the droplets aloft. At this point the cloud begins to fall as rain. The process whereby cloud particles fall to the surface without being evaporated on their journey is known as precipitation.

Ice clouds can only form at temperatures below the freezing point of water, which occurs frequently at high altitudes and at the high latitudes. They are formed by similar processes as liquid water clouds, but are found in colder parts of the world. Ice clouds can also form through a process of deposition, whereby water vapour freezes upon contact with existing ice crystals or ice cloud condensation nuclei. According to Rossow & Schiffer (1999) clouds may appear in non-convective layered sheets such as stratus, or take the form of thin fibrous wisps, as in the case of cirrus. Clouds can also show un-inhibited upward growth known as free-convection that form "cauliflower-shaped" collections known as cumulus. Deep towers of cumulus are formed through strong upward motion, often with icy interiors at their tops. These clouds are known as cumulonimbus clouds, forming frequently around the tropical regions, which are the focal high cloud type in this study.

Cloud representations in global weather and climate models are based on limited set of observations, such as cloud top altitudes, thermodynamic phase and their location. A global coverage of clouds from remote sensing instruments has recently provided a wealth of information on clouds (Rossow & Schiffer 1999). The use of this data complements prior in-situ measurements from aircraft and weather balloons that characterise local cloud parameters, such as particle size and shape spectra (Liou 1986, Stephens et al. 1990). The bulk property analysis that is used to characterise the average cloud properties found at different temperatures, humidities and pressures is known as cloud parameterisation. These representations of clouds present no consideration for the diverse variability in clouds that are observed in nature (Heymsfield 1984, McFarquhar & Heymsfield 1997). As a result, studies have presented a large range of sensitivities in response

to future changes in climate (Solomon et al. 2007). Recently, high quality data on the interior of high clouds have been provided by space-borne instruments, such as those onboard A-train satellites. These include: the MLS instrument onboard Aura, the Moderate-resolution Imaging Spectroradiometer (MODIS) onboard Aqua, and the twinned CloudSat and Cloud-Aerosol Lidar and Infrared Path-finder Satellite Observations (CALIPSO) mission (Stephens, Vane, Boain et al. 2002*b*). Together, these instruments report detailed and coincident information on the vertical composition of high clouds across the globe that was never before possible.

The remainder of Chapter 1 discusses the climate system and how clouds affect the Earth's energy balance. The A-train satellites and their instruments are described in Chapter 2. This includes details about the satellite orbital configuration, instrument viewing geometries, and the various different cloud products used in this study. Early in this study MLS ice cloud detections are validated in a quantified manner, using relevant data processing and the co-located methods described in Chapter 3. Two algorithms are developed in this study to derive cloud-top pressures for comparisons with MODIS and Clouds and the Earth's Radiant Energy System (CERES) data. Studies in Chapter 4 map statistics of high cloud coverage using their individual cloud-top pressures (CTPs) and the errors associated with each detection method. Using these errors, analysis was conducted to estimate whether CTPs derived from CERES and MLS are consistent with one another, and also whether they are consistent with the MODIS CTP product.

In the second half of this thesis, studies focus on tropical high clouds and the local radiation budget. Chapter 5 discusses how a cloudy-sky radiative transfer model (RTM), detailed in Section 1.6, can be used to further our understanding of high cloud processes. The RTM reports Outgoing Longwave Radiation (OLR) where the CERES instrument undertakes simultaneous measurements, so the validity and errors of cloudy-sky radiation budget calculations can be examined in the context of high clouds. The following analysis is based on the outputs from this model simulation. Firstly, two case studies are used to examine the local characteristics of high clouds in the context of several physical and chemical parameters; potential temperature, water vapour, ozone, liquid water content and vertical wind tendencies. A cloud-edge detection scheme is then presented in Chapter 6 to identify two types of high clouds associated with warm convection

that are frequent in the low latitudes; optically thick ice clouds within the interior of convective plumes, and adjacent optically thinner cirrus located within the outflow of convection. An estimate is then provided for the relative longwave cooling effect of high clouds within the conditions of different two scene-types. Final conclusions for this thesis work and opportunities for further studies are detailed in Chapter 7.

Several fundamental questions are addressed by this thesis: Are MLS detections of high clouds consistent with measurements from other A-train satellite instruments? What are the physical links between vertical motion, upper tropospheric water vapour and ice concentrations? How is moisture transported between the troposphere and stratosphere? Can relationship between ice clouds and the OLR be quantified? What are the cloud radiative forcing from tropical anvil clouds and their convective outflows? What value do co-located comparisons offer and how can their application improve the representation of cloud parameters in global weather and climate models.

1.1 Sources of Atmospheric Radiation

Electromagnetic (EM) energy is emitted as radiation from all matter. Energy emitted from the Sun and the Earth are characterised each by a unique intensity curve that is wavelength dependent. This is usually represented by a spectral energy density curve, defined as the energy per unit volume per unit frequency interval. The energy received from the Sun is known as the solar radiation, emitted from the surface corona at $\sim 5800\,\mathrm{K}$. Energy emerging from the Earth is known as terrestrial or longwave (LW) radiation, emitted at a mean temperature of 288 K. The solar and terrestrial energy curves do not overlap significantly, due to the striking differences in the temperature of these bodies. The total energy received by the Sun almost exactly equals that emitted as LW from the Earth's energy system, maintaining a relatively stable climate on Earth.

When energy from a body is emitted into space, the intensity of energy is distributed across a range of frequencies and its re-emitted radiation is characterised by a Planck curve. Planck's law states that black body radiation has a characteristic and continuous frequency spectrum that only depends on the temperature of the body. A black body is a theoretical object that absorbs all radiation falling upon it and in a steady state must re-emit the same amount of energy as it ab-

sorbs. Objects rarely absorb and radiate as a perfect black body. This is a special case defined by Kirchoff's law of thermal radiation where the spectral emittance, the ratio of emitted radiance to the radiance emitted by a black body, is equal to unity. Radiance is a measure of the quantity of radiation that passes through or is emitted from a surface (body) and falls within a given solid angle in a specified direction. A grey body is one whose spectral emittance is between zero and one, indicating that a portion of the incident energy is transmitted or reflected from that object.

When radiation enters the atmosphere facing the Sun it interacts with matter. The upward and downward energy fluxes from different components of the Earth's system in the atmosphere are best understood by a two-stream model of Earth's global energy budget. Figure 1 indicates the relative magnitudes of the main flux densities (irradiance) as global mean flux densities. These values represent the flow of energy per unit area and unit time in units of Watts per square metre, referred to in the following text as energy.

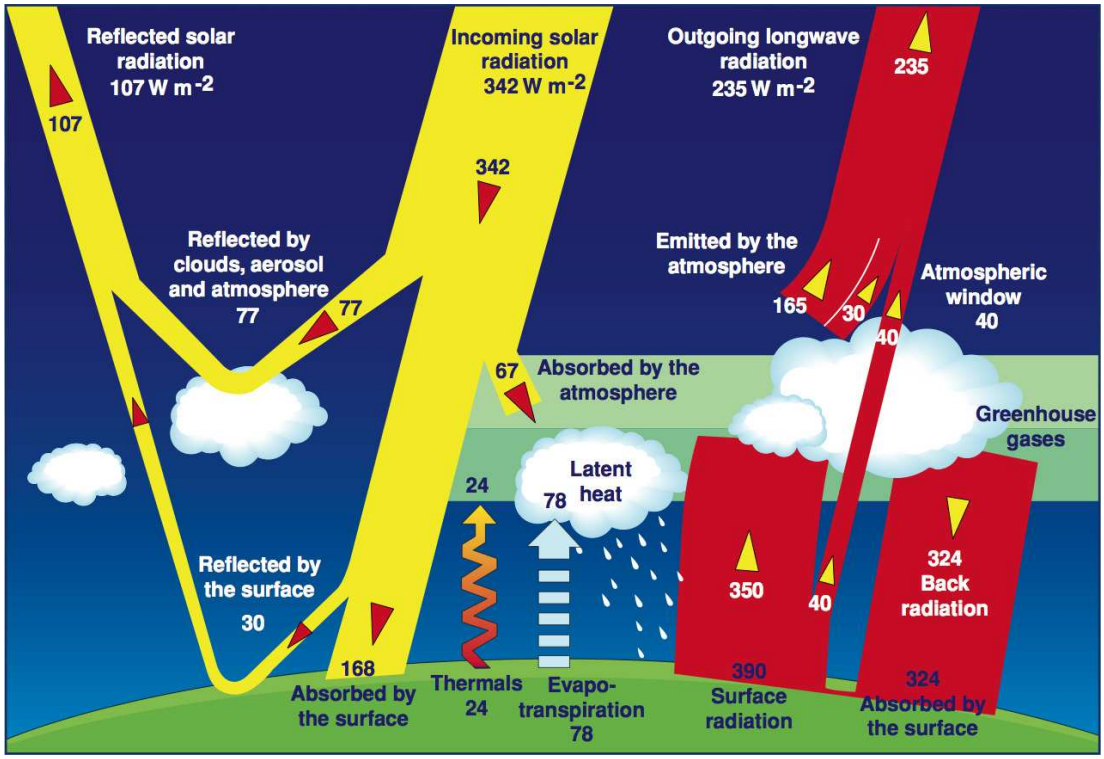

Figure 1: Figure showing the key components of the Earth's energy system. The arrows indicate the global and annual mean flux densities (irradiances in Watts per square metre of the Earth's surface) entering and leaving the system. Solar radiation is indicated in yellow, the terrestrial in red, convective transport by thermals as a red zigzagged arrow and the latent heat transport as a light blue dashed arrow. Source: www.science.larc.nasa.gov/ceres/.

1.2 The Global Energy Budget

The radiation budget is often defined as the net energy balance between the shortwave (SW) and LW components measured at the Top of the Atmosphere (ToA). LW radiation is emitted from the Earth's surface and atmosphere that is assumed, on a global space-scale and long-term climate time-scale, to balance the Absorbed Shortwave Radiation (ASR) (Wielicki et al. 2002). On a local scale the budget is measured per unit area in a column of atmosphere (Harries 2000). To enable us to visualise the global energy budget, we describe the mean flux densities in the atmosphere from different components of the system. Different components of the Earth's system interact with EM radiation of different frequencies in different ways. The main components of the Earth's energy budget are described later in this chapter. Section 1.3.1 highlights the principal greenhouse gases and how each has a unique spectral signature of absorption and scattering. A general description in Section 1.3.3 then summarises the importance of different types of clouds and their altitude in the moderation of the Earth's radiation budget.

As a global mean average $342\,\mathrm{W\,m^{-2}}$ of solar energy enters the ToA, and $107\,\mathrm{W\,m^{-2}}$ of this energy is reflected back to space by components of the Earth's energy budget surface that include: clouds, suspensions of tiny airborne particles known as aerosols and atmospheric gases. A small portion of solar energy, around $67\,\mathrm{W\,m^{-2}}$, is absorbed by the atmosphere and is irradiated back to space as LW radiation. The remaining energy that is directed downwards towards the Earth's surface is known as the down-welling SW radiation. Of the $198\,\mathrm{W\,m^{-2}}$ of solar energy that reaches the Earth's surface, $168\,\mathrm{W\,m^{-2}}$ is absorbed by the surface whilst around $30\,\mathrm{W\,m^{-2}}$ is reflected back to space. The incoming solar radiation at the top of the atmosphere (ToA) minus the reflected solar radiation is known as the ASR. A net absorption of solar energy at the surface is balanced by a net loss of LW radiation from the Earth's surface. Upwelling LW radiation is partially absorbed and scattered on its journey to space whilst it is transmitted through the atmosphere. In addition to LW and SW radiation, energy can be transported upwards by several different mechanisms. Evapotranspiration from vegetation and release of latent heat into the atmosphere comprises a net loss of $78\,\mathrm{W\,m^{-2}}$ from the Earth's surface, see Figure 1.

At the tropics, LW energy leaves the Earth's surface as heat within turbulent eddies. The transport of heat and moisture by positive buoyancy is known as

convection. As a net global long term mean convection comprises $24\,\mathrm{W\,m^{-2}}$ of the global mean upwelling energy. Convective storms dominates the atmospheric heat transport at the tropics, since the effect of the Earth's rotation that is required for cyclonic motion is weak near the Equator i.e. the respective Coriolis parameter is close to zero. Intense solar heating of air near the surface at the tropics results in pockets of relatively warm and moist air that is less dense than the air which overlies it. These pockets of buoyant air frequently form within the moist tropics, and within extra-tropical convective cells, heat energy is transported upward. Within the free troposphere, the portion of the Earth's atmosphere above any surface inversion and the effects of surface mixing, the unstable atmosphere where convection occurs is characterised by a decreasing temperatures as altitude increases. Rising air parcels within convective plumes cool as they expand, through a process of adiabatic expansion.

A saturation point is often met during moist ascent where water vapour precipitates either through; condensation (vapour to cloud water droplets) or by deposition (vapour to cloud ice particles), with suspensions of these particles in the atmosphere known as clouds. Condensation of water vapour into liquid cloud droplets involves the formation of inter-molecular bonds, releasing a global mean of $30\,\mathrm{W\,m^{-2}}$ into the atmosphere. As these phase changes involve forming bonds, heat latent heat energy is released. Precipitation that falls from these clouds dries the atmosphere, whilst radiative cooling of the cloud and mixing with the environmental air through atmospheric eddy currents and through its transport poleward causes descend. The region of sinking motion that occurs adjacent to convection is known as dissipation.

An excess of energy absorbed by the Earth's surface, atmosphere, oceans, cryosphere and biosphere causes the system to heat. Cloud particles and greenhouse gases in the atmosphere absorb a large portion of LW radiation upwelling from the Earth's surface, allowing only $40\,\mathrm{W\,m^{-2}}$ of energy to escape to space through the atmospheric window. A large portion of LW energy, $324\,\mathrm{W\,m^{-2}}$ of back-radiation, is emitted downward toward the surface from the atmosphere. The remaining $195\,\mathrm{W\,m^{-2}}$ of terrestrial energy is emitted in the upwards hemisphere by radiatively active gases and clouds. The globally averaged long-term mean of upwelling LW radiation emerging from the atmosphere and the surface is around $235\,\mathrm{W\,m^{-2}}$ (Harries 2000, Maurellis & Tennyson 2003). A recent update of the Earth's global annual mean energy budget of $239\,\mathrm{W\,m^{-2}}$ was provided by

Trenberth et al. (2009) with the use of new observations and data analyses from 2000 to 2004. This was achieved using data from the CERES instrument that forms part of NASA's Terra satellite. The main uncertainties in the calculation arise from estimates of cloud and aerosol absorption (Trenberth et al. 2009).

Since the late 1970's a steady increase in the net ToA LW emission has been observed from space-borne instruments, which have coincided with global temperature rises to present day (Wielicki et al. 2002, Trenberth et al. 2002). A lack of continuity in Earth Radiation Budget (ERB) measurements have resulted from a 3 month break in NOAA satellite monitoring in 1993, in addition to a recent offsets due to calibration changes accounting for an overall uncertainty of $\pm 2.5\,\mathrm{W\,m^{-2}}$ (Trenberth et al. 2002). Running between 1979 to present, ERB measurements have been undertaken by several different satellite instruments including the more recent CERES instrument onboard the Terra and Aqua platforms. It is unclear whether a decadal trend or cycle exists in the OLR due to a lack of consistency and overlap between different space borne datasets (Wielicki et al. 2002, Trenberth et al. 2009).

1.3 Interactions between Radiation and Matter

1.3.1 Greenhouse Gases

Greenhouse gases (GhGs) are those gaseous constituents of the atmosphere, both natural and anthropogenic, that absorb and emit radiation at discrete wavelengths within the spectrum of thermal infrared radiation emitted by the Earth's surface, the atmosphere itself, and by clouds e.g. Solomon et al. (2007). The five principal GhGs in the Earth's atmosphere ordered by their relative concentration are: water vapour (H_2O), carbon dioxide (CO_2), methane (CH_4), nitrous oxide (N_2O) and ozone (O_3). Most absorption by GhGs occurs at wavelength greater than $4\,\mu$m. Since GhGs are mostly transparent to solar radiation at wavelengths typically of $\lambda < 4\,\mu\,\mathrm{m}$, as indicated by Figure 2, they contribute to the warming of the Earth's atmosphere and surface.

Spectral line curvature is caused by molecular absorption at discrete frequency bands as EM radiation is transmitted through the atmosphere and is detected by a spectrometer. Spectral line curvature shown on Figure 2 indicates a combination of absorption and re-emission of surface radiation and from other layers of the atmosphere. The spectral signatures are unique to different components

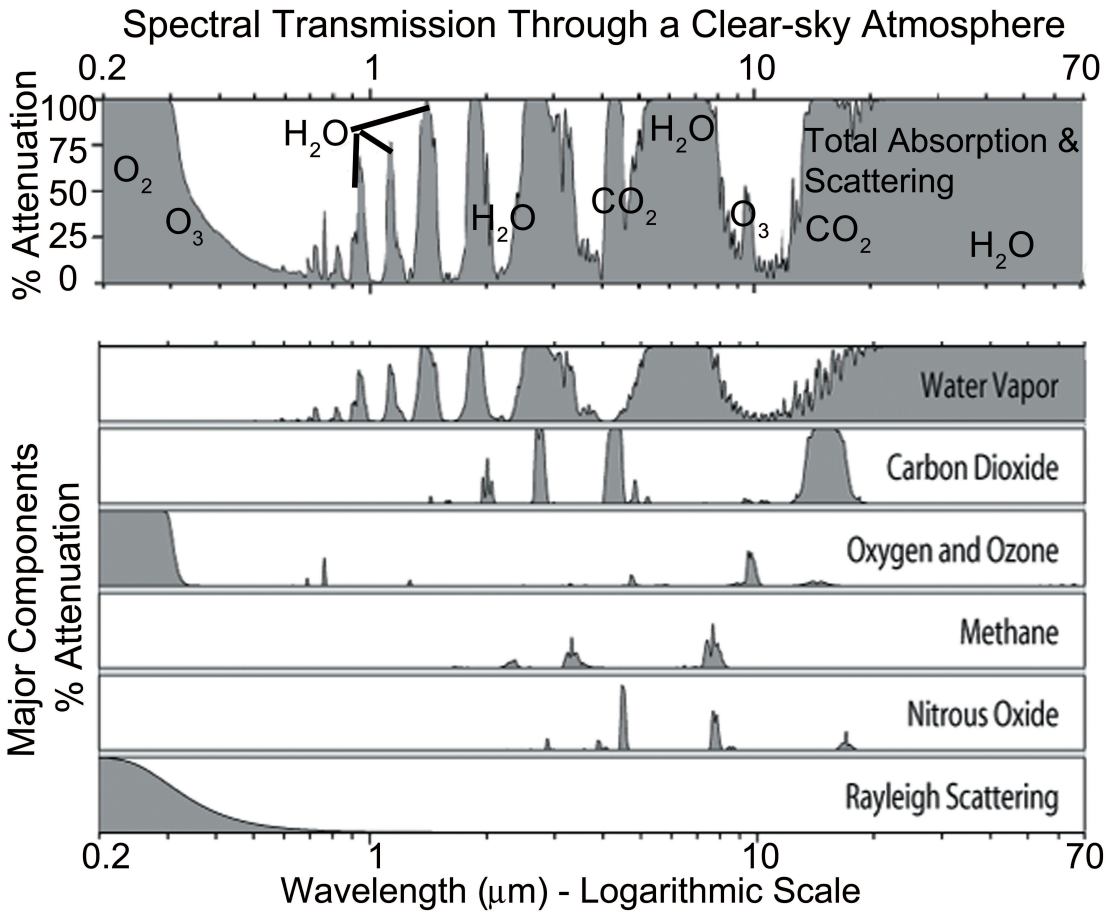

Figure 2: Figure showing a clear-sky atmospheric spectrum as viewed from the Earth's surface. The percentage of radiation absorbed or scattered through a clear-sky atmosphere is indicated by the y-axis, with respect to a range of wavelengths on the x-axis. The window bands are located where the percentage absorption is small, where the vertical sections are unshaded at a prescribed frequency interval. Bands where the atmosphere is strongly absorbing are indicated by 100 % *absorption, and are fully shaded in grey at that wavelength interval. The components of the spectral attenuation of EM energy reaching the Earth's surface are shown in the lower analysis. Source: Figure based on analysis by Dr Robert A. Rohde, University of California, Berkeley.*

of the atmosphere and allow us to identify the composition of the atmosphere and the relative concentrations of GHGs. Spectral lines present themselves on a spectrum where radiation is absorbed by bonds in molecules that vibrate, rotate or when electrons in atoms are excited to a higher energy level. Energy is then emitted back to the surroundings either as energised photons or as terrestrial energy as it is transferred through molecular collisions. In contrast to a black body curve, a spectral curve describes the transmission of radiation at different frequencies through a column of atmosphere. The atmospheric spectrum in

clear-sky conditions is shown by Figure 2.

The Earth's atmosphere acts like a grey body to upwelling LW energy at any specified location. It absorbs both a portion of upwelling LW emission and incoming solar radiation, but allows a portion of thermal energy to escape to space without significant molecular interaction within characteristic frequencies. The fraction of energy absorbed over the path of a photon depends on the greenhouse gas concentrations, solar zenith angle, and the character of clouds. Clouds exhibit a range of different spectral characteristics that depend upon particle phase, size and shape, layer thickness and cloud altitude. The regions of the thermal spectrum that are almost entirely transparent to the transmittance of radiation are known as atmospheric windows. A broad atmospheric window region is located between 8 and 12 μm, with a strong absorption from ozone at 9.6 μm.

Spectral Signatures of Greenhouse Gases Each GhG molecule has a unique absorption spectra in the thermal infra-red at characteristic frequencies known as spectral lines, as described in Section 1.3.1. These may include pure rotations at microwave and far-infrared frequencies, and vibration-rotation transitions in the thermal far-infrared. A pure rotational spectra is produced in the microwave frequency through molecular revolving about an axis directed along a centre of mass. In contrast, a vibration-rotation spectra in the infrared frequency is caused by higher energy transitions that occur between rotational sub-levels (electron orbitals) of another molecular vibrational energy level. There are two main types of vibrations: stretching and bending. During a stretch there is a change in inter-atomic distance along bond axis, whilst molecular bending occurs when there is a change in angle between two bonds. Each spectral line corresponds to absorption of radiation from photons of discrete energies, equally the frequency of the vibration-rotation levels of the bonds within a molecule. A vibration mode of a molecule is said to be Infra-Red (IR) active if there is a net absorption of EM radiation at the frequency interval of the respective atomic oscillation. Photons and atoms both possess angular momentum, a measure of spin or orbital motion. Molecules that have vibrational spectra may also have rotation spectra. This is produced through a net absorption of photons with an angular frequency that matches the atomic rotation frequency in an IR active molecule.

All GhG molecules have a minimum of one vibrational mode associated with

a non-zero dipole moment. The absorption characteristics of GhG molecules depend on their symmetry and bond strengths. A vibrational mode exists in a polar molecule where the atoms are directed asymmetrically about the centre of mass (Ebbing & Gammon 1999). In polar molecules, electrons are distributed non-symmetrically across the bond. A molecule that has an atomic dipole, but with a vibrational mode with no net change in dipole moment relating to its molecular symmetry, is not IR active. Atoms in a radiatively active molecule can oscillate by vibration and rotations. These oscillations are a function of the moment of inertia and reduced mass of the two bonded atoms (Andrews 2000). Molecules can rotate in a maximum of three orthogonal planes (xyz) about the centre of mass. When observing a substance with a space-borne broad-band instrument, the total radiated energy comprises of finite frequency intervals known as bands. Within each band, a pre-defined spectral-width, instruments can measure the intensity of molecular absorption of IR active gases in the atmosphere to estimate their concentrations.

The five principal GhG absorbers are: water vapour, carbon dioxide, ozone, nitrous oxide and methane. The key spectral lines produced by these atmospheric gases are indicated by Figure 2. Water vapour (H_2O) absorbs the largest portion of infra-red radiation, mainly due to its high abundance in our atmosphere. It absorbs strongly over a wide band of wavelengths near $6.3\,\mu$m and over a narrower band near $2.7\,\mu$m. It also absorbs over a much broader region at longer wavelengths of $\lambda > 16\,\mu$m, which is associated with its rotational transitions (Andrews 2000). Carbon dioxide (CO_2) is the most absorbing GhG produced by humans. The CO_2 spectral signature is characterised by a broad absorption line between $13\,\mu$m and $17\,\mu$m, as shown by Figure 2. Ozone molecules have a symmetric stretch that absorbs IR radiation at $9\,\mu$m, and asymmetric stretch around $9.6\,\mu$m, and a weak and broad band absorption associated with a bend at $14\,\mu$m. Both nitrous oxide and methane have several well-defined absorption bands in the infrared. Methane has two allowed modes at about $3.3\,\mu$m and $7.7\,\mu$m (Andrews 2000). These spectral lines are less well defined, as shown by Figure 2, because the spectral absorption is partially saturated by H_2O and CO_2 absorption in the same regions.

Perhaps the most important GhG is water vapour. Water molecules rotate asymmetrically about three axes, each rotational mode with a different moment of inertia (Maurellis & Tennyson 2003). In addition to the spectral lines, a re-

gion of extensive absorption across much of the IR and microwave spectral region has been identified for water vapour. This region of absorption is known as the continuum absorption and is a result of water vapour's three different rotational modes and vibration-rotation interactions. In contrast, carbon-dioxide is a linear molecule, yet it possesses an asymmetric stretch and two bending modes. Although carbon dioxide has two rotational modes, each with the same moment of inertia, it has no rotational spectrum. Water in the atmosphere frequently appears in vapour, liquid and ice phase, with each exhibiting strikingly different spectral characteristics. The main stretching band in liquid water is shifted to a lower frequency and the bending frequency increased by hydrogen bonding (Chaplin 2011). In addition, rotations tend to be hindered by hydrogen bonds, leading to rocking motions known as librations.

Spectral lines are subject to natural broadening, although this is negligibly small. Natural broadening arises because the energy levels of an excited atom can never be determined precisely because its lifetime is finite. There is also a collisional lifetime between atmospheric molecules (Andrews 2000). Two additional processes play a more significant role in the spectral line broadening and therefore decrease the precision of space-borne measurements. At higher pressures, frequent collisions occur between molecules of different discrete energies: Molecular excitation and relaxation takes place upon impact. Since higher pressures are found lower in the atmosphere, pressure broadening of spectral lines tends to decrease with altitude. For a prescribed spectral line, a Lorentzian (peak-shaped) absorption signature presents itself when pressure broadening dominates.

The second process results from Doppler broadening and occurs when observations are made during any finite point in time during the motion of molecules toward or away from the observer (Andrews 2000). At higher temperatures the average kinetic energy of molecules are greater, leading to a larger Doppler shifting and a greater spectral line broadening. The shift in observed frequency is detected about the central spectral line frequency, with a maximum absorption at its centre. At lower temperatures, Doppler broadening of the spectral lines produces a Gaussian-type distribution of atmospheric transmission about a central frequency.

1.3.2 Local Thermodynamic Equilibrium in the Atmosphere

Thermal equilibrium occurs when a system's macroscopic observations of temperature have ceased to change with time (Manabe & Wetherald 1967). This is not the case in the Earth's atmosphere, since a uniform temperature does not exist. In contrast, Local Thermodynamic Equilibrium (LTE) requires only that the equilibrium exists in some neighborhood of every point. For LTE to be valid, interactions of radiation with matter must be sufficiently weak to lead to negligible departures of the radiation from the Planck's Law, whilst matter must obey Boltzmann distribution that describes the molecular state of energies (Andrews 2000). In the case of a gaseous atmosphere, the Boltzmann distribution describes the equilibrium ratio resulting from collisions between the gas molecules. We consider exposing the molecules within an isothermal cavity to the surroundings; where upon the physical contact between molecules results in transferral of kinetic energy until the received and emitted energies are balanced. At this point the temperature of the isothermal cavity equals that of the surroundings in a steady-state (non-evolving) system.

It is often a good assumption that the atmosphere is in a state of LTE for calculations of solar and long-wave radiation transfer in a cloudless atmosphere. This is because the parameters that control the variability in temperature on a small space and time domain act too slowly to significantly affect our calculations of radiation transfer (RT). We refer to calculations of radiation flow through a column of atmosphere as radiative transfer theory (Saunders et al. 2005, Stephens et al. 2001). However, the atmosphere is rarely in a state of thermal equilibrium, as its vertical temperature structure is non-uniform due to diurnal cycles in the surface heating and cooling. The atmosphere constantly responds to changes in temperature, unmixed GhGs, solar zenith and clouds on a relatively short time-scales of less than a day.

In RT calculations, air contained within small vertical slabs of atmosphere that form the atmospheric column is treated as though in thermal equilibrium. In these simulations, each slab possesses a fixed temperature, density and comprises of uniformly mixed GhGs and where present uniform cloud particles. Adjacent slabs are treated as entirely separate in their physical properties. For cloudy-sky conditions the atmosphere is less likely to be in a state of thermodynamic equilibrium and RT calculations may require calculations at a much higher vertical

resolution than clear-sky calculations. In addition, vertical motions are constantly mixing particles in both the horizontal and vertical domain. This results in large uncertainties in cloudy-sky RT and calls for much closer comparisons of cloud properties and highly resolved vertical profiles, such as provided by several A-train satellite instruments.

On the short time-scales of cloud evolution, cloud droplets are often not in thermal equilibrium with the surrounding air. As a result, the cloudy-sky atmosphere is often characterised by a state of radiative-conductive exchange (Samuelson 1970). In this process, cloud particles heat by conduction with the surrounding gas molecules and adjacent layers of atmosphere, due to a thermal gradient between particles of a gas-cloud mixture.

1.3.3 Clouds

Clouds are important regulators of climate, and global changes in cloud properties can alter the flow of energy both into and out of the Earth's energy system. Both ice and liquid cloud particles reflect incoming solar radiation back to space, reducing the ASR by the Earth-Atmosphere system helping to cool the surface of the Earth. Ice particles contained within high clouds tend to reflect or scatter a large portion of incoming solar radiation, whilst LW radiation is generally absorbed. The overall effect of clouds on the radiation balance is not fully understood (Harries 2000).

High clouds, such as cirrus, are largely composed of ice crystals that form at sub-zero temperatures at high altitude where condensation nuclei are present. The process of ice cloud formation is described earlier in this chapter. Ice particles interact with electromagnetic radiation through a complex process of absorption, emission and scattering processes. The cloud-energy interactions at different frequencies depend upon the ambient temperature; and the aspect ratio and shape and size distributions of the particles contained within a specified cloud. For sufficiently opaque clouds the temperature of their tops are a key predictor to the local LW forcing. High clouds tend to possess cooler tops and therefore emit less radiation from their surface than low-level clouds with warmer tops. All clouds tend to result in a LW heating of the Earth's atmosphere and surface, by increasing the portion of down-welling energy and resisting the flow of LW radiation to space. Deeper convective plumes consist of an interior composed of both ice and liquid cloud particles throughout an extensive column, drastically

reducing both the ASR and OLR.

Clouds also induce a local heating of the atmosphere and feedback upon the surface temperature. The interaction of LW and SW radiation with ice and liquid particles contained within clouds depends critically on their size and shape distributions, particle number density, altitude and the frequency of the passing radiation.

Shortwave Effects In general cloud particles cause a SW cooling at the surface, as radiation is scattered and reflected away from the down-welling beam. Only a small fraction of short-wave energy is absorbed and transferred into kinetic or LW energy by atmospheric molecules and cloud particles. There are several different types of scattering that take place when SW radiation passes through a vertical column of cloud. Scattering by atmospheric molecules is dominated by Rayleigh scattering (Andrews 2000). This form of scattering applies when the dimensions of molecules are much smaller than the wavelength of solar radiation. Cloud particles are larger than atmospheric molecules, and therefore solar energy incident upon them undergo internal scattering by geometric optics. This process is common for liquid cloud droplets contained within warmer clouds. For smaller particles, such as ice crystals and aerosols, a more complex solution known as Mie scattering is often adopted (Andrews 2000, Mie 1908). This best represent the interaction with particles whose diameter (d) scales closely with the EM wavelength (λ). Mie scattering specifically applies when $d = \frac{\lambda}{10}$ to $(40 \times \lambda)$.

Studies indicate that a high proportion of solar photons are reflected from the atmosphere by clouds and aerosols, as these are more reflective than the Earth's surface below (Fu et al. 1995). Global and annual mean observations of the net solar radiation at the top-of-atmosphere are in a general consensus that the planetary albedo of the Earth is around 30 % (Trenberth et al. 2002). Cloud reflectivity depends largely on the size of the particles, and solar zenith angle. With an equal cloud water content, a large number density of small cloud droplets or ice particles tend to be more reflective and exhibit a shorter mean free path for the penetration of solar energy into the top of the cloud. Clouds with these properties are characterised by less frequent multi-scattering between cloud particles than a smaller density of larger particles.

Longwave Effects Clouds are optically opaque to longwave radiation, and a large portion of the surface radiation emerging through cloudy-sky scenes is absorbed. Some of the absorbed energy is emitted downward, known as the down-welling LW radiation or back-radiation. It is the down-welling fraction that results in a local LW heating of the atmosphere, known as the cloudy-sky greenhouse effect. Within cloudy layers, gaseous molecules may be in thermal equilibrium with each other at a local point, however frequent interactions between cloud particles and gases means that LTE approximations are less valid than the clear gaseous atmosphere (Samuelson 1970).

The fraction of infra-red radiation absorbed by clouds depends upon the macro-physical structure, size and number density of particles. Many clouds are grey-bodies, allowing many photons to pass through without interaction with cloud particles, whilst absorbing and scattering other photons. The strong inter-molecular forces between water vapour molecules in the liquid and ice phase make it difficult for vibrational transitions to take place. EM radiation is partially absorbed by cloud water droplets and ice crystals, leading to a radiative heating of these clouds. Many clouds trap a larger amount of upwelling LW energy than the SW radiation they reflect back to space, thus resulting in a localised increase in the ambient air temperature that is felt at the Earth's surface.

1.4 Radiative Forcing

A radiative forcing is an externally imposed perturbation in the radiative energy budget of the Earth's climate system (Harries 1996). The resulting imbalance in the radiation budget leads to a change in climate parameters that result in a new equilibrium state of the climate. The IPCC defines a forcing by a global and annually averaged estimate in the net perturbation of the flux density (Solomon et al. 2007). Solomon et al. (2007) also define a surface forcing as the instantaneous perturbation of the surface radiative balance by a forcing agent. Examples of climate forcing include changes in solar input to the Earth, release of volcanic ash and aerosols, or the release of IR active gases such as CO_2 through anthropogenic activities. Ramaswamy (2001) define the radiative forcing as; 'the change in net (down minus up) irradiance (solar plus longwave; in $\mathrm{W\,m^2}$) at the tropopause after allowing for stratospheric temperatures to readjust to radiative equilibrium, but with surface and tropospheric temperatures and state held fixed

at the unperturbed values'. A radiative forcing is defined as positive if the external process acts to increase the global mean downward longwave irradiance such that it is greater than the upward irradiance e.g. through the increase of anthropogenic GhGs. The converse is true for global mean increases in the upward solar irradiance through the accumulation of scattering aerosols.

1.4.1 Water Vapour

Clouds and water vapour in the atmosphere are the two biggest regulators of the Earth's climate. Water vapour in the atmosphere acts as a strong GhG, with an average forcing of $30\,\mathrm{W\,m^{-2}}$ over the globe (Maurellis & Tennyson 2003). Water vapour exhibit a high spatially variability and is the most abundant GhG in the Earth's atmosphere accounting for around 65 % of the observed greenhouse effect (Held & Soden 2000, Sun & Lindzen 1993). The clear-sky radiative forcing of water vapour accounts for a net forcing of $+75\,\mathrm{W\,m^{-2}}$ in comparison to a clear sky carbon dioxide forcing of $+32\,\mathrm{W\,m^{-2}}$, which means that water vapour is the dominant GhG in the atmosphere (Trenberth et al. 2002, Harries 2000, Jensen 1999).

1.4.2 High Cloud Radiative Forcing

The Cloud Radiative Forcing (CRF) is defined as the difference between the all-sky Earth's radiation budget and the clear-sky Earth's radiation budget in $\mathrm{W\,m^{-2}}$ (Solomon et al. 2007, Chap. 8). High clouds induce a positive longwave radiative forcing on our climate that is counteracted by a increase in reflected shortwave radiation. The magnitude of both components on the Earth's energy budget are greatly altered by increases in cloud optical depth, a measure of opacity to passing EM radiation (Hartmann, Holton, Fu et al. 2001). Whilst thin high clouds tend to warm, thicker clouds and low clouds result in a cooling effect at the Earth's surface. Detailed understandings of cloud radiative processes are essential in our estimates of the climate sensitivity (Lohmann & Roeckner 1995). Later in this study, a focussed study discusses the relative forcing of high cloud in the low latitudes that are composed of ice at their tops, to examine their relative forcing impact on climate.

The level of understanding regarding ice cloud microphysics is challenging and remains in its infancy (Benedetti et al. 2003). There are varied approaches

for the treatment of ice cloud physics in RT, and weather and climate models, yielding strikingly different results. In particular, the small ice crystals of irregular shape that are frequently found in thin tropical high clouds are often poorly represented (Ebert & Curry 1992). Tropical cirrus is thought to exert a relatively high positive CRF where it situated above the warm and moist low latitude atmosphere (Harries 2000, Lohmann & Roeckner 1995). Paradoxically, tropical cirrus forms within the coldest temperatures of the Earth's atmosphere in the Tropical Tropopause Layer (TTL). The scientific understanding of thin cirrus and its representation in General Circulation Models (GCMs) has been inadequate, producing large uncertainties in the CRF (Liou 1986, Solomon et al. 2007, Lohmann & Roeckner 1995). In contrast, the parameterisation schemes used to describe larger ice crystals, commonly found within deep convection plumes, are generally better represented (McFarquhar & Heymsfield 1997). Studies later in this thesis examine the flow of longwave radiation in both the conditions of both thick and thin high clouds, known as the longwave component of the CRF.

1.4.3 Longwave Radiative Heating Rates

As the atmosphere is in constant dynamical motion, a state of radiation balance at any particular point in the atmosphere is rarely in balance. Rather, in the absence of convection (sensible) or latent (diabatic) heat exchange, heating or radiative cooling takes place in the atmosphere. The rate, at which the atmospheric temperature would either raise or fall due to imbalances in radiation fluxes, is known as the local radiative Heating Rate (HR). In the absence of solar absorption, these values are known as the local LW HR. HR values are valid only at a finite observation time and at a specified position in space and are most commonly reported in units of K/day^{-1}. The magnitude and sign of the LW heating or radiative cooling rate above the surface model level depends upon the spectral emissivity and temperature of the atmosphere, clouds or surface that overlies and underlies a cuboid within a nominated atmospheric column. Considering the 2-stream case, where LW radiation can only be transmitted in the upward (F^+) and downward (F^-) directions, the net radiative flux at a vertical point on an atmospheric profile is given by $F_{\text{net}} = F^+ - F^-$. By using the grey-body assumption to the Planck function, the rate of change in the local temperature at this point is therefore related to $\frac{\mathrm{d}F_{\text{net}}}{\mathrm{d}z}$. Non-zero radiative heating or cooling averaged across the entire electromagnetic spectrum implies thermal dis-equilibrium. By

radiation terms alone, the temperature of a specified cuboid of atmosphere must therefore be unstable; either rising or falling at the time of observation.

A clear-sky and well-mixed atmosphere presents a near balance between emission and absorption of electromagnetic radiation by chemical species. Atmospheric emission dominates the radiation budget in the troposphere, with water vapour and carbon dioxide contributing to a net radiative cooling at the surface of $-1.5\,\mathrm{K\,day^{-1}}$ (Andrews 2000). In the stratosphere, radiative heating exceeds cooling, driven mainly by water vapour and ozone emission, with a net heating at an altitude of 50 km of approximately $+1.0\,\mathrm{K\,day^{-1}}$. On average, the atmospheric column experiences a net absorption of LW radiation, whilst it absorbs solar radiation during the daylight hours. On a global scale, as a temporal and spatial average, a close net balance exists between absorption and emission by the Earth-atmosphere system (Hansen et al. 2005) . A radiative balance is often not achieved on a regional scale, as cloud systems evolve and move from one place to another introducing spatial contrasts in atmospheric heating. In addition, non-mixed greenhouse gases such as water vapour also impose a net radiative forcing that is rather inhomogeneous across the globe.

Atmospheric air density also plays a key role in controlling the magnitude of HRs. The thermal inertia of the air within the cube depends on the density of atmospheric molecules. More energy is required to excite gaseous molecules of the same mixing ratio within a denser cuboid of atmosphere than a less dense one of the same unit volume. This means that higher HRs are often found within less dense air above the mid-troposphere, due to the higher sensitivity to trace gases such as ozone and also to optically thin clouds.

Interpretation of RT Calculations The magnitude of radiative heating provides an estimate to the local rate of change in temperature as a result of lowing radiation between layers of the atmosphere at the time of the observation. The sign indicates either cooling (negative) or warming (positive). Whilst the local LW HR is usually negative, indicating radiative cooling from emission; it can be also positive where LW absorption by atmospheric gases or clouds exceeds its emission. Each radiatively active gas is characterised by different absorption and emission spectra. In this study, heating rates are expressed as $H_{\mathrm{LW}}[m]$ in $\mathrm{K\,day^{-1}}$ for a specified layer of atmosphere m. Equation 1 is used to determine $H_{\mathrm{LW}}[m]$, where $t = 86400\,\mathrm{s}$ represents the number of seconds in one day. In this

expression, the amount of heat energy required to raise the temperature of 1 kg of atmosphere by 1°K is known as the specific heat constant of dry air and is denoted by $c_p \sim 1004\,\mathrm{J\,K^{-1}\,kg^{-1}}$.

$$H_{\mathrm{LW}}[m]) = \frac{B(T[m])}{c_{\mathrm{p}}[m]\rho_{\mathrm{d}}[m]} \times \frac{\delta\,\chi_{\mathrm{LW}}(z[m]\,,\,\infty)}{\delta\,z} \times t \tag{1}$$

In Equation 1, $\chi_{\mathrm{LW}}(z[m]\,,\,\infty)$ represents the LW transmittance, the fraction of radiation between the wave-numbers of 10 to 3250 $\mathrm{cm^{-1}}$ leaving the layer $z[m]$ with a mean density $\rho_{\mathrm{d}}[m]$ and passing through the overlying atmosphere to space ($z = \infty$).

The ability of a substance to emit energy by radiation is referred to as its emissivity (ϵ), where $\epsilon = 1$ indicates that all incident irradiance is emitted back to the surroundings with no net absorption within a cuboid of atmosphere. In the atmosphere, ϵ comprises of two main components: (a) absorber gas chemistry and (b) the cloudy-sky parameters. Component (a) emissivities are a direct output of the gaseous absorption and scattering properties, whilst for cloudy layers (b) the emissivity is governed by the number density, particle size and shape distribution of ice particles and water droplets.

1.5 Feedbacks and Climate Sensitivity

A change in a physical process of the Earth's system in response to a climate forcing is known as a feedback process. A climate feedback is not homogeneous, and does not have an equal effect over different regions of the globe. The magnitude of a feedback processes are often an outcome of model physics and parametrisation within a General Circulation Models (GCMs) that simulate the climate using an effective radiative forcing. Some of the feedback processes represented by GCMs include: changes in the global cloud coverage and distribution, water vapour, and changes in the regional coverage snow and ice. Climate processes that amplify changes in the global mean air temperature are known as "positive feedbacks", whilst those that dampen the effects of temperature are known as "negative feedbacks" (Harries 2000).

The climate sensitivity is defined as the global annual mean surface air temperature change after the system has reached a new equilibrium in response to a doubling of atmospheric carbon-dioxide (Solomon et al. 2007). It is also referred to as the equilibrium climate change.

1.5.1 Water Vapour

An increase in the atmospheric temperature is likely to increase the absolute humidity, based on the laws of thermodynamics. The Clausius Clapeyron equation describes the exponential relationship between the saturated vapour pressure of water at a prescribed temperature and atmospheric pressure (Maurellis & Tennyson 2003). Results from studies of the 1997 El Niño, indicate that water vapour increases in the atmosphere as surface sea temperatures rise in the tropical Pacific (Loyola et al. 2006, Soden 1997). Water vapour is linked to cloud cover by the hydrological cycle. It is claimed that the fraction of clouds may increase in a warmer world, increasing the planetary albedo, and exerting a negative feedback on the climate system (Maurellis & Tennyson 2003). In contrast, a net increase in high clouds in response to increasing surface air temperatures may amplify the rate of global warming in comparison to a standard atmospheric profile (Jensen 1999).

A change in the vertical distribution of water vapour can result in either a positive or negative feedback (Allan et al. 1999). Higher altitude water vapour poses a positive feedback on the system, whilst a relative increase in water vapour concentrations within the boundary layer acts as a negative feedback. Small increases in the absolute humidity within the upper troposphere results in a large greenhouse heating, as the effective emitting altitude of the atmosphere shifts upward (Jensen 1999, Hartmann, Holton, Fu et al. 2001).

1.5.2 Clouds and Precipitation

The Hadley Circulation is a zonal mean meridional (north-south) overturning of air masses between the tropics and subtropics. This large-scale circulation is characterised by two main components (Solomon et al. 2007). One of these is a general region of forced ascent is known as the Inter-Tropical Convergence Zone (ITCZ) and is the result of trade winds that converge at the surface. The second component; the Walker Circulation, is a zonal (east-west) and vertical overturning cycle. In the East Pacific strong westerlies prevail in the layer from 400 hPa to the tropopause, which forms the upper branch of the so-called "Walker circulation" (Fueglistaler et al. 2009). West of the dateline, equatorial easterlies prevail. The observed dipole is tightly coupled to the distribution of deep convection. Future changes in these circulation patterns that form part of the global hydrological

cycle are likely to lead to altered rainfall patterns that are essential for food and water security.

Tropical SSTs largely determine where the upward branch of the Hadley Circulation is located over the oceans. During El Niño, elevated sea surface temperatures over the central and eastern Pacific Ocean cause an increase in convection and re-positioning of the ITCZ closer to the equator. The term Monsoon generally refers to seasonal reversals in the low latitude surface winds and precipitation patterns. The global monsoon system is a low latitude overturning circulation that is closely associated with the seasonal variation of continental precipitation and over the adjacent oceans (Trenberth et al. 2002). The most intense monsoons occur over south-east Asia, with other monsoons over northern Australia and tropical Africa (Solomon et al. 2007).

Spatial variability in the distribution of clouds and water vapour reduce the outflow of LW radiation to space. This causes a large local variability in the OLR for cloudy regions of the Earth in contrast to the clear-sky (Harries 1997). Noticeably, in the tropics high clouds cause a zonal mean depression in the OLR. The feedback of clouds in response to anthropogenic climate change is one of the biggest uncertainties in current climate prediction research (Hartmann, Holton, Fu et al. 2001, Solomon et al. 2007). The magnitude and sign of the cloud feedback depends on long-term trends in cloud-top height, type and thickness in response to changes in the surface temperature (Wielicki et al. 2002, Chen et al. 2002). Clouds are both linked to and feedback upon the local dynamics in response to natural or anthropogenic perturbations to the surface temperature. Heating and cooling instabilities within larger scale cloud disturbances affect the global circulation (Liou 1986). The global distribution of water vapour and clouds are intrinsically linked, since clouds form in saturated atmospheres. Recent studies by Chen et al. (2002) indicate that an intensification of sub-tropical high pressures results in subsidence, which dries the upper troposphere and clears clouds.

Tropical high clouds that form during convection and their associated outflow cirrus exert a strong positive forcing on global climate. In addition, the associated latent heat generation in the ascending branches of tropical convection leads to large-scale condensation and precipitation, whilst the local evaporative cooling of these cloud particles drives both neighbouring descent and the large scale dynamics of the Earth's atmosphere. Several important links between convection, latent energy exchange and dynamics dominate the cloud feedback processes. Past

studies from climate models indicate that changes in troposphere-stratosphere exchange (STE) processes, such as the moistening of the upper troposphere, explain much of the observed tropical expansion (Allen et al. 2011). In contrast, increases in low clouds such as oceanic stratocumulus would exert a negative feedback on the climate system. These clouds are most abundant in the presence of a surface layer temperature inversion, so their cloud-top temperature and associated longwave emission can be higher than the underlying surface. Stratocumulus clouds usually consist of relatively small water droplets that more effectively reflect solar radiation back to space, thus cooling the Earth's surface (IPCC 2001).

Previous studies of tropical cloudy skies indicate a linear increase (7 %/decade) in upper tropospheric relative humidity over the tropical Pacific Ocean (Hartmann et al. 1992). This has coincided with global air temperature rises from the 1980's and an increase in the convective activity and fraction of high clouds. In the same study, the radiative cooling rate from the Earth's surface was found to increase by $3\,\%\,\mathrm{K}^{-1}$ in response to sea surface temperature rises, whilst during the same period atmospheric humidity and the resulting greenhouse warming of the atmosphere also increased. Cloud-tops in the vicinity of the tropical tropopause layer are very cold, and reduce the OLR more than low clouds (Trenberth et al. 2002). A play-off exists in the tropics between long-term increases in cloud top height and increases in atmospheric temperature. These two effects act to cancel out the instantaneous effect of increasing sea surface temperatures on the observed OLR. A radiative-convective equilibrium model confirmed that the temperature at the top of tropical anvil clouds remains roughly constant as the surface temperature input was changed (Hartmann & Larson 2002).

1.6 Radiative Transfer Models

Radiative transfer models (RTMs) describe the interactions that take place as electromagnetic radiation is transmitted from a point source to another distant point through a combination of absorption, emission and scattering. In the atmosphere, RTMs are used to specifically model the flow of EM radiation between the Earth's surface and space. This EM radiation is often categorised into the solar and terrestrial components, as indicated by Figure 1. RTMs outputs vary and are often specified by the user for their desired application. Whilst RTMs can perform calculations of the energy budget, greenhouse gas and cloud forcing

may also be produced. Furthermore RTMs may be used to estimate the climate feedback parameter; a measure of the radiative response of the climate system to a global surface temperature change induced by a radiative forcing in units of $\mathrm{W\,m^2\,K^{-1}}$ (Solomon et al. 2007). An increasing demand for increasingly accurate RTM calculations for weather and climate modelling must be met with a more complete description of the atmosphere through precise and detailed measurements. These efforts been partially hampered by lacking cloud measurements (Solomon et al. 2007).

The clear-sky RTM input comprise: atmospheric and surface observations of temperature, humidity and composition of absorbing atmospheric gases and non-water particulate suspended in liquid or solid phase in the atmosphere known as aerosols. A cloudy-sky radiative transfer model uses parameterisations and absorption coefficients that represent cloud optical properties in different conditions where atmospheric profiles contain water particles in the liquid or solid (ice) phase. The atmospheric profile describes how a quantity varies with altitude and forms a fundamental part of the RT input. Recent improvements to RT calculations and their validation are aided by a wealth of earth observations in conjunction with direct radiation budget measurements. Much of the required composition data used in this thesis is obtained from data products from the Aura chemistry satellite instrument MLS, whilst the CERES Aqua satellite monitors the radiation budget to allow direct comparisons between model simulations and observations. These instruments and their relevant products are discussed later in Section 2.3.

For radiative transfer models to perform an approximation to the radiative transfer equation, a suitable input of the spectral line positions and shapes are also required. Line parameters describe the distribution of emission and absorption across the electromagnetic spectrum and are pre-calculated for each spectral line over a range of conditions by laboratory spectral analysis. Each spectral line is characterised by a set of parameters; the zero-pressure line centre, pressure induced line shifting and the temperature dependence on spectral line broadening (a Voigt profile absorption curvature). A collection of line parameters is called a line list. The high-resolution transmission molecular absorption (HITRAN) database described in Rothman et al. (2009) forms a comprehensive line list and is the source of spectral data for radiative transfer calculations in this thesis. With use of these parameters the RTM emulates the absorption and emission at

the frequency of each spectral line as a function of pressure, temperature and gas concentration. It then computes the transfer of radiation between single, multiple, or the entire layer of a model atmosphere. Calculations are also computed that inform the user of the convergence of radiative energy at each modelled layer of the atmosphere, known as radiative heating rates. Radiative heating rates indicate the local balance between absorption and emission and their interpretation is discussed in Section 1.4.3.

To precisely produce a RT output over the entire atmospheric spectrum, the model must undertake calculations at narrow frequency separations to represent each interaction between matter and EM radiation. These so-called line-by-line radiative transfer models result in computationally tiresome and timely calculations. This is compounded further by recent increases in the number of required calculations; a consequence of both increasing observations and the requirement for numerical outputs of a finer spatial grid (Stammes et al. 1988). This increasing demand has outweighed computer processing power, calling for rapid radiative transfer models (RRTMs) that can report similar accuracy and perform calculations much faster. RRTMs require effective parameterisation to account for the non-grey (multi-scattering) gaseous absorption at each frequency interval, to model the change in spectral intensity as a function of frequency. RT calculations are enhanced by correlating the spectral line shapes to temperature and pressure to produce a set of correlated k-distributions that considers the inhomogeneous nature of the atmosphere.

1.6.1 Atmospheric and Environmental Research Model

There are several models that are capable of computing the LW RT for cloudy sky profiles; however the majority of these schemes report radiances that must be spectrally integrated to estimate the OLR. For this study, a LW RT code is chosen from the Atmospheric and Environmental Research (AER) called the Rapid Radiative Transfer Model (RRTM) Version 3 (Iacono et al. 2000). The AER RRTM code is much faster than line-by-line RT calculations (LBLRTM) that are performed at the same locations, reporting a mean bias that is just $0.5\,\mathrm{W\,m^{-2}}$ higher than LBLRTMs. The key attribute of the AER RRTM code is its ability to simulate both clear and cloudy sky radiative transfer. Due to high uncertainties in measurements and representations for cloudy-sky RT calculations, a moderate resolution model is often considered adequate. For this study, the RRTM is run

on a 15 level logarithmic scale between the surface and 68 hPa. These model levels take the form of the reported vertical field-of-view of the Aura satellite Microwave Limb Sounder (MLS) data product at a viewing frequency of 240 GHz. Further details on MLS instrumentation and its data products can be found in Chapter 2.

This study considers only longwave radiation, since this component is sensitive to cloud-top altitude and cloud particle concentrations whereas shortwave reflectance is also determined by particle sizes and shapes that are not reported by Aura MLS products. The longwave component of the model is known as RRTM_LW. The spectrally integrated irradiance (in $\mathrm{W\,m^{-2}}$) is used in this thesis and is calculated by the AER RRTM model by integration of spectral irradiance across all intervals between 10 to 3250 $\mathrm{cm^{-1}}$. A single value is reported for each atmospheric profile and is used in this study as an estimate to the outgoing longwave radiation. Cloudy sky transfer calculations are performed using values of cloud water content that consists of a liquid water content and ice water content component. Outputs of LW HRs were also obtained at each model level, where the number of levels is the same as the reported levels of the MLS cloud ice measurements.

The AER RRTM consists of stored data on gaseous absorption coefficients and cloud optical properties and a RT solver. Whilst all the user supplied options make use of gaseous absorption properties developed by the AER team, for cloudy inputs a set of optical properties are used that have been developed by others for which appropriate values are computed that correspond to the RRTM's bands. In this study the DIScrete Ordinate Radiative Transfer Program for a Multi-Layered Plane-Parallel Medium (DISORT) solver option is selected. The DISORT solver is embedded into the RRTM and has therefore been modified to be compatible with RRTM. It allows us to calculate the fluxes of LW radiation through cloudy sky profiles (Stammes et al. 1988). Calculations form an approximation to the radiative transfer equation. In this study radiation is allowed to propagate in sixteen discrete directions, known as a 16-stream radiative transfer calculation. This minimises the model bias compared to the most basic two-stream approximation for all atmospheric scenes across the globe. In the RRTM, LW scattering was neglected. Cloudy layers are treated with a discrete vertical layering, such that the fractional coverage at a nominated layer is either 1 or 0.

For our studies, we select the RRTM_LW option to use cloud treatment used

by the National Center for Atmospheric Research (NCAR) Community Climate Model (CCM) Version 3 (Iacono et al. 2000). This is a frequent choice for use in General Circulations Models (GCMs). This input option is most suitable for when water and ice particle concentrations are known, such that inputs can be provided on the cloud particle density of each model layer, but no additional information is available on the cloud particle size and shapes. The parameterisations for optical depths for both liquid and ice clouds used in this study are described by Iacono et al. (2000). The RRTM_LW uses absorption coefficients to calculate optical depths for cloudy-sky layers of atmosphere. RT calculations were performed for the non-grey case i.e. neglecting longwave scattering, and also make use of correlated k-distribution parameters as described earlier in this Chapter.

Cloud Treatment To best represent the longwave radiative properties of low tropospheric clouds, liquid water content (LWC) data is input into the RRTM from the Earth's surface to pressures (p) of 316 hPa. The data was obtained from the European Center for Medium-range Forecasts (ECMWF) Re-Analysis Interim product, detailed by Dee et al. (2011). LWC data was combined with Ice Water Content (IWC) data from the MLS Aura satellite instrument, described by Livesey et al. (2007). At the overlap region between these model input ($383\,\mathrm{hPa} > p > 316\,\mathrm{hPa}$) the RRTM input forms a mean of ice and liquid water content, whilst for $IWC < 0.03\,\mathrm{mg\,m^{-3}}$ only LWC was incorporated into the model. The fractional ratio of ice to water is calculated according to the GCM parameterisation of Del Genio (1996). This scheme relates the environmental temperature to the ice fraction, with a 50:50 ice phase contribution for clouds at temperatures of 256.5 K (-16.5°C) over the Ocean. The minimum allowed ice cloud particle effective radius RRTM input is 10μ m. This value is used as a default input for atmospheric layers where parameterised ice particle size calculations produce values below this bound. The adjustment was made to allow successful RT calculations for all atmospheric profiles.

Cloud effective radii parameterisations are based on the local air temperature that is input from the version 2.2x MLS temperature product, whilst for ice particle effective radii calculations the version MLS IWC product is used also.

1.7 Net Imbalances in the System

The climate system responds to small increases in GhGs over a long period of time by feedback processes and internal non-linear dynamics. The rate of GhG emissions in the post-industrial period from carbon dioxide are faster than the climate system can respond to. The Earth is now is a state of global imbalance, absorbing $0.85 \pm 0.15\,\mathrm{W\,m^{-2}}$ more energy from the Sun than it is emitting to space (Hansen et al. 2005). This is in comparison to the net instantaneous surface forcing from post-industrial emissions, aerosols and changes in land-use of $1.80 \pm 0.85\,\mathrm{W\,m^{-2}}$. These calculations were based on climate simulations by the NASA Goddard Space Flight Center (GSFC) between 1880 to 2003 using the GISS General Circulation Model (GCM)[1] (Hansen et al. 2005). The imbalance is in part attributed to the slow response of Ocean temperature to GhG increase, due to its high thermal inertia.

The Earth's energy budget is far more dynamic than previously thought (Wielicki et al. 2002). Studies indicate that there is a net increase in the heat content of the oceans, which is closely in line with imbalances in the surface radiation budget (Lyman et al. 2006, Loeb, Wielicki, Rose et al. 2007, Wielicki et al. 2002, Wong et al. 2005). The work is based on satellite observations of clouds and the radiation budget during the period from 1970 to 2006. Many long-term trends and variability in the inter-annual and decadal OLR, is attributed to changes in the global coverage and distribution of clouds, aerosols, and in the ocean currents. Ocean cycles include the El Niño Southern Oscillation in the tropical Pacific and the North Atlantic Oscillation. The oceans are also involved in the transport of heat from the tropics to the poles, known as the meridional heat transport.

1.8 Character of High Clouds

Since the MLS instrument cannot monitor warm-clouds at lower altitudes, studies detailed in this thesis are entirely based upon the physical properties of high clouds. Satellite instruments which view clouds from above often do not inform the observer about the vertical structure of a cloud, rather providing a 2-d prospective on the cloud. It is therefore often difficult to discern whether a high cloud comprises a deep convective plume in an unstable atmosphere, or a layer of ice cloud overlies multiple layers of warm cloud or clear-skies within

[1] `http://www.giss.nasa.gov/research/modeling/gcms.html`

a stable atmosphere. Several instruments onboard the A-train, including MLS, are capable of monitoring the 3-d structure of clouds. These include the Cloud Profiling Radar onboard CloudSat, operating in the radio-wave frequency, and Cloud-Aerosol Lidar and Infrared Path-finder Satellite Observations (CALIPSO): a mission carrying a visible / infrared Lidar.

1.8.1 Formation of High Clouds

High clouds are found in a range of different locations around the globe. The clouds that MLS observes are typically thick ice clouds at the top of large convective systems (Wu et al. 2009). Ice particles within high clouds form in regions of high relative humidity at high altitudes, where temperatures are below freezing. Diffusion of moisture occurs along a vapour gradient from super-cooled water droplets to ice particles. Crystals form more favourably in "dirty" air upon tiny microscopic particles known as ice nuclei, as this lowers the required energy. This is known as heterogeneous nucleation. The local concentrations of ice nuclei are fundamental in the microphysical formation of ice. Ice crystals cannot form in temperatures above 273 K, and the structure of the crystals depend critically upon the ambient conditions. Typical shapes include dendrites, prisms, hexagonal plates, and bullet rosettes. Results from previous studies of snowflakes identify certain temperature bounds in which different ice particle shapes are most frequent (Nakaya 1954). In general ice particles are favoured over super-cooled water droplets where the ambient air temperature is below 258 K (-15°C). Within atmospheric conditions characterised by ambient temperatures between 258 K (-15°C) and 273 K (0°) a combination of both ice and water particles exist, often referred to as mixed-phase clouds. Ice particles within convective towers are usually relatively large and are well represented by spheroids. Both high clouds associated with mid-latitude weather systems and convective outflow from tropical plumes are generally characterised by much smaller crystals of irregular shapes.

1.9 Overview

A global network of measurements is required to build a more complete picture of the coverage and intricate structures 3-d of high clouds. For weather forecasting, clouds have traditionally been monitored by geostationary weather satellites; such

as the National Oceanic and Atmospheric Administration (NOAA) Geostationary Operational Environmental Satellite (GOES) series (Bedka et al. 2012). Recent space-borne data has shed some light on the vertical cloud structure, which can be assimilated into models to improve descriptions of our atmosphere into the future. In Chapter 2, a group of satellites are discussed that address this common objective. These satellites are collectively known as the NASA A-train constellation, comprising of five Earth observation satellite platforms. A-train instruments view across a range of frequencies, determining the atmospheric composition and monitoring several different types of high clouds. The instrumentation and products that are used in this thesis are discussed in Section 2.2.

Much of this thesis is focussed on measurements of ice water content from the Microwave Limb Sounder (MLS) detailed in Section 2.3.1. Cloud-top height comparisons are later made with the Moderate-resolution Imaging Spectroradiometer (MODIS) instrument, to assess whether its instrument can view the same type of high clouds at the same time and locations. The MODIS instrumentation and products are detailed in Section 2.3.2. A further A-train data product provides measurements of the upwelling radiation that is emitted from the Earth's surface and clouds using broadband radiometers that form the Clouds and the Earth's Radiant Energy System (CERES) detailed in Section 2.3.2. CERES provides information on the thermal radiation leaving the Earth's atmosphere and how it may be related to the concentration of ice particles contained within high altitude cloud. Later in this thesis, methods are detailed for the combination of A-train data and its cross-examination to enhance our understanding of different cloud properties and processes. This thesis addresses the fundamental challenge of whether we can relate cloud observations from the Earth's surface to mid-troposphere ($0 - 9\,\mathrm{km}$) to upper troposphere ice cloud and water vapour detected by the MLS from $9 - 17\,\mathrm{km}$.

2 Earth Observations of Clouds from the NASA A-train

A stable climate is essential to sustain life on Earth; yet networks of observational data from across the globe indicate that the long-term mean surface air temperature is steadily rising (Solomon et al. 2007). Whilst previous climate studies were hampered by a lack of high-quality observations (Stevens et al. 2008), a large and rapidly growing body of Earth Observation (EO) data can observe the intricacies of global change from space. These instruments improve our understanding of natural and human impacts upon the land, atmosphere, biosphere, cryosphere, oceans and land-use to promote sustainability (Asrar et al. 2001). To maintain the data from these missions a network of data storage and processing centres are distributed globally. Earth Observation scientists and instrumentation teams are responsible for developing the retrieval systems and analysing the end-user data products to deliver societal or economic objectives to the public or private stake-holders.

The A-train forms part of the Earth Observing System (EOS), a series of polar-orbiting and low inclination satellites for long-term observations of global change in components of our planet's system. The A-train consists of several satellite platforms that each carry an array of instrumentation, referred to as their payload. The instruments are designed with a unique goal, whilst their common objective is to reduce our uncertainties in our predictions of weather and climate. The spacecraft circle the planet on a path that takes them over broadly the same observation point in quick succession. This unique orbital formation of the A-train paves the way for cross-instrument validations. In this thesis studies are focused on observations of clouds and upper tropospheric (UT) water vapour (WV) from an instrument known as the Microwave Limb Sounder (MLS). The MLS instrument, onboard the Aura satellite, provides a vertical profile of ice concentrations within suitable high clouds.

EO from space-borne instruments provides some clarity into the detailed structure of ice clouds and their effect on the radiation budget. A-Train observations help to improve the current parametrisation schemes that represent complex microphysical processes that describe ice particles contained within high clouds. This can be achieved by local scale analysis using the measurements from just one instrument, yet is best achieved by a combination of complementary data

from cross-instrument comparisons. Focus in this thesis is concentrated on the representation of several high cloud processes, the dynamics of tropical convection, and the impact of high clouds on the radiation budget. General Circulation Models (GCMs) require this detailed information on cloud processes, to accurately simulate the future climate.

2.1 Earth Observation Satellites and Space Innovation

Satellites orbits around a planet in order to gather information or to relay communication signals. Their missions are objective, with each satellite instrument installed for a pre-specified goal. Many different satellites now monitor the components of the Earth's surface, atmosphere, oceans, biosphere or cryosphere. These are collectively known as Earth Observation (EO) satellites, whose instruments may be either active or passive. A passive sensor comprises of at least one satellite dish that receives naturally emitted EM radiation from the Earth, such as the Microwave Limb Sounder (MLS) onboard Aura as described in Section 2.3.1. MLS views the atmosphere with two radio-telescope dishes: one to receive THz frequency EM radiation and another for GHz (Waters et al. 2006). CloudSat and CALIPSO's instrumentation that precede Aura in the NASA A-train make use of active sensors, as detailed in Section 2.3.3, and detect properties of clouds and aerosols (Dunbar 2007). Active sensors either detect a reflected or scattered beam of EM radiation that has previously been transmitted from the satellite. A mechanical arm allows a satellite dish to point toward the parts of the atmosphere in the vertical plane that requires sampling, whilst a back and forth motion of the arm in the off-track direction allows satellites to observe a wider section across the satellite's surface track.

Data is obtained by satellites as photons of radiation recorded as "counts" are transmitted to a receiving station back on Earth where they are converted into a radiance or brightness temperature. This raw data is further processed by one or several algorithms developed by an EO data specialist to provide the end-user with access to a data product. The data is often exploited by EO specialists for a diverse range of specific end-user applications (Ayazi et al. 2012). Data produced from weather satellites help scientists predict the surface conditions in the future and also provide observational data in near real-time. This type of satellite is known as a geostationary satellite and remains fixed in space relative

to a monitored region of the Earth's surface, thus providing the continuous set of measurements required for weather forecasting.

Geostationary satellites travel eastward with respect to the Sun-Earth plane at an approximate altitude of 35,786 km above the equator such that their speed matches that of Earth's rotation. Whilst Low Earth Orbit (LEO) satellites are also used for weather forecasting, data from their instruments is often difficult to incorporate into numerical models. This is because LEO satellites are characterised by a polar orbit. In addition, as polar satellites are closer to the Earth's surface, their orbital period is much shorter in duration. This leads to irregular temporal coverage of a specified region. In their favour, the relatively close proximity of LEO satellites to the Earth's surface allows them to obtain much better spatial resolutions than instruments onboard geostationary satellites. Larger datasets often result as a consequence of their large spatial sweep and rapid scanning arms - calling for efficiently designed data processing algorithms.

2.2 Geometry of Satellite A-train Observations

2.2.1 Nadir-Sounding

A nadir sounder views vertically downward through the atmosphere from space. There are several A-train satellite instruments that view the atmosphere at nadir, including both the Moderate-resolution Imaging Spectroradiometer (MODIS) and Clouds and the Earth's Radiant Energy System (CERES) instruments onboard the Aqua satellite platform that make measurements of the atmosphere and surface by infra-red and visible detection. Nadir sounding is characterised by a high horizontal resolution of remotely sensed data, providing a plan view of the Earth's surface and atmosphere. When nadir sensors operate in an infra-red window they are sensitive to the spectral characteristics of the cloud-top and surface. As they view clouds through a shorter path-length than sensors that view across the limb, their instruments are often less sensitive to low concentrations of trace gases in the UT and stratosphere. Therefore, nadir-sounding instruments are useful for global mapping where altitude resolved measurements are not required.

2.2.2 Limb-Sounding

Limb sounding is a remote sensing term used to describe the geometry of a satellite instrument that views across the edge (limb) of the atmosphere, such as the MLS

onboard the EOS Aura satellite platform. A limb-sounding instrument receives information from an extensive strip of atmosphere, producing lower horizontal resolutions but a higher sensitivity to clouds than nadir sensors. The across-track Field-of-View (FoV) of the instruments are narrow, often a few km at the tangent point. The tangent point refers to the centre of the limb detection, where the sensor footprint intercepts the lowest altitude. In general, this is where the largest portion of atmospheric emission detected by MLS radiometers originates, yet the penetration depth varies according to the viewing frequency and atmospheric composition. The exponential density profile of the atmosphere means that the majority of the detection arises from the gases at the centre of the limb view. The MLS instrument views passive mm-wave emission across the limb and retrieves trace gas chemistry and detects clouds above the mid-troposphere. In contrast, many trace gases are undetectable by nadir instruments, because of their short viewing path-lengths. The geometry of limb sounding instruments onboard Aura and the view about the nadir plane from Aqua instruments are shown by Figure 3.

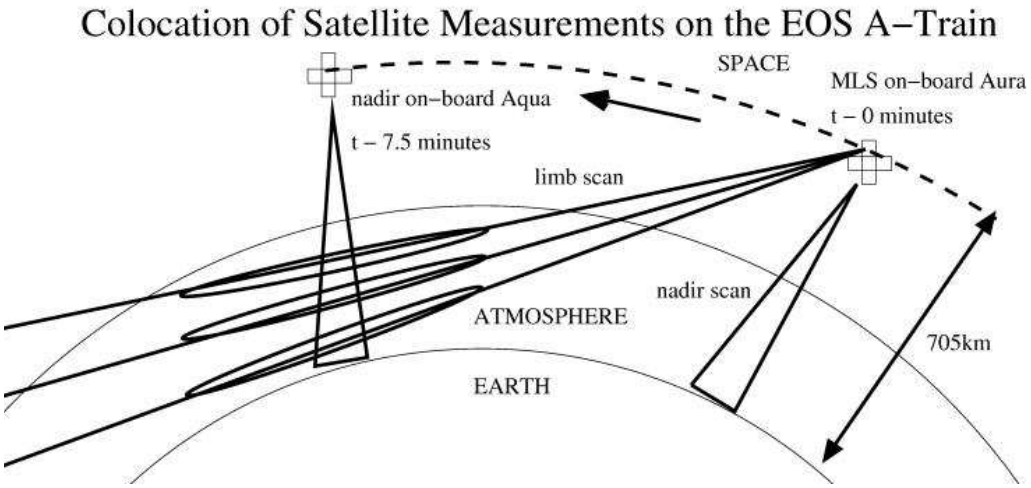

Figure 3: Geometry of nadir and limb-sounding instruments onboard two A-train satellites prior to July 2008. Observation times are shown with respect to Aura viewing the atmospheric limb (t minutes). The same region of atmosphere is sampled by Aqua nadir instruments at (t − 7.5 minutes).

Due to the exponential decrease of atmospheric density and pressure with height approximately 60 % of the atmospheric emission received by a limb-sounding radiometer originates from altitudes within 3 km of the tangent point (Livesey et al. 2006, Waters et al. 2006). The narrow FoV focuses the radiance detection on a much smaller section of atmosphere, resulting in narrow weighting

functions and a higher vertical resolution. Atmospheric profiles are obtained at a range of altitudes by mechanically sweeping the FoV in elevation.

Observations are made from the MLS instrument by assuming horizontal homogeneity between adjacent major frames, with an along-track separation of 165 km. For WV retrievals and especially for cloudy sky measurements, horizontal variability along track may be significant. Our studies demonstrate how co-located comparisons with other A-train measurements that are close in space and time can be used to reduce uncertainties in several high cloud properties.

2.3 Observations of Clouds from A-Train Instruments

In this thesis study a range of different A-train measurement data are compared for cloudy-sky scenes in the low latitudes. There are four A-train satellites that carry instruments suitable for monitoring clouds; Aura, CALIPSO (Winker et al. 2002), CloudSat (Stephens, Vane, Boain et al. 2002*a*), Aqua. We focus our studies on observations from the Aura and Aqua satellites. These satellites were launched during the early stages of A-train mission, so it is possible to undertake comparisons from late summer 2004. Our main focus is to validate the MLS detection of ice clouds and the conditions where limb-sounding is useful. The Aqua satellite possesses several wide-swath instruments viewing with a downwards geometry, that provide a high horizontal resolution of cloudy-scenes covering the same surface footprint as the MLS.

The "A-train" is referred to as the Afternoon-train. It currently consists of five polar orbiting satellites flying in formation. The planned configuration of the A-train comprises of two additional satellites: OCO failed during launch in 2009, and the Glory satellite launched on March 2011 also failed to reach orbit. All the A-train satellites are positioned in space at an altitude of ~ 705 km in a retrograde polar orbit, with a period of ~ 99 minutes. The satellite inclination, with an angle between the equator line and the orbital plane of 97.783°, means that A-train satellites are sun-synchronous. A-train satellites cross the equator at a local time of $1{:}38 \pm 8$ minutes in the ascending satellite orbit (northbound trajectory), depending upon the position of the satellite in the configuration. A-train measurements are also undertaken at the same latitudes in the descending orbit (southward track) exactly 12 hours later. The A-train configuration and satellite separation times are shown by Figure 4. Since MLS views forwards

along the track, spatially coincident observations are undertaken just 8 minute apart, see Figure 4. An overview of the NASA A-train satellite platforms and their instruments is shown by Table 1.

Later in the A-train mission, the positioning of Aura satellite in the A-train configuration was changed bringing it within 8 minutes of Aqua (Kelly 2007). Once the new A-train configuration was established, closer comparisons could be made between observations from Aura limb-viewed observations and nadir-viewed observations onboard Aqua. In addition comparisons could be undertaken between Aura observations, CloudSat and CALIPSO, with overlapping sensor footprints. Close comparisons of clouds with these two EO satellites were not previously possible, due to a 200 km offset from the main A-train orbit. The decision for the orbital dis-alignment was made during the pre-launch period due to sun glint. This would have adversely affected the CloudSat measurements during the afternoon ascending half-orbit.

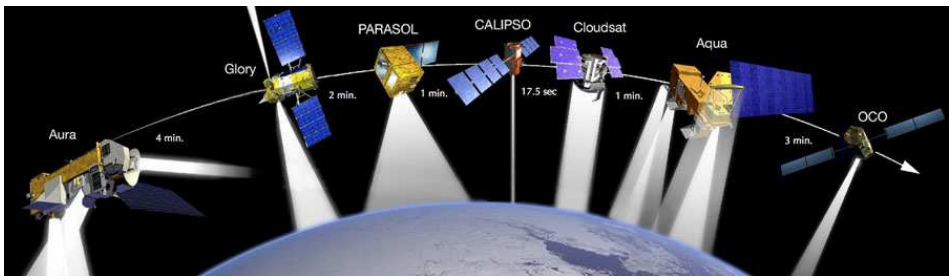

Figure 4: Artist's schematic of the NASA A-train satellites in orbit. The configuration shows the platforms: Aura, Glory, PARASOL, CALIPSO, CloudSat, Aqua and OCO. The figure also shows the time between observations undertaken by adjacent satellite instruments. The Aura times refer of different limb view, which is approximately 8 minutes behind Aqua nadir view. The Glory and OCO satellites do not form part of the NASA A-train configuration. On initial launch the local equator crossing times during the ascending (daytime) scan of the Aqua and Aura satellites were 1:30 pm and 1:45 pm respectively. The image is not to scale. Source: Nasa.gov.

The ground-tracks mapped out by A-train instruments cover much of the globe, except poleward of 82°. Their measurement footprints along the ground track beneath them are characterised by a westward migration between consecutive orbits. The spatial coverage of their observations enables sampling of much of the Earth's atmosphere and surface. When a satellite platform is southward bound with respect to the Earth's axis the orbit is referred to as descending, and whilst the platform is northward bound the orbit is known as ascending. There is

a cross-over in ground-tracks mapped out by A-train satellite instruments in the descending and ascending modes. The orbital repeat time of the A-train surface track is 16 days, as demonstrated by the surface footprints mapped on Figure 5.

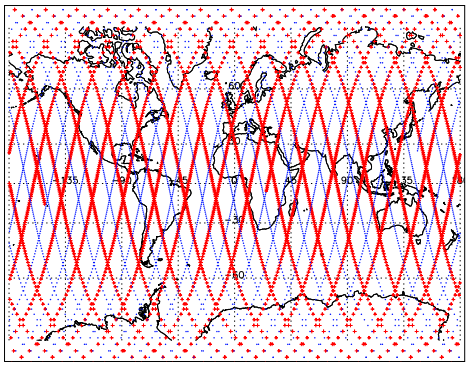

(a) +1 day track separation pattern

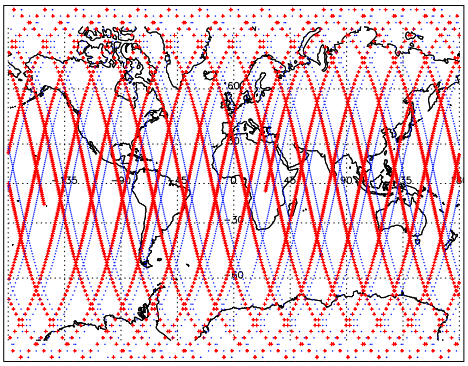

(b) +4 day track separation pattern

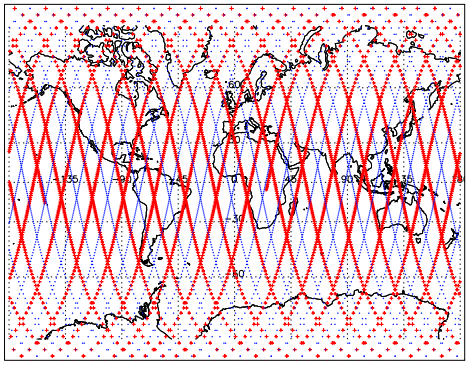

(c) +8 day track separation pattern

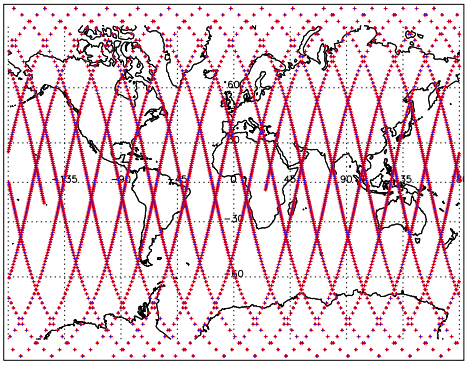

(d) +16 day track separation pattern

Figure 5: The ground-track of the Aura MLS instrument onboard Aura allows an even distribution of observations to be undertaken at latitudes of 82° *over a period of 16 days. This figure demonstrates the orbital repeat period for A-train satellites using data from 20th September, 2006 to 5th October, 2006. The mapped coverage extends from* 82°*S to* 82°*N. MLS profile positions for 20th September, 2006 are marked as small red crosses. Additional profiles are shown at separation intervals of* 24 *hr (a),* 96 *hr (b),* 192 *hr (c) and* 384 *hr (d) by small blue-filled circles. The orbital repeat period of 16 days is indicated by over overlying blue and red plots on panel (d).*

A-train instruments undertake a record of trace gases, clouds and the radiation balance by a diverse range of measurement techniques, and viewing geometries. Co-located comparisons of cloud data in this study are presented from three principal instruments onboard two of the EOS A-train satellites. These are the MODIS and the CERES instruments on the spacecraft Aqua, and the MLS

instrument onboard Aura. MODIS is an infrared and visible viewing instrument with a wide-viewing radiometer that views at nadir. The CERES instrument also views at nadir, whilst scanning either conically or sideways across the central A-train track within broad frequency bands. The differences in viewing geometry and resolution are overcome by averaging observations within the extensive limb view of MLS along the orbital track.

2.3.1 The Aura Satellite platform

In this thesis, we focus on limb-sounding observations of high clouds from the Aura satellite platform. Aura is the EOS Chemistry satellite, which was originally positioned at the back of the A-train (see Figure 4). Aura features an angle of orbital inclination (with respect to the equator) that is 25° higher, providing a near-continuous daily coverage of high latitudes. Its measurement tracks on successive orbits are 24.7° apart between each polar orbit, see Figure 5.

Aura carries a four-instrument payload, consisting of the Microwave Limb Sounder (MLS) (Livesey et al. 2007), Tropospheric Emission Spectrometer (TES) (Osterman 2008), High Resolution Dynamics Limb Sounder (HIRDLS) (Gille et al. 2011) and the Ozone Monitoring Instrument (OMI) (Levelt & Noordhoek 2002). The fine-resolution nadir and limb scanning TES instrument makes measurements of infrared radiances, in order to make estimates of atmospheric gas concentrations, temperature, and particles in the troposphere. The infrared limb-scanning instrument (HIRDLS) measures infrared emission from ozone, WV, CFCs, methane and nitrogen compounds in the troposphere, stratosphere and mesosphere. Solar back-scatter in the visible and ultraviolet is measured by the hyper-spectral OMI, which monitors ozone columns and profiles, aerosol, clouds, surface UV irradiance and several trace gases. The EOS MLS instrument is the focal instrument in this thesis. EOS MLS is a passive microwave limb detector onboard the Aura platform measuring several trace gas concentrations in the UT, stratosphere and mesosphere. EOS MLS is also able to make indirect estimates of geopotential height, and detect ice concentrations in suitable high clouds.

The MLS instrument The Microwave Limb Sounder (MLS) is a passive mm and sub-mm instrument that scans along the Earth's atmosphere at a 90° angle to nadir. Most of the natural microwave signal originates from atmospheric gases and clouds at a measurement "tangent" point. MLS was first deployed on the

-Satellite Platform	Instrument Payload			
Aura (1.1.1) **1:38pm (limb) / 1:15pm (nadir)**	MLS (Microwave Limb Sounder) mic / radio / limb	TES (Tropospheric Emission Spectrometer), ir / nadir / limb	HIRDLS (High Resolution Dynamics Limb Sounder), ir / limb	OMI (Ozone Monitoring Instrument), vis / uv / nadir
PARASOL (1.1.3) **(Polarization and directionality of the Earth's reflectances for atmospheric sciences coupled with observations from a LIDAR) 1:33pm (nadir)**	POLDER (POLarization and Directionality of the Earth's Reflectances), vis / ir / nadir			
CALIPSO (1.1.3) **(Cloud-Aerosol LIDAR and Infrared Pathfinder Satellite Observation) 1:31:15pm (nadir)**	CALIOP (Cloud-Aerosol Light detection and ranging (LIDAR) instrument with Orthogonal Polarization)	WFC (Wide Field Camera) (nadir / vis)	IIR (Imaging Infrared Radiometer) (nadir / radio)	
CloudSat (1.1.3) **1:31pm (nadir)**	CPR (Cloud Profiling RADAR), mic / nadir			
Aqua (1.1.2) **1:30pm (nadir)**	MODIS (MODerate resolution Imaging Spectro-radiometer), ir /vis / nadir	CERES (Clouds and the Earth's Radiant Energy System), ir / nadir	AIRS (Atmospheric Infrared Sounder), ir / nadir	(a) AMSR-E (Advanced Microwave Sounding Radiometer), mic / nadir; (b) AMSU (Advanced Microwave Sounding Unit), mic / nadir; (c) HSB (Humidity Sounder Brazil), mic / nadir
***OCO** (1.1.3) **1:15pm (limb)** ***Failed mission**	OCO (Orbiting Carbon Observatory), ir / nadir			
***Glory** (1.1.3) **1:33pm (nadir)** ***Failed mission**	APS (Aerosol Polarimetry Sensor), ir / vis / uv / nadir	TIM (Total Irradiance Monitor), solar pointing		

Table 1: Overview of NASA A-train instrument payload associated with each satellite platform. The table shows the full names of the instruments, operating frequencies, viewing geometry and equator crossing times in the ascending mode. Abbreviation key: instrument viewing across the atmosphere's edge (limb), instrument views in horizontal plane (nadir), microwave frequency detection (mic), radio-wave detection (radio), infra-red frequency detection (ir), visible frequency detection (vis).

NASA Upper Atmospheric Research Satellite (UARS) on September 12th, 1991 (Livesey et al. 2003). The UARS MLS instrument rotated 180° with respect to its platform, known as a "yaw manoeuvre", providing alternated views of the northern and southern latitudes at approximately 36-day intervals. Since UARS MLS viewed at 90° from the direction of orbital motion, its measurement tangent point was 23° latitude away from the satellite path (Barath et al. 1993). The 57° orbital inclination of UARS meant that its coverage of one hemisphere between orbital switches was just 24° from the Equator. In contrast, the most recent EOS MLS instrument is situated onboard Aura, a polar orbiting satellite that was launched into the A-train on July 15th, 2004 (Waters et al. 2006). EOS MLS data products are used for the analysis in this thesis.

EOS MLS receivers are selected to allow detections of many trace gases and species in the atmosphere including (OH, HO_2, H_2O, O_3, HCl, ClO, HOCl, BrO, HNO_3, N_2O, CO, HCN, CH_3CN), in conjunction with cloud ice, temperature and geopotential height at altitudes above the mid-troposphere. The EOS MLS instrument offers several advantages over UARS MLS; with a larger chemical species portfolio, higher vertically resolved measurements. One its main limitation is its narrow across-track view of less than 7 km. The vertical resolution of MLS detections depends upon the frequency of the local oscillator corresponding to the specified radiometer and the altitude of its detection. For retrievals of water vapour, the version 2 product reports much better (approximately double) the resolution of ice water content in the horizontal and vertical plane.

With use of the 240 GHz radiometer detection combined with clear-sky microwave radiative transfer, quantitative measurements of global cloud ice distribution. These are reported as an Ice Water Content (IWC) product on levels approximately 1.5 km apart and with a minimum precision of $\pm 0.7\,\mathrm{mg\,m^{-3}}$ at 261 hPa (Wu et al. 2008). The MLS algorithms for the cloud ice and water vapour products that are used later in this thesis are discussed further in Section 2.3.1.

MLS Objectives The three main objectives of the MLS mission are improvement to the understanding of stratospheric ozone chemistry; characterisation of the interaction of chemical species, atmospheric composition and its impact on climate; and pollution monitoring in the troposphere (Waters et al. 2006). MLS radiometers can view through many ice clouds, to enable scientists to examine their vertical structure to a high precision. MLS retrieval of atmo-

spheric gases for many cloud scenes are achievable where current data is lacking, due to the relatively high transmittance of microwave radiation through cloudy layers. The MLS provides precise measurements of UT WV and ice clouds, which allow us to decrease our uncertainties in estimates of the ToA longwave radiation budget.

How does the MLS Instrument Function? MLS radio-telescopes view forward in space, mechanically scanning upwards in a continuous cycle through 120 MInor Frames (MIFs) from the Earth's surface up to 92 km over a 24.7 s period. Each set of MIFs produces retrieved MLS profiles that are known as MAjor Frames (MAFs), and are separated 165 km apart along the Aura surface measurement track. In order for MLS to make retrievals in the middle troposphere MLS makes use of wide-band satellite dishes and pre-calibrated receivers, to measure a broad range of radiance measurements. Broad band receivers are necessary due to a process of pressure broadening, which dominates the width of the lower altitude spectral lines, as detailed in Section 1.3.

Two radio-telescopes are used to detect passive emission from the atmospheric limb, one wide band telescope calibrated for the GHz bands and another for the THz bands. The MLS is targeted at the UTLS, where a greater pressure broadening requires spectrometers with a larger bandwidth, although this is partially offset by increases in measurement noise. The five receivers are all double side-band, with exception of the receiver centred at 118 GHz. There are two band frequencies that result from modulation of a carrier wave at a prescribed frequency: one at higher and another at a lower frequency. Double side-band receivers are sensitive to the sum of radiances detected from both sides of the local oscillator frequency, whilst single side-band receivers view just one side. The GHz or THz mixer and polarised lenses of the instrument select the specified frequency range for analysis by the detector.

Atmospheric measurements of microwave radiances across the limb are strongly influenced by the atmospheric composition at the central field of view (FoV). The tangent point is the point on the line-of-sight that is closest to the Earth's surface. If the atmosphere is optically thin the regions around the tangent point will have the greatest influence on the radiances. The tangent point is also referred to as the MLS sensor location. The noise in a spectral channel depends on the system temperature, the integration time and the channel band-

width. This means retrievals at higher pressures are subject to higher detection noise.

For WV and temperature detection, retrievals at $p < 316\,\text{hPa}$ are deemed "scientifically useful", whilst data reported at higher pressures is considered to be subject to higher inaccuracies. As data reported on the mid to lower troposphere (LT) are often subject to large uncertainties in measurement data, the retrieval algorithm is heavily weighted by the assimilation data from numerical weather prediction (NWP) models (Livesey et al. 2006). The vertical resolution of MLS data products is compromised by the extensive along-track separation distance of 1.5° that lapses during the $24\,s$ scan cycle.

MLS Scanning Mode MLS functions by making indirect measurements of radiances from the pure-rotational transitions of radiatively active atmospheric molecules, as described in Section 1.3.1. The instrument scans the atmosphere's edge (limb) and to make retrievals from the middle of the troposphere to the mesosphere where in-situ measurements are scarce. The instrument spends 1/6th second integration time viewing each MIF, for which there are approximately 40 to 50 useful MIFs for each scan depending on the retrieved atmospheric gas. The instrument scanning process operates at three speeds, indicated by the different gradients on Figure 6, with an increasing scan speed from the surface to the top of the atmosphere to maximise the information obtained from trace-gases and clouds below the mid-stratosphere. To achieve this, the motor scan speed-up occurs at two discrete points, with a first speed-up between 20 and 30 km, and a second speed-up from 60 to 70 km.

Figure 6 shows how the two antennas are scanned across the atmospheric limb during three scan cycles. It shows the analog scanning cycle in the vertical plane with respect to time, which results in an array of measurement data from each radiometer. Three complete scan cycles are shown, with one retrieved profile for each limb scan. The MLS instrument comprises of two radiometers: one calibrated for THz and another for the GHz frequencies. The THz radiometer is more sensitive to atmospheric composition at higher altitudes and therefore spends more time viewing from $20 - 35\,\text{km}$ than the GHz radiometer to collect a higher quantity of data. At the end of each scan a routine radiometric calibration is undertaken by two known emitters: the "background" space, and an internal black body emitter (Waters et al. 2006). This calibration process is indicated by

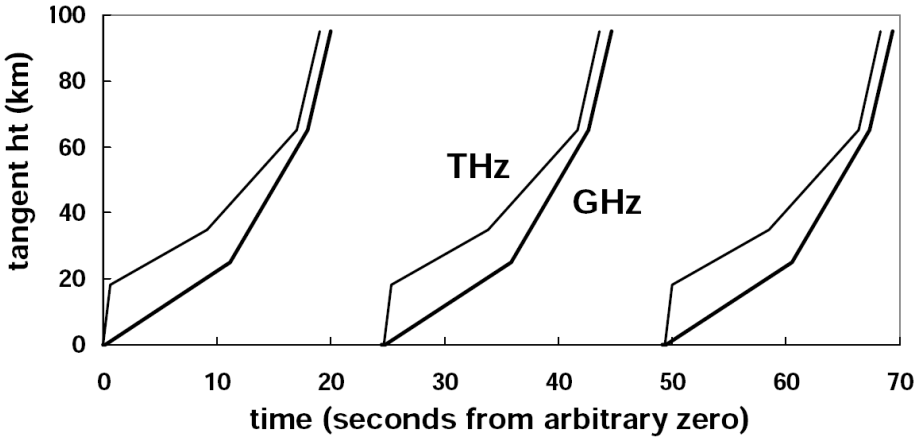

Figure 6: Schematic showing three scan cycles of the EOS MLS instrument. Each group of observations at different altitudes comprises a Major Frame (MAF). The three gradients indicate the scanning speed-up at two discrete intervals from the bottom of the atmosphere to the top. The speed-up process ensures that the MLS instrument obtains more information for algorithms of cloud and WV in the mid-troposphere. Solid black lines show the upward scanning process for the THz (thin line) and GHz (thick line) retrievals. The tangent heights for retrievals are indicated in km on the ordinate. Between each scan cycle there is a $24.7\,s$ *time-separation. Source: (Waters et al. 2006).*

the discontinuous scan lines on Figure 6, a 6 second period where no atmospheric radiance data is collected for use in the retrieval algorithms.

The MLS instrument detects microwave radiances using five radiometers that scan the atmosphere in the frequency range $118\,\mathrm{GHz} - 2.5\,\mathrm{THz}$. Each radiometer covers a set of several bands (within pre-defined frequency ranges), whilst each band consists of several channels. An optical multiplexer consisting of dichroic plates enables "switching" between different GHz radiometers and enables microwave detection of passive emission in both the horizontal polarisation (H) and vertical polarisation (V) (Waters et al. 2006). Radiometers (receivers) are centred at 118 (H,V), 190 (V), 240 (H) and 640 (H) GHz in the mm spectral range, and 2.5 (H,V) THz within the sub-mm spectral range.

There are three levels of MLS measurement data. Level 0 data are raw counts detected by the radiometers that have not been calibrated. L1B are the calibrated radiances, calculated using the raw counts transmitted directly from the radiometer. The NASA JPL team is then able to convert the L1B radiances into the retrieved L2 dataset, using the appropriate algorithm specific to the retrieved gas or atmospheric variable.

EOS MLS Retrieval Algorithm Algorithms are produced by the NASA data specialists to produce estimates of geophysical parameters from microwave radiances detected from the MLS. MLS data products include parameters such as temperature and atmospheric gas concentrations that are produced using calibrated MLS observations of microwave limb radiances known as Level 1B data (Livesey et al. 2006). The algorithms developed for MLS products are based on the standard optimal estimation approach, described in more detail by Rodgers (2000), using both forward and inverse retrieval models. Forward models are used to calculate estimates of the microwave radiances that would be observed by the MLS if the atmosphere was in a given state. The inverse model is the reverse of this computation that produces the most likely atmospheric state using a measured set of MLS radiances. Livesey et al. (2006) describes the MLS retrieval approach and how the inverse model is implemented. Further details on these calculations can be found in the MLS Retrieval processes Algorithm Theoretical Basis Document (ATBD) (Livesey & Snyder 2004).

In certain cases the atmospheric state is under-constrained and a slow scan speed may be required to undertake a greater number of observations, such as for the lower troposphere. The inverse theory must therefore be restricted or its uncertainty constrained, by the incorporation of a suitable set of a-priori data. Temperature retrievals are constrained by a-priori estimates from data assimilations of the atmosphere [2], whilst other a-priori data comes from a monthly zonal mean climatology. The a-priori provides information regarding the likely range of observations at each retrieval level. The a-priori is calculated by input of NWP data into a forward model or by use of suitable climatology data in the sensed region of atmosphere. The retrieved variable is found by routine comparison of the measured L1B radiances with the estimated radiance profile calculated from the forward model (Livesey et al. 2006). To minimise the Chi-squared type statistic known as the "Cost function", the non-linear nature of the data is considered, by an iterative process based on a least squares optimisation. The χ^2 type statistic describes the minimum error between the observed and predicted radiances in matrix form, see Equation 3. A forward model or observation operator (f), usually produced by radiative transfer modelling, is formulated that describes the radiances that MLS would be expected to observe ($\hat{\mathbf{y}}$) given a set of atmospheric state vectors $\mathbf{x}$, according to equation 2.

[2] `http://gmao.gsfc.nasa.gov/systems/geos5/`

$$\hat{\mathbf{y}} = f(\mathbf{x}) \tag{2}$$

The predicted radiances, $\hat{\mathbf{y}}$, are then compared to both the observed radiances and the a-priori, by the use of a matrix S_{y} (Equation 3). Here S_{y} describes the noise covariance of the measurements.

$$\chi^2 \;=\; [\mathbf{y} \;-\; \hat{\mathbf{y}}]^T \, \frac{1}{S_y} \, [\mathbf{y} \;-\; \hat{\mathbf{y}}] \tag{3}$$

A weighting function is then applied, which relates the sensitivity of predicted radiances ($\hat{\mathbf{y}}$) to state vectors ($\mathbf{x}$), known as the Jacobian matrix (Livesey et al. 2006).

Level 2 radiances are then interpolated to a set of fixed logarithmic pressure levels. Retrieval pressures ($p[k]$) for EOS MLS depend on the vertical resolution of the retrieved value, where the number of the level is denoted k. For temperature, WV, ozone and IWC, retrieval takes placed on levels that decrease logarithmically at a factor 10 per 12 levels ($l \;=\; 12$ levels per decade) in the UT and LS. A retrieval level can be calculated for each data product by l and k, using Equation 4.

$$p[k] \;=\; 1000\,\mathrm{hPa} \;\times\; 10^{\frac{1-\mathrm{k}}{l}} \tag{4}$$

MLS Water Vapour Detection WV is a strong greenhouse gas with highest concentrations in cloudy-sky regions. WV must be considered in conjunction with cloudy-sky observations to provide an accurate representation of the links between clouds and the radiation budget. In this thesis the effects of WV are studied using a vertical profile of precise observations from the MLS instrument. The MLS offers several advantages over previous instruments, providing a global coverage and high sensitivity to low concentrations of WV in the stratosphere, and a high penetration depth for viewing WV in the mid-troposphere. Particular focus is given to dynamics of moistening and dehydration from stratosphere-troposphere exchange (STE) associated with tropical cumulonimbus and their adjacent outflows.

The version 2 (V2) WV data product is produced using L1B calibrated radiances from the 190 GHz radiometer, by the use of the retrieval algorithm described above. V2 WV retrievals are resolved to 12 levels per decade (Livesey et al. 2007), with a scientifically useful pressure range of 316 hPa to 0.002 hPa. The spatial

resolution of the water vapour product is 180 km × 3.5 km in the along-track and vertical direction at 83 hPa (Livesey et al. 2007). The minimum precision of water vapour retrievals is 65 % at 316 hPa, whilst decreasing significantly to 15 % at 100 hPa (at the equivalent altitude of the tropical tropopause). Retrievals below concentrations of 0.1 ppmv detection threshold are not recommended for scientific use. Although earlier versions of the product were unpredictably affected by the presence of cloud ice in the field of view, the version 2 algorithm attempts to retrieve high quality data in cloudy-sky conditions. WV retrievals are affected significantly by cloud, and must be weighted accordingly in the gaseous retrieval to remove cloudy-sky radiances (Wu et al. 2006).

Thin clouds do not significantly affect MLS atmospheric gas measurements since their particle sizes are typically much smaller than the observed wavelengths. As a result, the algorithms for the MLS v2.2 data product that is used in this study can reliably retrieve composition in moderately cloudy cases. The radiance perturbation is removed through a small adjustment to the limb radiances, assuming a spectrally flat cloud signal. In contrast, thick cloud scenes affect the MLS radiances more significantly. The above approach to the retrieval algorithms therefore becomes less valid through cloud particle scattering. These affected radiance measurements are either excluded or their influence on the model retrieval are weighted downward accordingly.

Version 2.2x MLS WV data is scientifically useful at $p < 316$ hPa where precisions are better than 65 % for a reported value. In the vicinity of the tropical tropopause precisions fall to 15 %, with accuracies of 8 %. For individual profiles clouds in the MLS field of view significantly affect the standard deviation in the point-to-point difference from coincident measurements and degrade the v2 MLS WV data in an unpredictable manner. Examination of a large sample of cloud flagged MLS data with good quality Aura AIRS data shows a mean bias of just 10 %, so the recommendation by Livesey et al. (2007) is to disregard the high or low cloud status flag for scientific studies at $p \geq 100$ hPa that use large amounts of MLS data.

How does MLS detect ice clouds? The MLS instrument detects ice crystal concentrations within suitable ice clouds by viewing in the 240 GHz (mm-wave) band with the GHz calibrated radiometer along an extensive forward-facing view. In this band, ice crystal concentrations are detected across the limb at pressure

below 261 hPa. The MLS field of view varies both as a function of frequency and altitude. The along-track, cross-track and vertical extent of the atmospheric volume sampled by an individual MLS measurement reach a minimum resolution of approximately 200 km × 7 km × 5 km respectively at the lowest useful pressure of 83 hPa (Livesey et al. 2007). The Ice Water Content (IWC) product, described further by Wu & Jiang (2004), is produced by a different detection algorithm to atmospheric gas retrievals. At 240 GHz the signal is less strongly affected by atmospheric gases than at other microwave receiver frequencies. An algorithm has been developed by the JPL science team to characterise cloudy-sky emission at each pressure level within this band.

The algorithm must first determine a Cloud Induced Radiance (CIR), i.e. the radiance that emerges as a result of clouds rather than other atmospheric gases. As UT WV produces a continuum of weak emission over a broad range of microwave frequencies, its passive emission is particularly influential on the observed radiances. The CIR is defined as the difference between the measured radiance and the expected clear-sky radiance. It is calculated within a spectrally flat region of the microwave spectrum where little adjustment is needed for absorption and scattering from the cloud-free atmosphere. The estimated clear-sky radiances are first subtracted using a forward model that computes the effect of MLS gas radiances and temperature at the same tangent height in the absence of clouds (Wu et al. 2008, Read et al. 2007). The 240 GHz receiver band was chosen that is spectrally isolated from the principal gaseous spectral lines such that a weak clear-sky radiance signal is detected and the signal is largely sensitive to ice clouds (Wu et al. 2006).

Ice clouds are reported based on a linear proportionality to received power and ice particle concentration. A linear regression expression that relates the ice water content to a microwave brightness temperature T_{CIR} based on a spheroid ice crystal representation. CIRs at 240 GHz and are converted to brightness temperatures by the application of Planck's law, described further in Section 1.1. The relationship of T_{CIR} to IWC is indicated by the dotted line on Figure 7 with a gradient of $0.4\,(\mathrm{mg\,m^{-3}})\mathrm{K}^{-1}$. To ensure that MLS cloud detections are not a result of measurement error, a further iterative process is then undertaken to discard outliers if their radiances are $\geq 2\,\sigma$ from the zonal radiance mean in 10° latitude strips (Wu et al. 2006). The MLS cloud ice detection algorithm is most successful in the tropics, where the variability in clear-sky radiance shows less

dependence on the LT and surface conditions.

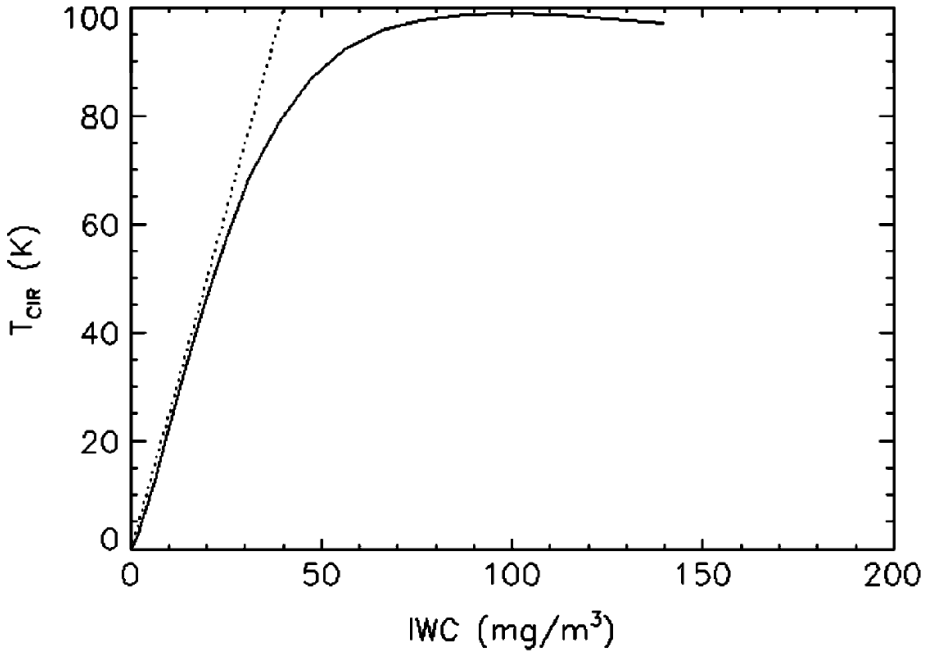

Figure 7: Modelled cloud-induced radiant temperature ($T_{\rm cir}$) / K as a function of Ice Water Content (IWC) / mg m^{-3} for the 245 GHz limb radiance at 100 hPa. The dotted line shows a linear portion of the relationship between $T_{\rm cir}$ and IWC, with a slope of ~ 0.4 (mg m^{-3})K^{-1}, and the solid curve shows the non-linearity associated with radiance saturation for IWC$\approx$ 50 mg m^{-3}. Figure reproduced from (Wu et al. 2006).

Cloud Ice Limitations The CIR may be either positive or negative depending upon the atmospheric conditions along the limb-view, cloud height, geographical location and the spectral properties of the cloud particles. At high altitudes the CIRs are usually positive whilst at lower heights optically thick clouds can induce either a positive or negative CIR. The shadowing effect of air absorption at the front of an absorbing cloud attenuates the magnitude of CIR. Cloud shadowing is not modelled in the earlier version 1 of the MLS clear-sky forward model, but has been developed for version 2 datasets.

Detection of ice does not function for mixed-phased clouds, and for clouds in the limb-view below the mid-troposphere. This is because liquid water droplets in warm clouds strongly absorb microwave radiation, often leading to a saturation of the signal received by the MLS radiometer. Strong absorption by liquid water clouds (LWC) found at higher pressures result in an over-saturation and loss of sensitivity to any overlying ice clouds. Saturation of the MLS radiances at cloud ice concentrations above 20 mg m^{-3} results in a non-linear relationship between

IWC and radiance depression. This is demonstrated by the simulated data reproduced in Figure 7.

The non-linearity in the IWC-T_{cir} relationship means that optically thick ice clouds cannot be detected at concentrations above $50\,\mathrm{mg\,m^{-3}}$. At lower concentrations and higher altitudes MLS is highly sensitive to optically thin high clouds. Ice located in the proximal limb-view of the MLS emits at a lower temperature than the atmosphere in the far view, exhibiting a positive T_{cir}. Ice towards the far end of the limb possesses a higher emitting temperature than higher altitude and space to the rear of the cloud, and so there is a tendency towards negative values of T_{cir}.

The reported precision for MLS cloud ice detection is $1.3\,\mathrm{mg\,m^{-3}}$ at 215 hPa (Livesey et al. 2007). Due to the spatial variability of cloud ice concentrations, the cloud ice detection functions well and its precisions are generally higher for homogeneous layers of ice clouds i.e. where particles are distributed evenly across the limb-view of MLS. For partially cloudy profiles, there are significant detection uncertainties, since ice crystals are distributed along only a portion of the limb. The JPL cloud ice algorithm treats ice as spheroids with a particle size distribution (PSD) based on the parametrisation of McFarquhar & Heymsfield (1997). Therefore, irregularly shaped ice crystals that scatter microwave radiation in a non-isotropic fashion often result in negative reports of IWC. The MLS cloud ice detection algorithm functions best in the low latitudes, since deep convective ice clouds that occur frequently in these locations contain spherical ice particles. In addition, the horizontal scale of these clouds is larger than many mid-latitude ice clouds and comparable with the maximum MLS along-track resolution of $\sim 300\,\mathrm{km}$. The horizontal homogeneous approximation is more valid for larger scale high clouds, than for small scale or scattered high clouds.

Multiple cloud layers cause additional errors in the retrieval of IWC, as their effects on the passage of radiation is different to single layer clouds. Future algorithms for MLS cloud ice detection would require the use of many MLS channels of different penetrating frequencies, to allow $\delta\mathrm{T_{cir}}$ to be accurately attributed to cloud ice content in inhomogeneous cloud layers (Wu & Jiang 2004).

MLS data Products and Availability Data products are released either as Level 2 profile data or spatially gridded Level 3 data products on a set of vertical levels. They comprise of a maximum of 3495 profiles per day, with occasional bad

data sectors caused by erroneous radiance measurements or calibration problems that adversely affect the retrieval.

In this study version 2.2x processed data [3] is used, which was upgraded in 2010 to V3 after the analysis was completed. The latest versions of MLS data products include improved retrievals of carbon-monoxide and sulphur dioxide in the presence of clouds, and enhanced ice water content detections through an improved set of algorithms produced by the Jet Propulsion Laboratory (JPL) science team.

2.3.2 The Aqua Satellite Platform

Aqua is a satellite platform which carries instruments capable of monitoring clouds, the radiative energy balance and WV from space. Aqua is positioned at the front of the A-train satellite constellation, see Figure 4. The Aqua platform comprises six nadir-viewing instruments, which are: the Atmospheric InfraRed Sounder (AIRS), MODIS, CERES, Advanced Microwave Sounding Radiometer (AMSR-E), the Advanced Microwave Sounding Unit (AMSU), and the Humidity Sounder Brazil (HSB) (as detailed in Table 1). The AIRS, AMSU, and the HSB form an integrated cross-track scanning mechanism for accurate temperature and humidity observations for clear sky and also in the presence of clouds (Aumann et al. 2003).

The AIRS infrared chemistry instrument, working in combination with the microwave AMSU, makes measurements across 2378 hyper-spectral infrared channels using a nadir sensor, with a spectral resolution 100 times that of previous infrared satellite instruments. AIRS (Aura) broadly covers the same spectral range as the High-resolution InfraRed Sounder (HIRS) satellite instrument and is therefore useful for the analysis of the HIRS spectral response function (Cao et al. 2005). AIRS makes retrievals of surface temperature, WV and cloud properties (Aumann et al. 2003).

The MODIS instrument makes measurements of visible and infra-red radiances in the same frequency range as the AIRS instrument, but at a lower spectral resolution and higher spatial resolution. MODIS has the ability to measure cloud top pressure, cloud particle effective radius, optical thickness and other cloud properties (Xiang & Barnes 2006).

[3] `http://disc.gsfc.nasa.gov/`

Clouds and the Earth's Radiant Energy System (CERES), is an instrument designed to measure the angular longwave and shortwave emission emerging from the Earth's atmosphere (Smith & Wielicki 2004).

CERES

The CERES Instrument The Clouds and Earth's Radiant Energy System (CERES) is a broadband instrument that monitors energy fluxes from the Earth's surface, atmosphere and clouds. The instrument is currently onboard three separate satellite platforms, at present instruments are operational onboard the Terra and Aqua platforms. Measurement of the Earth's radiant energy system by CERES forms part of almost continuous record of climate observations begun by the Earth Radiation Budget Experiment (ERBE) from the 1970's up to present day. The CERES instrument carries three radiometers calibrated to observe radiance within three spectral bands; shortwave 0.3 to 5.0 μm, longwave window 8 to 12 μm, and total radiance 0.3 to 100 μm, see Figure 8. The CERES instrument views a similar section of the atmospheric spectrum as MODIS, but its radiometers detect emission over broader frequency bands. This is useful for monitoring the Earth's net ToA radiation budget. The "redundancy" radiometric design is useful for instrument calibration, since with two known radiometer readings it is possible to estimate the third radiometric reading.

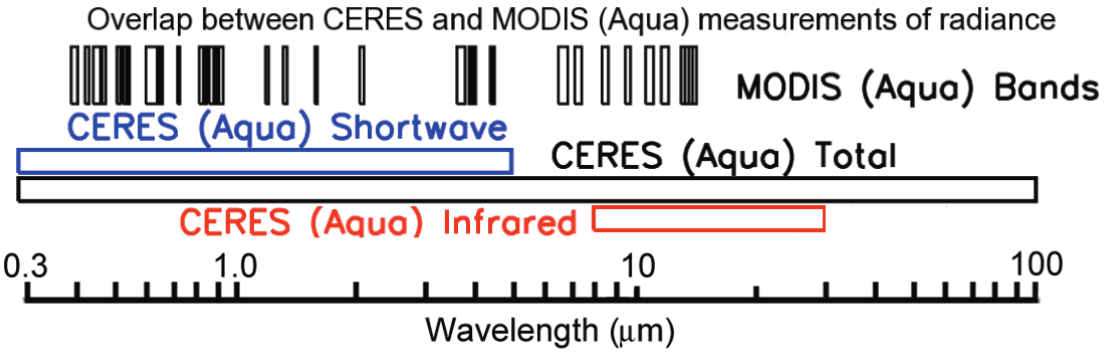

Figure 8: Figure showing the overlap of bands observed by the MODIS and CERES (Aqua) satellite instruments. The figure demonstrates that MODIS views within 36 narrow bands at infrared and visible wavelengths, whilst CERES observes emission over three broad bands covering the visible and solar radiation, the infrared, and the total radiation. The MODIS (Aqua) "channels" are annotated as black boxes below the x-axis. CERES (Aqua) broadband radiances are annotated as black (total radiance), red (infra-red) and blue (visible and solar), corresponding to the three onboard radiometers.

A cloud masking process is undertaken using MODIS (Aqua) measurements. MODIS information from a cluster of pixels is convolved to a CERES pixel. These include the variables cloud optical thickness, effective radius and cloud top height. The cloud information is used in the development of Angular Distribution Models (ADMs). ADMs give vital information to the scientific community regarding the angular dependence of observed radiances at each frequency range. The function of reflectivity with respect to radiation frequency and angle is often represented by ADMs (Smith & Wielicki 2004, Wielicki & Barkstom 1997). The coefficients for combining the angular components of emission are dependent upon scene type, latitude; and zenith and azimuth angle. The local solar zenith angle undergoes both a diurnal and annual cycle, affecting the reflectivity of cloud scene used to estimate shortwave irradiance. The algorithm removes the reflected and scattered shortwave components from the total upwelling emission

A CERES flagging system informs the use of bad quality data granules resulting from the presence of sun-glare, snow, ice, and optically thick aerosol concentrations. CERES flagging is classified into four main categories clear, cloudy, bad data and no retrievals. Information regarding CERES Aqua Edition 1B SSF can be obtained from the eosweb NASA website[4].

Two CERES instruments are situated on the Terra satellite, and are known as flight models 1 (FM1) and 2 (FM2). A further two CERES instrument payloads, flight models 3 (FM3) and 4 (FM4) are located onboard Aqua. The CERES radiance measurements are provided either as a filtered or unfiltered product, which are unadjusted for optical effects of the sensor. The filtered radiance is derived by the use of ground based software. The unfiltered radiance is spectrally flat when no emission or solar energy emerges from an angular segment of atmosphere. It is calculated by a regression algorithm that is calibrated on the ground and post-launch to determine coefficients for different scenes and angles.

The different flight modes allow the scientific teams to make better estimates of the distribution of radiances, by viewing the same point of the Earth's surface or atmosphere at different off-nadir angles. In particular, the conical scanning mode allows the angular component of upwelling radiation is used to make better estimates of both the upwelling LW and SW radiation through development of Spectral Response Functions (SRFs) associated with each sensor. The spectral response function (SRF) of an instrument describes the relative sensitivity of an

[4] `http://eosweb.larc.nasa.gov/PRODOCS/ceres/SSF/Quality_Summaries/`

instrument to electromagnetic energy of different wavelengths. Improvements to the electronics of the CERES instrument mean that its stability is much better than previous ERBE instruments (Smith & Wielicki 2004). CERES calibration is undertaken scanning monochromator prior to the launch of the satellite payload into orbit. Further details of the pre-flight calibration process and the CERES sensors are provided by Lee et al. (1996).

Mode of operation CERES operates in three scanning modes in order to collect measurements as an instrument pair onboard the same platform. To achieve this, one of the instruments operates in a fixed azimuth plane and scans from side-to-side across the A-train surface track. When the instrument operates in this mode it is known as the Cross Track Scanner (CTS). The other instrument scans in a Rotating Azimuth Plane (RAP), which means that a mirror rotates about the azimuth producing a conical surface scan pattern, with nadir measurements undertaken from a range of elevation angles. The latter provides an angular sampling of the entire hemisphere of radiation, whilst the former optimises the spatial sampling over the globe. The RAP scanner provides information for ERBE ADMs when combined with cloud classifications. CERES instruments on- board the same (or different) satellite platforms are identical in their design and can therefore operate in either the CTS or RAP scanning mode (Wielicki & Barkstom 1997).

In-flight calibrations are performed weekly to reassess the gain of the instrument sensor. The calibration between electronic count value and radiance units is undertaken by viewing black bodies of a known emitting temperature either onboard the platform or in space. The sensor observes different footprints in different operation modes, as demonstrated by the mapped observation points on Figure 9.

CERES SSF Data Product The Single Scanner Footprint (SSF) product is used in this thesis for analysis of top-of-atmosphere (ToA) fluxes. SSF products comprise both of radiant energy fluxes and a cloud mask, and are formatted as hourly granules. The SSF radiance information is available for every convolved geolocated pixel location within the swath, using a cluster of measurements received by the broadband radiometer. Full angular coverage is provided over a period of 16 days by the CERES RAP scanner (Wielicki & Barkstom 1997). The

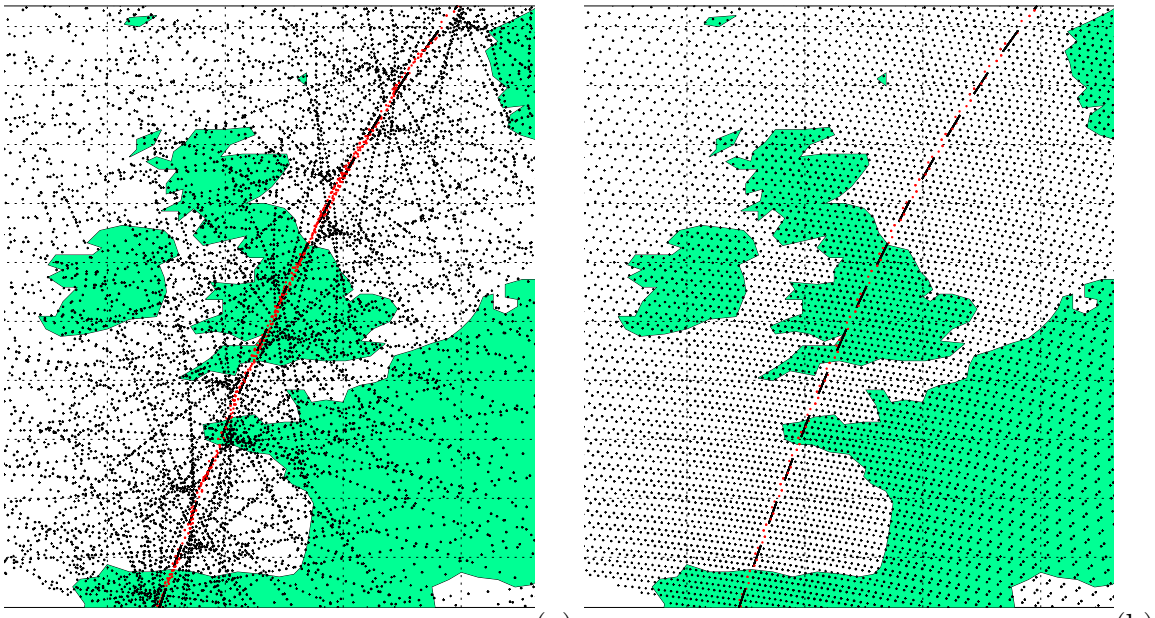

Figure 9: Figure showing the surface scan patterns of the CERES (Aqua) instrument during the period 0200 *UTC to* 0300 *UTC on 19th September, 2004. The Flight Mode 3 (FM3) conical scanning mode (a) produces a densely distributed pattern of observations with an angular component to the observed radiances. In contrast, the FM4 cross-track scanning mode (b) is characterised by a regular distribution of observations across the A-train track. The surface scan footprint is shown by black crosses and the continents are marked in green. The narrow field of view associated with the MLS instrument is marked by CERES footprints with red dots (a) and (b).*

mapped surface measurement points reported by the CERES instrument are more densely clustered around the central A-train track where angular scans overlap, and are more sparsely distributed towards the edge of the swath. Co-located SSF points within 20 km from the central track are indicated by red dots on Figure 9.

Data processing by the Goddard Space-Flight Center (GSFC) involves the integration of radiances using ADMs (Wielicki et al. 1996, Loeb et al. 2003). The outgoing longwave radiation (OLR) is then obtained by integrating spectral radiances over a broad range of wavelengths from $\lambda > 4\,\mu$m to obtain top-of-atmosphere (ToA) radiant power per unit area (W m^{-2}). Similarly, reflected shortwave radiation is obtained by integrating spectral radiances over wavelengths of $\lambda < 4\,\mu$m.

The accuracy of the CERES Aqua ADMs reported by Loeb, Kato, Loukachine et al. (2007) are validated against other ADMs. The results indicate an oceanic root-mean-square error (RMSE) of just 1.06 % with a modest 2.39 % RMSE for all

scene-types. A small regional-seasonal bias also exists in the order of $\pm 0.3\,\mathrm{W\,m^{-2}}$ with a respective root-mean-square bias of up to $0.6\,\mathrm{W\,m^{-2}}$.

The MODIS Instrument The Moderate-resolution Imaging Spectroradiometer (MODIS) instrument onboard Aqua plays an important role in the Earth Observation System, providing several measurements that advance on the present level of scientific understanding of the Earth's land, oceans, and atmosphere (Xiang & Barnes 2006). MODIS observes all the Earth's surface and atmosphere within a 2-day period. It reports information on clouds by examining the spectral properties of cloud-tops using passive detections at infra-red and visible frequencies. This helps to improve representation of clouds within weather and climate models, which are often poorly resolved (Rolland et al. 2000).

The MODIS instrument is a 36 band moderate resolution instrument, which detects radiation both in the visible and infrared producing measurement data for a set of Earth science products (Xiang & Barnes 2006). It scans across track from the nadir view with a Spectroradiometer that consists of a cross-track scan mirror and collecting optics, and provides a large swath width of 2330 km. MODIS instruments are currently operational on both the Aqua and Terra satellite platforms. MODIS detects atmosphere, ocean, cryosphere (surface ice) and land constituents to a more advanced level than previous generations of sensors in terms of spectral, spatial and temporal resolutions. MODIS channels, referred to as "bands" in the literature, have four product resolutions. MODIS infers properties by detection of terrestrial emission (bands $21 - 36$) or by surface reflectance. The 36 "bands" are marked on Figure 8 in relation to CERES (Aqua) broadband measurements. The spatial resolution of MODIS products at nadir varies depending upon the frequency. MODIS radiometers view discrete bands in the spectral range from 0.415 to 14.235 μm, as indicated by Figure 8. Bands from 0.41 to 2.1 μm provided at a resolution of 250 m (bands $1 - 2$), bands 3 to 7 at 500 m and bands 8 to 26 at 1 km resolution. The MODIS instrument applies an interference filter to select channels, which overlies a detector array as described by Xiang & Barnes (2006).

Data products are available either at the data processing level 2 (raw product) or 3 (globally gridded) and was obtained from a web interface to the Level 1 and Atmosphere Archive and Distribution System (LAADS) [5].

[5] `http://ladsweb.nascom.nasa.gov/data/`

Cloud-top pressure estimates from MODIS (Aqua) MODIS (Aqua) cloud top property data (MAM06S0) was collected for analysis. The MODIS cloud top product is provided on 5 $\times$ 5 km grid-boxes, in 5 minute data chunks. The MODIS cloud top product is produced by the NASA GSFC team. Their detection algorithm makes estimates of CTP by examining radiances from MODIS band pairs in the vicinity of the 15 μm carbon-dioxide absorption line. Further details of the algorithm, known as "carbon-dioxide slicing" are provided by (Frey et al. 1999). The subsetted product is produced by the NASA science team by discarding pixels less than 205 km (41 pixels) from the central A-train track. Subsetted datasets are more preferable, since it facilitates co-located analysis with measurement data from A-train instruments that scan a narrower footprint. Subsetting also reduce the computational time for selecting data for co-located analysis. The datasets are also smaller than for the full measurement swath, minimising the upload time from NASA servers to a local machine.

The transmission of radiation at different frequencies is sensitive to the spectral properties of the cloud-tops at different altitudes (Platnick et al. 2003). The NASA cloud-top CO_2 slicing algorithm conducts a routine examination of absorption over several MODIS infrared bands. In saturated bands, such as CO2 and H2O in the infra-red, the radiance is indicative of atmospheric temperature as a function of altitude. Carbon-dioxide absorbs thermal radiation over a broad band as shown by Figure 2, with a central 15 μ m spectral line that is sensitive only to high clouds, whilst the limbs of the band are sensitive to mid-level clouds (Menzel & Strabala 2006). The MODIS algorithm estimates CTPs to a precision of 50 to 150 m (Frey et al. 1999). The CO_2-slicing algorithm also makes use of temperature and atmospheric transmittance to provide information on cloud phase, cloud top temperature and effective particle radii (Frey et al. 1999).

Spectral analysis of band radiances in the locality of the CO_2 band is used to determine cloud top heights. The NASA GSFC cloud product makes use of the 11 μm window band in conjunction with the carbon dioxide bands to allow detection of low level clouds below 700 hPa. The MODIS algorithm makes comparisons of three main spectral pairs for its analysis of cloud-top. Band pairs are used in proximity to the carbon-dioxide absorption spectrum, with the wavelengths; 14.2 μm / 13.3 μm, 13.9 μm / 13.3 μm and 13.3 μm / 11 μm. The ratio of radiances from two nearby band pairs is used to estimate the CTP in both cloudy and clear-sky. CTPs are combined with gridded meteorological products (GMPs)

to report cloud top height and temperature variables (Menzel & Strabala 2006). The GMPs are datasets obtained by mapping using NWP assimilations to the MODIS data pixels.

To calibrate the instrument and estimate precisions MODIS airborne simulator (MAS) data was used to conduct a pre-launch test (Menzel & Strabala 2006). Multi-layered clouds were not identified by MAS, as the analysis was undertaken at a 50 m pixel resolution, a finer resolution than reported from MODIS. The algorithm does not always perform well at identifying mixed phased clouds, as a well-defined slope is required between selected spectral channels (King et al. 1997). This causes data quality issues when clouds consist of both supercooled water droplets and ice particles. There are also difficulties identifying optically thin clouds, where the MODIS instrument is more sensitive to the surface or underlying cloud layers. The MODIS CTP algorithm is highly effective for the detection of thin single-layered high clouds in the mid- to upper troposphere.

MODIS (Aqua) Cloud Mask MYD35_L2 is a high resolution product provided both on 1 km × 1 km and 250 m × 250 m grid containing information on the cloud classification and the certainty or of a section of atmosphere containing cloudy skies. The 250 m resolved cloud mask product is solely based on sensed data at visible wavelengths.

Cloud Phase Detection MODIS algorithms are mainly intended for plane-parallel LWC calculations (King et al. 1997), but are also successful for detection of ice clouds assuming spherical particles. In order to classify clouds into their liquid and ice counterparts, a MODIS algorithm is employed which examines the ratio of spectral reflectance measurements between 0.645, 1.64, and 2.13 μm reflectance pairs e.g. (King et al. 1997, Rolland et al. 2000). The reflectance pairs are compared to observations of the 11 μm infra-red window channel. Within window channel a space-borne instrument views cloud-tops and the Earth's surface properties from space. The spectral power measured at 11 μm depends on the temperature and emissivity of the surface. Spectral signatures of cold clouds are characterised by a reduced reflectance at 1.64 μm and 2.13 μm, in contrast to warm clouds. This allows an algorithm to discriminate between liquid and ice-phased clouds with otherwise similar optical and spectral properties. The algorithm is less effective at identification of mixed phased clouds, where the

cloud-top temperature are typically between -15° C and 0° C. At these locations, contrasting spectral signatures are received by the radiometers from a mix of both ice and water clouds.

2.3.3 Other A-train Satellite Platforms

CloudSat and CALIPSO - Cloud and Aerosol Monitoring The Cloud Satellite (CloudSat) and Cloud-Aerosol Lidar and Infrared Pathfinder Satellite Observation (CALIPSO) are a pair of cloud monitoring satellites, principally designed to detect cloud type, structure and phase. They make very close measurements just 15 seconds apart and are positioned in the centre of the A-train constellation, see Figure 4. Data from CloudSat and CALIPSO are not used in this thesis, as comparisons were not possible with the MLS until an orbital reconfiguration was completed during July 2008. Ideally further studies would undertake comparisons between MLS, CloudSat, and CALIPSO whose footprints are within 3 to 4 km in the horizontal plane.

CloudSat and CALIPSO were both launched on April 26th, 2006. CloudSat carries a 94 GHz Cloud Profiling RADAR (CPR) nadir viewing instrument with a 0.5 km vertical resolution. The CPR measures the power back-scattered by clouds as a function of distance from the radar. The RADAR provides information about the cloud type and structure. CALIPSO's payload includes a Cloud-Aerosol Lidar Instrument with Orthogonal Polarisation (CALIOP), a passive Infrared Imaging Radiometer (IIR), and visible Wide Field Camera (Dunbar 2007), providing valuable insight into the role that clouds and atmospheric aerosols play in regulating weather and climate. The CALIPSO operates in the visible and near-infrared part of the electromagnetic spectrum by sending pulses of light directly into the atmosphere and measuring cloud and aerosol back-scatter. This enables information to be gathered on the 3-d distribution of aerosols, their formation and evolution. Cloud phase can be obtained by orthogonal polarisation in the visible scanning instrument.

2.4 Observational data from the Low to Mid-Troposphere

Whilst the MLS instrument provides a reliable set of atmospheric composition, temperature and ice cloud data for much of atmosphere; scientifically useful measurements are not reported for the low to mid-troposphere. Limitations in the

MLS detections at these low altitudes are principally the result of high water vapour mixing ratios, which readily saturate a broad section of the microwave spectrum. Retrievals of atmospheric gases are especially problematic in thick cloud, notably for water vapour whose continuum absorption becomes readily overlapped with the cloudy-sky signal. For gaseous profiles, GEOS-5 atmospheric data assimilation system (ADAS) data is the "a-priori" information source for MLS, as detailed by Reinecker et al. (2007). GEOS-5 data is the main data source reported when profile data is not scientifically useful.

High clouds that form by free convective processes in the low latitudes frequently have liquid water at their base. These clouds are characterised by a warm cloud based at a lifting condensation level, a point where water becomes saturated for rising air parcels. The received microwave signal used in cloud detection is also frequently shadowed due to the relative high number concentration of liquid cloud droplets found within warm clouds. The near real-time representations of these underlying warm clouds is needed at the same location and time as high cloud detections, since a complete cloud profile is required to fully describe their association with circulation features, physical and microphysical cloud processes, and local radiative heating and cooling at different altitudes. Furthermore, more detailed information is needed on low to middle level clouds to explore how they are formed from the descending motions associated with neighbouring tropical storms.

2.4.1 European Centre for Medium-range Weather Forecasts (ECMWF) Data Products

The European Center for Medium-range Weather Forecasts (ECMWF) Reanalysis (ERA) Interim data product, detailed by Dee et al. (2011), is used in this study where no equivalent MLS data product is available. For temperature and water vapour data, GEOS-5 data is already located to each MLS profile and is therefore a preferred source. Later in this study liquid water content and vertical wind tendencies are examined (the latter generated as a derivative product of other atmospheric variables). The ECMWF provide 4D-Var assimilated data on a 6 hourly basis that can be used to provide additional information on cloud life-cycles and the processes responsible for their formation. Data assimilation is an analysis technique whereby observational data is combined together in a model that considers the consistency of each, how parameters change with time

and the physical properties of processes in the Earth's system [6]. 4D-Var is a simple generalization of representing data in 3 spatial dimensions (on a standardised horizontal and a vertical grid), commonly known as 3D-Var, that are also distributed in time.

ERA data products provide Global analyses that describe the state of the atmosphere, land and oceans from mid-1957 to mid-2002. ERA-Interim is used in this study and is described in Dee et al. (2011). It is a reanalysis of the period 1989-present for the next-generation of extended reanalysis to replace ERA-40 data. There are several differences in the data assimilation and use of observations for ERA-40 and ERA-Interim products. The ERA-interim product contains many meteorological parameters on a N80 Reduced Gaussian horizontal grid and on 37 vertical levels. A daily coverage of assimilated data comprises of 5 global datasets that are reported at: 0000, 0600, 1200 and 1800 UTC on the day of analysis; and also at 0000 UTC on the following day.

ERA Interim Re-Analysis Data Products Cloud Liquid Water Content (LWC) is used for radiation budget calculations later in this study, which is the mass of liquid water contained within a unit volume of dry air. Vertical motions were also investigated, which are provided by the ERA-Interim data product in pressure coordinates of $\mathrm{Pa\,s^{-1}}$. The main advantages of the assimilation include improvements to; spatial and temporal gridding, numerical predictions of variables, efficiency and accuracy of radiative transfer calculations. ERA-interim data uses improved representations wind, ozone and clear-sky radiance observations using higher quality observational data from a variety of sources.

2.5 Overview

Many different A-train satellites carry instruments capable of observing high clouds, all of them providing measurement data in close succession. Whilst the Aqua MODIS instrument through its cloud product monitors cloud-tops, the CERES instrument on-board the same platform can monitor radiation emitted from the same clouds. It is clear that through combination of these two datasets several questions could be answered about the cloudy-sky radiation budget; yet additional information is required to describe each cloud and to understand how

[6] `http://www.ecmwf.int/newsevents/training/rcourse_notes/`

the features of these clouds impact upon the outward flow of thermal energy. This requires us to explore several features of A-train cloud products such as the particle thermodynamical phase, particle sizes and shapes, and the cloud layer depth and thickness in which different cloud particles are suspended.

The CloudSat comprises of the CPR that detects many thick clouds, meanwhile the CALIPSO's payload includes a Lidar (CALIOP) calibrated to detect thin high-altitude clouds and aerosols. Together, these near coincident observations by active sensors are highly useful in the study of clouds, partially because their observation times are just 45 s apart. Whilst there is definitely future scope to study for the use of these measurements in high cloud studies, the focus of this thesis is specifically geared toward examination of the longwave energy transmission in the local of high clouds. One of the goals of the thesis is to attribute cloud features to the cloud radiative forcing defined by IPCC (2001) as the difference between the all-sky Earth's radiation budget and the clear-sky Earth's radiation budget. Since non-mixed greenhouse gases experience large variability in the presence of cloud, coincident greenhouse gas profiles are required at high vertical resolution for these calculations to be successful. The models that are used to compute the broadband energy emitted from these cloudy-sky profiles using composition and temperature data are collectively known as radiative transfer models.

The MLS instrument forms part of the atmospheric chemistry mission and provides many gas composition products through a set of inverse retrieval algorithms. MLS products provide insight into the spatial distribution of many greenhouse gases present in the Earth's atmosphere including the mixed gases: water vapour, ozone, nitrous oxide, carbon monoxide. These are reported on levels that are just $2 - 3$ km apart. In conjunction MLS also reports temperatures, and high cloud data through its ice water content product. MLS views with microwave-viewing telescopes, telling us much more about the icy layers of high clouds than previously possible - the focal cloud genre of this thesis. These measurements are still not complete; as such data is also needed on low to mid-tropospheric clouds. ECMWF data is used as a choice of liquid water content and vertical motion data, which in conjunction with MLS data allows the exploration of several possible formation and maintenance mechanisms of tropical cirrus.

The validation methods that follow in Chapter 3 show how narrow limb sound measurements, which there are now a growing number of, differ from measure-

ments as viewed at off-track angles from nadir. Studies in Chapter 4 show how by suitable spatial averaging about the limb measurement footprint, cross-instrument comparisons can be can be made in a valid manner to determine the bias and uncertainties in space-borne measurements of high clouds. This study shows that MLS has the ability to locate high clouds at the same regions across the globe and at an altitude that is broadly consistent with both MODIS and CERES products. After exploring the consistency of high cloud and radiation budget measurements, later studies isolate two low latitude high cloud types and establish causal links between their respective cloud radiative forcing.

3 Validation of MLS Cloud Data with Co-located A-train Datum

3.1 Introduction

There is a need for accurate data on ice clouds for numerical weather prediction (NWP) and climate models, as present representations vary considerably (Edwards et al. 2007, Li et al. 2005). This proves problematic, as measurements of many cloud parameters are difficult to monitor with more than one instrument due to the highly dynamic behaviour of clouds. Many cross-instrument comparisons of cloud datum are therefore subject to large uncertainties that result from off-sets in spatial and temporal sampling. In addition, coincident data are essential for in-flight validation studies. Whilst many local-scale studies have been conducted using space-borne measurements in the past using: ground based Lidar, vertical radiosonde profiles, flight path measurements, or direct observations from other in-situ devices (McFarquhar et al. 2000, Heymsfield 1984); these datasets have been validated only against a sparse network of local ground-based observations (Allan 2000, Wong et al. 2000). The recent launch of the A-train satellites provides a wealth of coincident measurements, with derived cloud products provided from the perspective of different instruments that are suitable for synergistic combination.

Previous validation studies have been undertaken by the science team at the Jet Propulsion Laboratory (JPL) to produce an improved version of MLS cloud ice data (Wu et al. 2008). Their studies compare cloud top pressure (CTP) estimates from MLS detections to data from Global Climate Model (GCM) simulations, Goddard Earth Observing System model version 5 (GEOS-5) data, and Numerical Weather Prediction models such as European Center for Medium-range Weather Forecasts (ECMWF) analyses (Li et al. 2005, Wu et al. 2009). The studies conducted in this chapter discuss additional comparisons between MLS measurements and those from other A-train instruments, to determine whether or not their detections are consistent. In this study, co-located Aqua nadir-sensed data is used to validate detections from the MLS (Aura) instrument, which make coincident observations of the same clouds within a narrow time-frame of no more than 9 minutes.

The main objective of this study is to conduct a large scale sampling of high

clouds by comparing point to point data. The questions addressed by this study are: What are the limitations of the MLS instrument associated with its viewing geometry and design? Are high clouds detected at the same altitude and the same measurement locations as other A-train instruments? How can synergistic information on cloud phase from the Moderate-resolution Imaging Spectroradiometer (MODIS) be used to improve these comparisons? Does the horizontal homogeneity of high cloud affect comparisons with MLS? This study will also indicate the effect of differences in instrumental design, to suggest improved versions of the MLS cloud-ice product and to develop future cloud monitoring instruments.

Vertical profiles of MLS ice water content (IWC) data, and Outgoing Longwave Radiation (OLR) data from Clouds and the Earth's Radiant Energy System (CERES) are each used to generate cloud-top pressure data. Co-located CTP datasets were then inter-compared with the MODIS cloud product using a sample of sixteen days of data. An initial processing was undertaken to spatially average nadir A-train data within the sensor footprint area of MLS, which is detailed in Section 3.2. The methods for estimating CTPs are then discussed in Section 3.3. The analysis begins by examining the ice concentrations within the cloud's interior detected by MLS and also examines the tops of the same clouds observed by MODIS. Initial studies compare and contrast MODIS cloud-top pressure measurements with MLS IWC detections. This study examines a cluster of tropical high clouds over the Pacific Ocean and the results are reported in Section 3.4. Several of the structural components of these high clouds are discussed in the context of the respective instrument viewing geometries and horizontal resolutions. Later in the chapter analysis was performed in the low latitudes and extra-tropics, where MLS detected high clouds are found most frequently.

By the use of MODIS thermodynamic phase data, the later part of this chapter demonstrates how to discriminate ice clouds to permit valid comparisons of MLS CTPs with nadir-sensed data. The results from point-to-point MLS CTP comparisons with MODIS are discussed in Section 3.5. Validation studies between MLS and CERES CTPs data are then discussed in Section 3.6. A summary of co-located CTP comparisons from A-train instruments concludes the chapter in Section 3.7.

3.2 Method for Co-location

The nature of the A-train orbit ensures that measurement footprints are distributed evenly over the globe, so that studies of clouds are representative of the analysis area. Comparing A-train measurements by matching neighbouring points by a gridding system that does not consider the polar inclination and difference in instrument geometries would however lead to a significant discourse between cloud measurements. A more valid system is described here known as co-location that ensures the same cloud scenes are analysed. For suitable across-track scanning instruments an initial first processing step is employed that is known as data subsetting, which is described further in Section 3.2.2. It proves useful for wide-viewing EO instruments, as it offers a simple and therefore more rapid processing routine that can remove much of the non-coincident measurement points. Comparisons using subsetted data alone would not be considered spatially coincident in the horizontal plane without the additional use of "co-location".

Co-location allows us to undertake spatial averaging over each MLS tangent point using the Great Circle distance to construct a triangulation. Three lengths are used to determine the off-track and along-track components for selection, denoted as d_0, d_1 and d_m on Figure 10. Data from MODIS and CERES were only used for comparisons with MLS clouds in they were spatially coincident.

3.2.1 Co-location of A-train Measurements with MLS

Even though the central tracks of A-train satellites are almost coincident, differences in viewing geometry mean that the surface footprints and resolution of observed atmosphere by different instruments vary considerably. Figure 10 shows an example of a coincident MODIS or CERES measurement footprints with their coincident observations marked by a red oblong. The MODIS cloud product is subsetted so that limb scans from the MLS, whose measurement footprint indicated by the blue oval, span approximately the same across track width. The data processing to prepare this data involved spatial averaging nadir data, of which there are many measurement points within each limb, over broadly the same horizontal area as MLS and during the same time window. CERES Aqua data on the other hand must be subsetted post-download. MLS sensor footprints cover an equivalent horizontal area in the x-y plane with an along-track scale of $y = 300\,\mathrm{km}$ and a narrow across-track view of $x = 7\,\mathrm{km}$ for the version 2.2x

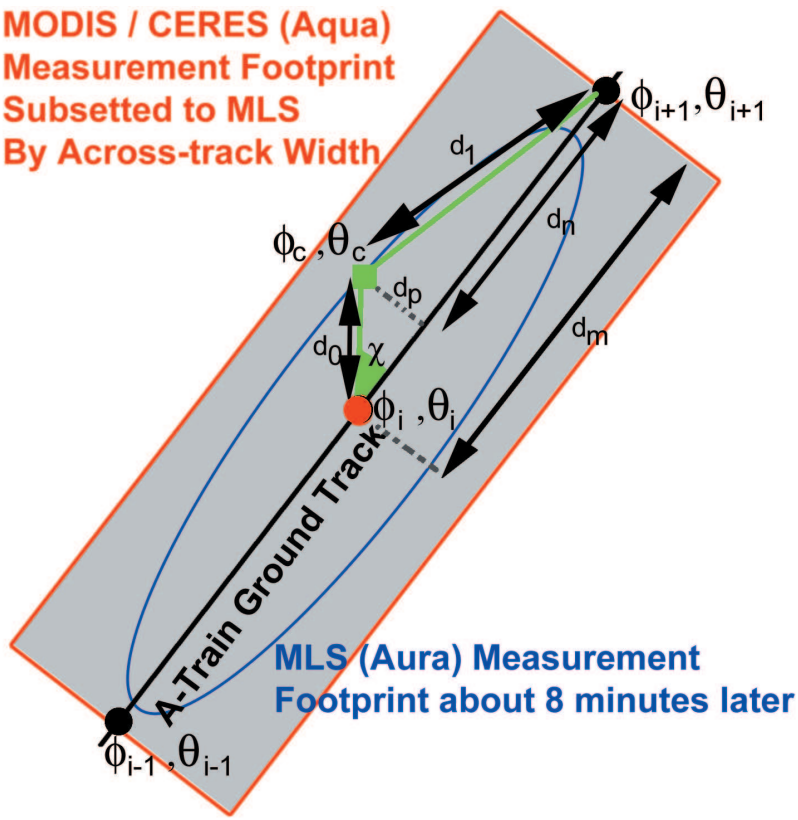

Figure 10: Figure showing the location of surface measurement footprints from two different satellite instruments; MODIS or CERES (Aqua) outlined in red, and MLS (Aura) in the blue oval. By using their coordinates and the off-track angle χ, data processing for this study calculates the separation distance between a correlative data point ϕ_c, θ_c (marked as a filled green square) and a nearby MLS tangent point ϕ_i, θ_i (marked as the central filled red dot). The process is used to assess whether the measurements are suitable for co-location. MLS sensor points are marked at three positions along the MLS ground track with a longitude (ϕ) and latitude (θ) at positions i, $i-1$ and $i+1$. The correlative data point is marked as (ϕ_c, θ_c).

IWC product. In this study the variability in off-nadir measurement data was calculated within each MLS sensor footprint to obtain more detailed information on high clouds properties.

The following method describes how to screen each nadir data pixel to assess the suitability for spatial co-location with MLS. Firstly we define a measurement point from MODIS or CERES at a position (c). This correlative point is marked with a co-ordinate ϕ_c, θ_c on Figure 10. A triangulation system is then constructed and calculations performed to compute the across-track (marked d_p) and along-track (marked d_m) separation distance between the MLS tangent point and each correlative nadir data point. There are three distances that are needed for the triangulation process to report these outputs and allow us to select coincident

measurement data.

Two distances of the triangulation are obtained by calculating the shortest length between ϕ_c, θ_c and each of the two adjacent MLS tangent positions. One MLS tangent point is denoted ϕ_i, θ_i at an initial point in time, whilst another ϕ_i, θ_i is observed 24 s later at the time of a consecutive scan cycle. The distance to MLS tangent point at index i is denoted d_0, whilst the length d_1 to point $i+1$ as shown by Figure 10. The third distance lies between the two adjacent MLS tangent points, in the along-track orientation (marked d_m). All these lengths are "Great circle distances", the shortest distances measurable between two points on the Earth's surface. To calculate these distances the haversine formulae was used, as shown by Equations 5 to 7. The radius of the Earth is represented here by $r_e = 6.371 \times 10^6$ m, whilst ϕ_i, θ_i defines the co-ordinates of the MLS tangent point at profile index (i).

$$d_0 = 2.0 \times \sin^{-1} \sqrt{\sin\left(\frac{\theta_c - \theta_i}{2}\right)^2 + \cos(\theta_i) \times \cos(\theta_c) \times \sin\left(\frac{\phi_c - \phi_i}{2}\right)^2} \times r_e \quad (5)$$

$$d_1 = 2.0 \times \sin^{-1} \sqrt{\sin\left(\frac{\theta_{i+1} - \theta_c}{2}\right)^2 + \cos(\theta_c) \times \cos(\theta_{i+1}) \times \sin\left(\frac{\phi_{i+1} - \phi_c}{2}\right)^2} \times r_e \quad (6)$$

$$d_m = 2.0 \times \sin^{-1} \sqrt{\sin\left(\frac{\theta_i - \theta_{i+1}}{2}\right)^2 + \cos(\theta_{i+1}) \times \cos(\theta_i) \times \sin\left(\frac{\phi_i - \phi_{i+1}}{2}\right)^2} \times r_e \quad (7)$$

Angle χ and distance d_0 are required to calculate the off-track distance d_p in metres. χ is the off-track angle between the ground track and the line adjoining the correlative data point (ϕ_c, θ_c). It is calculated using the Law of Cosines, as indicated by Equation 8.

$$\chi = \cos^{-1}\left(\frac{\cos(d_1) - \cos(d_0) \times \cos(d_m)}{\sin(d_1) \times \sin(d_m)}\right) \quad (8)$$

To calculate d_p, the sine rule is applied according to Equation 9, where d_0 is an arc length in radians. Length d_p is directed perpendicular to the A-train track and adjoins a point on the MLS ground track and the correlative nadir measurement point.

$$d_{\mathrm{p}} = r_{\mathrm{e}} \times d_0 \times \sin(\chi) \tag{9}$$

The along-track separation d_{n} was also calculated, to allow selection of measurement points in close proximity to the centre of the A-train track. d_{n} lies between $[\phi_{\mathrm{i}},\ \theta_{\mathrm{i}}]$ and the intersect of d_{p} with d_{m} (Figure 10). Calculation of d_{n} applies Pythagoras's theorem to the right angled triangle with sides of d_0 and d_{p}, as shown by Equation 10.

$$d_{\mathrm{n}} = r_{\mathrm{e}} \times \left(d_0^2 - d_{\mathrm{p}}^2\right)^{\frac{1}{2}} \tag{10}$$

For the analysis in this thesis, data from different instruments is only co-located if it meets the conditions of two spatial constraints. Firstly, the across-track distance between the correlative measurement points must be satisfied by $d_{\mathrm{p}} < 15\,\mathrm{km}$. Secondly, only data within $d_{\mathrm{n}} < 150\,\mathrm{km}$ of the MLS tangent point are included in the following analysis to ensure valid comparisons. Measurement data outside this range are excluded from our analysis. The choice of d_{p} was largely compromised by the size of the equivalent diameter of the CERES product of 20 km, with larger reported grid cell dimension than reported for the MODIS cloud-top product. d_{p} must therefore be sufficiently large to ensure that the correlative data from CERES is in a continuous strip along-track, whilst small enough to be broadly consistent with the narrow across-track view of MLS. An additional swath-width allowance of 5 km considers small variations in the alignment of the Aqua and Aura measurement tracks along their orbits. A time-constraint is also applied on the correlative data comparisons. Co-location in this thesis analyses data points from correlative instruments only if the Aqua observation time is less than 9 minutes ahead of Aura MLS measurements.

3.2.2 Subsetting Datasets

Subsetting is a useful first attempt to select useful measurement data for comparison with a specified set of instrument products by the use of an off-track viewing angle. Subsetting reduces the required server space substantially, depending upon the swath widths of the instrumental measurements being compared. MODIS data can be obtained with a swath subset width of 200 km prior to download from the NASA Goddard Earth Sciences Data and Information Services Center[7].

[7] `http://mirador.gsfc.nasa.gov/`

Datasets were subsetted further in this study by identifying measurement points within close proximity to the central swath of the nadir measurement footprints. Subsetting was performed post-download for both MODIS and for CERES (Aqua) data. Since sensor footprints from A-train instruments are centred over broadly the same region of the Earth's surface, observations by different instruments over the central track are coincident.

MODIS and CERES products were provided as hourly datasets and their data subsetted prior to co-location, to vastly limit the processing of data to those measurement points that were largely constrained to within the 7 km across-track view of the MLS instrument.

3.3 Estimating Cloud-top Pressures Using A-train Measurements

In this study cloud measurements from MODIS and CERES were compared with MLS cloud observations using the co-location methods described in Section 3.2. Cloud top pressure analysis was performed using correlative data within each MLS sensor footprint from 1st to 16th September, 2006. An autumn equinox data period was chosen for analysis to represent a similar portion of high clouds from both the north and south hemisphere. During this period the solar zenith angle is zero at the equator, such that the daytime surface heating drives the most intense and therefore deeper convection over the tropical continent. The pattern of solar heating during the autumn season therefore favours high cloud formation that is hemispherically symmetric. The choose of data from the equinox also gives consideration to the diurnal cycles in high cloud properties, since irrespective of latitude the sampling period ensures that equal portions of daytime and nighttime scenes are observed by the A-train instruments. Daytime sampling is in the early afternoon (1:30pm local time) in the northbound (ascending) satellite orbit. At this time of day intense solar heating over the continent means that more tropical storms are in the developing stage of their lifecycle.

In this chapter, comparisons were undertaken in the tropics and subtropics between the latitude range 50°S to 50°N. The latitude restriction to this study is applied to assure low latitude high cloud comparisons resulting from deep convective plumes. Extending the analysis to higher latitudes would encompass different types of high clouds that form part of extra-tropical storms; synoptic

type cirrus associated with weather fronts, and local thunderstorms that form on a much smaller length-scale than the MLS along-track field of view.

Two methods were developed in this study to estimate the Cloud Top Pressures (CTPs). One method estimates CTPs from a vertical set of cloud IWC observations from MLS. Another method estimates CTPs by calculating the effective emitting temperature viewed from CERES that measures outgoing longwave radiation, using the Stefan-Boltzmann relationship described in Section 3.3.3 and a co-located MLS temperature profile. The MODIS GSFC team provides a CTP product for analysis of ice clouds in the atmosphere, so no further algorithm was developed using this data. Valid comparisons were restricted to ice clouds, as the MLS cloud product reports no measurements of warm clouds in the low to mid-troposphere. The MLS signal is frequently saturated at lower altitudes by warm clouds, as discussed in Section 2.4. This was achieved by the use of thermodynamic phase data from the MODIS cloud product. For each MLS sensor footprint area containing high clouds statistics were collected and compared with the MLS observed high clouds. This includes information on the percentage coverage of high clouds of the total cloudy-sky scene, the average cloud-top pressures, and standard deviation of MODIS and CERES cloud-top pressures. The information was used to investigate whether CTPs are consistently measured by MLS, MODIS and CERES and how scattered or discontinuous sections of high cloud may adversely affect these measurements.

3.3.1 Estimating Cloud-top Pressures from MLS (Aura) Cloud Ice Measurements

CTPs were calculated at each MLS sensor location by examining ice water content, reported on 6 logarithmic levels from 261 hPa to 100 hPa. Ice clouds were not reported by the MODIS instrument at $p < 100$ hPa, thus not allowing comparisons between MLS and MODIS cloud products at these lower pressures. A description of the MLS IWC product can be found in Section 2.3.1. The algorithm developed in this study identifies the lowest reported MLS pressure level where cloud IWC exceeds $0.5\,\mathrm{mg\,m^{-3}}$, as illustrated by Figure 11. A value greater than zero was necessary, as the MLS IWC product is subject to point-to-point noise in the signal that introduce significant uncertainty in the presence of thin ice clouds located at lower altitudes.

The chosen concentration threshold for this study was selected by examining

the gradient of MODIS versus MLS CTP correlation using different threshold concentrations for IWC between 0.3 and 1.4 $\mathrm{mg\,m^{-3}}$ in intervals of 0.05 $\mathrm{mg\,m^{-3}}$. The analysis region was chosen using estimated mid-tropospheric precision in the version 2 IWC product, as reported by Livesey et al. (2007) that over the range 0.6 to 1.3 $\mathrm{mg\,m^{-3}}$ at 215 hPa. Data was collected by undertaking a Pearson's correlation between MODIS CTPs and estimated MLS CTPs. This initial study with a 16-day sample revealed a correlation with MODIS CTP data that is mostly linear and reports the lowest mean bias. The best threshold value must therefore be sufficiently high to ensure that a reported level contains ice clouds, yet not too low as to cause the algorithm to become over-sensitive to optically thin clouds and instrument noise. This leads to a low pressure bias in MLS CTP data. This may result in a weaker positive correlation of CTPs between MLS and the validating instrument.

In general, the cloud ice particle number density decreases at a rate that is proportional to the inverse logarithm of altitude. This is because the absolute humidity of the surrounding air-mass decreases at a similar rate. In this study, cloud profiles reported by the MLS are examined from the cloud top to the base assuming a negative vertical lapse rate in the relative humidity of environmental profiles and a tendency toward lower ice particle concentrations at lower pressures. The lowest pressure level is identified where a critical IWC concentration ($y_{\mathrm{c}}[i]$) was exceeded. In this study $y_{\mathrm{c}}[i] = 0.5\,\mathrm{mg\,m^{-3}}$ as justified above and marked on Figure 11. On Figure 11, the adjacent height level for interpolation is indicated by a major x-axis marking at a higher pressure level (lower altitude value) of $\kappa_{k+1}[i]$. For MLS IWC profiles where interpolation is not successful, the corresponding co-located limbs are discarded from the analysis.

The mathematical notation for the linear interpolation scheme is highlighted by Equation 11, where k represents the retrieved pressure level from $p = 261$ hPa ($k = 1$) to $p = 100$ hPa ($k = 8$) and $\zeta_{\mathrm{c}}[i] \propto -\log(\kappa_{\mathrm{c}})$ at an MLS index position i and indicates the cloud-top height (CTH) in kilometres. To create CTPs using the MLS algorithm a CTH scale is used for the linear interpolation, since this gives a set of fixed physical depths for each sampled slab of atmosphere that comprise an atmospheric column. Providing that each unit volume of the atmosphere is sampled equally, the instrumental offsets in units of kilometres between each dataset and the errors in their detection methodology are the same at all CTPs.

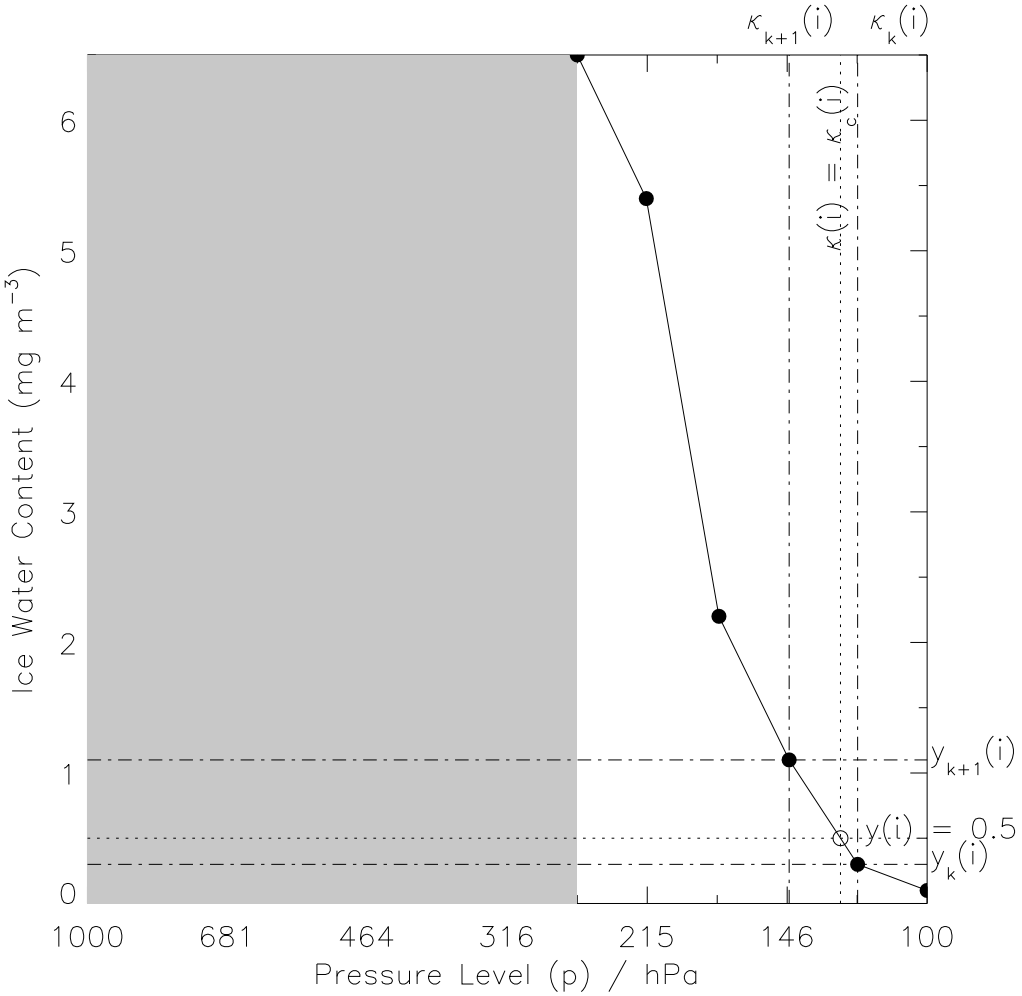

Figure 11: Example of an ice water content (IWC) profile (filled circles and line graph) for MLS sensor position i. The profile is shown with respect to a logarithmic pressure scale $-\kappa$ that is directly proportional to atmospheric altitude. $261\,hPa > p > 100\,hPa$ is a set of MLS pressure levels, as indicated by the minor divisions where IWC is reported. The grey-filled region indicates altitudes where the V2 IWC product does not report clouds. The figure demonstrates the location of cloud-top pressure (CTP) by the open circle at the intersection of the dotted lines where $\kappa[i] = \kappa_{\rm c}[i]$. The cloud-top pressure is found by linear interpolation between MLS pressure levels $\kappa_{\rm k+1}$ and $\kappa_{\rm k}$ to find the point where $y = 0.5\,mg\,m^{-3}$, a critical ice particle concentration that considers the IWC precisions reported by the V2 MLS product.

$$\zeta_c[i] = \zeta_{k+1}[i] + \left(\frac{y_c[i] - y_{k+1}[i]}{y_{k+1}[i] - y_k[i]}\right)(y_{k+1}[i] - y_k[i]) \tag{11}$$

The interpolation scheme in this study can estimate CTPs using MLS IWC data near the tropics to a vertical resolution of $CTH_{\rm k+1} - CTH_{\rm k} = 1.2\,{\rm km}$, where $CTH_{\rm k} = 16 \times (3 + \zeta_{\rm k})$. The height scale CTH used here is an approximation to the altitude in the low latitudes (Wu et al. 2009). Later comparisons

between CTP in this study are comparing a direct proportion of $\log(CTP_1)$ against $\log(CTP_2)$, where CTP_1 and CTP_2 are the cloud-top pressures of two independent datasets. The empirical relationship between the logarithm of pressure and altitude is based on a 16 km atmospheric thickness between the surface and dynamical tropopause, which is based on the standard tropical atmosphere as defined in Cole & Kantor (1962). All the algorithms generated for this chapter are calculated on a pressure scale, though the correlative data and regression in this study are strictly comparing the logarithm of CTPs.

The MLS cloud product only reports ice clouds, whilst MODIS view the same clouds from above at a higher horizontal resolution. Within each MLS footprint there are many MODIS measurements, with only a fraction of these viewing icy tops of clouds. As a result, near-nadir viewing instruments can often see through gaps in overlying ice clouds to lower altitude clouds that are composed of liquid cloud droplets and mixed (ice and liquid) phase clouds. To overcome this difference in viewing geometry and ensure like comparisons with MLS, MODIS thermodynamical phase data from the cloud-top product was used in this study to separate the cloud scenes into three portions. The thermodynamic phase algorithm discriminates between mixed-phase clouds, water clouds and ice clouds and forms part of the MODIS cloud top pressure (CTP) algorithm (Ackerman et al. 1997, King et al. 1997). Co-located data for cloud scenes were produced for this study within equivalent measurement footprint areas indicated by Figure 10. Later in this study, the analysis is focussed upon those scenes with almost homogeneous ice tops.

Statistical data on the percentage of ice clouds is produced for each MLS sensor location using the thermodynamic phase product that is detailed in Section 2.3.2. The high cloud fraction was estimated in this study, by counting the number of cloudy measurement points detected by MODIS ($n_{\mathrm{g}\wedge\mathrm{x}}[i]$) at a nominated MLS tangent point i, where x represents off-nadir detections of cloud with ice phase tops a or mixed phase b. The subscript $\mathrm{g}\wedge\mathrm{x}$ indicates the a conditional probability, where the correlative data is both suitable for comparison (g) and also meets another condition x that describes the thermodynamic phase of clouds.

The high cloud fraction detected from MODIS (Aqua) was determined by examining each cloud phase (ice (a), mixed (b), liquid (c)) in turn. Successfully detected cloudy pixels of each phase x at each MLS position i are each multi-

plied by a weighting according to their likelihood of containing ice clouds. The sum of these values ($A + B + C$) are subsequently divided by the total number of cloudy measurements within the same MLS measurement footprint i.e. $n_{\mathrm{g}\wedge\mathrm{a}}[i] + n_{\mathrm{g}\wedge\mathrm{b}}[i] + n_{\mathrm{g}\wedge\mathrm{c}}[i]$. This data processing provides an estimate of the relative fraction of ice cloud phase grid cells within each MLS sensor footprint. The percentage of cloud-tops with ice tops that are contained within a 150 km × 15 km co-located area at MLS position i is denoted I_g[i] and was calculated by Equation 12.

$$I_{\mathrm{g}}[i] = \frac{(A + B)}{(n_{\mathrm{g}\wedge\mathrm{a}}[i] + n_{\mathrm{g}\wedge\mathrm{b}}[i] + n_{\mathrm{g}\wedge\mathrm{c}}[i])} \times 100\,\% \tag{12}$$

The algorithm assigns a weighting of 1.0 where 100 % for coincident clouds viewed by MODIS within a MLS sensor area have tops composed of ice crystals. The total number of ice cloud measurement data from good MODIS pixels (white squares on Figure 12) is denoted $A[i] = n_{\mathrm{g}\wedge\mathrm{a}}[i] \times 1.0$. Mixed phase grid-cells (pixels) were allocated a weighting of 0.5 (50 % ice composition). The number of ice grid cells within a mixed-phase scene is given by ($B\,[i] = n_{\mathrm{g}\wedge\mathrm{b}}\,[i] \times 0.5$), assuming a 50:50 ratio of liquid and ice. For MODIS grid cells that are reported as liquid cloud scenes, represented by $C[i] = n_{\mathrm{g}\wedge\mathrm{c}} \times 0.0$, the algorithm asserts that no ice clouds are present (i.e. $C[i] = 0$). At the location of each MLS measurement footprint, correlative CTP data is only analysed where MLS views high clouds and MODIS also reports clouds. If the algorithm reports MLS CTPs ($p < 261$ hPa), but no thermodynamic phase information is available from MODIS, then the atmospheric limb at that MLS position is considered to be cloud free.

Clear grid cells were not included in the analysis, since no cloud of any phase was detected by MODIS in the nadir pixel cluster. The geometry of the MLS footprint and off-nadir grid cells from MODIS or CERES are indicated by Figure 12.

Limitations CTPs are highly subjective, especially as there is often no well-defined transition between ice water and clear sky within a nominated MLS profile. The choice of a 0.5 mg m^{-3} threshold value for detection of CTP works only for well defined tops, since there is a lower uncertainties in the altitude for which this value corresponds. This is particularly relevant for high clouds that are thick, where the neighbouring cloud in the MLS field of view induces a modest radiance signal at higher altitudes thus leading to a significant low pressure bias.

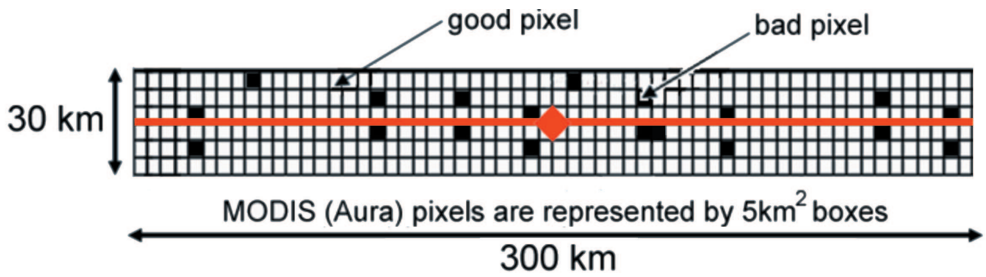

Figure 12: MODIS or CERES (Aqua) measurement points (square boxes with thin outlines) within a limb footprint of MLS (Aura). The A-train ground track is indicated by a central solid red line in the along-track orientation. A solid red diamond in the centre indicates the MLS tangent point location. To make comparisons between correlative data points, cloud-top pressure data from the nadir viewing instrument is averaged within the 30 km by 300 km strip. MODIS / CERES measurement data that are discarded are indicated by the filled black squares, which indicate nadir-sensed data that is not considered scientifically useful. Image is not to scale.

In contrast, thin high clouds with ice particle concentrations close to the cut-off threshold may go un-detected. Due to the variability in cloud top properties on a point-to-point basis, estimates are likely to either underestimate or over-estimate the CTP.

The main source of error arises from high clouds with a high IWC and scenes where ice clouds are unevenly distributed across the MLS limb. In particular, poor detection can result from shadowing or extinction associated with scattered clouds occupying a small fraction of an MLS limb (Read et al. 2007). In the best case scenario the MLS instrument can only resolve CTPs to within half a reported pressure level yielding uncertainties in the order of 20 hPa. Further details of the MLS cloud ice product are detailed in Section 2.3.1.

3.3.2 Cloud-top Pressure Estimates from MODIS (Aqua)

In this study, data from the MODIS cloud product was used to validate high cloud detections from the MLS. The NASA GSFC team was responsible for generation of cloud-top pressures using spectral information from different absorption bands in the infrared, as described in Section 2.3.2. Cloud data was extracted from the NASA MAM06S0 product and subsetted post download by selecting comparison data within 15 km (three grid boxes) from the central MLS ground track. The across-track grid-cell selection with respect to a central MLS tangent point is indicated on Figure 12. In this study, horizontal inhomogeneities in cloud cover were identified using calculations of standard deviation of MODIS CTP within

each footprint region. Higher CTP standard deviations indicate where clouds are viewed at off-nadir angles at a broad range of pressure levels within a MLS measurement footprint. Since the calculations are performed within the dimensional scale of a single MLS measurement footprint, they indicate the effect of viewing geometry and horizontal resolution on the validity of cloud comparisons. Since MODIS views at a wider across-track angle than MLS many clouds observed by MODIS are not observed by MLS. Successful comparisons of cloud products from different A-train instruments were achieved by restricting analysis to uniform cloud layers. These are defined by correlative data points with cloud height scatter lower than 100 hPa i.e. within the 4 km vertical resolution reported by Livesey et al. (2007). The layout of mapped MODIS grid cells within an MLS footprint are shown by Figure 12

Limitations There are several limitations to the MODIS CTP algorithm, such that some correlative cloud measurements are not suitable for comparison. Bad pixel clusters that comprise a grid cell may be caused by multi-layered clouds, where optically thin cirrus is highly scattered on a sub-grid level and overlies clouds of contrasting spectral properties. At these locations the MODIS algorithm is often unable to distinguish the thermodynamical phase and cloud-top properties that are responsible for signatures in the observed band radiances. Multi-layer clouds are identified using shortwave channels and analysed on dimensions of 1 km $\times$ 1 km and so are analysed on a sub-cell level for the MODIS CTP product. Bad grid cells may also be reported for cloud-tops greater than 100 hPa, where the CTPs cannot easily be resolved due to a near-neutral temperature lapse rate (Frey et al. 1999). Data from grid cells "flagged" as bad, reported as a fill value of -999, were not included in the mean and standard deviation calculations at that nominated co-located position.

3.3.3 Cloud-top Pressure Estimates from CERES (Aqua) OLR

CTPs were estimated from using measurements from the Outgoing Longwave Radiation (OLR) reported in the Single Scanner Footprint (SSF) product from the CERES (Aqua) instrument team. The SSF OLR product is described in Section 2.3.2 and detailed further in Wielicki & Barkstom (1997). Post-download subsetting was first undertaken to first discard 98.5 % of the unsuitable data, leaving only those measurements points that surround the central MLS measure-

ment footprint. Co-located analysis was then undertaken for the remaining grid cells within a 1.2° across-track angle of the CERES field-of-view at the surface (approximately ± 15 km from the nadir-view). This pre-processing is possible through routine examination of the SSF product metadata.

A processing system is developed for this study to estimate CTPs using indirect measurements of cloud-tops from CERES OLR, initially examining measurement to check whether the algorithm can perform valid calculations of CTP. Where no imager pixels can be identified as either clear or cloudy the CERES SSF parameters for those measurements are set to default values. Data at these grid cell locations are deemed poor quality and are not used in the CTP analysis. In addition, radiant intensities above 500 $\mathrm{W\,m^{-2}}$ (with associated brightness temperatures exceeding 306 K) were excluded from our high cloud analysis. For this study, it was assumed that these radiances are associated with either clear-sky or near-surface cloudy-sky emission. The resulting data is therefore assigned a CTP of 1013 hPa that is representative of the global mean surface pressure. The CERES CTP algorithm described below is not valid for these cases, because the Planck relationship between emission and temperature assumes a uniform representation of emissivity that is not the case for the Earth's surface. In addition the surface emissivity is independent of the character of the overlying cloud layers, making it difficult to attribute CTP data to cloud properties reported by MODIS at the same locations.

The CERES CTP algorithm functions by estimating the brightness temperature ($T_\mathrm{c}[j]$ / K) from single point CERES OLR measurement data. The brightness temperature refers to the apparent temperature of a surface by assuming an emissivity (ϵ) of 1.0. This is the temperature a black-body would be in order to produce the radiance perceived by the sensor, in this case the radiance received by the CERES broadband radiometer that is calibrated for $\lambda > 4\,\mu$m. At each point j that is located within the MLS footprint area, the algorithm resolves a CTP were valid CERES OLR data ($F^{+}[j]$ / $\mathrm{W\,m^{-2}}$) is detected. The method assumes that $F^{+}[j]$ measurements and $T_\mathrm{c}[j]$ are related by the Stefan-Boltzmann law, indicated by Equation 13. In this expression, the Stefan-Boltzmann constant is represented as $\sigma = 5.6704 \times 10^{-8}\,\mathrm{W\,m^{-2}K^{-4}}$. $T_\mathrm{c}[j]$ was calculated for each CERES measurement point that was classified as cloudy by MODIS within MLS sensor location i.

$$T_{\mathrm{c}}[j] = \epsilon \left(\frac{F^{+}[j]}{\sigma} \right)^{\frac{1}{4}} \tag{13}$$

The routine interpolates each value of $T_{\mathrm{c}}[j]$ to one of the 12 per decade pressure levels k where MLS version 2 temperature data is reported ($T_{\mathrm{m}}[k]$). The MLS temperature at pressure level k, is given by ($T_{\mathrm{m}}[i,k]$), for values of k in the range $k = 0, ...\, 14$ (1000 to 68 hPa) at MLS sensor position i. The closest pressure level (where $T_{\mathrm{m}}[i,k]$ is close to $T_{\mathrm{c}}[j]$) was obtained by Equation 14, which shows the mathematical notation for this process by set-theory. In this expression, $k \in \mathbb{N}$ indicates that k is an element of a set of natural numbers, which is given by $0 \leq k \leq 14$.

$$\begin{aligned} \{k \in \mathbb{N} \; : \; |T_{\mathrm{c}}[j] - T_{\mathrm{m}}[i,k]| = min\left(|T_{\mathrm{c}}[j] - T_{\mathrm{m}}[i,k]|\right)\} \\ = \{0 < k < 14, T_{\mathrm{c}}[j] - T_{\mathrm{m}}[i,k] > 0\} \end{aligned} \tag{14}$$

Equation 14 shows that for each singular CERES OLR measurement, reported at a certain grid-cell location j, the corresponding brightness temperature can be assigned to black-body emission from a finite pressure level k where the MLS temperature $T_{\mathrm{m}}[i,k]$ is closest. For this to be true the difference between the CERES brightness temperature and MLS brightness temperature must be at its minimum, i.e. $|T_{\mathrm{c}}[j] - T_{\mathrm{m}}[i,k]| = min\left(|T_{\mathrm{c}}[j] - T_{\mathrm{m}}[i,k]|\right)$, but values of k must first satisfy on further condition $T_{\mathrm{c}}[j] - T_{\mathrm{m}}[i,k] > 0$. This first condition states that the brightness temperature must be higher from CERES. As a result, the actual retrieved level (k) may correspond to a lower altitude than where the minimum difference between the brightness and measured temperatures, so it appears within the correct range of possible solutions. This ensures a consistent interpolation between T_{m} from pressures of $p_{\mathrm{m}}[k]$ to $p_{\mathrm{m}}[k+1]$, rather than in the downward direction from levels $k+1$ to k. The resolved pressure level resulting from the linear interpolation is referred to here as $p_{\mathrm{c}}[j]$. To obtain p_{c}, the algorithm developed for this study resolves a theoretical pressure level where $T_{\mathrm{c}}[j] = T_{\mathrm{m}}[i,k]$. This pressure level is located in the region $p_{\mathrm{m}}[k] < p_{\mathrm{c}}[j] < p_{\mathrm{m}}[k+1]$.

In a consistent fashion to MODIS data, CERES CTP estimates were then averaged over each MLS footprint within an area of 300 × 30 km by the methods described in Section 3.2. There are many CERES measurement points or grid-cells contained within each MLS sensor footprint, as indicated by Figure 10, with

each at a position defined by a profile number j. The co-location examines the algorithm output of the estimated CTP at each point, averaging them in the same region where MLS and MODIS also view clouds.

Limitations CTP estimates using CERES OLR data are most reliable for deep clouds that have an emissivity close to unity such as thick and uniform high clouds detected in the low latitudes. For suitable clouds, a large portion of the OLR must originate from the upper section of the cloud and the emission must also be well represented by a black body emitter. The effective emitting temperature used to estimate CERES CTPs depends crucially upon the transmission through a cloudy-sky column of atmosphere, a function poorly known for optically thin high clouds. In addition, the algorithm disregards upwelling emission that corresponds to a higher brightness temperature than the surface, making it invalid for thin or highly scattered cloud scenes. The CERES algorithm cannot alone distinguish the spectral properties of ice clouds and liquid water clouds unlike the MODIS cloud-top algorithm yet co-location with MODIS can help us to select suitable ice clouds for comparisons by combining cloud information from the same location. Some further limitations and errors associated with the use of CERES SSF data for CTP estimates are identified in Chapter 4.

Since the CERES instrument has broadband radiometers, the algorithm is deemed less accurate than high cloud observations from MODIS that can build a more complete picture of the cloud-top properties through the use of multi-spectral data. Generating estimates of the CTP from CERES are still considered useful for this study, as they demonstrate the general concept of how the longwave energy budget is related to the altitude of clouds. The data will also identify the types of cloud scene where this approximation is mostly valid and highlight locations where the energy budget is overwhelmed by the properties of other cloud features. Specifically, the consistency of the MLS CTP data is assessed by coincident comparisons with CERES derived CTPs to indicate a casual link between the rate of longwave cooling and tropical ice clouds. These comparisons form an important basis for more focussed studies of high clouds and the longwave energy budget in Chapters 5 and 6.

3.4 Case-study of a Tropical Cloud Cluster: Connections between MLS Cloud Ice and MODIS Cloud Top Detection

Observations are compared from the two A-train satellite instruments: MODIS and MLS, for a selected tropical location over the East Pacific Ocean. Figure 13 shows a "curtain-plot" of MODIS CTP and MLS IWC measurements over the latitude range from 15°S to 19°N on 20th April, 2005. The data is not co-located in this example, so along-track averaging does not smooth over the MODIS cloud-top pressure data. Instead the central 5 km of the MODIS (Aqua) track is plotted to highlight the importance of co-location for comparisons between different instruments that observe clouds in close succession. The case study demonstrates where observations of the same clouds monitored by MODIS on-board Aqua satellite and MLS on Aura during consecutive satellite passes are best consistent with each other. A curtain plot analysis is used for this analysis, which allows us to visualise the scene as a 2-d vertical cross-section that is swept out as a function of MODIS observation time as satellites travel across the Equator from the southern hemisphere (SH). The study makes direct comparisons of MLS IWC with MODIS cloud top data to assess whether their detections are consistent.

The lower panel of Figure 13 shows the x-y (horizontal) plane of the same region as the upper panel. The cloud product displayed on this panel demonstrates that only a narrow cross-section of the high cloud is sampled by the MLS instrument and that MLS IWC detections within the high cloud may not be representative of the entire cloud-mass. The horizontal length-scale of the central plume of these high clouds is ~ 900 km in the "y" direction. The tropical storm is characterised by a region of banded high cloud surrounding the main cloud-mass, where the MLS detects a maximum ice crystal concentrations of $12\,\mathrm{mg\,m^{-3}}$ at $p = 146$ hPa. The high values of IWC at observation times from 21:57 to 21:58 extend through much of the mid to upper troposphere, and the high altitude cloud tops detected by MODIS as low as $p = 146$ hPa, are characteristic features of a deep cumulonimbus plume. Data from Figure 13 show that the along-track variability in MODIS CTP is relatively small in this region, with standard deviations in the order of ± 25 hPa. These high clouds extend to the altitude of the tropical tropopause, which may be the result of locally strong vertical motion.

The data in Figure 13 also reveals some scattered high cloud formations

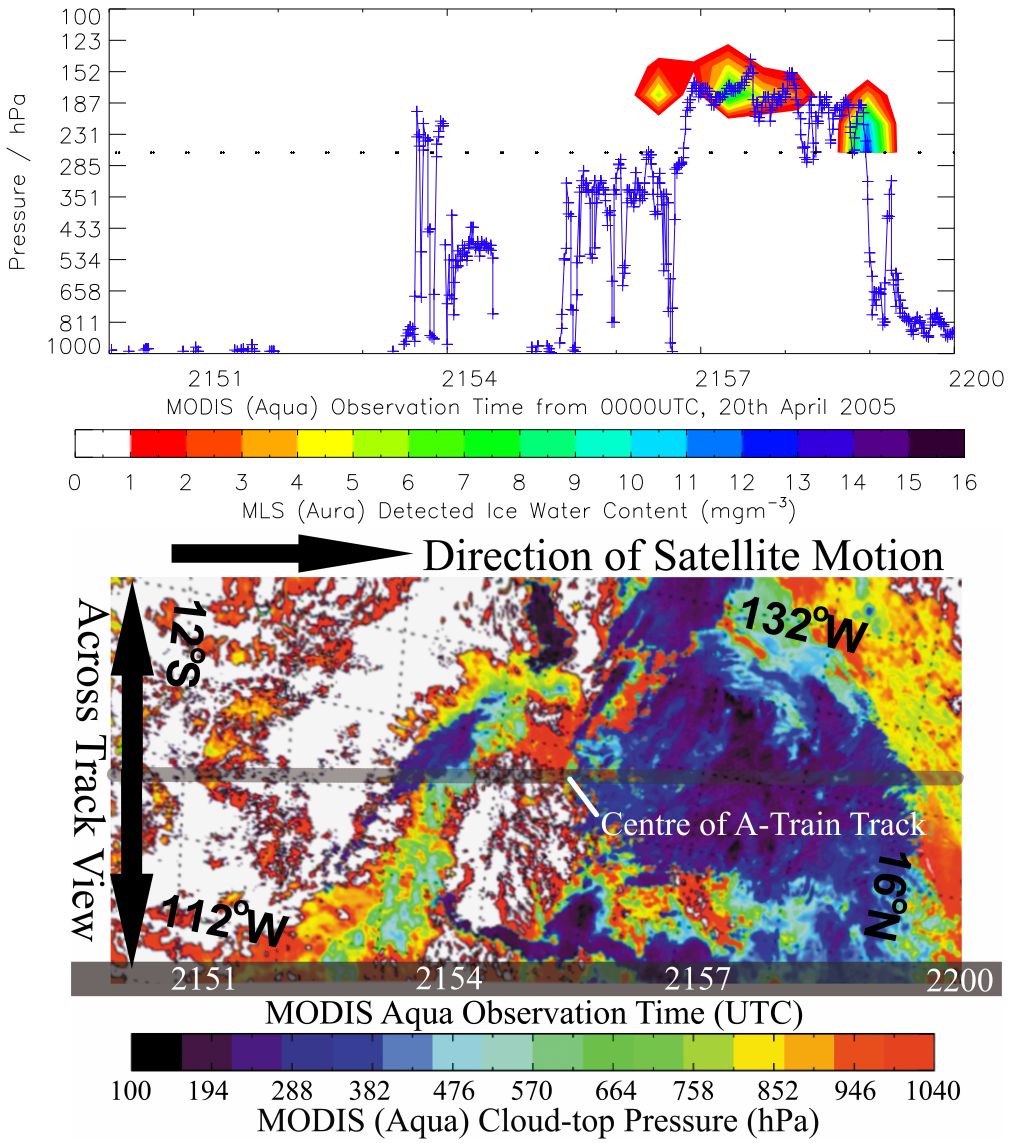

Figure 13: Coincident measurements undertaken by two different Aqua A-train instruments: MODIS and MLS, which both observe large-scale regions of high clouds. Top panel shows a vertical profile of cloud top pressure measurements from MODIS (purple line) and MLS IWC (filled colours) centred at MLS tangent points (marked by dotted line). Ice particle concentrations detected by MLS are shown at intervals of $1.0\,mg\,m^{-3}$*. The lower panel shows a plan view of the same section of atmosphere viewed by the across-track scanning MODIS (Aqua) instrument. The image maps MODIS data bounded by the co-ordinate [*$136\,W$*,* $108\,W$*,* $16\,S$*,* $20\,N$*], with latitude and longitude lines marked at* $4°$ *intervals. A grey strip shows the position of the MLS ground track. The "x" and "y" lengths indicate the across-track and along-track lengths of the measurement footprint respectively. The analysis used data from 20th April 2005 between 21:50 and 21:55 UTC.*

at observation times between 21:55 and 21:57 that are detected by MODIS at $800\,\mathrm{hPa} > p > 261\,\mathrm{hPa}$. The satellite imagery on the lower panel of Figure 13 indicates that there are narrow gaps between these high clouds that appear to be cirrocumulus striations, a structure that commonly forms on the leading edge of up-drafts within super-cells (NOAA National Weather Service 2010). The MODIS CTP data plotted on the top panel of Figure 13 shows a relatively large amount of variability in CTP in the order of $\pm\,40\,\mathrm{hPa}$, indicating that the high clouds are quite scattered within these MLS sensor footprints. Since these high clouds are associated with discontinuous ice clouds and their CTPs are very close to the maximum pressure for MLS detection, no IWC is detected above $0.7\,\mathrm{mg\,m^{-3}}$ at this location. These scenes appear to show cirrocumulus, which is often characterised by patchy ice clouds with isolated filaments rather than uniform horizontal layers. The data indicates that MLS may be particularly poor at detecting this type of high cloud, perhaps due to its broad along-track field of view.

There are some noticeable regions of discrepancy at the edge of a high cloud mass, where MODIS views low to mid-tropospheric clouds yet MLS views ice clouds. This region is associated with a tropical storm that extends some $\sim 1000\,\mathrm{km}$ along the A-train ground track, with an edge indicated by the boundary of the purple colours on the lower panel of Figure 13. The top panel of Figure 13 shows that shortly after 21:59 MLS detects a well-defined region of high clouds with ice concentrations exceeding $6\,\mathrm{mg\,m^{-3}}$. The lower panel of Figure 13, showing the broad across-track view of MODIS, highlights the location of high cloud-tops in a dark blue to black shading. It indicates that there are several locations where isolated clouds in the pressure range $500\,\mathrm{hPa} > p > 400\,\mathrm{hPa}$, whilst the MODIS line plot of cloud-top pressure resolved to a $5\,\mathrm{km}$ pixel shows that the surface is visible at some of these points. These cloud clearings in-between high cloud are detectable at MODIS observation times of 21:56 and 21:57 and shortly after 21:59.

One reason why MODIS views lower clouds in this region is due to differences in its instrument viewing geometry compared to MLS. Since MODIS is able to view between fragments of scattered ice clouds, it can see down to the underlying surface and low altitude clouds, whereas MLS cannot since it views along the limb. The MODIS data reveals that there is often a sharp along-track contrast in cloud-top pressure, which could prevent MLS detecting these clouds with its

300 km along-track field-of-view. Some of the discrepancies in the measurements may also arise from version 2 IWC product, which reports clouds on more levels than the MLS detection capability. The maximum vertical resolution indicated by Livesey et al. (2007) is 4 km at $p = 215$ hPa (i.e. $300\,\text{hPa} > p > 200\,\text{hPa}$). Reported IWC concentrations are sensitive to detections from neighbouring IWC pressure levels, with lower altitude thick ice clouds affecting the cloud-induced radiances in the levels above.

The case study highlights the importance of co-located analysis, a pre-processing ensures that MODIS and MLS comparisons are made valid. Later studies show that by averaging MODIS data within the measurement footprint of MLS, as shown by Figure 10, more valid comparisons can be made of a quantitative nature between instruments of different viewing geometries.

3.5 Co-located Comparisons of MODIS and MLS Cloud-top Pressure

Comparisons were made between MLS and MODIS measurements of CTP to assess whether their CTPs are consistent and how differences in their viewing geometry may affect the quality of future high cloud comparisons. For this study, a large sample of coincident satellite data (n = 1082 MLS profiles) were processed from 1st to 16th September. During this period, high cloud comparisons were reported only for cloudy-sky locations detected by the MLS instrument. This includes all scenes where the v2 MLS IWC algorithm reports scientifically useful i.e. in the pressure range $261\,\text{hPa} > p > 82\,\text{hPa}$. This analysis reports the pressure between two adjacent MLS pressure levels where a $0.5\,\text{mg}\,\text{m}^{-3}$ detection threshold is met. Further details of this interpolation and the MLS CTP algorithm developed for this study is described in Section 3.3.1 where the choice of a suitable IWC threshold is also justified.

Figure 14 shows a weak positive correlation between the estimated cloud-top height (ζ) from MODIS and MLS data. When the analysis is confined to ice clouds only, with tops reported above $\kappa\,(\text{MODIS}) = 261$ hPa, the positive relationship is much stronger with a Pearson's correlation coefficient of r = 0.72, (n = 508). The colours on Figure 14 show measurement points where MODIS thermodynamic phase data reports single phase ice (red), mixed phase (green) and liquid water (blue) clouds, as described in Section 3.3.1 (Figure 12). As colder ice clouds are

found at higher altitudes in the atmosphere, the corresponding red measurement points are more densely populated in the mid to upper troposphere from 5 to 16 km than the lower troposphere. These correlative data points are visible in the upper right quadrant on Figure 14. In contrast, liquid water clouds are more frequent at lower altitudes. This data is indicated by the dense blue measurement points to the left-hand side of Figure 14, located between the surface and 5 km.

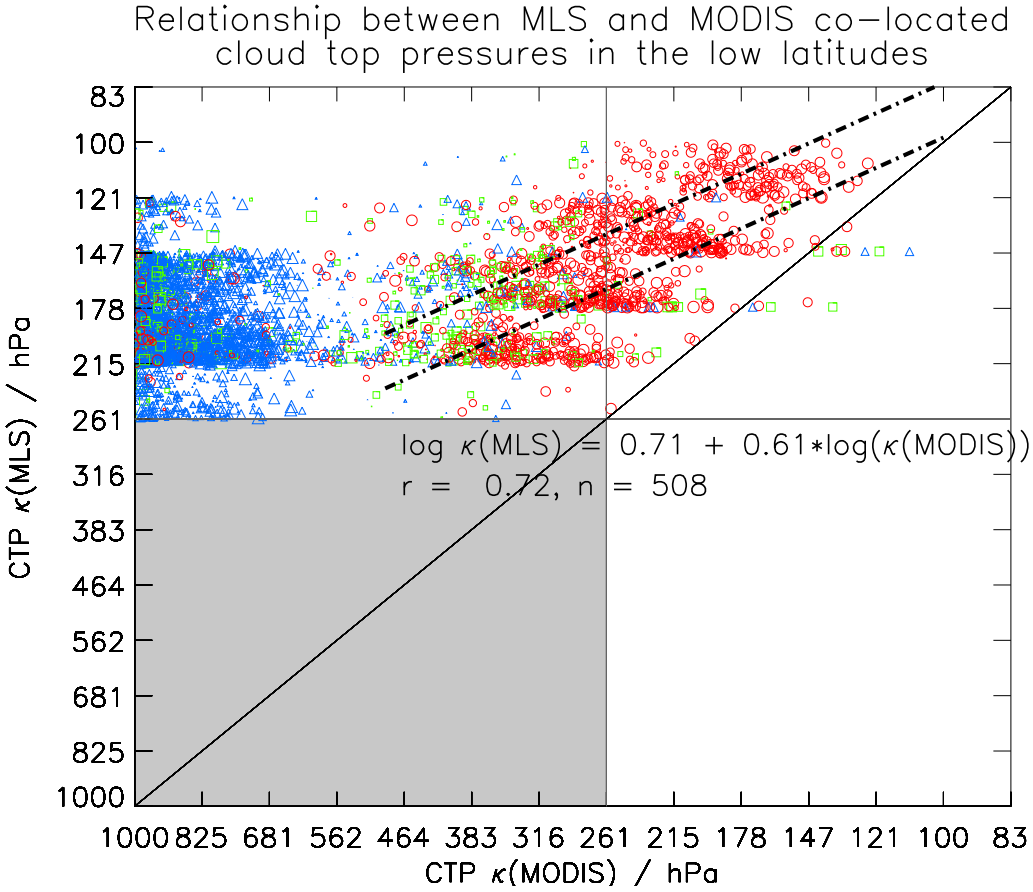

Figure 14: Correlative data showing cloud-top pressures (CTPs) measured by MODIS (κ(MODIS)) and MLS (κ(MLS)) at the same locations. The study includes all cloudy-scenes from 50°S to 50°N during the 16 day period 1st - 16th September, 2006. The correlative data demonstrates that cloud-top comparisons are more consistent for ice clouds (marked by open red circles). The blue triangles and green square correlative data points indicate the CTPs for liquid and mixed phase scenes respectively. Upper and lower best-fit lines of high ice clouds are shown by black dot-dashed lines.

The apparent mixing ratio of ice within clouds ($I_g[i]$) is calculated using MODIS thermodynamical phase data using Equation 12 (Section 3.3.1). In Figure 14 a spatially averaged cloud thermodynamic phase is also reported. The cloud phase indicates the fraction of MODIS measurements that are classified

as ice within an MLS measurement footprint. For liquid water clouds this is defined as ($I_{\mathrm{g}}[i] < 33\,\%$), whilst for mixed-phase clouds ($33\,\% < I_{\mathrm{g}}[i] < 66\,\%$) and ($I_{\mathrm{g}}[i] > 66\%$) for ice clouds. These correlative points are marked as red open circles in the top-right quadrant of Figure 14. The best fit analysis between co-located MODIS and MLS CTP measurement data, minimised by variance in ζ (MLS), is indicated by the two black-dashed regression lines. These show the minimum and maximum least-squares best-fit, using estimates of the CTP precisions associated with the respective detection methods. The best-fit analysis for ice clouds was also conducted in the scientifically useful range of v2 IWC measurements of $261\,\mathrm{hPa} > \kappa > 82\,\mathrm{hPa}$. The data in Figure 14 shows a general bias toward MLS cloud top heights (CTHs) higher than those indicated by co-located MODIS data, with a mean bias of $\Delta\,CTH\,(\mathrm{MLS} - \mathrm{MODIS}) = 2.0\,\mathrm{km}$. Mixed and water phase (warm) clouds are excluded from the analysis, since these detections are not deemed valid for comparisons with the MLS that does not report these clouds.

The measurement points in the top left quadrant show correlative CTPs where the MODIS instrument views both low and middle-layer clouds, whilst the MLS only views overlying ice clouds at the same location. Co-located data in this quadrant indicate locations associated with scattered high cloud. The more scattered high clouds become, the greater the fraction of lower clouds that can be observed at nadir by the MODIS instrument. The result is a higher CTP reported by the MODIS algorithm in comparison to MLS observations. In addition, differences in viewing geometry result in a weak positive relationship between MODIS and MLS CTPs for mixed and liquid phase cloud observations. These correlative data are indicated by blue triangles and green squares and are mostly visible in the left side of Figure 14. The data indicates that this accounts for much of the observed bias between co-located CTP estimates, since MODIS views many low clouds when the scene is covered in scattered high clouds, whilst the MLS cannot. For a specified MODIS CTP value, the results indicate a low precision in CTP estimates, with a mean co-located MLS-MODIS CTH point-to-point variability in CTP detections of $\pm\,3.0\,\mathrm{km}$.

In the bottom-right quadrant of Figure 14, any cloud present is at $p > 261\,\mathrm{hPa}$ and therefore MLS detects no cloud-tops and no correlative data points in this region. In the bottom left quadrant of Figure 14 co-located data is not reported, since these detections consist of low to mid-tropospheric clouds, rather than high

clouds that are only detected by MODIS and not by MLS. This area is represented by grey shading.

3.6 Analysis of Co-located CERES and MLS Cloud Top Pressures

The correlative data in Figure 15 shows a positive correlation between the $\log(\kappa\,(\text{MLS}))$ and $\log(\kappa\,(\text{CERES}))$. To relate the brightness temperature to cloud-tops only low latitude ice clouds were considered, since these are the focus of later studies. The lowest altitude where ice clouds could feasibly be detectable by CERES in the tropics is 490 hPa. This is based on the assumption that the ambient air temperature must be below 258 K for frozen water to dominate e.g. Liou (1986), Platt (1989), and a dry environmental lapse rate assumption from the boundary layer. The best fit analysis between MLS and CERES CTPs ($\log(\kappa)$) are conducted up to 100 hPa, a pressure level that is consistent with MODIS CTP comparisons. At the tropics $p = 100$ hPa coincides with the cold-point tropopause, above which clouds are a rarity due to a temperature inversion. This inhibits the influx of moist tropospheric air from convection into the stratosphere. The Pearson's correlation coefficient of CERES versus MLS CTP data is r = 0.70 (n = 1103). The mean $CTH(\text{MLS}) - CTH(\text{CERES})$ point-to-point variability is ~ 5 km for the correlative data points shown, that decreases the strength of the positive relationship between the two datasets. In general the data from Figure 15 demonstrates that MLS views high clouds, at the same locations as those viewed by the CERES instrument.

The results also show that depressed longwave emission is linked to high cloud tops for uniform high clouds located in the tropics. The relationship between correlative CTP data in Figure 15 is statistically significant at the 99.9 % confidence level; however the relationship is non-linear at lower altitudes. The non-linearity is likely to be a result of scattered high clouds scenes, where CERES views low clouds rather than continuous horizontal layers of high cloud. As for comparisons with MODIS, the results indicate that differences in instrumental viewing geometry dominate the correlation between the two CTP datasets. Again, comparisons with MLS data indicate that nadir instruments observe lower level clouds through scattered ice clouds. This results in a low altitude bias for both MODIS and CERES CTP measurements with respect to MLS CTP.

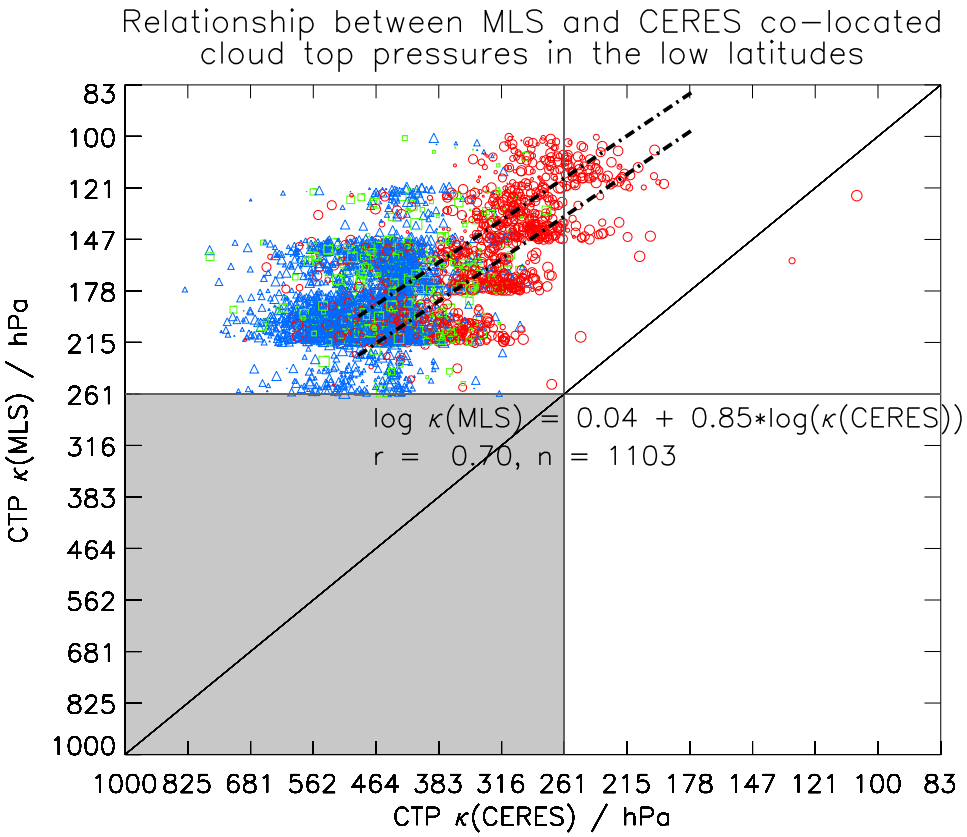

Figure 15: Similar to Figure 14 using co-located cloud phase data from the MODIS (Aqua) instrument (colours). Red, green and blue correlative data points indicate ice, mixed and liquid phase cloud detections respectively. The figure shows Cloud Top Pressures (CTPs) observed by CERES (Aqua) (κ (CERES)) identified by an algorithm developed from FM3 outgoing longwave radiation data on the x-axis. At the same locations, MLS (Aura) CTPs (κ (MLS)) are reported on the ordinate. The range of best-fits between the CERES and MLS κ values for high ice clouds are indicated by dot-dashed black regression lines.

Co-located data in Figure 15 shows a significant off-set between MLS and CERES CTPs, with high ice clouds detected by MLS from 261 hPa to 100 hPa correspond to an effective emitting temperature from levels in the atmosphere from 600 hPa to 200 hPa. Data in Figure 15 show that the mean bias in ζ(MLS − CERES) is greater at lower altitudes. This results in a weak positive Pearson's correlation coefficient of r = 0.37 when considering cloud data of all particle phases. The mean off-set between CTHs detected by the two instruments; CERES and MLS, range from $\Delta\,CTH$ (MLS − CERES) = 4.3 ± 0.5 km for κ (CERES) values of 261 hPa, to $\Delta\,CTH$ (MLS − CERES) = 4.3 ± 0.5 km at κ (CERES) = 100 hPa. This is a result of OLR for optically thin clouds scenes that are general lower than over deep cumulonimbus where the $\epsilon \sim 1$ approximation is more

valid. For these clouds, a large portion of longwave emission may arise from the atmosphere below the cloud base, explaining some of the observed CTH offset. Variability in low level cloud cover and properties also play a significant role in moderating the outgoing longwave emission than high clouds for scattered scenes. In addition, contrasting temperatures between high and low clouds tend to become more influential as the average cloud-top altitude increase, also causing a small positive bias in the CERES CTH data.

3.7 Discussion / Conclusions

Valid comparisons between clouds observed by different A-train instruments are achieved by co-location. Co-location ensures that the area of atmosphere sampled by different instruments is the same, so that measurements can be compared that are observed at different times and that are viewed with different geometries. In this study cloud measurements from different A-train instruments are compared to assess whether they are consistent. CTP methods are first developed to validate the version 2 MLS cloud product against other A-train satellite data. The results obtained from analysis of co-located cloud measurements, which allows us to confirm whether or not low latitude high clouds reported by MLS algorithm at higher altitudes are also detected in the same locations at higher altitudes by the MODIS and CERES (Aqua) instruments. By combining information reported by the same clouds by different instruments, this study shows that comparisons are best for horizontally uniform ice phased clouds.

On a case-study basis a "curtain plot" provides a visual tool to identifying discrepancies between cloud ice detected by MLS and cloud-tops measured by MODIS. This study investigates a tropical cloud mass and its neighbouring high cloud bands by the use of data subsetting without using co-location to resolve measurements to the same area. The results show that MODIS views high cloud where the MLS detects high ice particle concentrations in the mid- to upper troposphere, but only on length-scales that are generally less than the MLS along-track field of view. The MLS instrument however only reports clouds at $p < 261\,\mathrm{hPa}$ and reports an average IWC across a 300 km along-track strip even when much of the high altitude region is cloud-free. The same scenes are viewed on a much finer horizontal resolution by off-nadir instruments that can detect many low altitude clouds in the same regions as thick ice clouds. Previous studies with CALIPSO

satellite data indicate that tropical clouds extend through much of the troposphere, with bases located at pressure between 890 hPa ($z \sim 2$ km) and 950 hPa ($z \sim 0.8$ km) (Stith et al. 2002). MODIS views much of the clouds at these altitudes that extend outward from the tropical cloud base, so its mean cloud detection altitude is consequentially much lower where high clouds are horizontally scattered. As a result, later work in this thesis focusses on comparisons of large-scale collections of cumulonimbus, rather than scattered high cloud scenes.

Case study analysis in this chapter also shows that where narrow filaments of banded high clouds aligned orthogonal to the satellite track they are not well detected by the MLS instrument whose detections extend much further in the along-track than across-track orientation. On the other hand, at the edges of tropical clouds there is evidence of some detection of thin high clouds by MLS where MODIS only reports low clouds although this may partially be due to the MLS vertical field of view that extends into the mid-troposphere. The results again indicate that non-uniform high clouds, whose properties vary on length-scale less than 300 km, are generally poorly detected than larger scale clouds. This is due to the poor along-track field of view of the EOS MLS instrument. More valid studies are then undertaken by calculating the standard deviation within each co-located MLS measurement area. This allows the selection of more horizontally homogeneous cloud scenes, specifically where CTP standard deviation values are less than 100 hPa. The data shows that these scenes are monitored most consistently by different A-train satellite instruments. Further validity is achieved by constraining CTP comparisons to ice clouds, according to the MODIS thermodynamic cloud phase data.

Further cross-instrument comparisons are undertaken using CTPs. The reported Pearson's correlative coefficient between MLS and CERES CTP data, and MLS and MODIS CTP data were both significant at the 99.9 % level, indicating a general consistency in their detections of high cloud. Specifically, the study demonstrates that on average MLS detects high clouds at higher altitudes (lower pressure) than the MODIS instrument with a relatively small point to point bias of 2 km. Although CERES CTP estimated from OLR broadly demonstrates that less longwave radiation emerges from higher altitude clouds, its comparisons with physical cloud-top data from MLS IWC reveals a substantial offset and a 4 km point-to-point disagreement in CTP. The positive CTP bias presented in the CERES CTP data compared to MODIS CTP is thought to be attributed to the

non-uniform and grey-body nature of tropical high clouds. As a result, underlying low to mid-troposphere clouds greatly impact the cloud-top brightness temperature for nadir-sensed measurements. Overall, the data indicates that CTP is not an ideal input into climate models, whilst noting that the 4 km vertical field-of-view for IWC detection may account for much of the discrepancy with other A-train data.

MODIS thermodynamical phase data is used to demonstrate that MLS CTPs are both consistent with MODIS and CERES CTPs for ice clouds only. When the CTP comparison is constrained to ice clouds, much smaller biases are reported than when liquid and mixed phase clouds are viewed at off-nadir angles. Viewing geometry may also causes some discrepancy in the definition of CTP. This produces inconsistencies where MODIS does not report data on thin high altitude cirrus but MLS does. Further discrepancies in CTP are likely where the MODIS algorithm observes multi-layered clouds and cannot discriminate between the spectral properties of each cloud layer. Whilst MLS derived CTPs are unaffected by warm clouds, when scattered high clouds are present a low altitude bias is introduced when averaging MODIS CTP data in each MLS measurement footprint due to warm clouds that are visible in the downward view. This means that valid comparisons of CTPs for high cloud scenes must only include those scenes that are predominantly covered by a single layer of ice clouds. Previous studies by Dalanoe & Hogan (2010) demonstrates that synergistic measurements from CloudSat and CALIPSO penetrate further down into the clouds interior than MODIS, producing a low CTP bias.

Despite the reputed accuracy of MODIS CTP measurements, the MLS instrument provides extra detail on the interior ice particles and the atmospheric composition of high clouds. This data could be used to make further estimates of the OLR that can be compared in a much more valid fashion with co-located CERES measurements. Future algorithms to determine MLS derived CTPs may also prove more successful for thin high altitude cirrus. This could be achieved by adopting a detection threshold value that varies as a function of altitude, since the V2 MLS IWC product reports much higher precisions near the tropical tropopause.

4 Statistical Comparisons of MLS High Clouds with Co-located A-train data

4.1 Introduction

Few studies have been undertaken using data from the MLS cloud product to investigate the consistency of their high cloud measurements. Studies of this kind are valuable, as they demonstrate how data from different A-train instruments can be combined to improve our understanding and confidence of several high cloud properties. The combined information provided by multiple products on the same clouds is used to build a more detailed and accurate profile of cloud properties, which make some A-train measurements synergistic (Savtchenko et al. 2008). Past studies by Dalanoe & Hogan (2010) demonstrate how the use of synergistic data from the CloudSat and CALIPSO instruments can enhance our understanding on high clouds. Despite recent advances in space-borne observations, the distribution of high clouds and their future change in response to climate change remains uncertain (Solomon et al. 2007). Synergistic comparison can provide the accurate cloud data that is required for climate studies, superseding those currently provided by the International Satellite Cloud Climatology Project (ISCCP) Rossow & Schiffer (1999). This study shows how data from several A-train satellites can be closely cross-validated by co-location, offering an improved and more consistent record of high cloud data for future climate studies.

In this study, high cloud obtained from A-train MLS cloud ice measurements are validated against coincident Cloud-Top Pressure (CTP) data from the Moderate-resolution Imaging Spectroradiometer (MODIS). Comparisons are also undertaken with a derived CTP from the Clouds and the Earth's Radiant Energy System (CERES) instrument, using Outgoing Longwave Radiation (OLR) from the Single-Scanner Footprint (SSF) product. To achieve this, 16 days of data (an orbital repeat period) are analysed to represent each of the four seasons during 2006. During these periods, a representative coverage of surface measurements are reported by the MODIS, CERES and MLS instruments equatorward of 82°. The data is used to investigate the regional changes in high cloud distribution and fractions. This analysis also provide insight into the patterns of large scale circulation, and the relationship between high cloud fraction and the OLR from

which CERES high cloud fraction is determined. Profiles of ice water content (IWC) are first converted into high cloud fractions by co-location and further data processing. Statistics are then generated on a regional basis, using a set of fixed grid-cells, to determine whether two independent sets of high cloud data are significantly different. The bias between high cloud fractions is then presented as visual "traffic-light" coded maps, by examining the variability in co-located CTPs within each regional grid-cell using their respective cloud-top pressure mean and standard deviations. T-test statistics are then used to determine whether the datasets are different in a more quantitative fashion.

In this study, the success of the MLS instrument for detecting high clouds is investigated. This is achieve by coincident comparisons of MLS high cloud occurrence frequency with CERES and MODIS detections. Several questions are addressed: Are MLS measurements of high cloud fraction and seasonal distribution in the low latitudes consistent with other A-train instruments? Are cloud products sensitive to different types of high clouds situated at different altitudes? What is the relationship between deep tropical ice clouds and the longwave radiation budget? The study in this chapter investigates the regional character of high clouds, in contrast to Chapter 3 that compare the point-to-point correlation between cloud-top pressures (CTPs) to validate the MLS IWC product. The findings from this chapter will help improve confidence in the synergistic combination of satellite data for future climate records.

The study begins by developing a process for generating seasonal and regional distributions of high clouds using co-located CTPs. These methods and the associated error estimates of each method are detailed in Section 4.2. The results from this mapped cloud data and the inter-satellite covariance statistics are then presented in Section 4.3. This study then addresses whether MLS seasonal high cloud fraction and its regional distribution are consistent with MODIS and CERES in Section 4.3.1. Section 4.3.2 presents the covariance statistics for cloud-top datasets based on the mean and standard deviation of each to assess whether they are consistent. Discussions and conclusions are detailed in Section 4.4.

4.2 Methodology for High Cloud Mapping

The distribution of clouds can be mapped by further processing of the CTP data, produced in Chapter 3, to generate high cloud fractions. In addition, methods are

developed in this chapter to visualise and quantify the bias between high cloud fractions from MLS data and those estimated from the Aqua nadir instruments: CERES and MODIS. To decide whether high cloud data from different A-train instruments are consistent with one another, regional (or seasonal) discrepancies are quantified by examining the sensitivity of high cloud fractions to uncertainties in the upper and lower pressure range estimated for each CTP dataset. The overlap of different high cloud fractions are then examined using Welch's t-test statistics, which are aggregated to each grid box to quantify the likelihood of any bias between two different cloud data. To perform a statistical analysis, cloud-top data was averaged both spatially over each regional grid-box and also over the 16 day time period that represents a season.

Co-located A-train data was collected as described in Chapter 3 and cloud-top pressures (CTPs) generated for 5th - 20th April (spring), 14th - 29th June (summer), 1st to 16th September (autumn) and 14th - 29th December (winter) all in 2006. The average high cloud fraction was reported on a set of grid-boxes with dimensions of 12° longitude by 6.5° latitude, with regular grid-cell dimensions of $\sim$ 725 km in the extra-tropics. Within each grid-cell approximately 64 measurement tracks are represented of which half are ascending A-train orbits. The data was mapped in the range 52°S to 52°N, the maximum range in which significant high cloud data was reported in the CTP algorithm using MLS ice water content data. The CTP algorithm developed in this study allocates a high cloud confidence to the co-located nadir-sensed measurements that is classified with a 1 bit code: 1 for 100 % cloudy, and 0 for 0 % cloudy. High cloud is defined as either present (CTP $<$ 261 hPa) or absent (CTP $>$ 261 hPa). This critical pressure is based on earlier studies in Chapter 3, which show that cross-instrument comparisons with MLS are only valid when constrained to ice clouds at these pressures. Since MLS views along the limb it does not report information on the lower altitude mixed and warm phased clouds that are frequently viewed at off-nadir angles at the same locations as many high clouds. Each MLS footprint contains many MODIS and CERES measurement points as indicated by Figure 3, where CTP from MODIS and CERES is spatially averaged. Consideration is later given to the error in CTP to estimate the upper and lower range of CTPs within each MLS measurement footprint and therefore provide a likely range of high cloud fractions.

There are two main caveats of the data sampling used in this study. Firstly,

on an individual profile basis, a sparsely distributed set of data points are used to report cloud statistics. The quantity of nadir measurement data used to generate statistics depends on the instrument's horizontal sampling. For the CERES instrument $20 - 30$ measurements are co-located to each MLS profile, compared to $60 - 90$ for MODIS. Since the reported measurement grid-cell dimensions are sufficiently large and co-location ensures that they are equal, sampling errors are not considered as a significant uncertainty. Despite this, the irregular sampling of high clouds within each grid-cell would produce slightly different results if the analysis was replicated for the same regions using a different set of representative measurements. In addition, a limited selection of data is analysed from each seasonal period in 2006 that may not be representative of all years. As a result, only broad signatures and large-scale features of high cloud fractions are discussed.

4.2.1 Estimating Cloud-top Pressure Uncertainties

Each A-train instrument that observes high clouds has errors associated with its detection algorithm. Errors are dependent upon the vertical precision of cloud detections, which introduce uncertainties into each CTP methodology. These uncertainties are then combined with errors derived from instrument noise that is received by the sensor from cloudy-sky scenes. The precision of the MLS IWC product is determined by the noise at 240 GHz where cloud-induced radiances are reported, whilst measurement uncertainties are also associated with the CERES longwave calibrated radiometer. MODIS CTP errors are pre-calculated during in-flight validation studies by Ackerman et al. (1997), King et al. (1997).

The CTP data investigated in this study are produced using different A-train detections of various cloud properties. To calculate the differences in high cloud fractions at each region, the individual CTP errors are examined from each instrument. Cloud data is considered "very likely" to be significantly different, if the distributions of CTP data given by their respective mean and standard deviation on a regional grid-box scale do not significantly overlap. This is initially determined from the population mean of the two correlative measurement $\bar{c}$ and $\bar{d}$ each with a corresponding standard deviations (σ) where $\bar{c} + \sigma_c < \bar{d} - \sigma_d$ for $\bar{d} > \bar{c}$. In the case that the two correlative data do not meet this condition they are deemed significantly different, and a significant bias exists in their CTPs. The likelihood of two correlative datasets being similar is quantified by the use of a Welch's t-test statistics, which is conducted a seasonal basis for all regional grid-

cells equatorward of the mid-latitudes. These values are used to decide whether high cloud data from MLS are more than 99 % likely to be different than MODIS or CERES (Aqua) cloud data.

MODIS The errors associated with the MODIS (Aqua) cloud-top slicing are detailed by Menzel & Strabala (2006) and are summarised in Section 2.3.2. Validation of the MODIS (Aqua) cloud-top algorithm was achieved by comparisons with radiosonde moisture profiles and other remotely sensed cloud products. A CTP root-mean-square error estimate of 40 hPa is reported in the (MYD035) cloud-top product algorithm theoretical basis document by Ackerman et al. (1997), Menzel & Strabala (2006). This study adopts this CTP error estimate to calculate the likely range of high cloud fractions at each grid-cell location.

CERES There are several sources of error associated with CERES CTP estimates developed for this study. Firstly the quality of the Outgoing Longwave Radiation (OLR) data for generation of cloud-top information is assessed. A CERES radiometer is calibrated to detect longwave photons that are emitted from cloud, aerosols, atmospheric molecules and the Earth's surface. Uncertainties arise from estimate of upwelling irradiance (flux density) from different scene types. For high clouds from optically thick plumes and for overcast scenes, the root-mean-square error associated with the Single Scan Footprint (SSF) top-of-atmosphere flux from the edition 2A algorithm[8] is estimated at 6 %. This value differs by less than 0.1 % between the land and ocean surface scene types. The quality of the angular distribution models (ADMs) that describes how detected radiances vary as a function of instrument viewing angle, also affects the precision of the longwave estimates that are used to estimate cloud-top pressures for this study (Wielicki & Barkstom 1997). Further details on how the CERES instrument functions and ADMs are discussed further in Section 2.3.

The main source of uncertainty in CTP estimates arises from our algorithm design. Principally, the method outlined in Section 3.3.3 limits cloud-top estimates to those below the tropopause, where a well-defined vertical temperature gradient exists. In the tropics, a saturated lapse rate is associated with tropical convection (Tompkins & Craig 1999). This enables the algorithm to function for most cloudy-sky profiles in the vicinity of the equator, except for profiles where

[8] `http://eosweb.larc.nasa.gov/`

convective anvil outflows are detected in the tropopause. In this case the algorithm may not be able to interpolate to an MLS temperature at that MLS sensor location. To achieve a valid study, the MLS and MODIS data at these profile locations are also removed from the analysis. In addition, the CERES algorithm developed in this thesis views optically thin high clouds at a much lower altitude. This is because thin ice clouds are largely transparent to upwelling longwave radiation that originates from the underlying cloud layer. Optically thin ice cloud is characterised in a radiation budget context by an emissivity of $\epsilon << 1.0$ (Fu & Liou 1993).

As detailed in Section 3.3.3 the CERES algorithm relies upon a vertical temperature profile, which was obtained from the version 2 MLS product. CERES CTP estimates are therefore not strictly independent data; since their calculation are subject to higher uncertainties in presence of thick cloud that arise from limitations in the MLS temperature retrieval (Livesey et al. 2007). Clouds have an unpredictable effect on the retrieved V2 MLS temperature detection, reporting individual biases on a profile basis that are as large as 10 K within deep tropical plumes. For these calculations, the assumption is that cloud-screening of the version 2 temperature product data is adequate to keep these errors to a minimum, allowing CERES data to provide additional insight into the high clouds distribution and fraction. An MLS temperature input is preferred over alternatives, since its data can be co-located to exactly the same location as CERES views cloudy-sky emission.

MLS temperatures are used to estimate the radiant flux densities on a set of 15 levels for comparison with those observed from CERES at the same locations. The error in this CTP algorithm is estimated on a profile basis and is given by $\Delta\,\zeta = \sqrt{(}a^2 + b^2)$. In this expression "$a$" is the uncertainty in the vertical placement of clouds in units proportional to height (ζ km) and is assessed by the separation of reported pressure levels of the V2 MLS temperature product i.e. $a = \zeta_1 \pm 0.5\,\Delta\,\zeta$ where $\Delta\,\zeta = \zeta_2 - \zeta_1$. Here ζ_1 and ζ_2 are the adjacent vertical co-ordinates of the MLS product in the vicinity of T_c where $\zeta_2 < \zeta_1$. For data correlations, the assumption is that ζ height scale is directly proportional to $-\log(\kappa)$, where κ is the CTP. This proportionality was demonstrated previously in Chapter 3 (Figures 14 and 15). Linear interpolation used in the MLS CTP algorithm also uses this metric.

"b" is the maximum error in ζ that results from uncertainties in the input

of F^+, the measured outgoing longwave radiation (OLR) from the CERES SSF product. The errors from component "b" are also dependent on the local vertical gradient in the v2 MLS temperature profile and are greatest when the environmental temperature lapse rate, the rate at which temperatures decrease with respect to altitude, is close to zero. b is largely insensitive to small errors in the CERES measurement data F^+, as the brightness temperature of the cloud top T_c is related to in the CTP algorithm by the expression $T_\mathrm{c} = (F^+)^{0.25}$. The errors in F^+ are almost consistent for all brightness temperatures although are higher for observations of optically thick clouds within tropical scenes, where a 6 % uncertainty is reported by Wielicki & Barkstom (1997).

MLS There are several limitations to cloud detection developed by the JPL science team. A major factor is shadowing of microwave radiation that arise from ice clouds whose length-scales occupy less than the separation distance between adjacent scans (Read et al. 2007). For those profiles, the detection can be either over or under-saturated. Ice clouds with high particle concentrations overwhelm the emission, shielding microwave emission emerging from clouds lying in the near-view of the limb before it reaches the MLS detector. In contrast, ice clouds in the far-view often appear warmer than the space and higher atmosphere that they shield, causing an enhancement of microwave detection. In this case, the MLS algorithm reports negative cloud induced radiances and cloud ice concentrations. The CTP algorithm in this study is therefore limited to dense ice clouds that extend the entire length of an MLS limb. These high clouds are associated with deep convective plumes (cumulonimbus formations), which are the focus of this study. Cumulonimbus scenes are defined by strongly positive IWC values exceeding a vertical mean of $5\,\mathrm{mg\,m^{-3}}$ between 261 hPa and 100 hPa. This restriction avoids errors in CTPs that exist for multi-layered cloud profiles, ensures that MLS detects high clouds above the $2\,\sigma$ (95 % certainty) threshold and that a definite single cloud-top can be identified irrespective of viewing geometry. Cross-instrument comparisons with these uniform high cloud profiles are therefore deemed more valid.

In this study, CTP errors are calculated according to the pressure difference between adjacent vertical levels of MLS. Clouds reported by MLS have depths $\Delta\,\kappa$ (hPa) in the range of $20\,\mathrm{hPa} < \Delta\,\kappa < 60\,\mathrm{hPa}$ (Livesey et al. 2007). The error estimates in this study assume that IWC can be resolved to within a half-interval

of CTP $\pm 0.5\,\kappa$. Errors also arise from limitations in the precision of the MLS ice water content product, which are reported by Wu & Jiang (2004) as a function of pressure. The resulting MLS CTP errors from each source were combined using a similar analysis as described earlier in this section for CERES CTP errors.

4.2.2 Methodology for Determining High Cloud Statistics

Statistics of high cloud fraction were mapped onto a regular grid by calculating the frequency of "cloudy" co-located footprints where the mean CTP is classified as high, using the methods described in Section 4.2. The lower altitude bound (maximum CTP of 261 hPa) represents the critical threshold level that interfaces high and mid-level cloud levels. The JPL science team only report clouds at lower pressures than this threshold e.g. Livesey et al. (2007), which are assumed to be entirely composed of cloud ice in this method. The upper altitude bound (minimum CTP of 100 hPa) represents the critical threshold for MODIS cloud-top slicing estimates to be deemed valid (King et al. 1997). CTPs below this value from MLS and CERES are all discarded as unsuitable, since they are not consistent with the limitations of the MODIS cloud-top slicing methodology. In our analysis, the minimum high cloud fraction reported is 5 % (one contour interval). This allows us to focus the analysis on patterns of large-scale high clouds in the low latitudes. The threshold was carefully selected to filter out short timescale variability in the mid-latitudes high clouds from the character of quasi-stationary high clouds that dominate the seasonal pattern of the tropics. Smaller high cloud fractions indicate that local ice water content detections are detected on short timescales (of 1 day out of 16), which occur most frequency at high latitudes as isolated systems track poleward following a tropical storm. These detections present great inter-annual variability and are not therefore representative of the seasonal mean high cloud fraction.

4.3 Analysis of High Clouds in the Tropics and Subtropics

4.3.1 Analysis of High Cloud Distribution Observed by A-train Instruments

The results of our seasonal high cloud distribution investigation are displayed by Figures 16, 17, 18 and 19. The data reveals that high clouds are more abundant over the tropical oceans, with patterns that migrate northward during

the northern hemisphere (NH) summer. The prevalence of high clouds over the tropics is due to convective instability and a deeper troposphere (Tompkins & Craig 1999). The mapping also demonstrates that regions with high cloud fractions exceeding 50 % are most frequent over the tropical regions: Central Africa, Central America and Indonesia. During the September and March Equinoxes the mid-day Sun is directly overhead at the equator and the Inter-Tropical Convergence Zone (ITCZ), a discontinuous band of high cloud, is aligned directly over the equator. During these periods $> 95\,\%$ of high clouds are detected within the latitudes of $\phi < 25°$, by all three A-train instruments; MODIS, CERES and MLS. Notable discrepancies between estimated cloud fractions are found in the Indian Ocean and Indonesian regions (tropical warm pool). At these locations high cloud fractions are generally the greatest, with maximum values of around 90 %.

High clouds are also detected in the extra-tropics, but are sparsely distributed ($< 5\,\%$ of global coverage) and are generally isolated. The rarity of optically thick mid-latitude ice clouds is likely to be attributed a lower tropopause height, restricting the prevalence of deep convection in the extra-tropics characterised by CTP $<$ 261hPa. During September MODIS detects a local region of high clouds at [37°S, 10°W] over the South Atlantic Ocean that is resolved at just one grid-cell location. These extratropical high cloud detections by MODIS are prevalent during September and are likely to be synoptic type ice clouds in the wake of large scale planetary wave displacements. Neither the MLS nor CERES instruments view much of these high clouds above a 5 % coverage at the same locations, indicating that MODIS tends to view more high clouds in the extra-tropics. This is consistent with studies by Wu et al. (2008) that show a low bias in V2 IWC product at extratropical latitudes compared to CloudSat due to systematic errors in the MLS retrieval. These clouds are also found at the tops of tropical storms and decayed hurricanes. On Figures 16(b) and 18(b) a large-scale region of high cloud is observed over the south-eastern states of the USA. These clouds arise from a dissipating tropical storm named Alberta, visible on the Geostationary Operational Environmental Satellite (GOES) East infrared imagery after 14th June (Franklin & Brown 2007). The tropical storm accounts for a $\sim 5\,\%$ high cloud fraction in this region.

Another isolated region of high clouds is detected by both MODIS and CERES instruments during June and September 2006. These high clouds are centred over

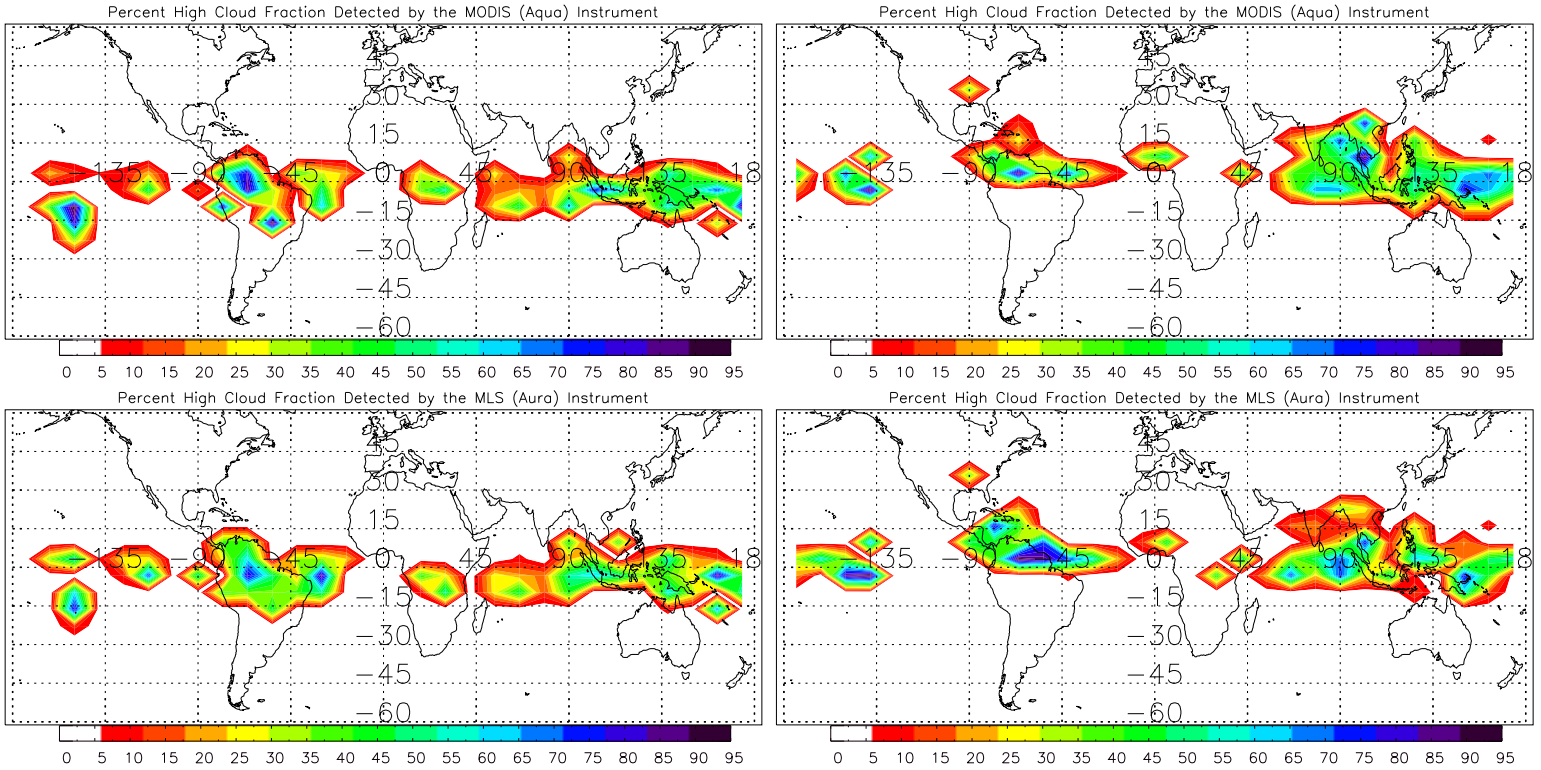

(a) 5th - 20th April, 2006 (b) 14th - 29th June, 2006

Figure 16: Seasonal maps of high cloud coverage as detected from MODIS cloud-top slicing (top panels) and estimated from MLS IWC (bottom panels) for two 16-day periods, covering two seasons: (a) April 5th - 20th, 2006 and (b) June 14th - 29th, 2006. MODIS and MLS cloud tops are colour contoured at 5 % *per contour. The maximum CTP for high cloud classification was defined as* 261.0 *hPa.*

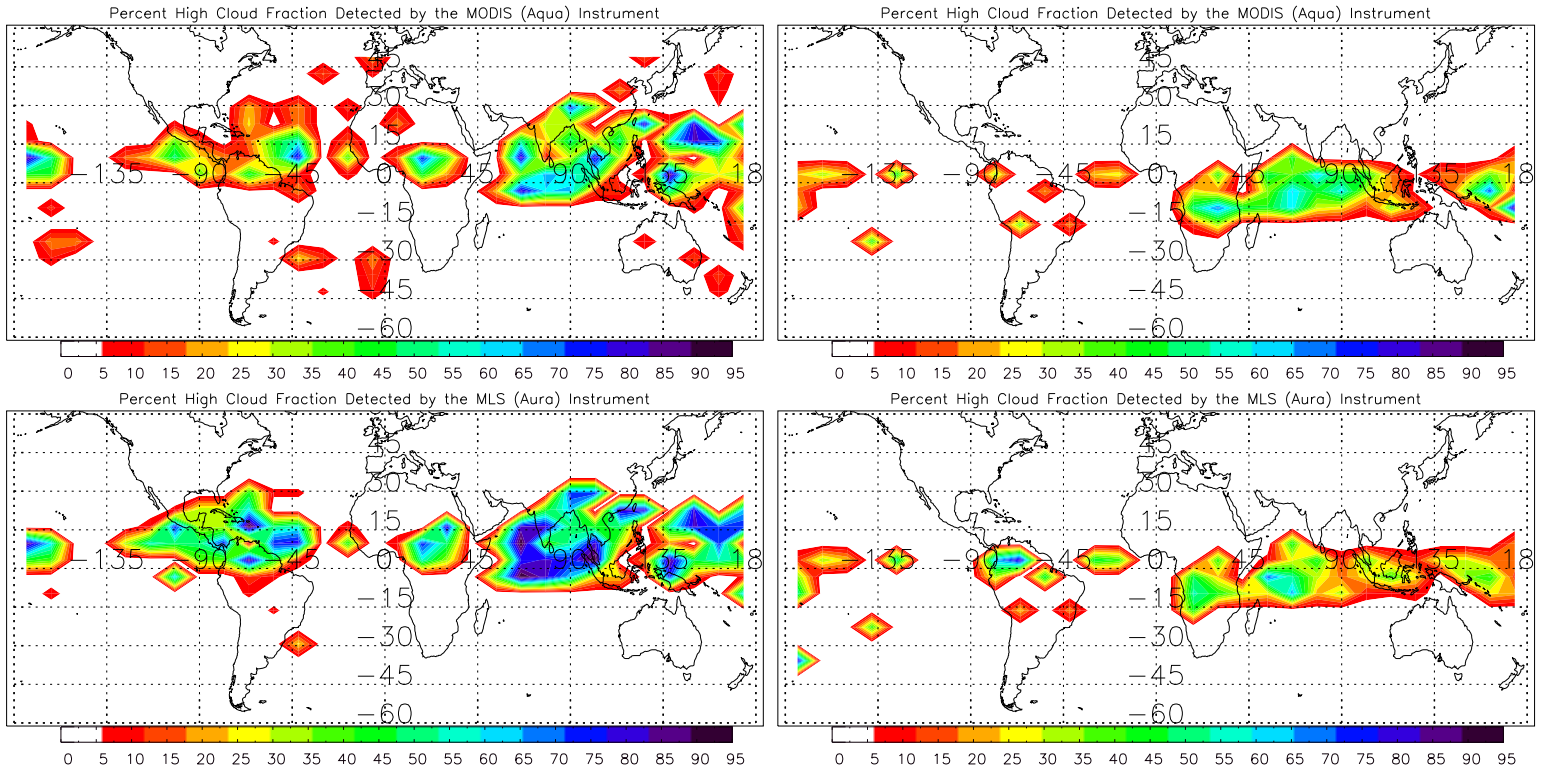

(c) 1st - 16th Sept, 2006

(d) 14th - 29th Dec, 2006

Figure 17: MODIS and MLS Statistical cloud maps as Figure 16 only for September and December 2006 analysis.

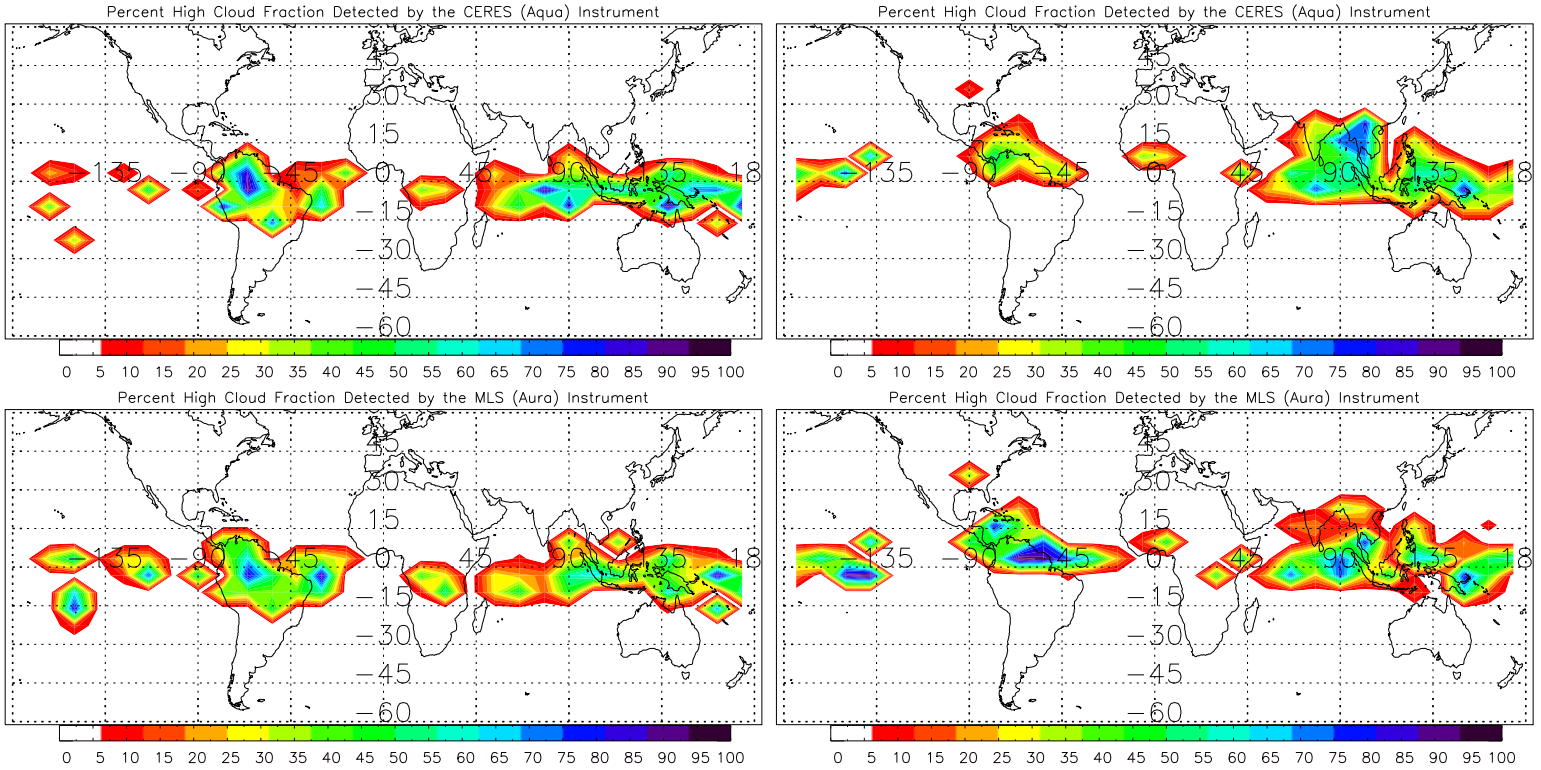

(a) 5th - 20th April, 2006 (b) 14th - 29th June, 2006

Figure 18: Seasonal maps of high cloud coverage as detected from CERES (top panels) and estimated from MLS IWC (bottom panels) for two seasons: (a) April 5th - 20th, 2006 and (b) June 14th - 29th, 2006. CERES CTPs were estimated by application of the black-body approximation to calculate an effective emitting pressure. Coloured contours of percentage cloud coverage are at levels of 5 % *per contour for CERES and MLS. The maximum CTP for high cloud classification was defined as* 261.0 *hPa.*

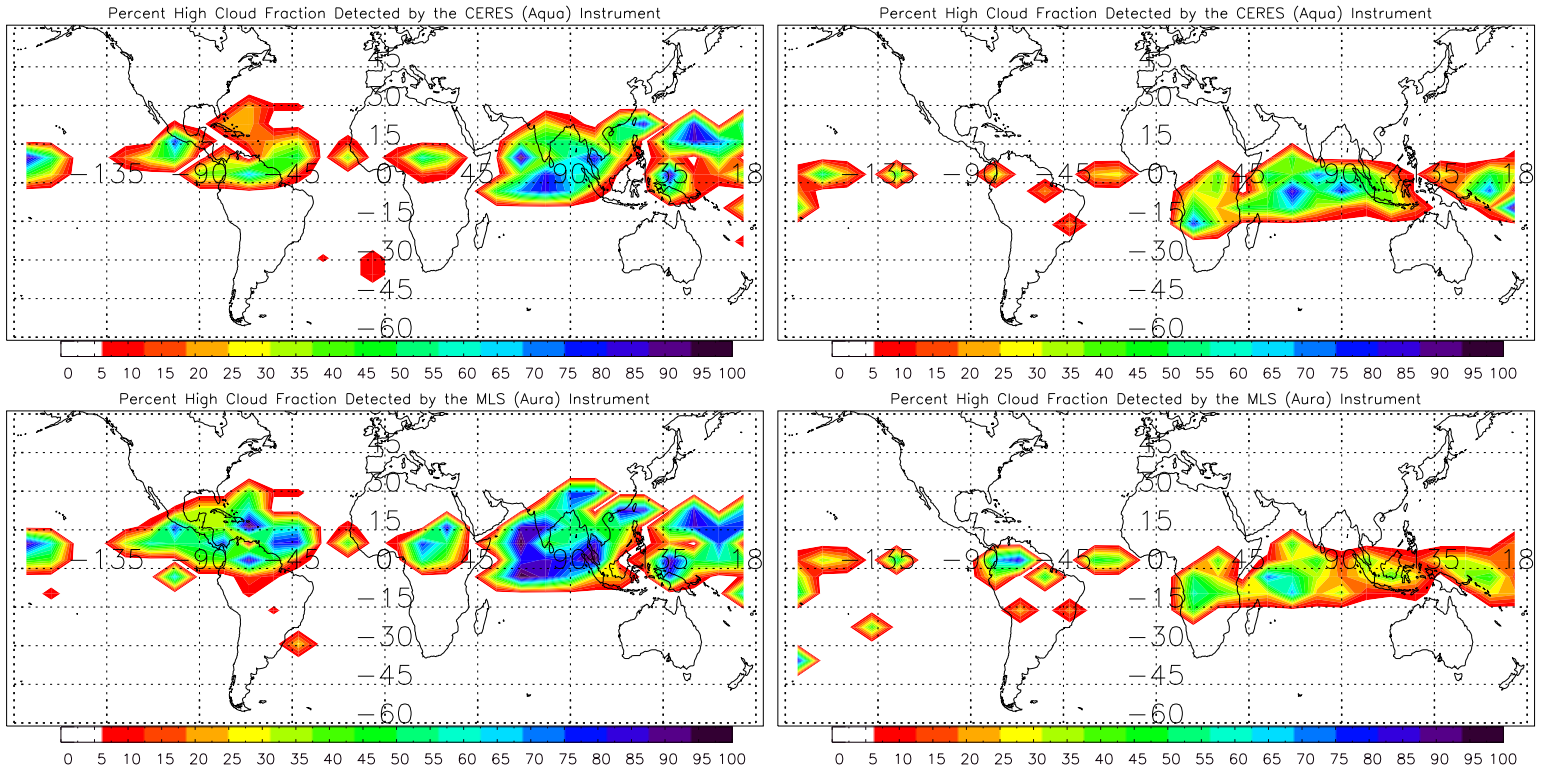

(c) 1st - 16th Sept, 2006

(d) 14th - 29th Dec, 2006

Figure 19: CERES and MLS Statistical cloud maps as Figure 18 only for September and December 2006 analysis.

[30°N, 90°W] during June, whilst during September the high clouds tend to cover a larger scale region extending from the Central American tropics. The MLS data does not detect mid-latitude ice clouds at this location, again indicating that MLS is more sensitive to tropical clouds.

The annual signature of high cloud reveals MODIS detections of high cloud coverage that is approximately 10 % lower than MLS, 5.6 % for MODIS compared to 6.2 % for MLS over the same seasonal period and regions. In general the data shows a larger high cloud fraction from MLS than either MODIS or CERES during September, 2006. These findings are in agreement with results from Chapter 3, indicating that the scattered nature of some high cloud scenes results in a systematic high altitude bias of 2.0 km and 4.3 km in comparison to those from MODIS and CERES respectively.

The maximum cloud fractions detected during each season are identified by MLS and MODIS in the same general regions of the globe. During the April period, high clouds are detected most frequently over north Brazil, whilst during June high clouds are highly prevalent, with a coverage exceeding 60 % in a general band over equatorial South-America. Both the MLS and MODIS algorithms identify these seasonal cloud features. During the September and December period, MODIS and MLS are both in agreement that a greater high cloud coverage is found just south of the equator, associated with the Asian monsoon. These clouds extend from 10°E to 100°E, with maximum grid-cell high cloud coverage of 65 % during September within a large-scale tropical disturbance.

Seasonal maps of high cloud fraction indicate that MLS detects more low latitude clouds than either MODIS or CERES where convective plumes are most frequently observed. In particular, data shows a seasonal dependency of high clouds detected by MLS in the Asian monsoon region with an annual mean fraction that is approximately one third greater. This data presented in Figure 16(b) provides evidence that MLS may detect some thinner outflow cirrus, since the atmospheric tape-recorder effect implies that higher upper tropospheric humidities succeeds the peak of the Asian monsoon (Gettelman et al. 2004, Udelhofen & Hartmann 1995). This source of water vapour is transported around the globe by upper level winds, with higher relative humidities detectable in the tropical tropopause layer that are a pre-cursor to thin cirrus (Haag et al. 2003). This may explain why during the autumn period, when Asian convective clouds are dissipating, our data reveals that significantly ($\sim 53\,\%$) more high clouds are observed

from MLS than either CERES or MODIS that exceed differences identified from all other seasons.

4.3.2 Cross-Instrumental Statistics

Figures 20 and 21 present the covariance statistics for the presence of high cloud on a grid-box scale, as inferred from different A-train satellite observations. The data shows that all three instruments agree that high clouds are most prevalent over the tropics between 30°S to 30°N. Correlative comparisons with MLS also demonstrate agreement on high cloud presence in the vicinity of the tropics during all four seasons, and the results from both validating instruments indicate that the spring is characterised by the least tropical ice clouds, with only a 10 % grid-box coverage by synergistic combination of MODIS and MLS high cloud data. For comparisons of CERES with MLS, cloud fractions indicate that 11 % of regions are confidently covered in some high cloud. All three instruments are in agreement that the autumn period from September 1st to 16th is pronounced with a higher frequency of high clouds. During this period 15.2 % (16.4 %) of grid-boxes are likely to contain high clouds within the mapped region using MLS and CERES (MODIS) data combinations respectively. For CERES and MLS comparisons the annual mean agreement on high cloud fractions was 32.9 %. This was calculated by dividing the fraction of grid-cells with overlapping CTP error bounds, with the total number of high cloud grid-cells.

Welch's t-test Statistics Further analysis on the cross-instrument consistency of CTP data was conducted using Welch's t-test statistics (Clarke 1973). This is similar to the student t-test, but allows two independent samples of the same size to be compared with unequal rather than the same variance. The use of co-location ensures that the number of MLS, MODIS and CERES CTP data measurements within each regional grid-cell is the same. In this study the variance of CTP data is calculated from the error analysis described earlier in this Section. The test assumes a Gaussian distribution of values about the sample mean of each data. In the case of the CERES CTP methods, the main assumptions is that the errors of the MLS temperature product reported by Livesey et al. (2007) are not the greatest source of error in the analysis. Another assumption is that Version 2 MLS temperature retrievals are not biased, such that the spatially gridded data is largely valid for cloudy-sky profiles. In the test, there are $(N \times 2 - 2)$ degrees

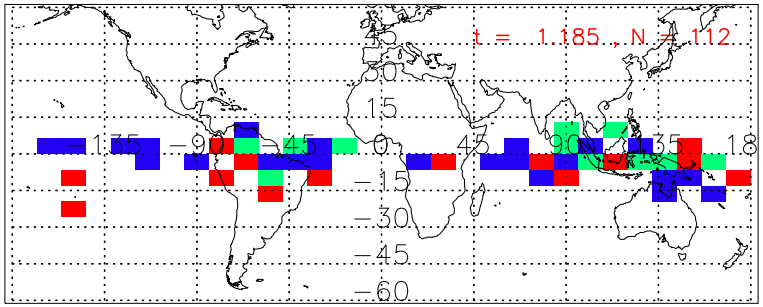

(a) 14/04/06 - 29/04/06

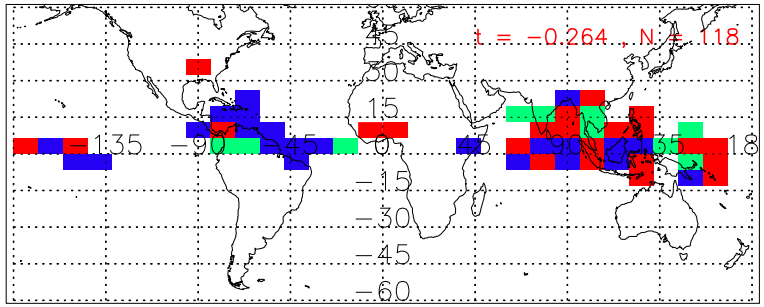

(b) 05/06/06 - 20/06/06

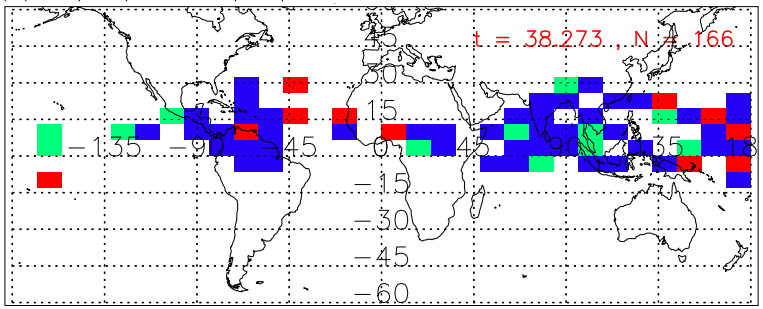

(c) 01/09/06 - 16/09/06

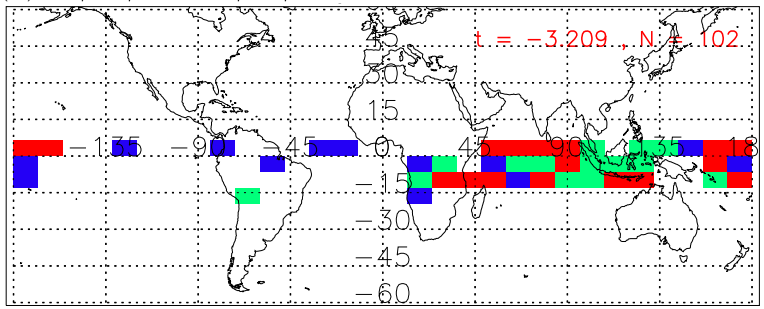

(d) 16/12/06 - 29/12/06

Figure 20: Seasonal high cloud maps indicating regions where two independent A-train measurements are consistent. Cloud maps (a) to (d) show the high cloud covariance between MLS and MODIS cloud-tops analysed for 12° *longitude by* 6.5° *latitude grid-cells. The colours indicate the inter-instrumental covariance of high clouds with co-located MLS CTP estimates. The green colour coding indicates regions where MLS and MODIS cloud-tops are consistent within the* $\pm 1\,\sigma$ *error bounds associated with both methods. Red and blue filled grid-cells indicate where MODIS detects significantly more or less high cloud than MLS respectively. Numbers indicate the two-tailed Welch's t-test values "t" for a number of correlative data grid-cells "N". The analysis includes white cells where neither instrument detect high clouds.*

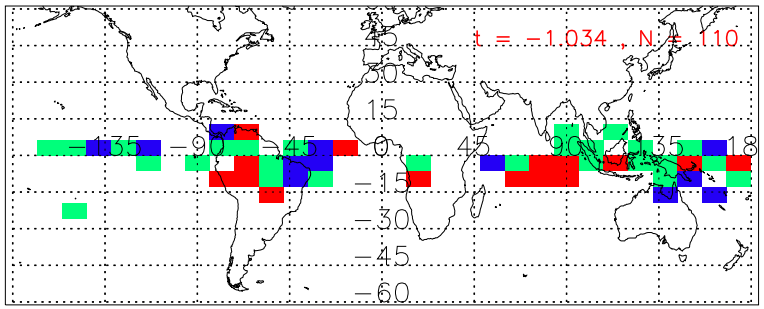

(a) 14/04/06 - 29/04/06

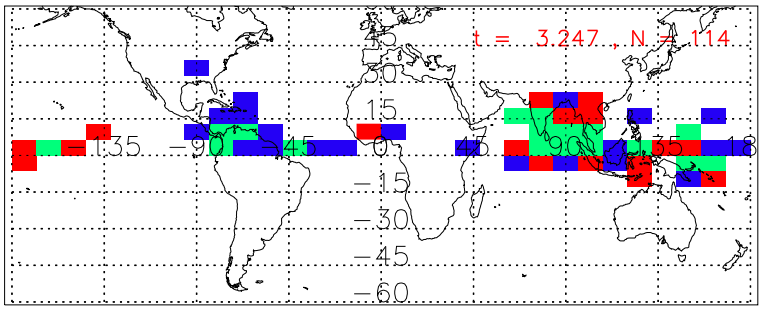

(b) 05/06/06 - 20/06/06

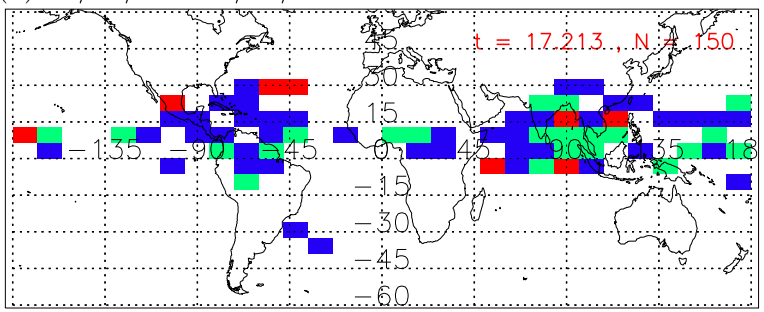

(c) 01/09/06 - 16/09/06

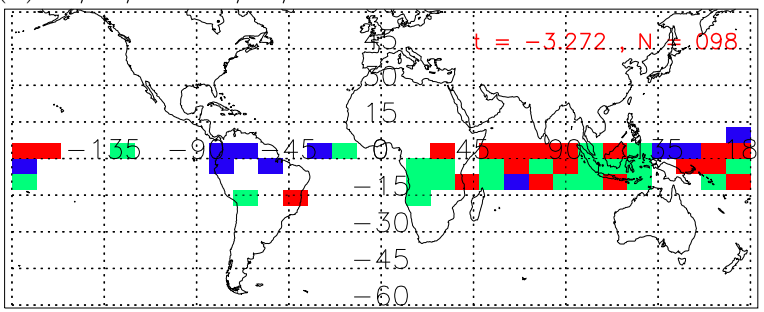

(d) 16/12/06 - 29/12/06

Figure 21: Cloud maps (a) to (d) show the high cloud covariance between MLS and CERES. As Figure 20, but analysis shows comparison charts for CERES (Aqua) rather than MODIS (Aqua).

of freedom (d.o.f.), where N is the number of regional grid-cells where MLS and the validating instrument both report high cloud fractions exceeding 5 %. The d.o.f. indicates the number of values in the final calculation of the statistics that are allowed to vary. A two-tailed t-test is assessed, since no hypothesis is made about which high cloud fraction data may be higher than the other. The null-hypothesis was rejected if the magnitude of look-up value exceeds a 99 % probability threshold.

In this study, the null hypothesis states that the two samples have the same mean high cloud fraction given the unique variance of each, given that the samples are independent of one another. Rejection of the null hypothesis confirms that the mean high cloud fractions estimated from two specified A-train instruments are significantly different. The sign of the t-test value informs about the direction of bias between the two sets of data, where a positive (negative) value indicates that the mean high cloud fraction reported by MLS is greater (lower) than the validating instrument. The degrees of freedom and t-test results are reported for each season and are displayed on the top of Figures 20 and 21 in red typesetting. The results show a significant difference in high cloud fractions for most seasons, with a ($p > 99\,\%$) bias reported between MLS and the validating instrument. The sign of the t-test statistics are positive during most seasons, which indicate a greater high cloud fraction is detected using MLS data than either MODIS or CERES. This bias is most significant in the mapped statistics for September ($t = 17$), when the ratio of deep blue to red grid-cells in Figures 20 to 21 is highest. In contrast the December data shows the converse, where MLS high cloud fractions are lower than either MODIS or CERES.

The null hypothesis was also rejected for high cloud fraction comparisons with CERES, for all periods with exception of April where the null hypothesis is accepted. By increasing the sample size using data from multiple years, replication of the analysis is less than 1 % likely to demonstrate that CERES and MLS cloud fractions are consistent given the error estimates. The annual t-test value for CERES and MLS high cloud fraction validations in 2006 was 6.95 ($N = 372$), which suggests that the mean reported high cloud fraction from MLS is significantly greater than CERES ($p > 99\,\%$). In contrast, for comparisons between MODIS and MLS, the results indicate that the null hypothesis was accepted for half the seasonal periods during 2006. The overall mean t-test value was 15.29 ($N = 498$), an overall rejection of the null-hypothesis, supporting the case that

MODIS high cloud fractions are significantly greater than MLS. As a final test, the CERES and MODIS cloud fractions were analysed to test the null hypothesis that their means are significantly different. The results demonstrate that our method for generating CERES and MODIS high cloud fractions produces results that are broadly consistent ($t = 0.49$, $p < 99\,\%$), and the null hypothesis was accepted. This result is consistent with warm CTP biases reported by MODIS and CERES in contrast to MLS reported by Figures 14 and 15 in Chapter 3. The bias is likely to be due to differences in the viewing geometry of MODIS and CERES instruments, which allows warm cloud data to be reported whilst more trust is provided by MLS measurements that reports data only on high clouds.

Seasonal Cycles in High Cloud Fraction To examine whether the seasonal cycle in high cloud fraction is consistently monitored, regional data was combined to give a single value for each period using cloud-top pressure data from three A-train instruments: MODIS, CERES and MLS. From this data, estimates of the high cloud fraction for each season are refined by synergistic combination. The high cloud fractions for each period are displayed by Figure 22, assessed by the mean regional grid-box high cloud fraction, equator-ward of 52° using the data presented in Figures 16 to 18. Each instrument detects high cloud properties using different frequencies and with different algorithms that convert their respective measurements into cloud-top pressures. Despite this, their co-located data shows striking similarities even though the previous results from Figure 20 to 21 show no in agreement on an individual grid-box level, on average they agree reasonably well.

A quantitative comparisons of seasonal high cloud coverage from the MLS, MODIS and CERES A-train instrument are presented in Figure 22, revealing a broad cross-instrument consistency. In particular, the vertical error bars in blue and red indicate the agreement between high cloud data from CERES and MODIS (Aqua) data broadly consistent, since their two independently measured values present standard deviations that coincide with one another (i.e. they present significant covariance). The A-train instruments report the most disagreement in the September period, with $6.5 \pm 1.5\,\%$ high cloud coverage observed by CERES, yet a significantly larger $10.4 \pm 1.3\%$ from MLS. This is in agreement with our findings from Section 4.3.1 that indicate that a larger portion of thin high clouds may form during the dissipative stages of the Asian monsoon, which MLS is more

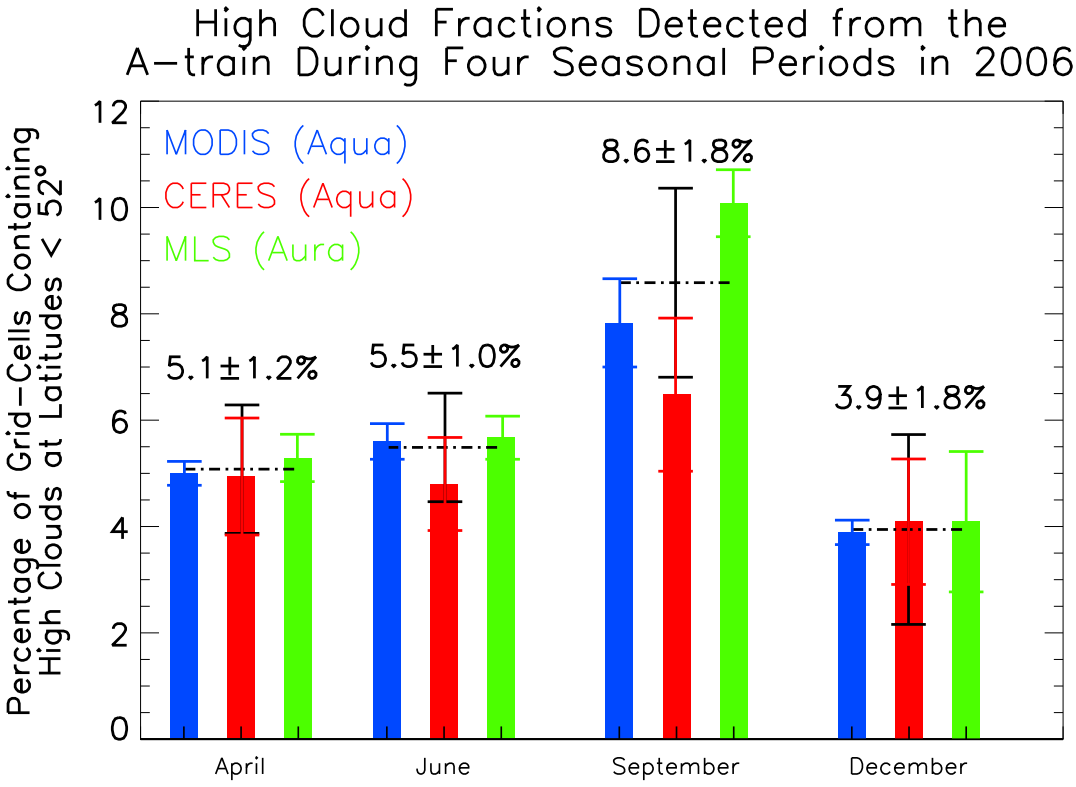

Figure 22: Bar chart indicating the percentage high clouds by averaging A-train high cloud fraction data within $12° \times 6.5°$ *in the latitude range from* $52°S$ *to* $52°N$ *using 16-days of co-located satellite data for each. The analysis presents the data mean and expected measurement range in a colour coded fashion with bars and lines respectively in blue (MODIS), red (CERES) and green (MLS). The figure also indicates the synergistic combination of the data to produce a collective mean and standard deviation, as annotated in text for each seasonal period. The mean and range of this combined value is indicated by the dashed-dot and black vertical lines respectively.*

sensitive to. In general the data presented by Figure 22 indicates that CERES and MODIS generally observe less high clouds than the MLS instrument in 2006, which is consistent with the overall positive sign observed by the earlier Welch's t-test scores.

The horizontal black lines of Figure 22 show the mean seasonal high cloud fractions by combining the three A-train data; MODIS, CERES and MLS by weighting each CTP mean by $1\,\Delta\,\kappa$, where $\Delta\,\kappa$ represents the errors in CTP for each dataset. A requirement for synergistic comparisons of this kind is a minimum of three independent data, to make any refinements valid. These seasonal mean high cloud values reveal more high cloud during September 2006, represented by $8.6 \pm 1.8\,\%$ of regional grid-cells in the latitude range 52°S to 52°N, again con-

sistent with the tropical monsoon season. During the spring and winter periods of April and December 2006, the number of grid-cells containing high clouds are consistently lower with cross-instrument means of 5.1 ± 1.2 % and 3.9 ± 1.8 % respectively. The results demonstrate that CERES OLR data is closely linked to the regional patterns of high clouds during different seasons across all the four seasons of 2006 that is consistent with MODIS instrument. MODIS CTPs are deemed the most trust-worthy, since they are provided by the NASA GSFC product development team and report the lowest errors of all three datasets.

By combining this trio of A-train data, the confidence in the seasonal patterns in the high cloud fraction is increased. The uncertainty in these estimates, indicated by the black error bars on Figure 22 using a combination of MODIS, CERES and MLS data is just ± 1.5 %. Uncertainty in the representation of high clouds could be reduced further through an increase in the quantity and quality of coincident measurement data from a variety of different sources - such as by the inclusion of CloudSat and CALIPSO A-train data. In general, the data indicates that future improvements in the quality of high cloud measurements are generally needed to help refine our estimates for input into global weather and climate models.

4.4 Discussion / Conclusions

4.4.1 MODIS High Cloud Detection

Consistency in the definition of CTP is essential to make valid comparisons with MLS. The study in this Chapter compares high clouds over the same regions by averaging co-located data. This allows us to conduct a statistical analysis of high cloud fractions. CTPs were estimated from MLS and CERES using different methods and so introduce considerable sampling bias, as confirmed by our results both in this chapter and Chapter 3. Co-location reduces the sampling errors, by examining the same locations at a similar time, but cannot account for differences in instrument geometry. Viewing geometry strongly influences the detection of non-uniform and smaller scale high clouds, as surface and low level clouds are viewed by nadir instruments that are not detected by MLS. It is foreseeable that without careful spatial co-location of MODIS data, the sampled region of atmosphere may be strikingly different to that observed across the narrow FoV of MLS. There are also errors associated with MODIS cloud-top retrievals algorithm,

since unlike estimates using CERES OLR data they do not depend upon the vertical structure and composition of cloud.

This study indicates that whilst MODIS views more mid-latitude ice clouds than MLS, it reports smaller high cloud fractions in the low latitudes. As a result MODIS reports significantly less high clouds during the year of 2006, a result that is consistent with CERES and is most pronounced during the autumn when the Asian monsoon is dissipating. During this period the tropopause relative humidity in this region is at its peak, so thin cirrus is more likely to form. Differences between the reported MLS and MODIS high cloud fraction may be attributed to the higher sensitivity of MLS to thin high clouds that frequently surround tropical convection. The fraction of high cloud detected from MLS was found to be 44 % greater than MODIS. The inability of MODIS to detect the uppermost high clouds may in part be a consequence of invalid measurements of cloud-tops in the vicinity of a temperature inversion that characterises the dynamical tropopause. This is a result from the design of the MODIS CTP algorithm that bases its calculations on radiances viewed at infrared and shortwave window bands that are highly sensitive to the cloud-top brightness temperature.

4.4.2 CERES High Cloud Detection

The method for calculating CTPs from CERES assumes that the MLS temperature profile, from which CERES brightness temperatures are referenced to, are accurate and the dataset does not exhibit any systematic bias for cloudy scenes. The CERES detection methodology demonstrates a significant covariance with MODIS data, although the high uncertainties associated with generation of CERES CTPs make its data a poor choice for synergistic combination. The results from Figure 22 show that there is considerable discordance between cloud-top data, with CERES detections much lower than MLS and reporting a range of values that are mostly outside the A-train mean of high cloud fractions. In agreement with MLS CTP data, September data from CERES exhibits the highest fraction of all observed high clouds at 6.8 ± 1.2 %, in agreement with the seasonal high cloud cycle observed by MODIS and MLS.

There are many assumptions to the CERES algorithm presented in this study. The black-body approximation used to calculate brightness temperatures can only be valid for deep convective clouds, since small perturbations to the upwards flux of thermal radiation from low altitude emission causes large errors in the

estimate of a suitable CTP. This warm bias is presented in the results of Chapter 3 Figure 15. It is worth noting that CTPs are subjective and are perhaps not the best way to demonstrate consistency between different A-train cloud data. Further work needs to be undertaken to establish the link between MLS IWC detections and CERES OLR.

4.4.3 MLS High Cloud Detection

The regional MLS high cloud patterns are in general keeping with remotely sensed observations derived from the Aqua instruments; MODIS and CERES, as demonstrated by synergistic comparisons. MLS also captures the main features and distribution of high cloud successfully with few large-scale regions of high cloud that are undetected by either the CERES and MODIS algorithms.

There is a general agreement between large-scale regions of high cloud detected by MLS, MODIS and CERES are consistent during all four seasonal periods during 2006. The results indicate that the grid-cell locations with the maximum high cloud prevalence are close to the equator and commonly occur at longitudes around 90°E, 30°W and 60°W, irrespective of season or instrument. These regions of the globe are associated with quasi-permanent clusters of deep cumulonimbus type convection. In the extra-tropics, ice clouds are often detected less successfully.

4.4.4 Overview

High cloud mapping in this chapter shows that MLS high cloud distribution shows a general consistency with other cloud-top measurements, with the benefit of its highly vertically resolved measurements of ice water content. Its significantly higher fractional coverage of reported high clouds tends to indicate that the limb-viewing instrument is more sensitive to high altitude tropical cirrus than either the MODIS and CERES nadir sensors. As the MODIS CTP and CERES OLR measurements are sensitive to surface temperature they cannot easily detect clouds in the vicinity of the cold-point tropopause that is characterised by an inversion layer. Microwave limb-sounding instruments therefore offer a much better sensitivity to the upper troposphere than infra-red nadir-sounders. Since climate predictions depend upon valid representation of high thin cirrus for calculations of the top-of-atmosphere radiation budget - emission from the cloud in

the cold-point tropopause can result in significant reductions in the flow of outgoing longwave radiation leaving the Earth's climate system. The seasonal nature of the high cloud consistency provides tantalising evidence to support the case for enhanced MLS detection of thin anvil outflow clouds that emanate from deep tropical convection, which are more prevalent during the autumn period due to higher relative humidities in the tropopause region following an influx of moisture from the Asian monsoon in the preceding summer.

The study in this chapter attempts to minimise differences in viewing geometry between nadir and limb-viewing instruments by undertaking cloud comparisons of equivalent sampling area. This is achieved by averaging of CERES and MODIS data over the larger horizontal footprints of MLS. In addition, the nature of the A-train ensures that the same high clouds are observed at approximately the same time. Despite this co-location process, previous investigations in Chapter 3 indicate that scattered cloud within a limb footprint can allow instruments to view lower clouds when observed from above, which may introduce a high pressure bias in the horizontally averaged nadir-sensed data. A caveat is therefore introduced to ensure that only high clouds are monitored ($p < 261\,\mathrm{hPa}$). Indications from the seasonal variability in the consistency of the comparisons indicates that a dynamical feature, such as large-scale circulation or convection, affects the consistency of high cloud data during the autumn sampling period (1st to 16th September, 2006). This feature is likely to result from low-latitude vertical wind shear that leads to a higher prevalence of thinner cirrus following the Asian monsoon season.

Further validation of the ice water content product with operational data, such as from the European Center for Medium-range Weather Forecasts (ECMWF), would be needed to confirm whether MLS views additional thin cirrus that is not currently reported for numerical weather prediction models. The study also highlights the need for improved horizontal resolutions of limb-sounding data. Comparisons with current limb-sounding measurements, such as with HIRDLS (Aura) multi-spectral radiance data, could be used to ensure that differences in viewing geometry cannot be attributed to differences in high cloud fraction. Future validations between MLS IWC and the HIRDLS Ice Water Path data product described by Gille et al. (2011), could confirm whether MLS is able to detect thin cirrus. This validation may explain the apparent autumn bias in MLS high cloud fraction over the Asian Monsoon compared to nadir detections.

HIRDLS data could also provide a positive alternative to the use of CERES OLR data, whose uncertainties are enhanced due to its broadband radiometers.

Since MLS detections are proves proficient in monitoring high clouds in the extended low latitudes (equatorward of 35°) the IWC product is useful for specifically estimating the coverage of tropical convective clouds and their anvil outflow cirrus in these regions. Future high cloud mapping would benefit from a multi-level and synergistic approach to make best use of a wealth of cloud-top and interior data. These improved climatologies of high clouds could provide a modernised update to those currently reported by Rossow & Schiffer (1999).

Later in this thesis, studies will calculate the outgoing longwave radiation emerging from tropical high cloud scenes using a radiative transfer model, with a suitable input from the ECMWF, MLS atmospheric gas retrievals and cloud measurements. This will identify areas of improvement for future satellite detections in the presence of low latitude high clouds. Some detailed case studies of these high clouds will also aid the identification of several interesting characteristics of high clouds and their representation in climate models.

5 Longwave Radiative Transfer through Low Latitude Anvil Clouds

5.1 Introduction

One of the main uncertainties in our prediction of future climate arises from differences in the model representation of ice particles within low latitude convective clouds. A wealth of data is now available from Earth Observation System satellite instruments that provide more detailed and accurate information on high clouds. The observations can provide more adequate representations of the microphysical ice particle properties and large-scale physical processes involved in the formation and maintenance of high clouds. Detailed Earth Observations of high clouds are therefore essential to enable accurate simulations of cloud feedback responses in General Circulation Models (GCMs) (Lohmann & Roeckner 1995, Solomon et al. 2007). Furthermore, a deeper understanding of low latitude high cloud processes such as; their influence on stratospheric dynamics, interactions with aerosols and their role in the hydrological cycle, has large societal benefits (Seidel et al. 2008).

In this chapter, comparisons are made between the observed and estimated outgoing longwave radiation (OLR) using coincident data. The study focuses on the longwave (LW) energy transfer through tropical ice cloud scenes that are difficult to monitor due to their short life-cycle. This study is unique, as it undertakes valid comparisons of cloud properties in conjunction with radiation budget measurements by using coincident A-train observations. The analysis of this co-located data allows the wider climate science community to refine model estimates of LW energy transfer. Earlier studies in Chapter 4 indicate that tropical ice clouds are well detected by Aura Microwave Limb Sounder instrument. This study initially shows, using coincident Clouds and the Earth's Radiant Energy System (CERES) Single Scanner Footprint (SSF) data, that these high clouds exert a strong longwave radiative forcing on climate. Representations of tropical clouds in climate models can be improved by better descriptions of regional circulation patterns and the dynamical, chemical and radiative coupling between the stratosphere and troposphere (Holton 1995).

A study by Stevenson et al. (2006) highlights the importance of correctly representing stratosphere-troposphere exchange (STE) that occurs most frequently at the tropics, since an influx of ozone into the troposphere exerts a relatively

long-lived positive forcing on our climate (Solomon et al. 2007). Reductions in the stratospheric ozone concentration also have adverse impacts on health, allowing dangerous levels of ultra-violet electromagnetic radiation to reach the surface (Randel et al. 2006). Much of the measured stratospheric ozone is produced at low latitudes where intense solar radiation causes photolysis of oxygen molecules. Ozone is then transported poleward by the Brewer-Dobson circulation (Goddard Space Flight Center Retrieved Jan 2012). Future change in tropical dynamics can therefore alter the global distribution of stratospheric ozone, since increases in humidity can lower its concentration.

Tropical Mesoscale Convective Systems (MCSs) are a major element of the global circulation system, since they account for much of the precipitation and latent heating within the low latitudes (Cetrone & Houze 2009). MCSs are cloud systems that consist of a collection of supercell "thunderstorms", which produce a region of precipitation exceeding 100 km in horizontal scale, with lifetimes of several hours or more. The character of these systems makes them ideal for detailed analysis using A-train satellite data. Within the MCS cores, deep and moist convection of plumes containing water and ice hydro-meteors frequently overshoot the tropopause cold-point with a vertical circulation that is partially driven by convective overturning (Cetrone & Houze 2009). It is both valuable to understand the effect of MCSs on the tropical hydrological cycle and to improve our representations of STE processes Seidel et al. (2008).

Past studies reveal a high frequency of thin clouds detected by the Cloud Profiling Radar (CPR) of the Aura CloudSat instrument that are attributed to anvil outflow clouds (Cetrone & Houze 2009). These ice outflows extend outward at altitudes between 14 and 20 km and extend several hundred kilometres outward. Outflow cloud form when ice cloud at the top of the convective anvil is swept horizontally due to strong vertical wind shear in the proximity of the tropopause. In this chapter several features of tropical clouds are explored. These include the spatial variability in atmospheric greenhouse gases, cloud composition; and physical processes such as atmospheric motion, temperature and longwave energy transfer. All these components together characterise the atmospheric dynamics and conditions that are present in different tropical and sub-tropical atmospheres where high clouds form most frequently.

The features annotated (1) and (2) in Figure 23 indicate the main high clouds that will be identified in this study, which are both are associated with deep

tropical convection. This study focusses on the identification of anvil cirrus (f) where warm convection "d" prevails. In contrast, isolated cirrus (e) is often thinner and therefore more difficult to measure and locate, generally formed at a distance from convection by an unknown mechanism (Jensen et al. 2001, Lee et al. 2009). Feature (1) describes the bulk properties of ice clouds that form directly at the top of deep tropical convection, whilst (2) indicates the adjacent outflow cirrus swept outward laterally from its top that is generally much thicker than in-situ cirrus e.g. Lee et al. (2009). High clouds are found either side of a boundary point "f", with the postulation that their bulk properties are distinguishable from each other.

Previous studies of tropical atmospheres indicate that deep convection, and the strong LW radiative cooling associated with these scene types, may be partially counteracted by neighbouring subsidence (Sun & Lindzen 1993). Strong subsidence is found where the water vapour (WV) concentration is much lower than its surroundings, allowing more thermal energy to escape to space by lowering the local greenhouse effect. Other studies show that the vertical and horizontal variability of WV and thin cirrus in the vicinity of the tropical tropopause layer (TTL) both play a significant role in the LW radiation budget (Trenberth 1998). There is a general consensus that variability in these upper tropospheric (UT) components exhibit a much greater impact on the longwave transmission to space than low cloud and moisture (Jensen et al. 1996, Boehm et al. 1999, Hartmann, Holton, Fu et al. 2001). In addition, thin cirrus can result in a weak LW radiative cooling if it overlies a convective anvil e.g. point "e" on Figure 23. In contrast, thin cirrus in the absence of an anvil may result in a modest warming (Jensen et al. 1996, Boehm et al. 1999, McFarquhar et al. 2000).

In this chapter, the goal is to identify structural features of high clouds in the vicinity of the tropopause and relate these to physical and chemical features. Several pieces of data are analysed to provide a more complete picture of the low latitude atmosphere that include: ice water content (IWC), potential temperature, WV and ozone from version 2.2x MLS data; liquid water content (LWC), vertical motion from assimilated European Center for Medium-range Weather Forecasts (ECMWF) ERA-Interim data; and OLR and longwave radiative heating rates (LW HRs) simulated from the Atmospheric and Environmental Research (AER) Rapid Radiative Transfer Model (RRTM) code Version 3. Data from the MLS instrument is used to perform accurate RT calculations for selected high

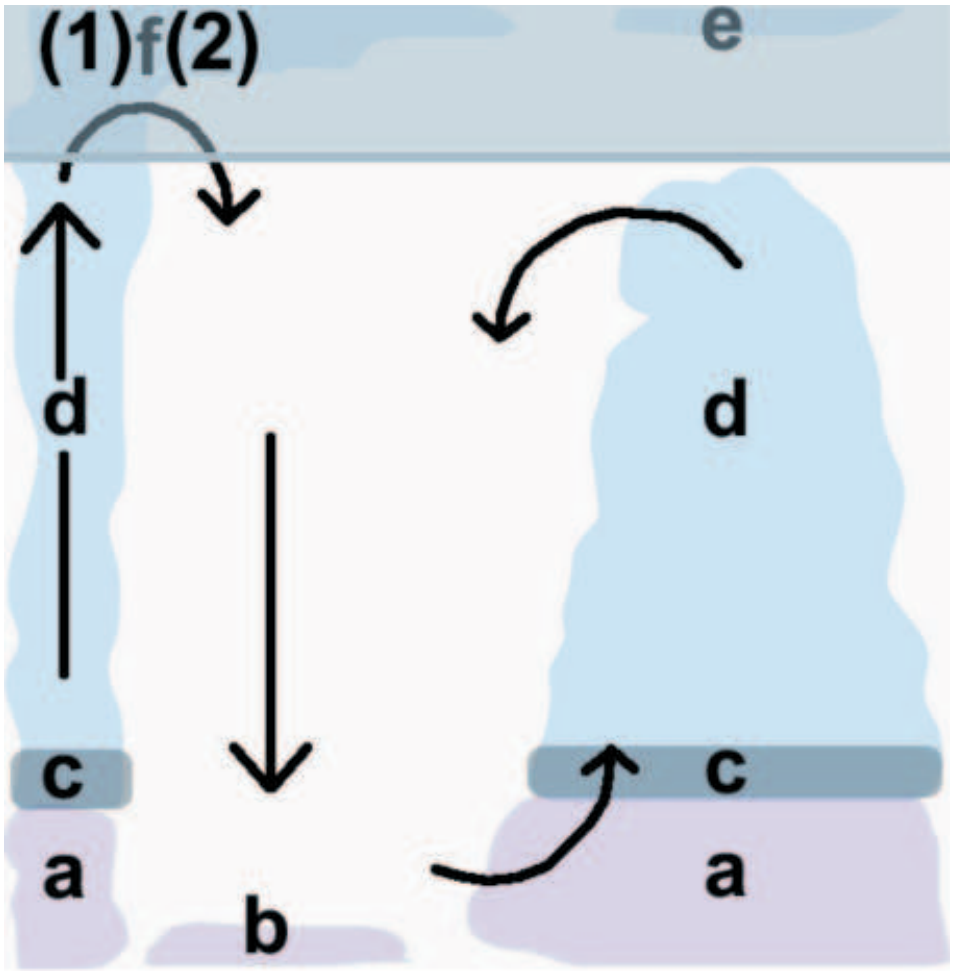

Figure 23: Vertical cross-section of model convective atmosphere, showing structural formations of convective scenes in coloured shading and their associated dynamical features as marked by black arrows. On the left, ice clouds are shown "d" that reach the tropical tropopause by free convection and are then swept out laterally as anvil outflows across a midway point "f" over a region of subsidence. This formation represents a region of mature or intense convective with cloud that extends from the top of the boundary layer into the tropical tropopause layer (shaded in grey) by over-shooting. The neighbouring subsidence is associated with shallow low level warm clouds "b" that are either located below or just above the boundary layer. Icy interior of high clouds are indicated by the pale blue colours, which are located within the mid to upper troposphere "d". Liquid (warm) clouds associated with convective clouds droplets are shaded in pale red / pink "a", whilst mixed-phased clouds are indicated by deep blue "c". A second scene-type is identified, on the right, where thin cirrus form in-situ as isolated thin cirrus "e" outside of deep convection or within a region of weaker or developing convection without an anvil. This case is shown on the right of the schematic. Two neighbouring and distinct high cloud scenes are marked (1) and (2), which are the focus of our studies.

cloud profiles in the tropics.

Two case study profiles are were selected that pass equatorial high clouds, which are discussed further in Section 5.2.1. The advantage of the MLS instrument over other space-borne instruments is its limb scanning geometry. This allows the instrument to provide precise data on several greenhouse gases, temperature and IWC, with a high sensitivity above the mid-troposphere, and a higher penetration depth through clouds layers than many instruments with a nadir-viewing geometry. It is first demonstrated how by the use of co-location, valid comparisons of the measured and simulated OLR can be made for the same high clouds. To achieve this, CERES data is examined at the same time and location as LW energy transfer calculations that are performed using MLS data inputs.

The OLR and radiative cooling rates are examined across a broad range of tropical and subtropical latitudes using MLS, CERES and ECMWF data for the suitable choice of case studies in Section 5.2. A method is also detailed for the selection and running of a RT model for the simulation of LW energy flow. The following analysis then examines the general features of low latitude circulation processes, and chemical and physical anomalies that are associated with high clouds. The distribution of ozone in the presence of deep convection is also explored, to investigate the role of local dynamics on STE. The results and associated errors are discussed in Section 5.3. Discussions and general conclusions from the case study analyses are then presented in Section 5.4.

5.2 Methodology

5.2.1 Local Studies of High Clouds and the Radiation Budget

In this study two curtain plots are examined to assess the ability of the cloudy-sky RT model to detect the general characteristics of cumulonimbus type clouds over the extended low latitudes. The validity of these comparisons is aided by the use of co-located Outgoing Longwave Radiation (OLR) measurement data from the CERES (Aqua) SSF data product. CERES data was co-located for each MLS measurement point using the method described in Section 3.2.1. In addition, the characteristics of the atmosphere are explored in the presence of ice particles that contribute to LW radiative cooling, vertical motions and potential temperature anomalies both in the stratosphere and troposphere. To investigate STE

mechanisms, ozone is mapped over the same region and is used as atmospheric tracer. For the same case studies, WV is used to locate the likely locations of thin anvil outflows, where the reported absolute humidities are often higher than the surrounding atmosphere. Each case study examines high clouds that are viewed along satellite tracks of equal length, with measurements that are centred about the equator on 19th September, 2004.

The two case studies differ considerably in the extent of deep convection covering the low latitudes from 25°S to 25°N. Previous studies in Chapter 4 indicate that MLS identifies high clouds of the Inter-Tropical Convergence Zone (ITCZ) that are consistent with both the Moderate-resolution Imaging Spectroradiometer (MODIS) and CERES (Aqua) instruments during 2004. This study focusses upon the character of these tropical clouds to aid our understanding of the feedback processes that control the El Niño Southern Oscillation (ENSO) and monsoon rains described in Section 1.5.2. For each study, the properties of the air mass surrounding the high clouds are examined in an attempt to discern the physical and chemical properties that are characteristic of convective ice clouds. This study also explores the possibility of developing methods to discriminate thin high altitude cirrus from convective ice clouds, and to estimate the LW cloud radiative forcing (CRF) of each.

5.2.2 Running the Radiative Transfer Model

Atmospheric and Environmental Research RRTM_LW Model A full description of the AER code attributes and its function in our cloudy-sky radiative transfer calculations are discussed in Section 1.6. MLS (Aura) data is used as the main source of input in this study, since it is reported at the same locations as ice clouds. The version 2 MLS data products used for our calculations include: temperature, ice water content (above the mid-troposphere), water vapour, ozone, nitrous oxide and carbon monoxide. Carbon dioxide input is assumed to be well-mixed throughout the entire troposphere, with a volume mixing ratio of 370 ppmv that is representative of the September 2004 study period. Since no warm cloud data is reported by the MLS, suitable inputs are provided for $p > 261$ hPa using ECMWF data, as justified in Section 2.4. The ECMWF Re-Analysis (ERA) interim product provides liquid water mixing ratios ($\mathrm{kg\,kg^{-1}}$) that must first be converted to liquid water content (LWC) values using the method described in Section 5.2.4. LWC must also be co-located to each MLS measurement footprint,

a process that is discussed further in Section 5.2.3. The AER RRTM input for surface emissivity is represented by a uniform value of 0.98, as also adopted by Borbas & Ruston (2011). Further studies would be needed to represent the local emissivity over the land and ocean surfaces.

A factor of 0.27 was applied to the IWC data, which was found to effectively reduce the mean bias between the RT model outputs and co-located measurement data from CERES. The exact cause of the bias is unclear and there may be a combination of factors at play such as; the parameterisation schemes e.g. Acker et al. (1996), Iacono et al. (2000), optical coefficients adopted by the CCM3 in the RRTM, a general cold bias in the MLS temperature data in the presence of thick cloud, or a high altitude bias in MLS data that is consistent with our cloud-top pressure comparisons in Chapter 3. An iterative scheme was devised to systematically select different IWC factors to minimise the mean difference between the estimated OLR produced by the radiative transfer model and direct measurements undertaken at the same locations. The iterative scheme was performed for 100 MLS sensor positions in the extended low latitudes i.e. for profiles equatorward of 35°. The effect of ice water content measurement uncertainty on the RT inputs was also factored accordingly at each reported level, although ice water content data presented in Figure 27 present values directly from the version 2 IWC product.

The AER model required inputs of heights $z[k]$ that divide each model layer, although measurements from MLS and ECMWF are reported on pressure levels. To resolve this input issue, coincident data from the Version 2 MLS temperature product was used to calculate the density of each layer m using the expression $(\rho[\bar{m}] = (\rho[k] + \rho[k+1])/2)$. Heights of each model level are then computed from the surface upward, using the hydrostatic approximation given in Equation 15 to iterate from level k to $k+1$ with the initial condition of $k = 0$ at the surface. Equation 15 demonstrates how the rate of pressure decreases with respect to increasing altitude ($\frac{\delta p}{\delta z} < 0$).

$$\frac{\delta p}{\delta z} = \frac{p[0]}{h} \times \exp(-\frac{z[k]}{h}) = -\rho_{\mathrm{d}}[k]\, g \tag{15}$$

Longwave Radiative Heating Rates The local longwave radiative heating rate (LW HR) can be visualised by first considering a stack of 14 cuboid volumes that each represent a model of MLS inputs on 12 levels per decade. The surface

layer extends from 1000 hPa to 825 hPa, with along-track and across-track lengths in accordance with the MLS field-of-view at 240 GHz. The RRTM_LW computes the transmittance (χ_{LW}) to the top of the highest model level, which is located at $p = 56\,\mathrm{hPa}$ ($z \sim 20\,\mathrm{km}$). Together these cuboids comprise that atmospheric profile, with the approximation that each 3-d volume of atmosphere can be treated as horizontally averaged 2-d profile for treatment in RT calculations i.e. with only an upward and downward varying profile. Each cuboid has sides of $[x,\, y,\, z]$, which possess lengths of $[7\,\mathrm{km} \times 300\,\mathrm{km} \times 4\,\mathrm{km}]$ that correspond to the across-track, along-track and vertical levels of the version 2 cloud ice water content product provided by the NASA JPL Science team (Wu et al. 2008). Each cuboid of air has a nominal temperature (T) and pressure (p) and density ρ_{d} averaged between the layers boundaries, contains the five main absorbing gases (CO_2, H_2O, O_3, N_2O, CO) and may also contain cloud particles. LW HRs (H_{LW}) were calculated by the AER RRTM code and output on the same set of model layers (m) as the RT model inputs.

The interpretation of radiative heating rates is described in Section 1.4.3. The magnitude of the LW HR is partially governed by the ambient air temperature at the mid-point of each atmosphere layer m that lies between the levels k and $k+1$ where $z[m] = \frac{(z[k]+z[k+1])}{2}$. LW HRs also depends upon the LW transmittance averaged over the upward hemisphere χ_{LW}, which considers all slanting paths. The vertical gradient in transmittance is referred to as the atmospheric weighting function. When the weighting function ($\frac{\delta\,\chi_{\mathrm{LW}}(z,\infty)}{\delta z}$) is at its maximum, the heating rate is more sensitive to small changes in temperature. In contrast, when the weighting function is low the temperature of a layer has a much smaller effect on the magnitude of the H_{LW}.

Outgoing Longwave Radiation The outgoing longwave radiation (OLR) was calculated by the AER RRTM_LW model for each co-located MLS profile, by reading the longwave radiation output for the upper-most model level ($p = 56\,\mathrm{hPa}$ or $\sim 20\,\mathrm{km}$). The following analysis assumes that this represents a suitable top-of-atmosphere value. The modelled OLR was then compared with data from the FM3 CERES (Aqua) product that reports OLR at the same locations. Measurement data from the CERES (Aqua) instrument in the rotating azimuth plane (RAP) mode was used to validate the modelled OLR, whose mode of operation is discussed in Section 2.3.2. RAP data was preferred, since its data presents a

higher density of surface measurements in the centre of the track than for the cross-track scanning mode, as indicated by Figure 9 in Chapter 2. Its measurements are therefore more spatially coincident with MLS, allowing more of its data to be co-located and therefore leading to more valid comparisons.

5.2.3 Co-location of Liquid Cloud Data from ECMWF

Additional information is required to obtain a more complete picture of the warm clouds located in the mid to lower troposphere (LT) and for radiative transfer simulations of the longwave energy budget. The choice of this data that is described in Section 2.4 and forms the input for the first 6 layers of the RRTM input i.e. $p > 261\,\text{hPa}$ ($z \sim 9.33\,\text{km}$). The ERA-interim product described in Dee et al. (2011) and reports both liquid water mixing ratios and vertical motions that are discussed later in this Chapter. ECMWF data was interpolated to the same set of pressure levels as our MLS inputs, spanning the surface to 261 hPa. The vertical model levels in the RRTM model need not be regularly spaced throughout the column, however they must remain consistent for each atmospheric input. A regular vertical grid ensures that ECMWF data can be effectively combined and inter-compared with MLS products at the same pressures.

To maximise the spatial coincidence between ECMWF and MLS data inputs the measurements were co-located. Observation times were compared to identify the 6 hour data segment of ECMWF data that covers the same sampling time as MLS. ECMWF re-analysis data is reported for numerical weather predictions and so a daily coverage of assimilated data comprises datasets at 6 hourly intervals (detailed further in Chapter 2). As a consequence, a t$<$ 3hrs temporal offset exists between MLS and ECMWF compared to t$<$ 0.15hrs between co-located Aura and Aqua data. As clouds often evolve on short time scales, horizontal variability in ECMWF data may not be directly associated with A-train data features, whilst it provides a good indication to larger scale atmospheric features without the need for further analysis of A-train data.

To combine data in the most valid manner, gridded ECMWF data was co-located over a 0.7° by 1.4° (1 by 2 grid-cells) in the longitudinal and latitudinal orientations respectively about each MLS sensor point. The process of co-location reduces the ECMWF data products to a $\sim 100\text{km}^2$ grid that is broadly consistent with the MLS instrument. As a consequence ECMWF data is used to analyse the larger scale features of circulation and warm clouds in the tropics, such as the

free convection and bands of subsidence associated with the tropical circulation. Vertical wind tendencies were also obtained from the same data product, to gain a clearer picture of the dynamics associated with tropical ice clouds. This data was co-located using the same method as for LWC.

5.2.4 Calculation of Liquid and Ice Water Paths

To perform accurate RT calculations for cloudy-sky profiles, the RRTM code required inputs of liquid and ice water paths (IWPs). The IWP is defined as the integral of the ice water content (IWC), through the depth of an ice cloud layer (Heymsfield et al. 2003). This was based on data from the version 2 IWC product described in Livesey et al. (2007). To convert the cloud inputs into the correct format it was necessary to determine the thickness of each model layer ($m = 0, ... 14$). Model layers are separated at 12 levels per decade, with the surface layer $m = 0$ located at $1000\,\mathrm{hPa} > p > 825\,\mathrm{hPa}$. The top model layer $m = 14$ is located at $68\,\mathrm{hPa} > p > 56\,\mathrm{hPa}$. The cloud water paths ($CWP[m]$) in $\mathrm{g\,m^{-2}}$ were then calculated using the inputs of CWC ($CWC[m]$) in $\mathrm{g\,m^{-3}}$ at each tropospheric model layer using Equation 16. The values produced by Equation 16 consist of LWC for warm clouds that is input between layers $m = 1, ... 5$, whilst model layers $m = 7, ... 14$ comprise of IWC within high clouds. The transition layer between upper-troposphere ice clouds and liquid clouds (layer $m = 6$) assumes a 50 % contribution from ECMWF ERA-Interim liquid water content and version 2 MLS IWC data.

$$CWP[m] = CWC[m] \times (z[k + 1] - z[k]) \tag{16}$$

The total column of the RT model uses inputs on 15 levels (k) from 1000 hPa to 56 hPa where $k = 1, ... 15$ represent the 12 per decade MLS levels. To calculate the thickness of each layer, it was necessary to determine the boundary altitudes of $z[k + 1]$ and $z[k]$. The thickness of each model level was calculated by the use of the hydrostatic equation, whilst the mean layer density ($\rho[m]$) was determined using the ideal gas equation using version 2 temperature data from MLS. Using an iterative scheme, the altitude at level k was calculated using Equation 17, with the boundary conditions of $z(0) = 0\,\mathrm{m}$ and $z[k] > z[k + 1]$.

$$z[k + 1] = \frac{p[k + 1] - p[k]}{-\rho[m]\, g} + z[k] \tag{17}$$

5.3 Case Studies of two A-train Satellite Passes

Two case studies are presented in this chapter to identify reinforcing similarities in the general character of high clouds and their associated atmospheric features in the extended low latitudes. The analysis follows on from studies in Chapter 4, which identifies more extensive high cloud coverage over the Asian monsoon during September and a distinct region over the equatorial Pacific that is marked by a discontinuous band of high clouds in a less defined and rather discontinuous region of the inter-tropical convergence zone. These case studies offer a more detailed insight into both these regions and will explore, by examining bias between the modelled and measured OLR, whether the MLS can successfully detect features of thin high clouds in addition to the anvil clouds of tropical convection.

Case studies were selected that show both a large dynamic range in OLR and at least one well-defined region of high clouds around the equator-line. The first case study, referred to as case study c1, reveals high clouds centred at 10°N of the equator over the east Pacific Ocean. The tropical Pacific is examined during the daylight hours at 23:15 to 23:35 UTC approaching from the south, whilst the Southeast Asian clouds (case study c2) are viewed at night-time from a descending half-orbit of the A-train at 19:05 to 19:20 UTC. During this period the CERES and MLS instruments both observe regions of tropical convection centred around 1000 km north of the Equator. The suppressed OLR in this region of high clouds is marked by the light blue to purple coloured measurement points that correspond to CERES (Aqua) FM3 OLR values below 200 $\mathrm{W\,m^{-2}}$ in Figure 24.

A second case study c2 examines a section of atmosphere where the humidity and high cloud coverage indicates a much broader Hadley cell, with widespread deep tropical clouds associated with the late monsoon season. The variability in OLR related to these high clouds is presented by Figure 25. Case study c2 was selected as it identifies an interesting feature of high clouds over the same low latitude band, which is more widespread in nature rather than isolated. Whilst both case studies highlight a general region of convection detected by both the MLS and CERES instruments, c2 presents a scene with a large range in the OLR of 100 to 280 $\mathrm{W\,m^{-2}}$. Travelling southward, the CERES instrument views a small region of high clouds at 31°N, with the main section of high clouds extending from 18°N to 8°S later in the Aqua satellite pass.

Both studies locate the high clouds of the ITCZ centred between 5 and 12°N of

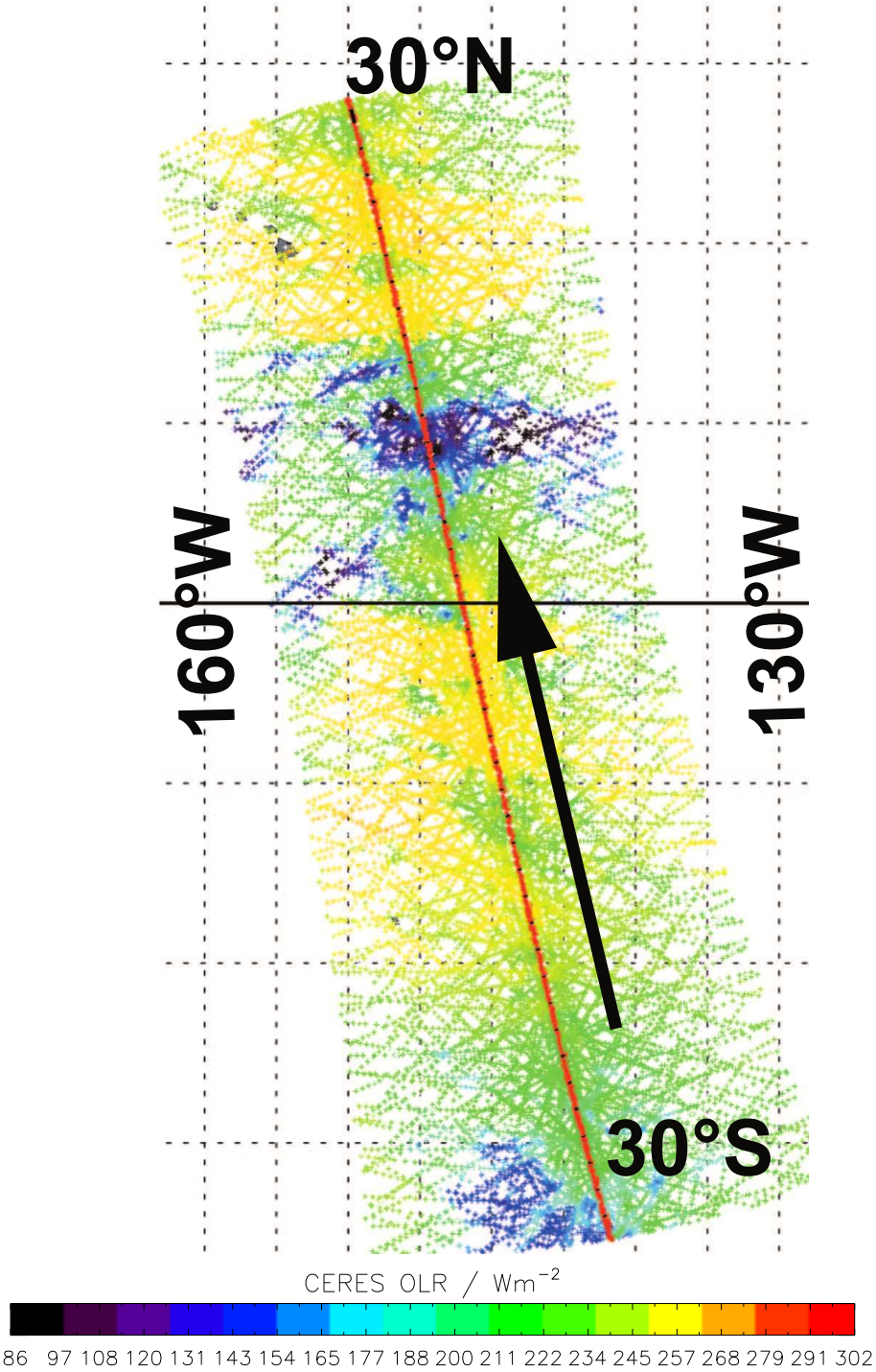

(c1)

Figure 24: Mapped CERES (Aqua) footprint from the FM3 instrument (Single-Scanner Footprint (SSF) product) operating in the rotating azimuth scanning mode. Figure shows an equatorial satellite pass on 19th September, 2004 from 23:15 UTC to 23:35 UTC during the daylight hours. A red line indicates the centre of the A-train surface track over the Pacific Ocean. The black dashed lines indicate the longitude and latitude grid-lines at $3.75°$ *and* $10°$ *intervals respectively, whilst the solid black line indicates the equator-line. A black arrow shows the direction of orbital motion.*

(c2)

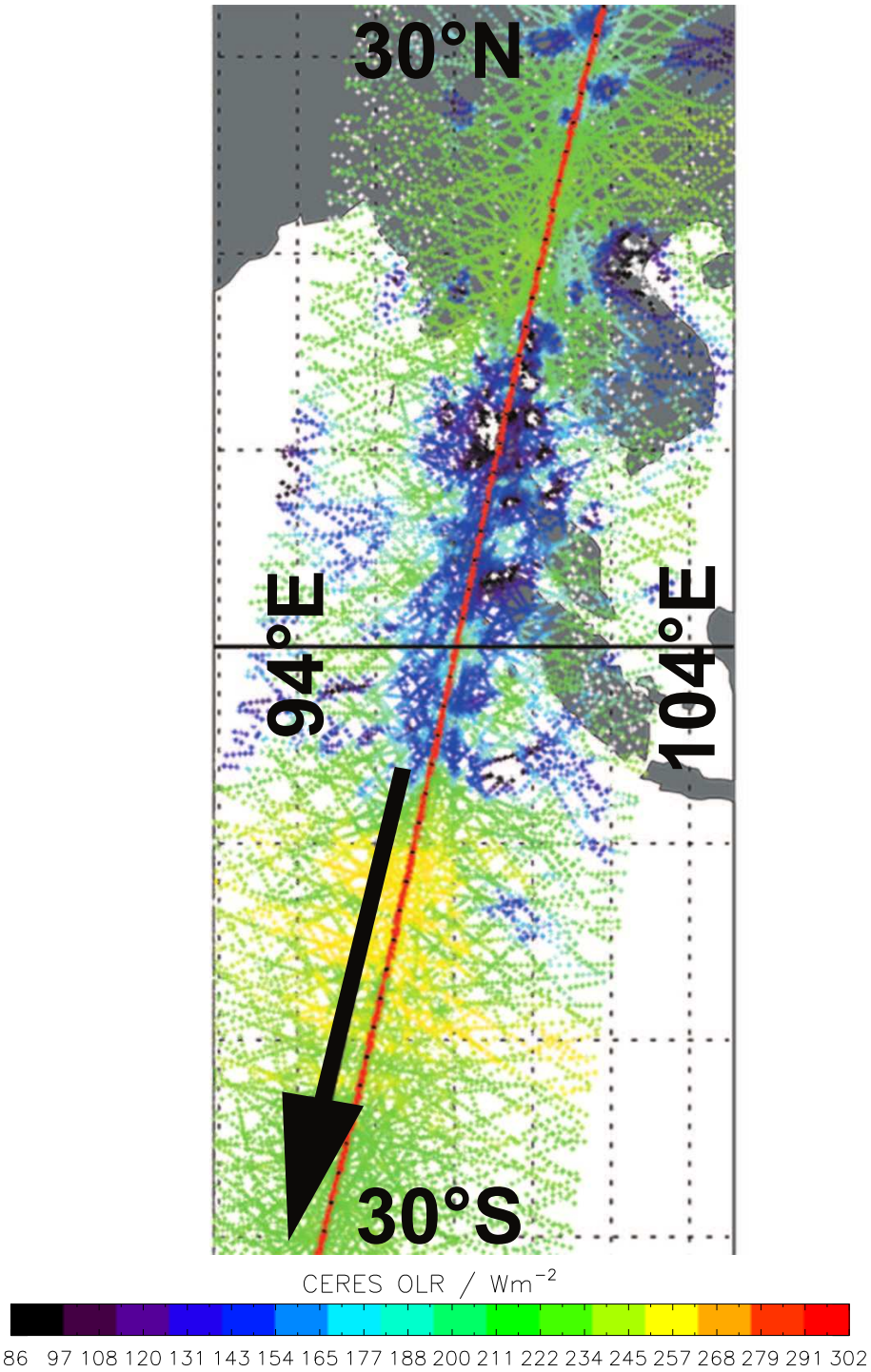

Figure 25: Mapped CERES (Aqua) footprint from the FM3 instrument (SSF product) operating in the rotating azimuth mode for an equatorial satellite pass on 19th September, 2004 from 19:05 UTC to 19:25 UTC during the night-time hours over the Indian Ocean and Southeast Asia. The red line indicates the centre of the A-train surface track where MLS and CERES measurements are compared. The black dashed lines indicate the longitude and latitude grid-lines at 2° and 10° intervals respectively, whilst the solid black line indicates the equator-line. The black arrow shows the direction of orbital motion.

the equator, marked by a pronounced band of convective clouds associated with a local minimum in the measured and simulated OLR. Three more deep plumes are visible on Figure 27 of case study c2 than c1 over the same along-track distance, indicating more active free convective that takes place west of the dateline that is consistent with our knowledge of the Walker Circulation pattern described in Section 1.5.2.

Points marked "e" and "f" on the measurement data and LW HRs of Figures 27 to 31 identify the same features as in Figure 23 to help characterise the physical and chemical conditions for each. There are two additional points of interest marked. The letter "g" is a direct indicator of where minimum longwave radiative cooling rates are found within the dense cloud, based on the AER RRTM_LW output analysed in Section 5.3.4. Points marked (h) indicate the plausible locations of stratosphere-troposphere intrusions that are diagnosed from v2 MLS water vapour measurements are discussed further in Section 5.3.6. The slanted lines on Figures 26 to 31 marked at MLS profile positions $3410 - 3413$ (case study 1) and $2797 - 2800$ (case study 2) indicate the postulated locations of upper troposphere - lower stratosphere (UT-LS) exchange, appearing adjacent to overshooting moist convection. These features are identified by relatively dry atmosphere that is identified by MLS water vapour profiles and are discussed further in Section 5.3.6.

5.3.1 Comparisons of OLR Measurements and Simulations

Figure 26 (c1 and c2) presents co-located comparisons of the high clouds and along-track OLR variability associated with the ITCZ. On the left-hand ordinate of Figure 26 a reverse scale is used for OLR, as lower values result from deeper tropical convection that extends to higher altitudes. Where the red and grey coloured bands overlap, the modelled and measured OLR demonstrate a general consistency within those co-located footprints of MLS.

Measurements of cloud ice are plotted along-side longwave radiation budget measurements from CERES. The analysis in Figure 26 (c1) shows a region of depressed OLR in both the CERES measurements and RT simulated data that extend the MLS profile positions $i = 3410$ to 3418. Case study c2 shows several peaks and troughs in the along-track OLR that is associated with clouds, with a noticeable region of discrepancy in the modelled OLR (F^+) at $i = 2813, ... 2822$ in the presence of middle level clouds that are characterised by observed (obs) values

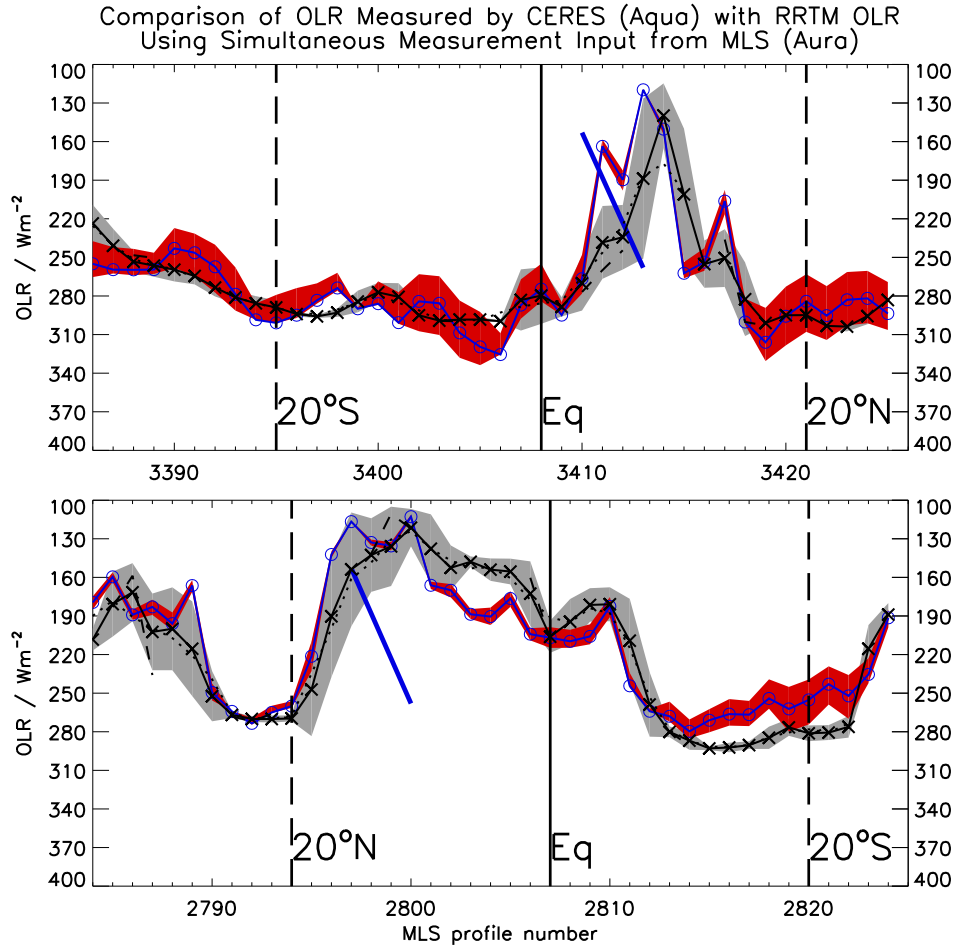

(c1)

(c2)

Figure 26: Figure shows the outgoing longwave radiation (OLR) measured and modelled during two A-train satellite passes. For case study c1 the A-train satellites travel northward for the ascending half orbit, whilst (c2) shows a southward scan during the night-time. OLR is calculated using AER RRTM_LW (version 3) that is fed by MLS (Aura) data and ECMWF liquid water composition data and is shown by the open blue circles. The red shaded overlay corresponds to the RT calculation error from uncertainty in v2 MLS IWC. CERES (Aqua) SSF measurements of OLR are indicated by the black crosses, with a grey shaded underlay area in accordance with the standard deviation in OLR within each co-located MLS point. The black long-dashed and dotted lines indicate the respective values when CERES OLR is averaged at along-track distances of 50 *and* 500 *km about each MLS tangent point. A solid black vertical line indicates the position of the equator.*

of $F^{+}_{\mathrm{obs}} = 300$ to $280\,\mathrm{W\,m^{-2}}$. Despite the lower prevalence of high clouds that extend through case study c1, the root-mean-square of the model-measurement error is comparable with c2 at $\sim 25\,\mathrm{W\,m^{-2}}$.

The analysis of OLR over the mapped region shown by Figure 26 (c1 and c2) reveal that co-located CERES OLR measurement data show a depression

associated with tropical high clouds just north of the equator that is consistent with the broader along-track view presented in Figures 24 and 25. In these regions OLR is typically $\sim 100\,\mathrm{W\,m^{-2}}$ lower in our case studies than measured at 5 degrees to the north or south in the surrounding atmosphere. The lower OLR in these regions is largely attributed to the positioning of the Inter-tropical Convergence Zone (ITCZ), described in Section 1.5.2. Figure 26 shows a vertical cross-section of modelled and measured OLR across the centre of the same sections of atmosphere and reveals a similar picture. In case study c1 modelled (mod) outputs of OLR reach a minimum at profile position 3413 ($F^{+}_{\mathrm{mod}}[3413] = 115 \pm 5\,\mathrm{W\,m^{-2}}$), with CERES reporting a nearby minimum at the adjacent MLS profile of $F^{+}_{\mathrm{obs}}[3414] = 150 \pm 30\,\mathrm{W\,m^{-2}}$ at the adjacent northerly profile. In general agreement, case study c2 presents modelled and observed values of OLR that reach a minimum at MLS profile 2800. In contrast, data from Figure 26 (c2) indicates a sharper along-track gradient in OLR on the northerly edge of the curtain plot, which is likely to be due to a clear patch in the low to middle level clouds around profile $i = 2792$. The results are in agreement with studies by Fueglistaler et al. (2009) that identify a distinct transition in the height of the tropical tropopause between its low over regions of subtropical subsidence in the northern hemisphere (NH) to its high at the tropics.

Figure 26 (c1 and c2) also explores the possibility of two different co-locations to produce a minimum and maximum possible coincident set of CERES OLR measurement data. One is spatially averaged within MLS sensor footprint with an along-track length (y) of $\pm 50\,\mathrm{km}$, whilst another assume at $y = 500\,\mathrm{km}$. The two outcomes presented are shown by the black long-dashed and dotted lines indicate how uncertainties in the MLS footprint size impacts upon comparisons between CERES and MLS data. The data reveals maximum uncertainties of $\sim 15\,\mathrm{W\,m^{-2}}$ equatorward of 20°N. Outside of the tropical plume far smaller co-location uncertainties are present, particularly where CERES and MLS are shown to be consistent. For these profiles, indicated by overlapping shades grey and red on Figure 26, co-location errors are less than $\pm 5\,\mathrm{W\,m^{-2}}$. This study focuses on a high cloud pass covering the extended low latitudes, so the RT model input errors (red shade) is not representative of the average global atmosphere.

In case study c2, the magnitude of the co-location errors are largest at point $i = 2790$, using the spatially averaged CERES OLR measurements of $y = 50\,\mathrm{km}$ and $500\,\mathrm{km}$. The OLR data shows that this cloud "window" is rather isolated

with $F^{+}_{\rm obs}(y\,=\,50\,{\rm km}) - LW_{\rm obs}(y\,=\,500\,{\rm km}) = 20\,{\rm W\,m^{-2}}$. The low variance in $F^{+}_{\rm obs}$ in this region indicates a gradual transition between two contrasting scene types with strikingly different longwave emission. It is more likely that any convective outflow clouds would be detectable at $i = 2794, ...2796$, as the gradient in OLR with respect to the A-train satellite orbit is most sharp. The data in Figure 26 (c2 and c1) both suggest a large model - measurement offset of $F^{+}_{\rm mod} - F^{+}_{\rm obs} \sim 50\,{\rm W\,m^{-2}}$ at MLS profile positions at the edge of tropical convection. The data therefore indicates that significant bias and random errors may arise from longwave radiation budget calculations in the vicinity of the tropical plumes and their convective outflows.

There are also small uncertainties in the RRTM_LW simulation of OLR relative to line-by-line RT calculations of $0.30\,{\rm W\,m^{-2}}$ averaged over all atmospheric scenes (Iacono et al. 2000). The results from our study, based on the earlier analysis of data from Figure 26 (c1), indicate that these errors are likely to be overwhelmed by uncertainties in the quality of MLS input and the uncertainties involved in co-location of CERES OLR measurements. Later in this Chapter our data shows that much of the variability in OLR can be attributed to upper tropospheric water and high clouds, so RT calculations depend critically upon their accurate input.

The red shaded region of RT modelled OLR in Figure 26 shows the v2 MLS IWC uncertainties reported by Wu et al. (2006). Three sets of LW RT calculations were performed; one for the lower ($IWC[i] + 1\,\sigma$), mean ($IWC[i]$) and upper ($IWC[i] + \sigma$) thresholds values, where $IWC[i]$ represents the reported MLS IWC at point i. The resulting uncertainty in the OLR output (ϵ) is then given by $\epsilon\,F^{+}[i] = F^{+}_{\rm max}[i] - F^{+}_{\rm min}[i]$, where the subscripts represent the maximum and minimum likely values of OLR. The resulting red vertical range on Figure 26 indicates that uncertainties are smaller ($\epsilon\,F^{+}_{\rm mod} < 10\,{\rm W\,m^{-2}}$) where the OLR is lowest i.e. from 5 to 15°N where tropical clouds are present. In contrast, uncertainties up to $35\,{\rm W\,m^{-2}}$ are present for optically thin high cloud scenes. The results indicate that RT model is highly sensitive to thin high altitude ice clouds, whilst are most valid for studies of tropical plumes than for their adjacent outflows. The converse is true when examining errors from the co-location of CERES measurement data, with a maximum uncertainty of $\epsilon\,F^{+}_{\rm obs} > 65\,{\rm W\,m^{-2}}$ over the same regions, indicating a large horizontal variability in OLR. These errors overwhelm instrument errors that result from calibration and measurement noise of

the CERES radiometers, which report small RMSE in the order of $3\,\mathrm{W\,m^{-2}}$ over the tropical oceans (Currey & Green 1998).

For this case study our RT analysis is able to simulate the magnitude of OLR within the bounds of 85 % (36/41) profiles using data input on liquid and ice clouds, the main absorbing gases and atmospheric temperature. The large error bars within the central plume represent the range of CERES OLR observed within the selected co-location region. Localised clusters of scattered high cloud can be totally bypassed by the narrow MLS limb scan, though by extending the along-track length-scale for our co-located analysis it is more likely that a representative cross-section of this ice cloud will sampled. The main discrepancies between the model and measurements arise at the edge of the tropical plumes, in the postulated regions of anvil outflow and subsidence at profile positions $i = 3405$ to 3406 and $i = 3411 ...3413$. The MLS instrument does not detect any ice clouds in these regions; however CERES measurements indicate a substantial amount of variability of $\epsilon\, F{+}_{\mathrm{obs}} > 35\,\mathrm{W\,m^{-2}}$ at the same location that is likely to be the result of scattered high clouds.

There is a sharp contrast in both the measured and modelled OLR in both case studies that is likely to be associated with the contrasting scene-types viewed either side the high cloud edge. At these points uncertainties in the horizontal positioning of high clouds are apparent. Whilst both the modelled and measured OLR report the largest along-track gradient in the same general locations, at MLS profile positions $3410 < i < 3416$ in case study c1 and $2794 < i < 2799$ (c2) they are offset by up to 1 MLS profile position in each direction. As a result, the largest discrepancies between the modelled and observed OLR occur at these locations, with $F^{+}_{\mathrm{mod}} - F^{+}_{\mathrm{obs}}$ differences of $\sim 60\,\mathrm{W\,m^{-2}}$ at $i = 3412$ and $\sim 45\,\mathrm{W\,m^{-2}}$ at $i = 2796$ that result from this along-track offset. This finding highlights the importance of close spatial and temporal comparisons of high vertical resolution and accuracy for studies of high clouds. Later studies must allow for these uncertainties when identifying the division point between tropical high clouds indicated by points marked “f” on Figure 23.

MLS data offers no detailed knowledge of the LT, where low to middle level cloud and WV influences the magnitude of OLR. The detections in the UT must be combined with LT data to obtain a full representation of the LW radiation budget. ECMWF LWC data offers some detail on low clouds that enables us to refine our RT simulations. The inclusion of LT data, and its implications for our

high cloud characterisation, is discussed in further detail in Section 5.3.5.

Errors Associated with Co-located Comparisons of Clouds The data in Figure 26 present a very good relative comparison between simulated and observed OLR. There are several discrepancies however between model and measurements in the presence of high clouds, which are thought to arise from uncertainties in their position. These are investigated further using a larger sample of co-located data in Chapter 6. Accurate estimates of the cloudy-sky radiative forcing calls for improvements to instrument spatial resolution for future space observations of cloud. High quality composition data is required for input into the RRTM to provide reliable estimates of the longwave radiation budget, whilst the parameterisation of ice particle size and shape distributions in the model also impact cloudy-sky calculations. In particular, the RT model neglects the effects of LW scattering that may be significant for calculations within thick high cloud profiles that contain ice. Improvements to the parameterisation of ice particles within high clouds may be aided by detailed co-located comparisons to test the validity of each scheme against direct observations.

It is apparent from Figure 24 and 25 that the narrow field of view of MLS results in an atmospheric dissection that may not be representative of the entire high cloud system. Positioning uncertainties may occur as clouds move orthogonal to the A-train track i.e. off-track placement errors. Since MLS and CERES measurements are undertaken up to 10 minutes apart, this could account for several kilometres of misalignment. These uncertainties are however less significant than in the extra-tropics where a zonal jet-stream drives low pressure systems and their associated clouds. Small across-track offsets are generally only relevant for scenes dominated by scattered and small-scale high clouds (less than 25 km across), where they could plausible impact upon the quality of co-located comparisons.

5.3.2 Links between Potential Temperature and High Clouds

Both case studies show high clouds that are located between the equator and $20^{\circ}N$, that are characterised by $IWC > 36\,\mathrm{mg\,m^{-3}}$. Three deep convective clouds are detected by the MLS instrument through the northward cross-section (Figure 27 c2). These are found at profile positions $i = 3411, 3412, ...\,3414,\ 3417$ with pronounced OLR signatures associated with subsidence in-between these plumes.

The CERES measurements of OLR indicate a rather continuous decrease in OLR towards the dense icy centre of the tropical cloud at profile 3411 where the average IWC exceeds $45\,\mathrm{mg\,m^{-3}}$ across the limb scan. In contrast to c1, case study c2 shows a more extensive region of high clouds characterised by shallower convection at $i = 2784, ...\,2789$, where IWC is less than $20\,\mathrm{mg\,m^{-3}}$. Both studies reveal significant anomalies in the potential temperature field in the presence of mid-tropospheric clouds that point to small-scale intrusions, with a horizontal length-scale of $x \leq 150\,\mathrm{km}$, where cold-dry air from the stratosphere mixes into the troposphere from above.

The solid red isentrope on Figure 27 (c1) represents the $\theta = 350\,\mathrm{K}$ surface, which is aligned almost parallel to the pressure surface in the vicinity of the tropopause boundary. In the presence of high clouds a local dip ($i = 3413$) on the $p = 150\,\mathrm{hPa}$ level indicates a modest cool region, with a $+2\,\mathrm{K}$ anomaly relative to the mean for case study c1, just to the north of the deep convection at profile 3412. Case study c2 also shows an overall peak in the θ surface associated with warm convection, which also presents a characteristic dip. At the limbs of the convective cell, the UT air possesses a much lower potential temperature. As a result, the $\theta = 345\,\mathrm{K}$ isentropic surface is located on a pressure level of $p = 316\,\mathrm{hPa}$, compared to $p = 147\,\mathrm{hPa}$ within the centre of the tropical plume. The $\theta = 345\,\mathrm{K}$ surface demonstrates a distinctive warm anomaly at the location of the deep ITCZ convection in both case studies, as high mass concentrations of cloud ice and WV provide a source of latent heating.

Studies by Holton & Gettelman (2001) indicate that the temperature profile of the stratosphere is characterised by a large static stability that extends from the tropopause upward. The data in Figure 27 indicate that the resulting increase of potential temperature, a result of decreasing pressure and a weak environmental temperature profile, causes the observed large LW radiative cooling anomalies discussed in Section 5.3.4 that tend to increase in magnitude from $-2.0 < LW_{HR} < -0.5\,\mathrm{K\,day^{-1}}$ from 100 hPa to 68 hPa. Further examination of the v2 MLS temperature data also indicates that temperatures are above 228 K ($-45°\mathrm{C}$) at $p = 316\,\mathrm{hPa}$ where the input into the RRTM_LW code assumes mixed phased cloud are present.

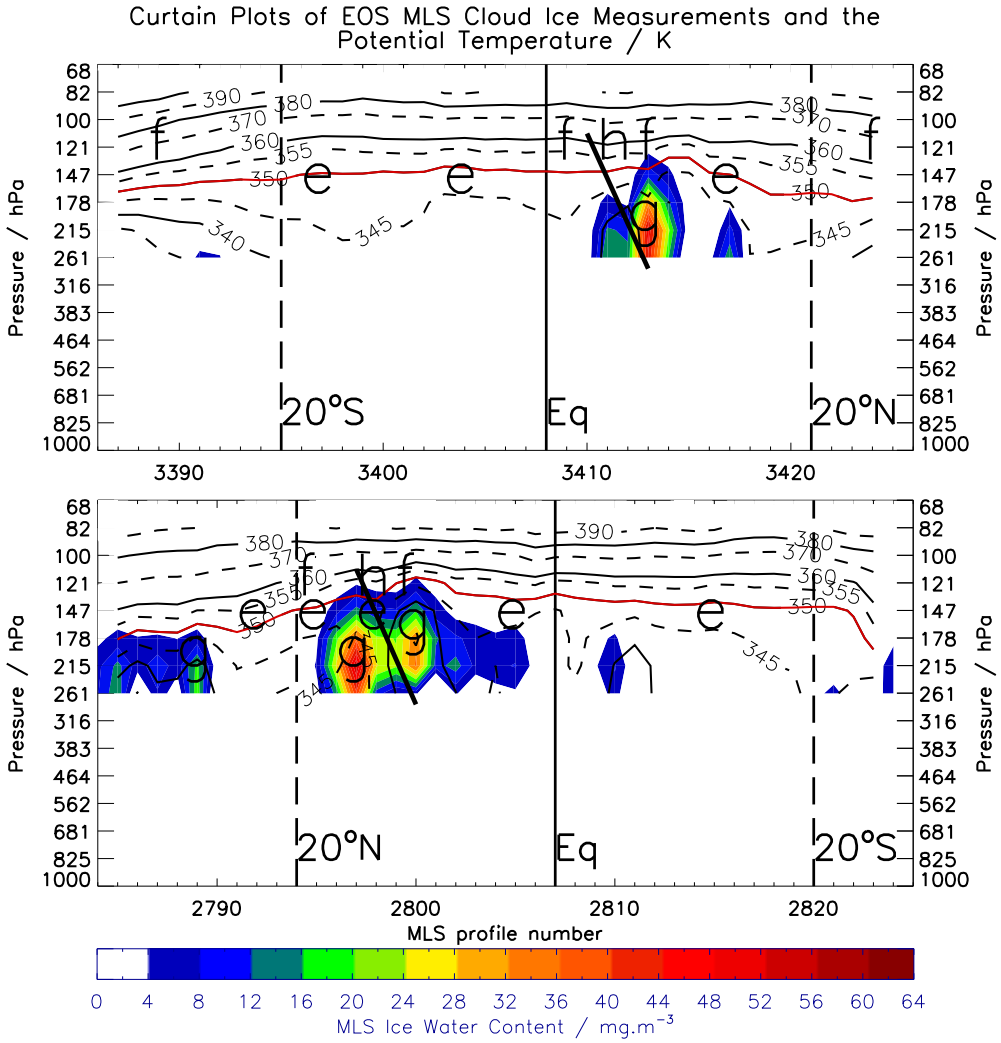

(c1)

(c2)

Figure 27: "Curtain plots" showing the measured ice water content (IWC) from the EOS MLS instrument for the same case study as Figures 26 to 26. The curtain plot indicates the potential temperature field by black contours labelled at 5 K intervals up to 360 K and 10 K intervals for higher values. A solid red isentrope indicates the 350 K surface. MLS v2 IWC is contoured at intervals of 4 mg m^{-3} with a range indicated by the lower colour bar. Points marked "e" indicate the postulated locations of thin cirrus outflows, "f" shows the likely location of anvil outflow cirrus, "g" indicates the location of maximum longwave cooling, whilst "h" and the slanted line highlight the dry air intrusions from the stratosphere.

5.3.3 Links between Water Vapour and High Clouds

Figure 28 reveals a high saturation of the tropical troposphere near the ITCZ relative to the extended low latitudes to the north and south. Within the tropical plumes, WV concentrations ($[WV]$) are often an order of magnitude higher than the sub-tropics at $[WV] > 10\,\mathrm{mg\,m^{-3}}$ at 261 hPa at MLS profile indices $i =$

2791, 3413, 3416. MLS WV appears to be positively correlated with high clouds, with more frequent icy plumes indicated by Figure 27 (c2) in contrast to c1 that is attributed to the broader band where raised water vapour concentrations above the surroundings are found up to 200 hPa in the location of plumes that extend in the extra-tropics. Locally, at the top of deep convection marked "f", the water vapour concentration exceeds regional average at pressure levels up to 150 hPa. This is associated with vertical transport of water vapour within the vertical columns of convection. The data also shows that the convective clouds associated with the ITCZ are noticeably broader in Figure 27 (c2) than c1 that appears to be associated with higher absolute humidities in this region. The case studies show that the $[WV] = 2\,\mathrm{mg\,m^{-3}}$ (light blue to dark green) surface in the low latitudes is ~ 100 hPa higher in Figure 28 (c2) than c1, based on 40 profiles in each case-study. The enhanced low to mid-tropospheric moistening is also associated with more defined drying of in measurement profile from 150 hPa to 100 hPa, associated with the cold temperatures of the tropical tropopause layer (TTL).

Past studies by (Sherwood & Dessler 2001) indicate that nearby circulation may provide a steady supply of water vapour to these relatively cold regions that enables the sustenance of high relative humidities required for in-situ high clouds. At points marked "e" on Figure 28 the vertical gradient in water vapour drops off readily with increasing altitude up to 150 hPa, with largely homogeneous concentrations of 0.5 to $2\,\mathrm{mg\,m^{-3}}$ in the TTL. It is plausible that a balance exists between sedimentation and evaporation to maintain a narrow layer of thin ice cloud in these regions, which is not detectable by MLS.

An interesting feature shown by Figure 28 (c1) is that the WV data shows a more defined tropopause boundary than case study c2, which may provide more favourable conditions for the formation of outflow cirrus that emanates from deep convective plumes. The sharper transition between the two atmospheric layers also indicates an inhibition to cross-tropopause transport. This is in agreement with the findings from Chapter 4, which indicate that the high clouds of the autumn ITCZ are much more widespread over Southeast Asia than other tropical regions.

Some relatively drier air detectable in the MLS WV product in the vicinity of convection are postulated to be the result of stratospheric air intrusions and are marked (h). These apparent dry slots between the two plumes of Figure 28

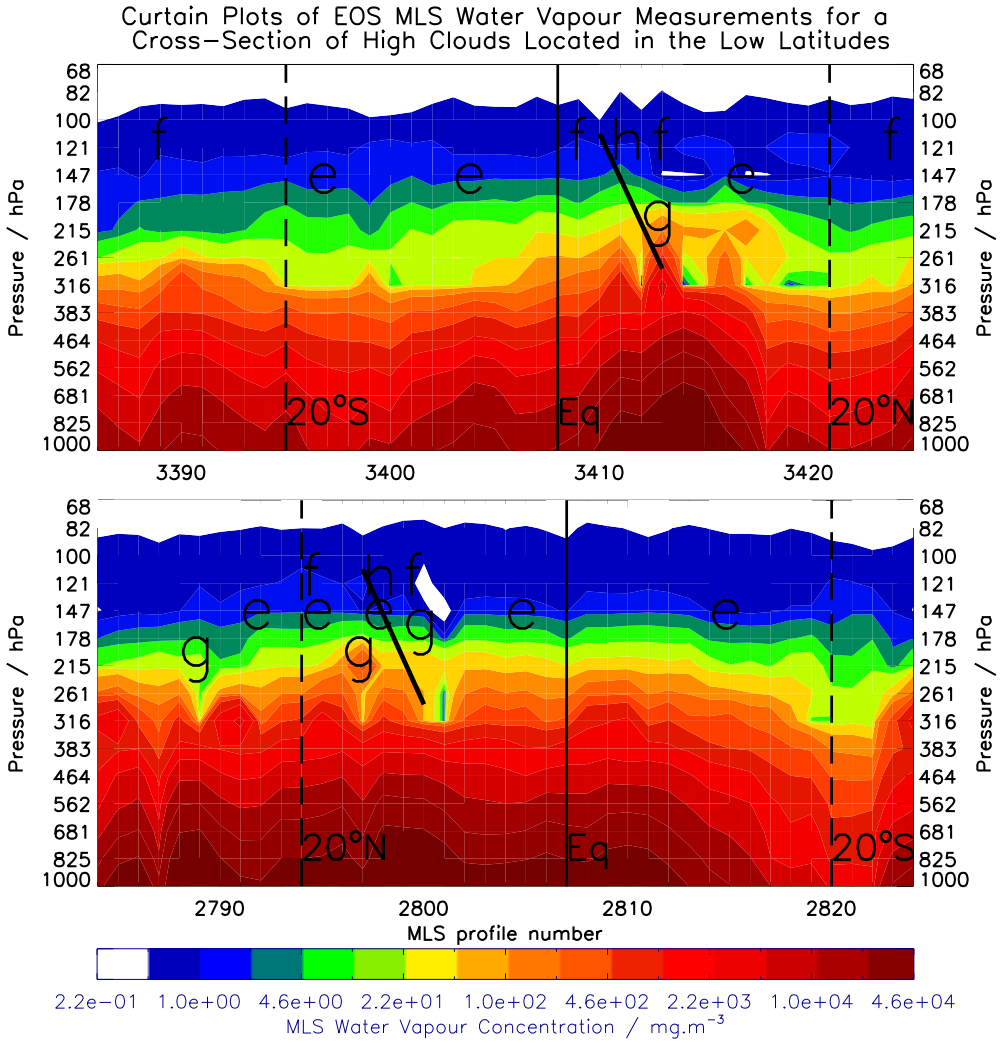

(c1)

(c2)

Figure 28: "Curtain plots" showing the measured water vapour (WV) from the EOS MLS instrument for the same case study as Figures 26 to 29. WV concentrations are contoured on 16 logarithmic levels with a rate of increase of 3 per decade according to the divisions on the lower colour bar. Annotations refer to the description in Figure 27

(c1) indicate a subsiding air mass that is likely to be part of the compensatory overturning of the tropical convective cells. These mesoscale dynamics associated with convective cells appear to be a frequent occurrence of the tropics, appearing also in case study c2. The advection of cool and dry air from the stratosphere into the troposphere vastly reduces the local greenhouse warming by reducing the absolute humidity and by the clearance of ice clouds. Studies by Forster & Shine (1999) also indicate that water vapour entering the stratosphere from the troposphere is important to the radiative energy budget and a plausible cause of stratospheric cooling.

Errors associated with MLS Water Vapour Measurements Uncertainties in the MLS WV detection in the presence of thick high clouds are difficult to remove by screening, as described in Section 2.3.1, however a larger scale study with numerous co-located profiles could feasibly be used to describe their bulk properties. Co-located averaging of different MLS data products cannot always ensure spatially coincident measurements, as each has a different along-track resolution. Notably, the v2 MLS water vapour product has approximately half the vertical and horizontal resolution as the IWC product at 261 hPa of 1.5 km and 200 km respectively.

Livesey et al. (2007) also indicates that a known systematic bias exists in the V2 MLS detection for volume mixing ratios > 500ppmv with occasional erroneous low mid-tropospheric values found in the tropics of < 1ppmv. This documented artefact may account for the apparent intrusion of dry air from the stratosphere into the tropical troposphere in the presence of deep convection. Further detailed studies are required to examine whether the WV anomalies reported by the v2 MLS data product result in a general bias or artefact in the modelled longwave radiation through direct comparisons with co-located CERES measurement data.

5.3.4 Links between Longwave Radiative Heating Rates and High Clouds

Figure 29 (c1 and c2) LW HRs on a curtain plot for the same case study introduced in Section 5.3. To examine the character of the ITCZ in further detail the general features of the data are analysed in the context of earlier findings. Figure 27 highlight the main components of the general global circulation system. The absence of high clouds and low WV concentrations in the sub-tropics result in relatively low LW HRs in the UT, indicated by negative values of $|H_{\mathrm{LW}}| < 1\,\mathrm{K\,day^{-1}}$ i.e. indicating modest longwave radiative cooling. Whilst in the lower stratosphere, the dominant source of LW radiative cooling is from low concentrations of WV.

Figures 29 (c1 and c2) show dry slots in the posterior of the high cloud detection at MLS points $i = 3414$ and 2801. These features may be a result of MLS measurement error known as "shadowing", a process whereby absorption in the near-view block the microwave signal from penetrating from the tangent point to the receiver is known as shadowing as described by Read et al. (2007). Case study data indicates that these anomalies only occur for dense ice clouds. A dry-slot is also just visible for one MLS profile at $i = 2797$ within another

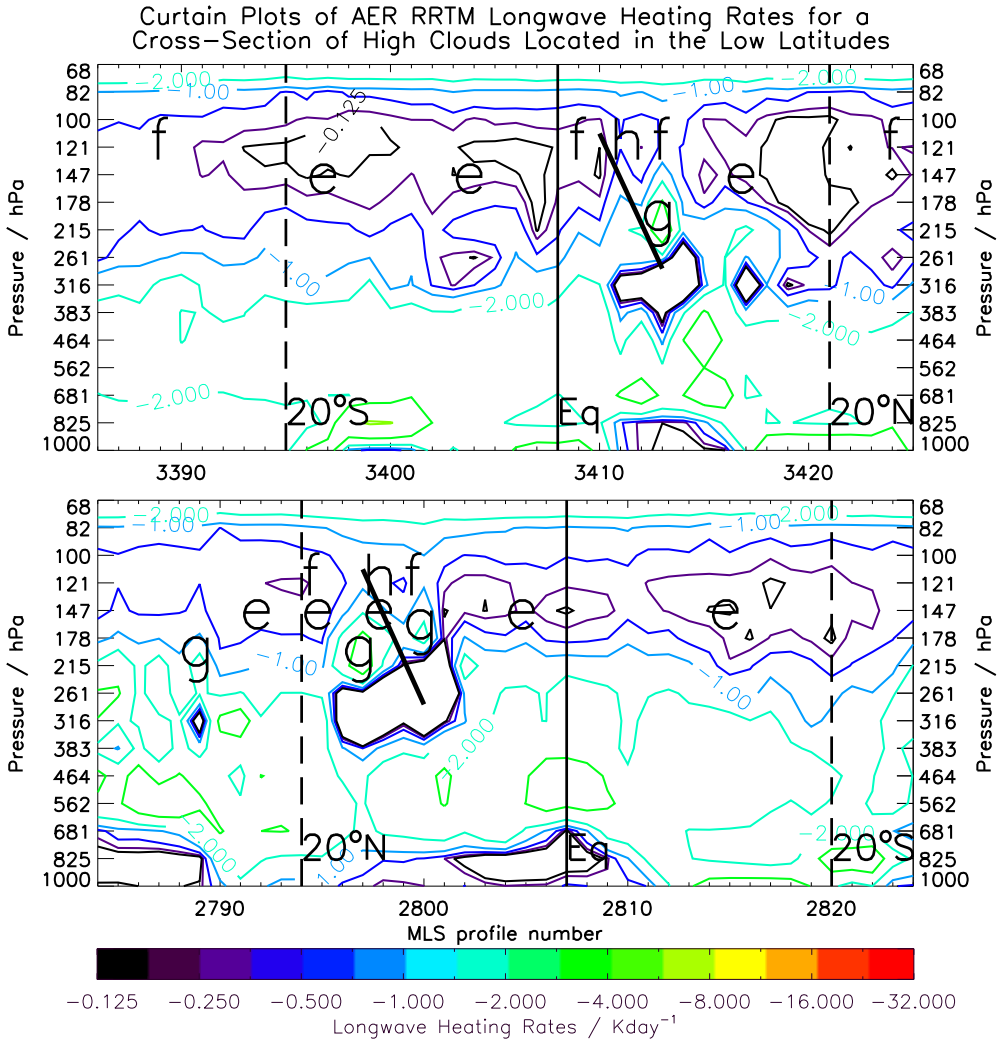

(c1)

(c2)

Figure 29: "Curtain plots" showing the simulated longwave heating rates from the AER RRTM_LW version 3 radiative transfer code. Coloured contours are shown at -0.13, -0.25, -0.50, -1.00, -2.00, -4.00, -8.00, -16.00, $-32.00\,K\,day^{-1}$) based on the lower colour scale for the same case studies as Figures 26 to 29, with annotations according to the description in Figure 27.

deep ice plume, which Figure 27 suggests is characterised by $IWC > 36\,\mathrm{mg\,m^{-3}}$. A significant dry anomaly does not occur in the data at $i = 2787$ behind a less pronounced plumes of ice clouds, of $IWC < 24\,\mathrm{mg\,m^{-3}}$. An extended co-located analysis is undertaken in Chapter 6 to determine whether or not comparisons between measured and modelled OLR can shed light on these features and the plausibility of stratospheric intrusions in the vicinity of deep convection.

Figure 29 (c1 and c2) are both are in general agreement that the strongest longwave radiative cooling rates are found in the mid-troposphere ($600\,\mathrm{hPa} > p >$

400 hPa) of up to $-8.0\,\mathrm{K\,day^{-1}}$ and also at ($200\,\mathrm{hPa} > p > 150\,\mathrm{hPa}$) above the maximum ice concentrations of high clouds. Interestingly, the LW cooling rates are almost neutral within the interior of thick clouds or very moist air, an observation that arises from radiative cooling that is shielded by weak transmission to space in these regions of the tropical cloud scene. Relatively large rates of LW radiative cooling may be maintained within convective plumes by a compensating process that opposes the rate of radiative cooling. This is based on the assumption that shortwave (SW) absorption is an order of magnitude smaller than LW absorption within optically thick cumulonimbus (Harries 2000, Hartmann, Moy, Fu et al. 2001, Hartmann & Larson 2002). The AER output indicates that the strong longwave cooling to space that dominates aloft of high clouds may be intensified by the presence of any dry intrusion.

Whilst the MLS v2 ice water content product does not currently detect thin in-situ cirrus, longwave radiative cooling rates shown by Figure 29 (e) that characterise near-neutral longwave radiative cooling rates of $HR_{LW} > -0.3\,\mathrm{K\,day^{-1}}$ in the tropical tropopause layer (TTL) where past studies by Jensen et al. (2001) implies it may form. The TTL is a non-distinct boundary that exhibits both properties of the troposphere and stratosphere, which is defined by Fueglistaler et al. (2009) as the bound $150\,\mathrm{hPa} > p > 100\,\mathrm{hPa}$ in the extended low latitudes. The observed longevity of in-situ cirrus, existing on timescales of up to 1 day e.g. (Fueglistaler et al. 2009) and radiative stability must be required during both the day and night-time period. As a result, a hypothesise is made that the simulated near-zero points in the LW HRs at these regions are attributed to isolated thin cirrus, marked "e" on Figure 29. Interestingly, the stability of these heating rates in Figure 29 within the TTL are notable in both case studies (day and night) and are almost independent of the variability in tropospheric water vapour concentrations outside of deep convection plumes. Any other conditions would lead to unstable temperatures that would readily lead to either evaporation or sedimentation. These high cloud features in the LW HR data tend most often extend outward from the convective plumes.

Past studies by Jensen et al. (1996) indicate that radiative heating of these clouds may lead to diabatic uplift, by a process known as cloud lofting. The ice that is evaporated during this heating is replenished through freeze drying, whereby water vapour is removed by deposition in low relative humidities and strong horizontal winds. Figure 29 also shows a $-0.3\,\mathrm{K\,day^{-1}}$ LW radiative cool-

ing in a postulated region of subsidence as indicated by the black slanted lines. At these regions a strong horizontal (along-track) gradients are observed in the rate of LW radiative cooling within the TTL. Further examination of these intrusions is discussed in Section 5.3.6.

Errors associated with RRTM Longwave Heating Rates There are substantial RT model errors in the simulation of LW radiative cooling in the stratosphere. The average maximum stratospheric LW HR error is $0.27\,\mathrm{K\,day^{-1}}$ compared to lblrtm calculations for RRTM_LW (Clough et al. 2005). Errors in the simulated LW HRs also arise from the chosen number of measurement input layers, as inferred from Equation 1 in Section 1.4.3. Since the RRTM model calculates LW HRs using the LW transmittance between neighbouring model layers, significant uncertainties arise at the model slab boundaries. As a result, the two layers at the top of the co-located profiles (68 to 82 hPa) and at the bottom (1000 to 825 hPa) are subject to large inaccuracies and are not scientifically useful.

The data shows that MLS IWC detections also carry significant uncertainties that dominate the error in the output of OLR, as indicated by the red shaded on Figure 26. LW HRs in the presence of high clouds should also consider sampling errors. Since the LW HR error of the AER RRTM_LW output scales closely with that of the speculated thin tropical cirrus, marked at points "e" on Figure 29 it is difficult to locate these high clouds on a case study basis. This could be tackled by examination of a large number of cases to produce a population mean or their errors minimised using co-located synergistic cloud data from many other independent observations.

5.3.5 ECMWF Vertical Motion and Liquid Water Content Data

Figure 30 (c1 and c2) show the positioning of warm clouds and their associated vertical wind tendencies for the same curtain plot area examined in Figures 24 to 27. ECMWF Re-Analysis interim (ERA-interim) data was used for this analysis, which was co-located to each MLS profile by the method described in Section 5.2.3. Figure 30 presents the underlying liquid water clouds that underlie a region of deep tropical convection with a LW heating rate minimum (marked "g") at $200\,\mathrm{hPa} > p > 150\,\mathrm{hPa}$. Data from the curtain plot c2 (Figure 30) indicates enhanced warm convection over the Asian monsoon compared to tropical Pacific, with 26 profiles where liquid water clouds extend to the mid-troposphere

compared to just 7 in case study c1.

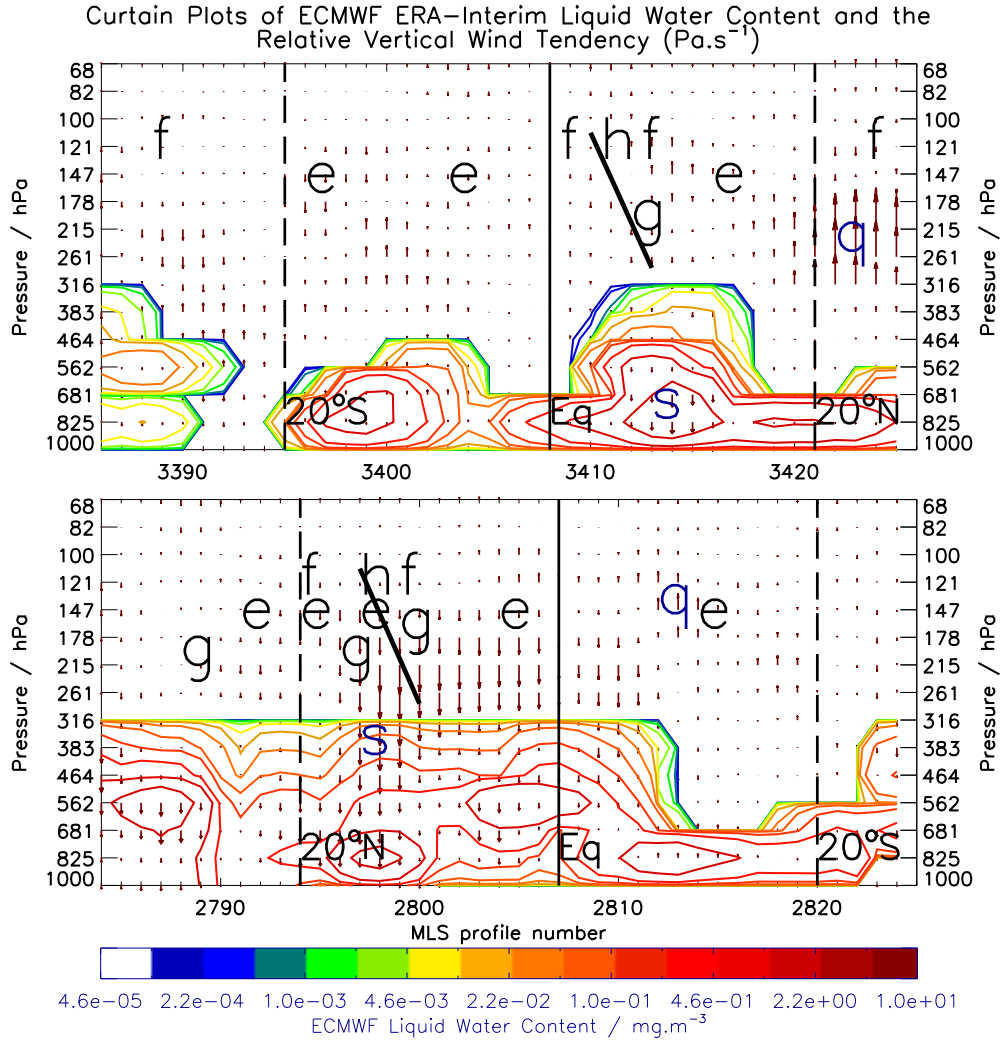

(c1)

(c2)

Figure 30: "Curtain plots" showing the assimilated ECMWF ERA-interim liquid water content (LWC) data and vertical wind tendency in Pa s^{-1} co-located to the same MLS sensor locations as data presented from the same case studies in Figures 26 to 29. The LWC in mg m^{-3} is contoured on 16 logarithmic levels with a rate of increase of 3 per decade according to the divisions on the lower colour bar. The lengths of the vertical arrows indicate the strength of the vertical motion relative to the scene maximum, whilst the arrows point toward the direction of motion. Lettering and the black slanted line refer to the descriptions in Figure 27. Additional letters "q" and "s" indicate the case study maximum ascent and descent rates of the co-located ECMWF ERA-interim vertical wind tendency respectively.

Adjacent to large-scale deep convection, shallow regions of cloud are present , i.e. below the proposed anvil regions marked as "f" on Figure 23. Within these zones, the descending branch of the cumulonimbus plumes is dominated by slow descent of air from latent cooling (hydro-meteor evaporation within sub-

saturation air) and falling cloud particles (with vertical motions less than particle fall speeds) that suppresses moist ascent and increases the stability of the environmental temperature profile. In agreement, the liquid and ice water content data indicates that high cloud formations are almost entirely absent with warm clouds largely confined to the lower troposphere. This is indicated by liquid water content (warm clouds) in Figure 30 that extend $1000\,\mathrm{hPa} > p > 600\,\mathrm{hPa}$ at $10 - 25°\mathrm{N}$ in c1 and $15 - 25°\mathrm{S}$ in c2, which is frequently associated with subtropical high pressure zones.

The length of the vertical arrows in Figure 30 indicates that the maximum relative vertical wind tendencies from the ECMWF ERA-interim data product described in Section 2.4. The maximum vertical ascent and descent in both curtain plots are marked by the blue letters "q" and "s" respectively. For case study c1 (Figure 30) these are indicated within a region of mid-troposphere. In this case study, the lower level subsidence is located at MLS profile positions $i = 3422, ...\, 3423$, with a peak in vertical tendency centred at 250 hPa and marked "s". The MLS WV and ECMWF liquid water content data (Figures 28 and 30) both indicate a transition in tropopause chemistry in this region that is likely to be due to the northern hemisphere sub-tropical jet-stream. It is noted therefore that the ECMWF vertical wind tendencies reported here may not be trustworthy, since small absolute uncertainties in the horizontal motion of this jet-stream may lead to large errors in the assimilated vertical motion from ECMWF. A region of strong descent marked "s" is noted in the lower troposphere where MLS IWC detects an overhead deep icy plume. This is perhaps due to broader neighbouring subsidence that compensates for locally confined ascent, which is therefore better resolved than the upward motion we commonly associate with deep convection. The ECMWF data appears to better resolve large-scale circulations, such as those associated with the Walker circulation.

For case study c2 in Figure 30, the ECMWF data indicates that the maximum relative vertical descent "s" is also found within a column of thick ice cloud identified in Figure 27 that is associated with deep convection, again suggesting that the ascent associated with tropical convection is more localised than its neighbouring subsidence. This has implications for weather and climate predictions, calling for the need of down-scaling to correctly resolve tropical cloud processes. The ECMWF ERA-interim data again indicates that the maximum ascent in Figure 30 (c2) is found near a transition point in liquid and water composition data,

suggestive of a link between vertical motion and the sub-tropical jet-stream located at 10°S in the southern hemisphere. In both case studies maximum implied vertical ascent from the ECMWF is located at $300\,\mathrm{hPa} > p > 100\,\mathrm{hPa}$ within the tropopause layer.

The results presented in Figure 30 demonstrate that optically thick clouds that extend as high as $p = 350\,\mathrm{hPa}$ are often associated with ice clouds aloft, confirming that ECMWF and MLS are both viewing the same clouds in broadly the same region of atmosphere. Features in the data reinforce one another, since the MLS ice water content product is not currently assimilated into numerical weather prediction models and is therefore independent of the ERA-Interim ECMWF liquid water content product used in our analysis. The analysis also demonstrates that strong along-track gradients in LWC also exist at the edge of tropical plumes. Below point "e" at profile $i = 2815$ (case c2), at the OLR maximum, it is apparent that LWC is only present in the lower model layers from the surface to 600 hPa (3 km), with little vertical motion present within the atmospheric column. The absence of high clouds in this region is likely to be associated with the presence of a Pacific high pressure system that increases atmospheric stability and inhibits convection. The character of case study c2 also presents a shallow layer of low clouds between profiles $i = 2814$ to 2817 that coincide with a maximum in the measured and simulated OLR over the Indian Ocean.

At the location of deep convection, presented by icy plumes on Figure 27, warm clouds are reported by ECMWF at MLS profile positions with vertical wind tendencies that extend upward to the mid-troposphere. In spite of a clear link between vertical motion and warm convection in the lower atmosphere, it is worth noting that high vertical winds above the middle troposphere ($p < 261\,\mathrm{hPa}$) are often reported by the ECMWF within many of the smaller scale ice plumes. Convection to the far north (LHS) of curtain plot Figure 30 (c2) does not coincide with any significant ascent in the ECMWF data, perhaps due to the up-scaling of ECMWF to the coarse spatial resolution of the MLS data.

Within the regions of deep convection, where dry intrusions are visible, strong vertical wind tendencies are often reported by ECMWF. Specifically, at profiles $i = 3413$ to 3414 and $i = 2787$ to 2798 where LWC locally exceeds $10\,\mathrm{mg\,m^{-3}}$. Within the depths of warm clouds the vertical wind is generally stronger here, with a noticeable region of intense subsidence centred at profile 3420 that coincides with a column of drier air in troposphere on Figure 30. Strong subsidence

acts to dry the air by an adiabatic (katabatic) thermodynamical process, as cool and dry air from the UTLS displaces the warmer and moister air below.

Subsidence usually takes place in a stable atmosphere that is characterised by the dry adiabatic lapse rate of $\frac{dT}{dp} < 2.5 \times 10^{-3}\mathrm{K\,Pa^{-1}}$ at $p = 261\,\mathrm{hPa}$. The MLS v2.2x data indicates a near-neutral static stability in the TTL region, consistent with the findings of Fueglistaler et al. (2009).

5.3.6 Stratospheric Intrusions and Evidence of Cross-Tropopause Exchange

The mechanism for entrance of moisture into the stratosphere at the tropics is important in the understanding of stratospheric chemistry and circulation (Randel et al. 2006). In particular, the maintenance of vertical motions within tropical convection provides a dynamical forcing for the poleward transport of both moisture and ozone e.g. Goddard Space Flight Center (Retrieved Jan 2012). The data in Figure 29 (c1 and c2) show two locations where stratosphere air appears to mix with the troposphere. These regions are indicated by the black sloping lines and labelled "h" at their intersection with the tropopause. The dynamics in these regions indicates a stratosphere-troposphere exchange (STE) process, which is diagnosed by cross-tropopause transport of high altitude water vapour (an atmospheric tracer). The MLS measurement WV data presented in both case studies by Figure 28 show that dry slots of air characterised by $[WV] \leq 0.5\,\mathrm{mg\,m^{-3}}$ with reported retrieval errors in the order of 30 % (Livesey et al. 2007). These WV concentrations are more typical of the stratosphere; appearing in the WV data to extend 4 km across the tropical tropopause ($p \sim 100\,\mathrm{hPa}$) into the mid-troposphere to $p \sim 250\,\mathrm{hPa}$. Water vapour concentrations are much higher at the neighbouring MLS profile positions at $\sim 2\,\mathrm{mg\,m^{-3}}$. Deep plumes of high cloud are also detected by MLS at these regions, as shown by Figure 27.

MLS WV data presented by Figure 28 highlights at least one proposed STE in each case study, occurring only where deep tropical convection is present. These are located at MLS profile 3411, with perhaps a smaller scale subsidence at $i = 3413$ in c1. Whilst in c2 only the northerly most plume at $i = 2788$ reveals a dry-slot in the MLS WV data. Not all ice clouds show these features, notably with three small-scale convective plumes detectable at $i = 2785$ and 2789 in c2 around 25°N no significant dry-slot is detectable in the MLS WV data. Since these dry slots in the WV data are only visible in thick ice clouds,

they may only be a tropical feature. The plume is only identified by a single MLS profile, so convective ascent is very local in nature. Due to the localised nature of cumulonimbus, it is plausible that isolated stratospheric intrusions occur throughout the tropical atmosphere that is not measured by the MLS due to its narrow field of view.

The MLS WV data in Figure 28 indicates that stratospheric air at these positions either has negative buoyancy or is forced to descend by a neighbouring convective cell. It is plausible that the STE may be the result of freeze-drying upon heterogeneous deposition of WV on the surface of ice crystals (Jensen et al. 2001). The local drying of the air that results from freeze-drying at the top of convection may lead to isolated pockets of negative buoyancy, exchanging with the moist air of the upper troposphere. Downward motion may also be generated in the vicinity of the tropopause by falling ice crystals, with a mean terminal velocity that outweighs the ascent generated by latent heating and free convective ascent. In either case, for the freely convective atmosphere to experience drying at its top the vertical mass flux of WV must be outweighed by the rate of ice deposition and fall-out.

The ECMWF vertical wind tendency data presented in Figure 30 show maximum downward motion where ice clouds extend to the tropopause (points marked n). Interestingly, case study c2 shows downward motion that extends throughout the entire tropospheric column, whilst in c1 descent is confined to the low to middle troposphere ($p > 500\,\mathrm{hPa}$) with apparent ascent aloft. This is most likely a consequence of the broader region of high clouds in c2 compared to c1 (Figure 27), whose dynamics are better spatially resolved. As a result, a larger sample of co-located data is required to support any link between MLS ice detections and UT winds.

In case study Figure 28 (c1) the dry intrusion is located aloft of deep tropical convection, which crosses the cold point tropopause at points "h". Initial tracing calculations indicate that adiabatic cooling associated with the descending stratospheric air mass at the dry adiabatic lapse rate ($-9.8\,\mathrm{K\,km^{-1}}$) over a depth of 4.5 km would result in a +44 K increase in temperature, whilst conserving much of its moisture in the process. A deformation of the isentropic surface is therefore also an indicator of vertical motion, inferred by changes in the rate of potential temperature increase from the tropical tropopause layer into the stratosphere. Whilst the $\theta = 350\,\mathrm{K}$ surface (maroon line) on Figure 27 (both cases) indicates a

significant pool of warm air above deep convection, a similar feature is not seen at the $\theta = 360\,\mathrm{K}$ surface that would indicate STE. This is possibly due to the localised effect of the exchange process, which is not spatially resolved by the MLS. In addition, the rapid evaporation of ice crystals as the relative humidity with respect to ice is lowered is likely to result in entrainment of the dry tongue of air, with additional mixing within the warm and moist ambient air of the neighbouring convection.

The horizontal length-scale of the intrusions must scale closely with the MLS IWC along-track resolution $\sim 300\,\mathrm{km}$, since they only occur for a single MLS profile. The intrusions also appear to be aligned off-vertically in the direction of A-train satellite orbital motion, as indicated by the gradient of the slanted line in Figures 26 to 31. Since there is a low level convergence of moist air into the tropics from higher latitudes, a slight equatorward tilt may be expected. This may indicate a small horizontal mis-alignment in the MLS WV product in the UT that is level dependent. More detailed studies are needed to confirm this finding. Later in this thesis the effect of cloud shadowing on anvil cirrus detection is investigated, to assess the influence of measurement error on radiative budget calculations.

MLS measurements of water vapour and ice water content indicate that deep convection penetrates the tropopause and appears to "inject" a plume of moist tropospheric air into the stratosphere displacing dry stratospheric air that subsides into the adjacent convective outflow. Whilst upper tropospheric water vapour measurements in Figure 28 are locally lower, analysis of the modelled OLR data in their presence shows some inconsistencies with respect to measured OLR. At the location of these intrusions, indicated by the blue slanted lines in Figure 26, large relative model-measurement off-sets are found of $\sim 30\,\mathrm{W\,m^{-2}}$.

Subsidence associated with the intrusion may be part of the mechanism for the formation of outflow cirrus. Studies by Sherwood & Dessler (2001) indicate that cross-tropopause transport takes place through radiative cooling and large-scale sinking around the location of deep convection that may be balanced by radiatively balanced lofting. This is an interesting feature, since the latent heat exchange and tropical dynamics that drive deep convection generally do not extend into the stratosphere due to a temperature inversion that limits the height of the vertical plume.

5.3.7 Ozone Anomalies Associated with High Clouds

To investigate further the possibility of STE in the low latitudes, the ozone mixing ratio was examined for the same case study of high cloud scenes over the Pacific Ocean. The data from this analysis is shown on Figure 31 for the pressure levels $p < 215\,\text{hPa}$. Data reported on these levels are scientifically useful in the absence of optically thick cloud scenes (Livesey et al. 2007). Cloud particle scattering can lead to low reported mixing ratios of ozone mixing ratios in the UTLS. The version 2 MLS ozone product was used as a suitable input into the RT model that formed part of the gaseous input. The version 2 MLS ozone product is considered a valuable component of the RT calculations since it is co-located directly to other MLS gas retrievals, with limitations to scientific use at altitudes above the tropopause where its concentrations are highest.

At points marked "h" on Figure 31 (c1 and c2) locally enhanced mixing ratios of ozone up to $200 \pm 180\,\text{ppbv}$ are found at the cold-point tropopause. This is coincident with the tops of deep convection and upper tropospheric ice clouds, aloft of points "g" where the LW HR maximum points are found in Figure 29. These disturbances in the retrieved MLS ozone coincide with the underlying warm convection, where WV measurements and liquid water clouds are also found in Figures 28 and 30. Highly elevated values of ozone with respect to the tropopause mean that are coincident with high clouds indicate a process of STE, whilst the smaller scale along-track fluctuations in ozone mixing ratio that occur frequently irrespective of tropospheric composition may indicate artefacts in the version 2.2x ozone data (Livesey et al. 2007). Ozone data provides supporting evidence of a convection related stratosphere to troposphere exchange process, whilst due individual measurement uncertainties an extended study is generally required due to the large relative errors ($\sim 55 \pm 5\,\text{ppbv}$) reported by Livesey et al. (2007). In addition, uncertainties in the ozone data also arise from systematic errors in the MLS instrument calibration and spectroscopy on the retrieval.

Despite known errors in MLS ozone retrieval, both case studies reveal a general pattern of disturbance around the centre of the ITCZ at $100\,\text{hPa} > p > 80\,\text{hPa}$, just above the cold-point tropopause. These are located at profiles $i = 3410 \ldots 3417$ in Figure 31 (c1) and for c2 at $i = 2788 \ldots 2803$. The exchange of ozone between the stratosphere and troposphere may have implications for the radiation budget since longwave radiative cooling is felt more strongly in the

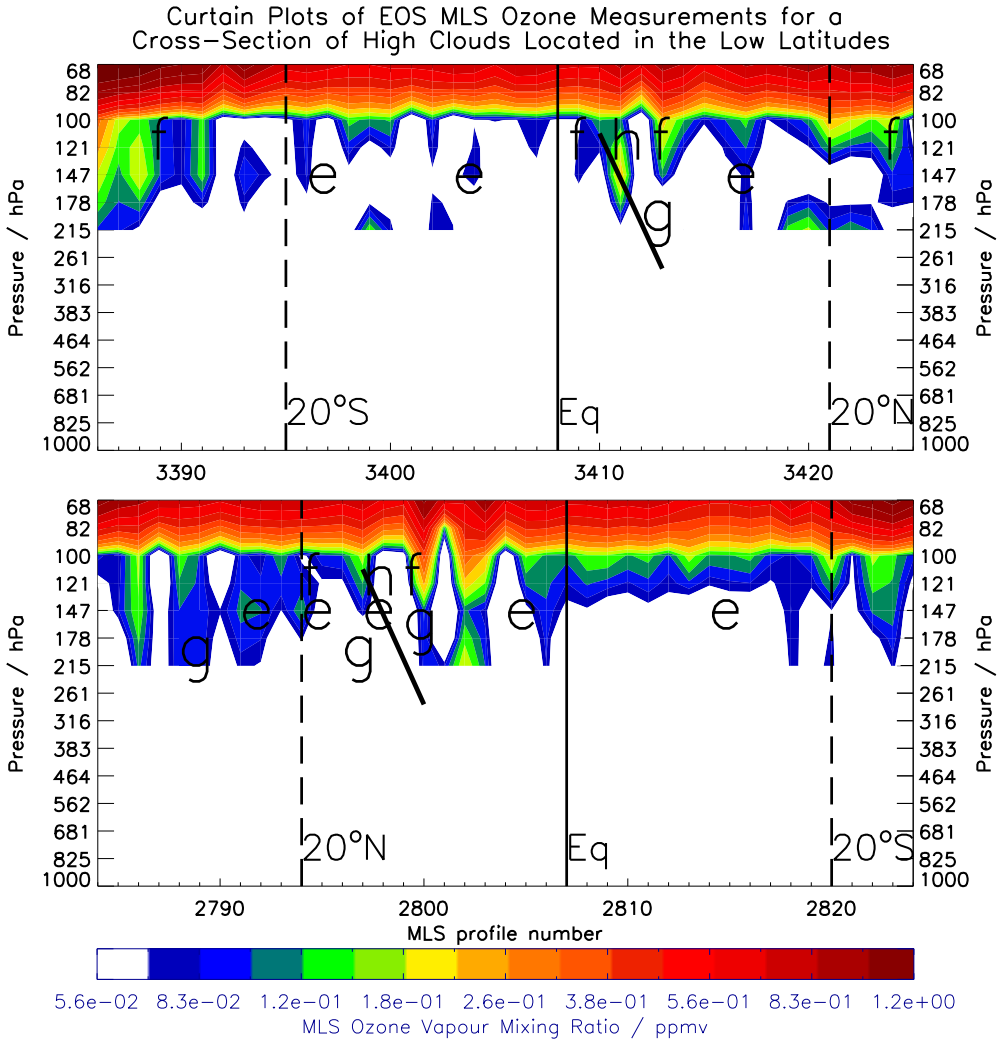

(c1)

(c2)

Figure 31: "Curtain plots" showing the Version 2.2x MLS ozone mixing ratios from the same case studies as Figures 26 to 27. Ozone is contoured on 16 logarithmic levels with a rate of increase of 12 per decade according to the divisions on the lower colour bar. The black slanted line and lettering indicate the same high cloud features as Figures 27 (c1 and c2).

TTL than shortwave heating (Fu et al. 1995). The longwave radiative cooling rate output from the AER RRTM_LW, presented in Figure 29 also indicates that cooling at the top of high clouds plays a significant role in the local radiative forcing.

Large scale features in the ozone data are also presented in Figure 31 that is located at off-equatorial latitudes of 20° to 25°. These are characterised by relatively high mixing ratios $[o_3] > 100\,\text{ppbv}$ at $p \sim 200\,\text{hPa}$. The vertical distribution of ozone indicates that the tropopause undergoes a sharp transition to lower altitudes in the region of the sub-tropical jet-stream. Studies of the

meridional distribution of ozone by Stevenson et al. (2006), Highwood & Hoskins (1998) also support this finding. The MLS data shows that ozone measurements could be used as an atmospheric tracer, since ozone is bound in the stratosphere by the tropopause. In addition, the data shows that ozone is found only at low humidities of $[WV] > 5\,\mathrm{mg\,m^{-3}}$ as indicated by Figure 28. Previous studies by Randel et al. (2006) agree with this finding, indicating that low water vapour concentrations and cold temperatures in the lower stratosphere were coupled with an observed depletion in the global ozone concentration from 2001 to 2005. The lower tropopause altitude in the sub-tropics explains why earlier high cloud distribution studies in Chapter 4 show that large-scale free convection to levels sufficiently cold for ice cloud formation is a rarity outside of the tropics, partially explaining the absence of stratosphere-troposphere exchange at higher latitudes.

5.3.8 High Clouds and the General Circulation

The Hadley cell is an important component of the general circulation that is associated with low level convergence that dominates the dynamics in the vicinity of the equator and upper level transport of water vapour to the extra-tropics. In our data large scale subsidence between the Ferrel and Hadley cells are most well observed at 19°N for case study c1, whilst in c2 a region of descent is present at 21°S. In both cases the subtropical jet that defines this boundary is marked by an abrupt lowering of the tropopause with a dry transition at $261\,\mathrm{hPa} > p > 178\,\mathrm{hPa}$ moving poleward. The asymmetry in the humidity about the equator is attributed to regional and seasonal weather patterns and surface temperature. In this study the local scale transport of WV is explored within several tropical convective cells, however further studies of a larger sample of tropical cloud scenes are necessary to investigate the general character of UT WV.

The northward displacement of the ITCZ (Hadley convective cell) during the autumn equinox of the NH (at around 10°N) is consistent with the findings from low latitude high cloud comparisons in Chapter 4. The study in this chapter shows the "drier" intermediate zones ($WV < 10\,\mathrm{mg\,m^{-3}}$ at $p = 261\,\mathrm{hPa}$) associated with the boundary between the Ferrel and Hadley cells. Figure 28 also shows dry regions can be observed at MLS profile positions $i = 3396, \ldots 3403$ and $i = 3418, \ldots 3422$ in both hemispheres for case study c1, and less noticeably at $i = 2819, \ldots 2822$ for c2 in the SH only. The general dynamics of the sub-tropics is

characterised by bands of large scale ascent that are centred at around 16°S and 22°N in case study c1.

Between the convective zones large regions of subsidence take place within dry tropospheric air, which is almost entirely clear of ice clouds. Case study c2 also shows a general circulation feature from 10 to 20° that is associated with large scale subsidence. At this location low WV concentrations extend the profiles from $i = 2819$ to 2822, due to a sub-tropical anticyclone over the Indian Ocean. The region of subsidence forms part of a compensatory motion of the Hadley and Walker Cells, which characterises the general circulation of the tropics (Kelly & Randall 2001).

5.3.9 Summary of Results

Figure 32 shows a summary of the main structure and features of an overshooting convective plume that frequently form at the tropics, as identified in Section 5.3. The analysis uses data from ice water content, water vapour, ozone (version 2 MLS products); liquid water content, vertical wind tendencies (ECMWF ERA-Interim); outgoing longwave radiation (CERES SSF FM3 and AER RRTM_LW); and longwave radiative heating rates (AER RRTM_LW).

Using a combination of MLS measurements and RT outputs a deep convective plume is defined by cloud ice water content measurements above $4\,\mathrm{mg\,m^{-3}}$ that extend from 261 hPa (the mid-troposphere) to pressures below 150 hPa, which represents a continuous deep region of moist convection in the sub-zero troposphere. Near neutral LW HRs are used to identify the tropopause e.g. Andrews (2000), associated with the cold-dry signal of the tropopause at ~ 20 km (100 hPa). The field of view of the MLS instrument at 240 GHz indicates an uncertainty of ~ 50 hPa in the vertical MLS position, as estimated in Section 4.2.1, which is considered in our identification of tropical clouds with anvils. As deep convection extend the low to mid-troposphere, further confidence of their detection can be provided by identifying those regions where higher MLS water vapour mixing ratios are present from the surface to 400 hPa. This cannot include the mixed-phase region of atmosphere, since this part of the troposphere is not well specified by measurement data.

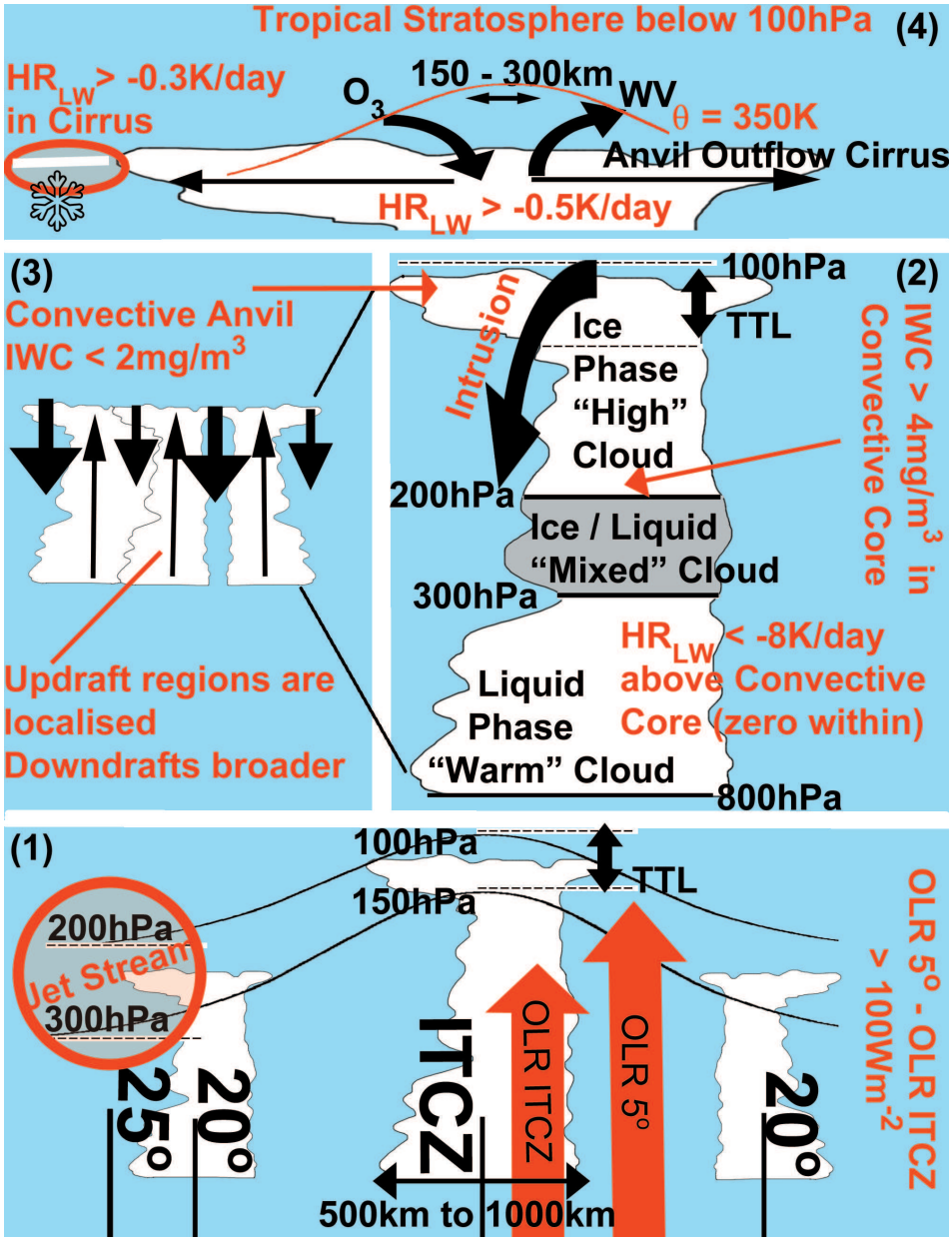

Figure 32: Key features of tropical troposphere scenes (clouds in white) identified from co-located measurement data from MLS (Aura), ECMWF ERA-Interim and the AER RRTM_LW. The analysis summarises findings from case study data from 19th September, 2004 (c1, c2). Tile 1 shows a cross-equatorial transect of high clouds with altitude and latitude indicated by the vertical and horizontal plane of the schematic and latitudes relative to the Inter-Tropical Convergence Zone (ITCZ). A red circle indicates the position of the subtropical jet-stream, whilst the red arrows indicate the relative amounts of Outgoing Longwave Radiation (OLR). Tiles 2 and 3 show the sub-structure of the high clouds of the ITCZ (centre of Tile 1), indicating the mesoscale convective clouds with an anvil and the location of maximum longwave radiative heating (HR_{LW}). Tile 3 shows the finer structure of the same cumulonimbus clouds and relative vertical motions (thick black arrows). Tile 4 (top) shows the anvil cloud within the Tropical Tropopause Layer (TTL), with stratospheric exchange of ozone (O_3) and water vapour (WV) and outflow of ice particles indicated by black arrows. This figure is not to scale.

5.4 Discussion / Conclusions

The study in this chapter demonstrates how co-located measurements can enhance our understanding into the character of high clouds that can be used for the benefit of climate science. This is achieved by investigating the chemical and radiative characteristics of high cloud scenes that are signatory to their detection. The case study examines two "curtain plots" that cover the subtropical branches of the general circulation and pass the equator at the tropics and explore the key features including WV, ozone, potential temperature and longwave radiative cooling. In particular, the v2.2x MLS data reveals some interesting features in the WV and $\theta = 350\,\mathrm{K}$ potential temperature field that are characteristic of the tropical tropopause aloft of deep convective clouds. The analysis also reveals that the mid-tropospheric air within a deep convective plume contains more than twice the concentrations of WV than the neighbouring profiles. This observation is thought to be partially attributed to a process of STE.

A more unique signal in the water vapour data is noted from MLS at the edges of convection, which are defined by much drier air than the UT than the background level. In these regions two to four times less WV is detected than within the surrounding air in the absence of high cloud detection. The characteristic is likely to be part of a compensatory subsidence within the convective outflow region. Analysis in this chapter also indicates that routine examination of the along-track variability in WV concentrations could be used to ascertain whether a region is likely to be cloudy. In particular, the use of along-track characteristics of high clouds could be used in combination with a statistical technique to explore MLS measurement signals that are a high cloud pre-cursor.

The presence of anvil outflow cloud in this chapter is speculatory and warrants further statistical analysis using a larger sample of high cloud scenes, however this study shows that the UT air adjacent to the convective plumes is characterised by a negative longwave (LW) radiative heating (cooling) in the order of $H_{\mathrm{LW}} \geq -0.3\,\mathrm{K\,day^{-1}}$. Studies by Fueglistaler et al. (2009) indicate that outflow cirrus in the presence of the tropical tropopause layer are both optically and sub-visually thin, which may contain ice mass concentrations equating to less than $0.02\,\mathrm{mg\,m^{-3}}$ at 100 hPa. As the reported precision of the MLS ice detection at the same pressure is $0.05\,\mathrm{mg\,m^{-3}}$, the instrument may not be able to detect much of the thin outflow cirrus (Livesey et al. 2007).

LW HRs also coincide with potential temperature anomalies, indicating a process of STE that appears at least one plausible location in each of the two low latitude case studies. Fluctuations in the vertical profile of potential temperature and WV data from their mean values also hint at a large scale dynamical process at the same locations. Although the MLS ozone data is not scientifically useful in the mid-troposphere, some significant lower stratospheric anomalies in the ozone data appear above deep convection in both case studies. WV and ozone anomalies above the convective cloud tops indicate a downward motion through diabatic cooling and an associated TTL dehydration. These results are consistent with findings of UTLS ozone anomalies from Chase et al. (2011), using 9 months of co-located CloudSat, CALIPSO and MLS data over the tropics. The analysis indicates that tropical dynamics and the LW radiation budget are closely linked by a process that acts to dry the troposphere whilst injecting moisture and latent heat energy into the stratosphere. The dynamical forcing observed in these locations may arise through a mass balance of air masses with neighbouring convection e.g. Lindzen et al. (2001).

Whilst ECMWF ERA-interim low troposphere cloud data provides a useful confirmation of deep convection where MLS also views high clouds, its vertical wind tendencies provide little extra insight. The analysis tends to suggest that small-scale vertical motions on a similar scale to water vapour anomalies may be found within tropical cloud, neither of which can be resolved on MLS length-scales. This calls for space-borne instruments with better horizontal sampling, particularly in the presence of dry stratospheric intrusions where local WV fluctuations may cause much of the observed model-measurement bias in OLR. Since UT WV is a major contributor to the OLR, much lower longwave suppression are locally observed in the dry atmosphere adjacent to high clouds that need to be better represented in future weather and climate models.

Studies in this chapter also explore the consistencies of OLR simulations by the RRTM in the presence of ice clouds. This is achieved by the use of co-located comparisons of OLR simulations with CERES measurement data that is monitored over the same low latitude locations. The estimated errors in the OLR simulations only include the quality of the MLS data input, whilst uncertainty in the measurements from spatial variability in the nadir data arise from co-location at each MLS sensor footprint. The results indicate that the sensitivity of OLR to IWC is greater for optically thin clouds at high altitudes. This highlights the

importance of using cloud products that report a good vertical precision in the upper troposphere to accurately monitor tropical cirrus.

CERES measurements are also used to assess whether the high cloud scenes are horizontal homogeneous, a condition that is only valid for a subset of MLS profiles. A scene may consist of scattered clouds of different altitudes, so the OLR on a point-to-point basis often varies considerably within a nominated sensor footprint. In contrast to the errors in the simulations, the results indicate that the greatest spatial co-location errors are present around tropical high clouds where the variability in OLR has the greatest implication for climate. The variability in nadir-sensed OLR data within limb-sensor footprints provides a useful diagnostic tool for future studies that calculate Cloud Radiative Forcing (CRF) uncertainties in the presence of high clouds. In Chapter 6, it is shown how a combination of MLS data and coincident CERES OLR observations can be used to refine estimates of the longwave CRF.

Past studies indicate that tropical expansion exceeds projections produced by climate models (Solomon et al. 2007). This may be due to inadequate understanding of the tropical hydrological cycle and representations of STE processes. This case study analysis reveals details of several intricate processes that take place within tropical convection and their ice clouds, providing coincident measurements that suggest coupling between atmospheric chemistry and composition within. The findings in this chapter make advancements on previous studies, providing direct observations of OLR and atmospheric composition in the presence of tropical high clouds. More detailed studies of tropical ice clouds and their impact on the longwave radiation budget are undertaken in Chapter 6. This study uses a large sample of atmospheric composition data, which is examined in presence of two different high cloud scene-types.

6 A Focussed Study of Tropical Cirrus OLR and Radiative Forcing under Different Conditions

6.1 Introduction

This investigation examines the local change in the rate of longwave (LW) cooling through radiant energy loss under the conditions of different tropical high clouds. Two prevalent high cloud scene types are identified in the low latitudes: optically thick ice clouds within deep cumulonimbus plumes, and the thinner ice clouds associated with the anvil outflow that emanate from mesoscale convective storms. Earlier studies in Chapter 4 using synergistic A-train measurements show that mesoscale convective storms are almost entirely confined to the extended low latitudes (equatorward of 35°) and cover 3 to 7 % of the Earth's surface. Other studies by Liou (1986), Rossow & Schiffer (1999), Stephens, Starr, Sassen & Lynch (2002) indicate that the high clouds associated with this convection account for 15 to 40 % of the total global ice cloud fraction. As these high clouds coincide with substantial reductions in the rate of longwave cooling to space they play a significant role in the regulation of global climate.

The formation and maintenance of thin cirrus is particularly poorly understood are therefore poorly represented in weather and climate models (Lohmann & Roeckner 1995, Solomon et al. 2007). Detailed investigations of upper tropospheric water vapour in the presence of tropical convection are therefore required. Further studies are particularly needed to explain why relatively thin tropical anvil cirrus, that is frequently observed to extend outward from convective plumes, is a stable feature of the tropical atmosphere. This is in spite of the high vertical wind shear and the high ambient humidities of the tropical tropopause layer that leave the relatively small ice crystals of anvil cirrus both prone to vapourisation and to sedimentation. There is presently insufficient evidence from in situ measurements to support the freeze-drying hypothesis (Jensen et al. 2001), a concept that implies a net flux of water vapour (WV) from the stratosphere to the troposphere via the diffusional growth of ice crystals within the over-shooting plumes followed by gravity driven fall-out of larger ice particles.

Tropical cirrus also has implications for global warming of the Earth's atmosphere and surface. In particular, thin high cloud poses a potentially strong positive forcing on climate, which is directly exerted by the suppression of long-

wave radiative cooling. Observational evidence from the Earth Radiation Budget Experiment (ERBE) show that the longwave (LW) and shortwave (SW) components of the radiative budget are both strong over the tropics and are in near cancellation (Harries et al. 2001, Ramanathan & Inamdar 2006, John et al. 2011). Other studies indicate that the forcing of tropical thin cirrus may be overwhelmed by the strong greenhouse effect imposed by a thick layer of WV (Larson & Hartmann 1999). High clouds are also responsible for many indirect effects on other components of the global climate system through less well understood cloud feedback mechanisms. In particular, changes in cloud parameters play a fundamental role in the response of climate to future changes in greenhouse gas concentrations (Wielicki et al. 2002, Chen et al. 2002). A full description of ice clouds is therefore required to fully understand their impact on the global radiation budget.

The radiative feedback response of low latitude high cloud to global climate change is a particular subject of debate (Solomon et al. 2007). A recent study by Williams & Webb (2009) indicate that differences in the representation of the cloud feedback response accounts for much of the variation in climate sensitivity amongst Global Climate Models (GCMs). Several studies into tropical clouds propose a fixed temperature hypothesis, whereby anvil temperatures are largely independent of changes in surface temperature imposed by rising greenhouse gases (Hartmann & Larson 2002). Other studies indicate that the vertical position of mid- and upper-tropospheric (UT) ice cloud and humidity signatures are dependent upon the surface temperature (Tompkins & Craig 1999). In favour of a negative climate feedback process, Lindzen et al. (2001) speculated that the overall tropical area covered by anvil clouds may decrease with rising temperature; this idea is known as the "iris hypothesis". High quality WV measurements are therefore important for a complete and accurate characterisation of the Earth's global circulation and energy balance; in particular increases in UT WV present a dominant positive feedback in response to global temperature increase (Soden et al. 2005).

In this study, the Outgoing Longwave Radiation (OLR) is examined in a range of different conditions in the extended low latitudes. Specifically, the longwave (LW) Cloud Radiative Forcing (CRF) is calculated - the difference between the all-sky Earth's radiation budget and the clear-sky Earth's radiation budget in $\mathrm{W\,m^{-2}}$ (Solomon et al. 2007, Chap. 8). LW CRF calculations are examined in the context of upper tropospheric water vapour and cloud ice, which account for much

of the observed variability in cloudy-sky greenhouse effect. Model calculations of the CRF are currently subject to large uncertainties, particularly for thinner cirrus that is often poorly detected and whose ice particles are more difficult to parameterise (Wyser 1998, Iacono et al. 2000, Hong et al. 2009). The resulting calculations of the LW CRF will help quantify the uncertainty in the climate sensitivity, a metric used to characterise the response of the global climate system to a given forcing (Solomon et al. 2007).

To correctly represent high clouds within numerical models that emulate future change, it is first necessary to ensure reliable representations of cloud observations for input into Radiative Transfer Models (RTMs) that simulate the OLR in cloudy-sky and cloud-cleared conditions (i.e. by removal of cloud layers). To validate calculations of the LW CRF, a set of low-latitude Aura Microwave Limb Sounder (MLS) measurement data are firstly identified as a reference scene, where neither anvil outflow nor convective plumes are detected. The simulated LW CRF is then directly compared against observational data from the Clouds and the Earth's Radiant Energy System (CERES) at the same locations to assess the uncertainties associated with high cloud forcing and its consequences for climate uncertainty. This study therefore shows how spatially coincident "co-located" A-train data can be used to refine estimates of cloud radiative properties. The Clouds and the Earth's Radiant Energy System (CERES) instrument onboard the Aqua satellite platform offers highly stable and accurate radiation budget data (Smith & Wielicki 2004, Wielicki et al. 1996). The findings will assist the climate community in identifying the main sources of error in calculations of OLR in the presence of tropical high clouds.

A method is first described in Section 6.2 that identifies two high cloud scene-types using previously identified features in the Version 2.2x MLS Ice Water Content (IWC) data and ECMWF ERA-Interim Liquid Water Content (LWC). Section 6.3 then presents an analysis of co-located OLR within tropical convective plume and a prototype anvil scene-type using low latitude measurements. The OLR variability is examined in each scene that is supported by direct observations to calculate estimates of the LW CRF. The second part of the analysis in Section 6.4 then explores the attribution of differences in LW radiative cooling and its relative sensitivity to ice clouds and water vapour in the mid- to upper troposphere. The final conclusions are then summarised in Section 6.5, where the validity and implication of the proto-anvil cloud detection scheme is evaluated.

There are several purposes of this study: (a) to produce valid estimates of the cloudy-sky greenhouse effect under different conditions, (b) to explore possible discrepancies in CRF estimates from MLS and CERES and the implication of these uncertainties for climate prediction, (c) to make suggestions of the main limitations in instrumentation and atmospheric measurements that must be overcome to further refine these estimates. This study also addresses the key questions: Can the MLS instrument detect any discernible features that characterise the properties of anvil outflow cirrus and its respective LW CRF? How can coincident A-train measurements help to refine and characterise high clouds radiative properties?

6.2 Methodology

The study in this chapter investigates the radiative properties of high cloud scenes between the extended low-latitude bounds of 35°S and 35°N on 19th September 2004, representing 57.4 % of the total Earth's surface. The Single Scanner Footprint data product (FM3) is used in this study to provide direct observational evidence of how high clouds affect the OLR. At the same locations OLR is also simulated using the Atmospheric and Environmental Research (AER) Rapid Radiative Transfer Model (RRTM) with input of coincident MLS ice clouds and greenhouse gases, and European Center for Medium-range Weather Forecasts (ECMWF) Re-Analysis (ERA) Interim data. Further details about the choice of radiative transfer model can be found in Chapter 2. The data was prepared and input into the AER RRTM_LW using the same methods described in Chapter 5 to simulate the OLR.

Convective profiles with anvil cirrus were identified by a high cloud scene detection algorithm detailed in Section 6.2.1. Data from three different low latitude scene types were investigated that comprise: (a) deep convective profiles; (b) their adjacent outflow clouds located at an MLS profile either side; (c) a reference scene referred to as the "background" that consists of all other profiles not detected by (a) or (b). For cloud radiative forcing calculations this reference scene is more specifically defined as a cloud-cleared background scene. This is the RRTM_LW simulated OLR in scene (c) with all cloudy-sky layers removed. Data that characterises scene (c) may contain scattered high clouds (detected by MLS at $p < 261\,\mathrm{hPa}$), low to middle-level clouds (reported by ECMWF at $p > 383\,\mathrm{hPa}$)

of varied optical thicknesses and an intermediate layer of mixed-phase cloud.

Features in the simulated OLR data in these conditions was validated against coincident observations of OLR from CERES, and was modelling using MLS and ECMWF data. A schematic of a region of deep convection and neighbouring anvil outflow region is indicated by Figure 33, where $7 < k < 13$ indicates the pressure index levels at 12 per decade where MLS IWC is reported and fed into the Atmospheric and Environmental Research (AER) Rapid-Radiative Transfer Model (RRTM) code to simulate OLR. The lower troposphere is indicated by $0 < k < 5$, where co-located ECMWF ERA-Interim LWC data (downscaled to a $100\,\mathrm{km} \times 100\,\mathrm{km}$ grid) is input in the model at the same pressure levels. There are a total of 15 model layers, which are indicated by the letters (m) on Figure 33. Calculations of atmospheric density, temperature, atmospheric path-length and cloud water path calculations are reported for each of these layers. Intermediate levels ($5 < k < 7$), shaded in grey, indicate the mixed phase layer where a combination of ECMWF and MLS data is used to represent a 50:50 mix of liquid and ice cloud particles.

The analysis in this study is limited to a daily dataset, as large amounts of RT calculations are computationally tiresome. Calculation times are substantially reduced by using the Atmospheric and Environmental Research (AER) Rapid Radiative Transfer Model (RRTM) that is detailed in Section 5.2.2. The longwave component of the model (RRTM_LW) is used that incorporates MLS retrieved gases including WV, ozone, nitrous oxide, carbon monoxide; a well-mixed value of carbon dioxide (370 ppmv) and cloud data (MLS IWC and ECMWF LWC). Outputs of the OLR from the RT model used in this analysis were obtained using the upward flux emerging from the top of the model slab located at $p = 56\,\mathrm{hPa}$ ($k = 15$).

Measurement Uncertainties This study makes use of 1186 extended low latitude atmospheric profiles on 19th September, 2004 to undertake reliable and quantifiable estimates of the tropical high cloud radiation budget and its uncertainty in different conditions. By averaging the data over many different tropical high cloud cases, random error is reduced. To quantify the absolute accuracy, the variance (mean differences) in each identified high cloud measurement is assumed to arise from systematic bias alone. These systematic errors cannot be reduced by increasing the sample size, but do not affect the relative comparisons between

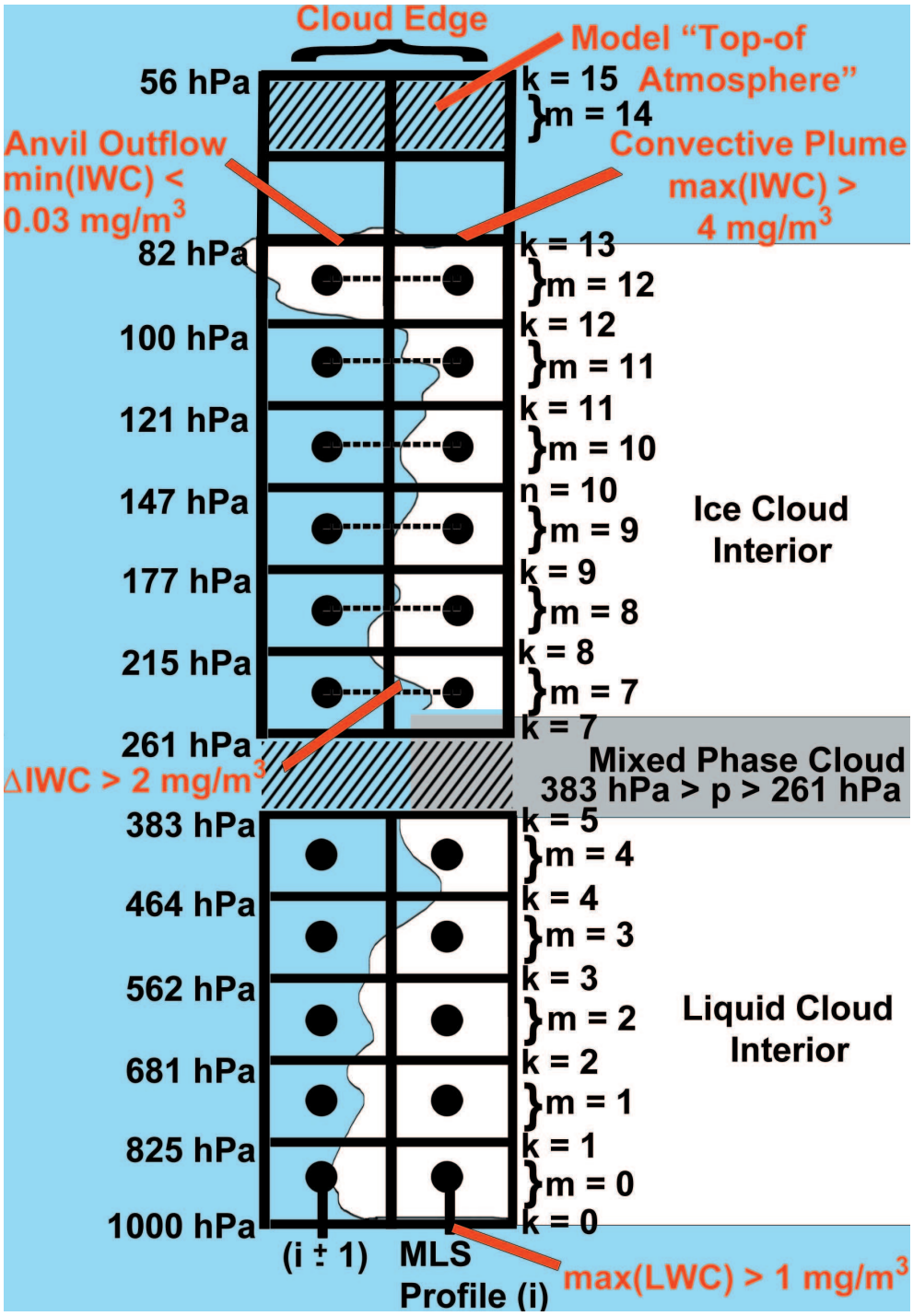

Figure 33: Schematic of a Proto-Anvil Detection Scheme and model input layers for the Atmospheric and Environmental Research (AER) Rapid Radiative Transfer Model (RRTM) using data from the MLS version 2 Ice Water Content and ECMWF ERA-Interim Liquid Water Content (LWC) products. Points marked i and $i \pm 1$ indicate an MLS profile located at the edge of a tropical plume poleward of 35°. The white area shows the interior of the convective cloud, whilst the grey region indicates the mixed-phased component of the cloud that is not well specified by measurement data. The black circles indicate the centre of a model layer (m); whilst n indicates the model levels used in the AER RRTM_LW radiative transfer simulations. Dashed horizontal lines indicate a gradient between two adjacent MLS profiles.

different scene-types.

The relative uncertainty in CERES OLR is reported as the standard deviation of all the individual measurement data at a MLS sensor footprint location i and is denoted $\epsilon(F^{+}_{\mathrm{obs}})$. Smaller errors of up to $8\,\mathrm{W\,m^{-2}}$ ($\sim 1\,\%$) in F^{+}_{obs} arise for the clear-sky ocean due to the CERES Single-Scanner Footprint (SSF) Angular Distribution Model (ADM) described in Section 2.3.2. Similar uncertainty exists in the modelled OLR data. The reported error ($\epsilon(F^{+}_{\mathrm{mod}})$) indicates the simulated output when $IWC[i] \pm 1\sigma[IWC[i]]$ values are fed into the AER RRTM_LW model. The respective IWC precisions of the version 2.2x Ice Water Content (IWC) were obtained from Livesey et al. (2007). Meanwhile, MLS uncertainties arise from small spatial misplacement of ice clouds in the vertical and horizontal and from errors in MLS ice water content (IWC) detection. The relative magnitude of measurement errors in different atmospheric conditions is discussed earlier in Section 5.3.1.

Oceanic measurements were used in this study due to the high variability in OLR over land surfaces due to a diurnal cycle, contrasting land-sea temperature gradients, non-uniform surface emission from differences in land surface type and striking differences in the sensible and latent heat fluxes. A diurnal cycle in solar radiation and clouds still exists however, since A-train measurements are consistently undertaken during the early afternoon and night-time local times as described in Section 2.3.

Each selected high cloud scene was flagged according to whether the postulated anvil-outflow cirrus was viewed behind or ahead of an adjacent convective ice profile with respect to the MLS viewing geometry presented by Figure 3 (Chapter 2). The ratio of these high clouds that were detected in the near and far-view were analysed by routinely counting the instances of each. Where convective plumes were identified by the proto-anvil detection scheme at a consecutive profile position $i + 1$ and outflow cirrus at index position i the outflow is in the near-view (behind in both space and observing time). The converse is true for the $i - 1$ case when the plume appears in the profile proceeding the outflow cirrus. The data shows that anvil outflow scenes are most frequently detected in the far-view of MLS (120 cases) then in the near-view (113), indicating a significant shadowing effect in the MLS retrieved radiances. The consequence is a general low IWC bias in the MLS data when thin cirrus is viewed behind thick icy plumes, which would also lead to a falsely low sensitivity of upper troposphere

ice concentration to OLR suppression.

6.2.1 Description of a Proto-Anvil Detection Scheme

Extensive analysis of measurement data in Chapter 5 reveal how atmospheric measurements coincide with tropical convection and indicates several identifiable features of high clouds. A detection scheme to identify deep convective and anvil outflow high clouds is described here based on this analysis and is referred to as a proto-anvil detection scheme. A detection scheme such as this has implications for climate science, since it allows us to report the radiative properties of different high cloud types including the poorly understood anvil outflows. The detection scheme is based on characteristics in the mid to upper tropospheric MLS (Aura) Ice Water Content (IWC) and co-located lower troposphere Liquid Water Content (LWC) data from the European Center for Medium-range Weather Forecast (ECMWF) Re-Analysis (ERA) Interim data product. Much of the emphasis is on the version 2.2x MLS cloud ice water content (IWC) product, which provides the most valuable insight into the interior of tropical convection at both high vertical resolution and precision. The MLS IWC product demonstrates good inter-satellite consistency with CloudSat IWC (Wu et al. 2008, 2009), whilst earlier studies in Chapters 3 and 4 demonstrate that A-train MLS high cloud distributions and heights are also broadly consistent with both the Moderate-resolution Imaging Spectroradiometer (MODIS) cloud-top pressures and the spatial distribution of OLR suppression observed at the same locations by CERES (Aqua).

The main features of intense and deep tropical free-convection are plumes of ice cloud that tower above liquid clouds over a broad 500 km to 1000 km area of the extended low latitudes. Whilst these large-scale tropical systems are characteristic of Mesoscale Convective Systems (MCSs); each of these contains a smaller sub-structure of isolated cumulonimbus plumes that frequently extend to the Tropical Tropopause Layer (TTL). The detection scheme described in Section 6.2.1 identifies discontinuous ice clouds adjacent to deep convection where Figure 23 (Chapter 5) indicates that outflow cirrus is typically found. Anvil outflow cirrus, defined outward swept ice crystals, is an inherent feature of overshooting free convection that penetrates into the TTL or lower stratosphere. The proto-anvil high cloud detection scheme combines more than one independent measurement feature to reinforce a consistent picture of these deep tropical plumes.

The key features of deep tropical convection with anvil outflow cirrus are annotated by Figure 33 at neighbouring MLS profile indices of $i \pm 1$ and i. The proto-anvil scheme first identifies a MSC with mature cumulonimbus plumes identified in Chapter 5. These are characterised by a high ice particle density with a maximum value of $IWC > 4\,\mathrm{mg\,m^{-3}}$ in the upper-troposphere ($261\,\mathrm{hPa} > p > 82\,\mathrm{hPa}$) according to the MLS v2.2x data product. To ensure that these high clouds are located at the edge of a plume, where anvil outflows may be found at an adjacent MLS position, a maximum horizontal gradient ($|IWC[i \pm 1] - IWC[i]|$) of $2\,\mathrm{mg\,m^{-3}}$ must be detected at any reported pressure level. At the position of the largest gradient (the most well defined cloud-edge) the minimum IWC must also be less than $0.03\,\mathrm{mg\,m^{-3}}$, indicating that no ice clouds are present below the tropical tropopause layer (TTL ($p < 150\,\mathrm{hPa}$) according to the precision of Livesey et al. (2007). This condition must be true, since anvil outflows occur outside of the free upper-tropospheric convection and could not be stable within due to strong up-drafts. To confirm that the ice clouds are associated with a deep plume that extends throughout the atmosphere, the data must also satisfy the condition $LWC[i] > 1\,\mathrm{mg\,m^{-3}}$. This critical value represents the minimum LWC where previous analysis in Chapter 5 shows deep convection takes place with confidence.

The proto-anvil detection process does not make use of OLR observations, since any information about its variability in the presence of high clouds would unnecessarily bias the calculations of radiative forcing. Instead a hypothesis is made, supported by observation data in Chapter 5 that states: for successful detection of anvil-outflow cirrus, the average magnitude of OLR suppression relative to the clear-sky atmosphere must be less than for the convective scene-type. There are two structural features of convective clouds which also support this view: Firstly, convective plumes and their neighbouring anvil outflows are characterised by similar cloud top pressures due to quasi-horizontal detrainment of ice particles. Secondly, a larger portion of longwave (LW) emission is transmitted from the surface and low level clouds for anvil outflow scene types, since warm convection within the plumes are associated with a thick and deep column of cloudy-sky.

The maximum IWC threshold value is deemed sufficiently large to identify the majority of tropical storms with anvil outflows, although the scheme cannot detect all cases due to limitations in the definition of each scene-type. The scheme

best detects the edges of larger scale tropical plumes, with a horizontal length that scales closely with the MLS along-track field of view (150 km to 300 km) i.e. with the anvil displaced at exactly one MLS profile aside. Whilst this seems like a crude detection method, it is likely that anvil outflow profiles identified contain many of the distinguishable features of thin cirrus emanating from the plumes. It is also likely that tropical plumes contain many of the features of deep convection that extends into the TTL. The proto-anvil detection scheme can therefore be used to generalise about the bulk properties and longwave radiative properties in the different conditions of these tropical scene-types.

6.2.2 Pre-Assessment of CERES and MLS Spatial Consistency

For each MLS sensor footprint many off-nadir CERES measurements of OLR are undertaken within the same area. To make valid comparisons, MLS and CERES high cloud data footprints must be first made spatially equivalent to resolve features of the same scale. As each MLS product used in this analysis is based on received radiances at different viewing frequencies and also depends on the scene-type, such that a spatially consistent footprint dimension is unknown. To test the consistency between correlative A-train measurements ten evenly spaced along-track distances were selected to spatially average CERES data. The chosen intervals are centred around the version 2 MLS Ice Water Content (IWC) along-track field-of-view at $p = 261\,\mathrm{hPa}$ presented by Livesey et al. (2007), since earlier studies indicate that IWC accounts for much of the observed large-scale reductions in tropical OLR. Each limb-scan of MLS occupies an along-track range of y in either direction about a central tangent point at index point i, where the retrieved signal is closest to the Earth's surface.

Pre-analysis of CERES OLR for spatial consistency with MLS was achieved by averaging data from $y = 25\,\mathrm{km}$ to $250\,\mathrm{km}$ at intervals of $25\,\mathrm{km}$. Processed CERES OLR data ($F^{+}_{\mathrm{obs}}[i]$) was then compared to a simulated OLR value (F^{+}_{mod}). The data revealed that a $y = 150\,\mathrm{km}$ threshold was most suitable, reporting the smallest mean model-observation difference in OLR of $+0.8\,\mathrm{W\,m^{-2}}$ and a root-mean-square error (RMSE) of $23.1\,\mathrm{W\,m^{-2}}$ for convective plume and anvil scene-types. A processed OLR dataset was then produced that is broadly equivalent to MLS (i.e. $F^{+}_{\mathrm{obs}}[i]$). Further details of the general co-location process can be found in Chapter 3.

6.2.3 Reporting Atmospheric Properties in the Presence of High Clouds

Ice water paths (IWPs) and water vapour paths (WVPs) were calculated for each profile within the selected scene types through the depth of any ice cloud layer, as in Equation 16 in Chapter 5. The vertical ice-cloud thickness was calculated for modelled layers from $m = 7$ to 14, as indicated by Figure 33 annotations, assuming a zero layer thickness where no ice was present. WVP calculations are based on the same model layers are used as for the IWP calculations, so path-length increases with the ice cloud thickness.

Cloud Water Path (CWP) values were used to assess the relative effect of WV and clouds on the LW CRFs within profiles of the two scene types. Values of the IWP and WVP are useful in characterising the high cloud scene types, since in a given profile they both exhibit a near linear proportionality to OLR and logarithmic relationship to optical depth (Allan et al. 1999, Heymsfield et al. 2003).

6.2.4 Calculating the Longwave High Cloud Radiative Forcing

Calculations of the longwave CRF are important for validating Global Climate Models (GCMs), which currently reported wildly different sensitivities to clouds (Williams & Webb 2009, Solomon et al. 2007). A method is discussed here to calculate the longwave CRF (C_{LW}) using simulations and measurements of the top-of-atmosphere (ToA) longwave radiation budget, known as the Outgoing Longwave Radiation (OLR). Whilst the clear-sky ToA radiation budget can be estimated reasonably well using OLR data, a latitude constraint is imposed upon this analysis to limit RT computation time. This makes the all-sky RB an unsuitable choice for comparison, especially as any other estimate would need to consider the seasonal and inter-decadal variability for the chosen period of study. This calculation is not necessary however, since CRFs from the high clouds in this study are not evenly distributed across the globe. Analysis in Chapter 4 indicates that few large-scale high clouds are outside the subtropical band that defines the transition from the tropics to extra-tropics.

In this chapter, a spatial mean OLR value is calculated in the absence of tropical ice clouds and is used as a suitable "background" (or reference) scene reference ($F^{+}_{\mathrm{background}}$). By subtraction of the mean OLR over a specified high

cloud scene (F^{+}_{cloudy}) a single LW CRF value for C_{LW} is produced as indicated by Equation 18. Since high clouds reduce the OLR, a component that acts to warm the planet, LW CRFs are almost exclusively positive. MLS profiles are first used to diagnose different high cloud scene types, so estimates of the LW CRF (C_{LW}) can then be undertaken using coincident CERES (Aqua) measurements. Similarities in the simulation of CRF are then reinforced from the co-located measurement data, whilst highlighting uncertainties in representing high clouds in global circulation models. Whilst the AER RRTM calculations have already been shown to be broadly consistent with measurements (Section 5.3.1), a large quantity of direct observational evidence is needed to validate these simulations.

$$C_{\text{LW}} = F^{+}_{\text{background}} - F^{+}_{\text{cloudy}} \tag{18}$$

In Equation 18 F^{+} in $\text{W}\,\text{m}^{-2}$ is the simulated or measured OLR in $\text{W}\,\text{m}^{-2}$ averaged over all the profiles of a specified scene type. Rather than past studies that base calculations on the all-sky OLR, a near-equivalent reference scene is represented by the surrounding profiles in the low latitudes equatorward of 35°.

The definition of the cloudy and clear-sky scenes for LW CRF calculations differs slightly from Solomon et al. (2007). The adapted calculation was undertaken on the assumption that clear-sky OLR values can only be accurately calculated in the absence of thick ice clouds, owing to the unreliable MLS gas retrievals in their presence. In addition, only high clouds are well monitored by MLS with a much poorer specification about clouds in the low to mid-troposphere by the ECMWF. This means no truly clear-sky scene can be determined, rather the remaining scene that consists of all co-located data where the atmosphere is likely to be free of ice clouds. Later analysis in Section 6.3.1 describes how a reference scene is emulated to provide an estimate of the OLR. This is achieved by a process of cloud-clearing, whereby the AER RRTM_LW cloudy sky input layers are set to zero.

The shortwave (SW) component of the CRF is neglected, as this is subject to high uncertainties from the complex single-scattering properties of ice clouds and any resident aerosols. The reflected SW component of the Earth's RB exhibits a strong diurnal and seasonal variability, as unlike the longwave component the upwelling shortwave irradiance is dependent on both the zenith angle and the Earth's position in its orbit with respect to the Sun. The SW CRF is therefore particularly difficult to monitor with instruments onboard the same

Sun-synchronous polar orbits due to their fixed ascending and descending local equator-crossing times. Sensed data from several different polar or geostationary orbits must therefore be combined to provide realistic estimates of the shortwave CRF. In addition, measurements are particularly prone to variability in surface albedo and Ocean sunglint issues that deem some data unsuitable.

LW CRF calculations in the following analysis are valid only for chosen period on 19th September, 2004 due to variability in cloud coverage and properties up to decadal time-scales. Future analysis will assess whether it is justified to expand the sampling period, at the expense of extensive computational time.

Global Cloud Radiative Forcing Currently it is not seen as scientifically sound to expand the LW CRF analysis to a global mean forcing, due to large uncertainties in the fractional coverage of each high cloud scene-type. Whilst these calculations could be achieved by applying a factor to scale the regional forcing to a global unit area, this is based on several assumptions. The main assumption in the global LW CRF calculations is that no large-scale cumulonimbus scenes are detected by the MLS poleward of 35°. In addition, the regional to global up-scaling of the analysis assumes that the effect of high clouds on the OLR is only felt on local to regional spatial scales. The method is therefore only valid if tropical high clouds have no de-localised impact on the clear-sky OLR in the extra-tropics. This is because tropical clouds feedback upon both the poleward export of heat and moisture by altering the global circulation patterns. The hydrological cycle is also perturbed by tropical weather, specifically by enhancements in the lower stratosphere and upper tropospheric water vapour and the seemingly related impact on ozone depletion as discussed in Chapter 5. Studies by Lindzen et al. (2001) also imply that the character of tropical high clouds may be intrinsically linked to the surrounding clear-sky radiation budget by a radiative feedback process.

6.3 Direct Comparison of Simulated Outgoing Longwave Radiation with Observations

This analysis explores the contrasts in OLR between two high cloud scenes that are selected by the cloud-scene detection algorithm described in Section 6.2.1. Specifically, deep convective plumes are defined by thick ice

plumes ($\max(IWC) > 4\,\mathrm{mg\,m^{-3}}$) and underlying liquid clouds ($\max(LWC) > 1\,\mathrm{mg\,m^{-3}}$) as indicated by Figure 33. Thinner ice clouds are identified adjacent to these plume, with a vertically discontinuous ice column, defined by $\min(IWC) < 0.03\,\mathrm{mg\,m^{-3}}$. These are referred to as the anvil outflow scene-type. The remaining scene-type forms a reference for LW CRF calculations and is known as the "background-scene".

AER RRTM_LW simulations (modelled OLR) show estimates of how the rate of longwave cooling to space, whilst spatially coincident CERES measurements (observed OLR) provide a direct verification of features in the modelled output. The main sources of measurement error in these calculations are discussed in Section 6.2. Firstly the selection of a suitable background scene is discussed and the justification for its cloud-clearing to provide a more reliable and long-term record of the clear-sky OLR.

6.3.1 Characterisation of a Reference Scene for Cloud Radiative Forcing Calculations

A background scene is first analysed that consists of all non-convective profiles in the latitude bound $35\,\mathrm{S} < \phi < 35\,\mathrm{N}$ on 19th September 2004, defined as scene (c) in Section 6.2. The background data comprises 1186 MLS profiles and is plotted by Figure 34. Notably, the extended low latitude OLR is more spatially uniform owing to the absence of thick high clouds. The scene is characterised by a minimum of 250 over the Asian sub-tropics attributed to the thick low clouds of the monsoon and a maximum of $300\,\mathrm{W\,m^{-2}}$ over the clear-sky tropical Ocean. These clouds are apparent in Figure 24 (Chapter 5) as suppressions in the OLR in the proximity of the A-train ground-track. Despite this, the OLR of this background scene is likely to lack long term reliability due to covariance between water vapour and remnants of tropical convection that are not identified by the proto-anvil detection scheme. In support of this view, John et al. (2011) describes a dry bias in calculations of the UT humidity in the low latitudes with the exclusion of convective zones. The study indicates dry anomalies of up to $-30\,\%$ in the calculated UT RH data that coincides with periods of widespread tropical convection.

Ideally a clear-sky reference scene that is representative of the entire analysis region is required to calculate the CRF. This can be achieved by cloud-clearing, whereby the modelled OLR is generated with all cloudy-sky layers set to zero.

This is problematic for several reasons; mainly because cloud-clearing thick layers of ice and liquid water requires a detailed knowledge of cloud properties. Any false detection of ice clouds by the MLS in clear-sky conditions can produce by large uncertainties and bias in the local simulation of OLR. Secondly, greenhouse gas retrievals by MLS in thick cloud are often inaccurate. In particular, for this study reliable simulations of convective OLR by the AER RRTM_LW code depend critically on UT water vapour retrievals. The model output is therefore adversely impacted by the erratic behaviour of the Version 2 MLS water vapour product, as reported by Livesey et al. (2007). A more consistent reference scene and therefore reliable CRF estimates are instead achieved by cloud-clearing the background scene (c) where only thin ice clouds and low altitude liquid clouds are present. As a result, much more reliable MLS gas retrievals are found that ensure a valid cloud-clearing process. As expected the cloud cleared values (on the x-axis) indicate higher OLR when both ice and liquid clouds are removed from the model, noticeably with some consistency from 210 to 330 $\mathrm{W\,m^{-2}}$ (with cloud), to 240 to 350 $\mathrm{W\,m^{-2}}$ (cloud cleared). The data therefore implies a 28 $\pm$ 22 $\mathrm{W\,m^{-2}}$ longwave forcing (C_{LW}(background)) from liquid and thin ice clouds in scenes identified as non-convective.

A spatially uniform rate of longwave radiative cooling (OLR) is indicated by a weighted best fit slope of near unity (1.07) between the cloud-cleared and cloudy-sky simulations. The data therefore indicates a bank of low clouds across ice-cloud free areas that are largely independent of the regional and latitudinal variability in surface temperature. This is implicit of a near-constant cloud-top brightness temperature for low clouds in the extended low latitudes, seemingly independent of regional variability in surface and atmospheric conditions. The data indicates that low clouds are therefore much easier to account for in future climate change predictions, rather than high clouds whose cloud-top temperatures vary wildly from location to location. These low clouds exert a rather uniform reduction in the rate of longwave radiative cooling.

The most noticeable feature from Figure 34 is a region at the lower tail of the correlative data with RT simulations of OLR including cloud layers of 110 $\mathrm{W\,m^{-2}}$ compared to correlated cloud-cleared OLR values of $\sim$ 240 $\mathrm{W\,m^{-2}}$. This implies that relatively small numbers of background scene profiles present a relatively strong positive cloud forcing. These profiles are likely to be found over the northerly extent of the Asia Monsoon clouds, as indicated by Figure 24 (Chap-

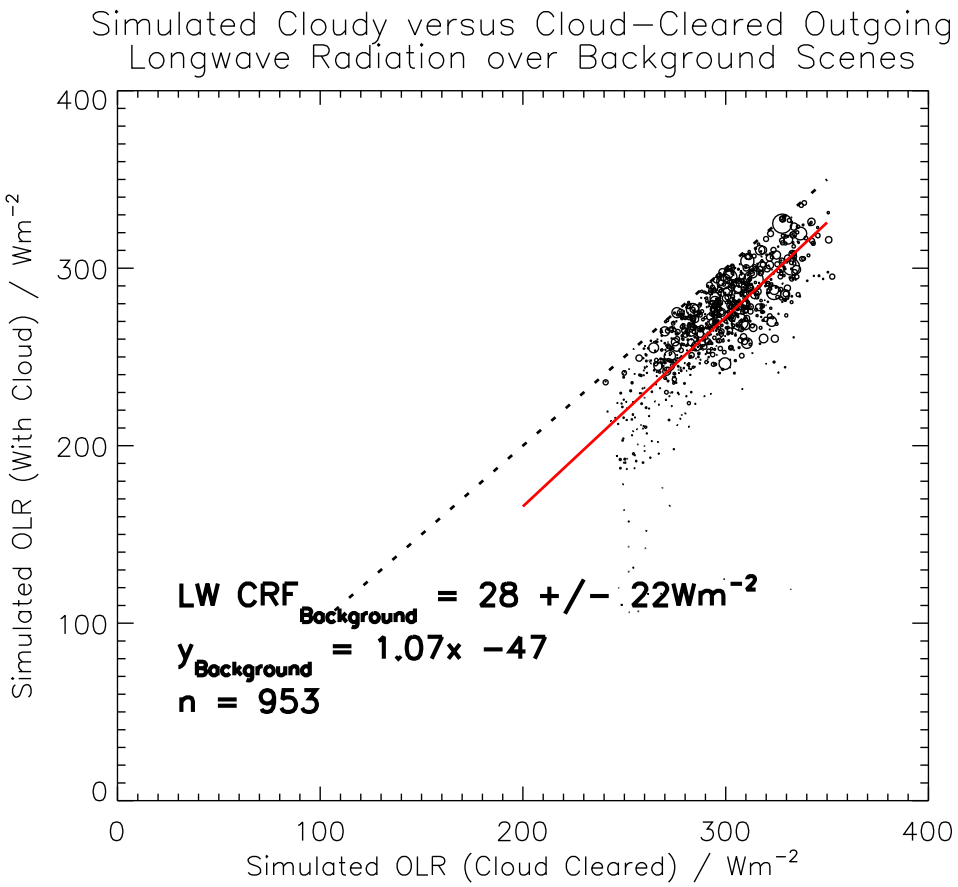

Figure 34: Correlation between the reference "background scene" Outgoing Longwave Radiation (OLR) with both liquid and ice water clouds included (with cloud) against OLR simulated for the same profiles with all cloud layers set to zero (cloud cleared). Both background scenes indicate the Outgoing Longwave Radiation (OLR) simulated by the AER RRTM_LW, using the Version 2 MLS data products: O_3, CH_4, N_2O, Water Vapour, Temperature and Ice Water Content. Additional ECMWF ERA-Interim Liquid Water Content data is input at $p > 316$ and a well-mixed CO_2 concentration of 370 ppmv. The analysis indicates the longwave Cloud Radiative Forcing (LW $CRF_{\text{background}}$) as the mean difference of OLR (with cloud) minus OLR (cloud cleared) equatorward of 35° on 19th September 2004. The background is defined as the remaining MLS sensor locations where no convective plume and anvil outflow detections are found by a proto-anvil detection scheme. The solid red line indicates the best fit of the data.

ter 5), or over the American sub-tropics where thick mid-latitude liquid clouds are most frequently found. Since the specification of these clouds by the ECMWF ERA-Interim product are poorer than ice clouds detected by MLS and are not well spatially co-located, cloud-clearing calculations at these locations are likely to produce greater uncertainty in the description of the reference scene OLR.

6.3.2 Longwave Component of the High Cloud Radiative Forcing

The correlation of OLR simulations in the "convective plume" and "anvil outflow" scene-types with observation were analysed. These were then referenced against the background scene using the cloud-cleared data described in Section 6.3.1 to provide an indication to the LW CRF. The remaining 32 % of the extended low latitudes consisting of 466 profiles, as specified by the method in Section 6.2.1, with an equal sample size of the convective plume and adjacent anvil outflow scene-types. As the observations cannot be cloud-cleared, the cloudy-sky background scene data is shown by the grey circles on Figure 35). Notably, the simulated cloudy-sky background data demonstrate excellent consistency with CERES OLR measurements. Observations and the model both report a mean OLR of 260 $\mathrm{W\,m^{-2}}$, with an expected error of just 10 $\mathrm{W\,m^{-2}}$.

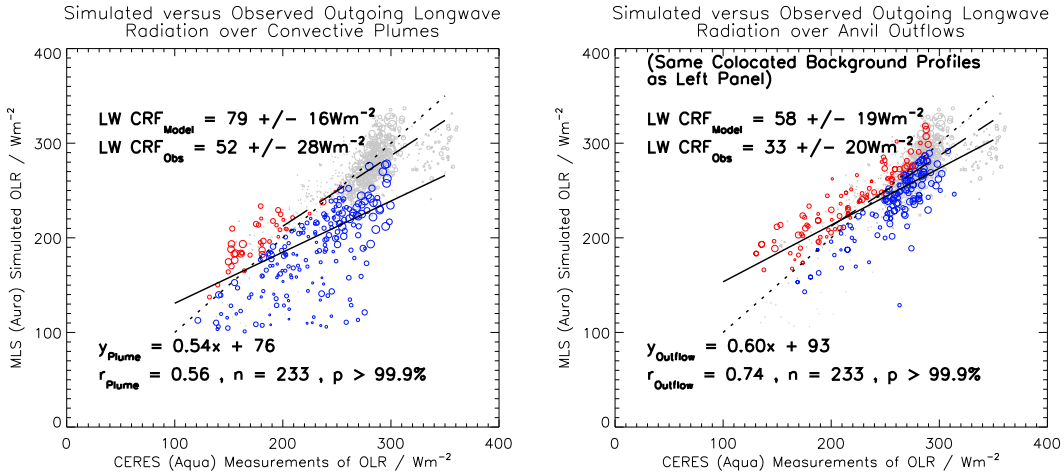

Figure 35: Comparisons between CERES (Aqua) Outgoing Longwave Radiation (OLR) measurement data (F^{+}_{obs}), versus AER RRTM_LW simulated OLR (F^{+}_{mod}) using co-located MLS and ECMWF data. The analysis uses data from 19th September 2004 equator-ward of 35°. *Panels: (left) Correlative data for convective plume scenes; (right) adjacent anvil outflow cirrus. Both scene-types were identified using the proto-anvil detection scheme described in Section 6.2.1. The short dashed black lines show the expected correlation between the two data. The grey open circles and long-dashed line of bet fit refer to the remaining "background" co-located profiles in the low latitudes. Red and blue correlative data points indicate where the RRTM simulates OLR values that are higher and lower than the measurements respectively. The area of each circular point is inversely proportional to a the combined error:* $1/\left(\sigma\left(F^{+}_{\mathrm{obs}}\right)^{2} + \sigma\left(F^{+}_{\mathrm{mod}}\right)^{2}\right)$ *in the region* $i \pm 1$, *where* i *is the MLS index position of a convective plume identified by a proto-anvil detection scheme.*

The strength of the fit and point-to-point variability in the OLR correlative data for is shown by the offset of the solid lines from unity and scatter about

the line of equivalence respectively on Figure 35. AER RRTM_LW simulations demonstrate that in general the rate of longwave cooling to space is broadly consistent with spatially coincident observations, giving rise to a positive covariance. Whilst it is worth noting that individual measurement point error ($F^{+}_{mod} - F^{+}_{\mathrm{obs}}$ bias) is as high as $180\,\mathrm{W\,m^{-2}}$, indicating a high level of uncertainty in this relationship. The data indicates that spatial variability in the mid- to upper tropospheric measurement data, where high quality MLS measurements are fed into the RT model, is accountable for much of the relative magnitude of the observed OLR. Figure 35 shows a positive relationship between high cloud and OLR in the plume scene, with the underlying points in grey representative of the background scene (all other low latitude scene-types).

Figure 35 also indicates the OLR mean difference (background - cloud) local mean CRF in the conditions of the two convective scene-types. By comparing the consistency of the modelled and measured, it is possible to estimate the errors associated with CRF in the conditions associated with thick ice plumes and thinner adjacent cirrus. The key finding is that OLR modelling in the convective plume ($r_{\mathrm{plume}} = 0.56$) region is much worse than for the adjacent thin ice cloud data identified as the anvil outflow ($r_{\mathrm{outflow}} = 0.74$). For each scene-type equal sized datasets and equivalently sized measurement footprints were used, so there are no differences in scene sampling that could be responsible for this observed difference.

Figure 35 also highlights, by direct observational data, areas of potential weakness in radiative transfer simulations and the validity of its input fed from MLS retrieved atmospheric composition in tropical atmospheres. Notably, the convective plume scene data consists of co-located profiles where simulations reveal a much colder cloud-top brightness temperature (large OLR suppression) with respect to direct CERES OLR measurements. This cold model bias is indicated by the large offset of 100 to $200\,\mathrm{W\,m^{-2}}$ of the blue circles on left-hand plot of Figure 35 from the short-dashed line. Further indications of a high altitude bias in estimated cloud-tops from MLS (of $\Delta\,P \sim 100\,\mathrm{hPa}$) are noted from inter-comparisons with MODIS (Aqua) cloud-top pressure data, presented in Chapter 3 (Figure 12). In spite of these uncertainties, the data are in general agreement of a strongly positive LW CRF in regions of thick tropical ice clouds, with observed ($C_{\mathrm{LW}}(\mathrm{obs})$) and measured ($C_{\mathrm{LW}}(\mathrm{mod})$) of $52 \pm 16\,\mathrm{W\,m^{-2}}$ and $79 \pm 28\,\mathrm{W\,m^{-2}}$ respectively and are therefore broadly consistent. The main uncertainty in cloudy-sky measurements

arises from the poor horizontal sampling of MLS, with a large spatial variability in OLR measurements from CERES that comprise the spatially equivalent co-located data.

In contrast, the thinner ice clouds of that represent some of the properties of an "anvil-outflow" indicate a lower relative local LW CRFs, as expected. The observations and modelled LW CRFs are in general agreement that that thinner ice clouds are responsible for a significant (but less strong) longwave radiative warming of the Earth's atmosphere, with respective values of $C_{\mathrm{LW}}(\mathrm{obs}) = 33 \pm 20\,\mathrm{W\,m^{-2}}$ and $C_{\mathrm{LW}}(\mathrm{mod}) = 58 \pm 18\,\mathrm{W\,m^{-2}}$. The relative magnitude of the difference and uncertainties of each indicate a large error in the simulation of local high cloud CRFs in the order of 60 % of the absolute mean. This is mainly due to the coarse horizontal field-of-view of MLS, which cannot resolve the isolated plumes of ice water content associated with convection. Notably, in spite of the view that thin cirrus is poorly represented in Global Circulation Models e.g. Lohmann & Roeckner (1995), Solomon et al. (2007), the more spatially uniform nature of cloud-top pressures for stratified layers of high clouds enables us to report lower uncertainties in the measured OLR data that produces a much clearer positive relationship with the simulations.

The gradient of the error-weighted fit for this high cloud scene-type of $r_{\mathrm{outflow}} = 0.74$ and its function indicates a slight overestimate of OLR reduction where thinner ice cloud is present (at higher OLR values). This apparent effect is relatively larger in the convective plume data than for anvil outflow cirrus. In contrast, for thicker ice clouds of the anvil outflow, a notable warm-biased OLR is presented by the model indicating that the OLR suppression induced by ice clouds is underestimated. The effect may be due to a dry-bias in the water vapour data in the presence of thick cloud. This finding is supported by the apparent stratosphere-troposphere exchange (dry-slot) in the Version 2 MLS measurement data Chapter 5 (Figure 28).

6.3.3 Evaluation of the Longwave High Cloud Radiative Forcing

The co-location procedure used to convolve the CERES (Aqua) SSF OLR data to MLS uses an along-track averaging distance of $\pm\,150\,\mathrm{km}$. The coincident OLR data with these MLS sensor footprints are therefore sensitive to clouds of a similar horizontal length-scale. If the length-scale of isolated convective plumes is much shorter than the MLS along-track field-of-view, the sensitivity of simu-

lated OLR to MLS IWC concentration is overestimated. Since scattered tropical cirrus is more common at higher altitude the correlative data corresponding to these profiles may present themselves as an apparent as a cold model bias for low OLR suppressions, characterised by CERES OLR measurement of 100 to 200 $\mathrm{W\,m^{-2}}$. In contrast, lower altitude ice cloud is more prevalent (characterised by the densely populated correlative data points of 200 to 300 $\mathrm{W\,m^{-2}}$ and occupy a much broader horizontal length-scale, so the modelled OLR is more closely consistent with measurements.

The smaller correlative measurement points of Figures 34 and 35 indicate a high magnitude of combined modelled and observed OLR measurement error. The poorer consistency for these measurements may reflect the presence of scattered high clouds. These are most noticeable in the cold-biased simulated OLR data for the convective plumes of Figure 35. Past studies in Chapter 4 also indicate that scattered clouds are often less well represented than uniform clouds due to the poor along-track resolution associated with the limb-viewing geometry of MLS.

Many gaseous MLS retrievals are adversely affected by the presence of cloud and so are not recognised as valid inputs by the AER RRTM_LW. The result can be that the RRTM is not able to calculate the OLR for a particular profile and instead reports data from the previous successful calculation. Precautions were made so these model "out-of bound" events were restricted by applying minimum concentration values to the water vapour and IWC data to correctly simulate the parameterised optical properties of ice clouds. Other sources of error arise from the simulation of OLR by the AER RRTM_LW, which are detailed further in Section 6.4.4.

The convective plume LW CRF cannot be realistically expanded into a global CRF, since the percentage coverage of each high cloud type is not well defined. The results instead indicate the relative effects under two strikingly different tropical ice cloud conditions where LW CRF (C_{LW}) values are typically 30 to 40 % lower in the presence of anvil outflow clouds than for neighbouring convective plumes.

6.4 Sensitivity of Cloud Radiative Forcing to Upper Tropospheric Ice and Water Vapour

The response of high cloud parameters to future change temperature change is a cornerstone in the climate debate (Solomon et al. 2007, Chapter 1). In particular, cloud ice and upper troposphere water vapour (UT WV) exert the largest impact on the rate of longwave cooling in the tropical atmosphere. The sensitivity of the Earth's radiation budget to these parameters depends upon the atmospheric conditions in which high clouds are formed. In this study "Bulk analysis" was undertaken using data from the same proto-anvil and convective plume data as analysis in Section 6.3.2. An indication is given to the pressure that high clouds form in each scene type, by applying a linear cloud-ice weighting for each MLS profile. In addition, the precisions of the MLS Version 2 IWC data product are examined at each reported pressure level to provide a range of sensitivities are also provided.

This study will indicate how parameters are related to the longwave CRF that will help improve future representation of high cloud within Global Climate Models (GCMs).

6.4.1 The Effect of Atmospheric Conditions on Longwave Forcing in a Convective Plume Scene

Ice Water Path and LW CRF Figure 36 shows the local LW CRFs under the conditions identified as tropical plumes, as indicated by the Δ OLR ordinate. The data shows that these thicker and deeper ice clouds are characterised by $10\,\mathrm{g\,m^{-2}} < IWP < 400\,\mathrm{g\,m^{-2}}$. LW CRFs calculated from simulations shown in Figure 36(a) present a clear linear simulated LW CRF versus $\log(IWP)$ relationship, with a confidence of 99.9 % indicated by a Pearson's correlation coefficient of $r = 0.94$. The steepness of the weighted best fit of the observed OLR contrasts on Figure 36 indicates the relative sensitivity of $\log(IWP)$ in the upper troposphere to LW CRF. The top panel Figure 36(a) shows the calculation for simulated OLR data, whilst the lower panel (b) shows the analysis at the same locations for the measured data.

The dashed best-fit lines on the left of Figure 36(a) indicates a range of Δ OLR sensitivities to IWP of 61 to $95\,\mathrm{W\,g^{-1}}$ that is broadly consistent with the simulations (b) of 86 to $113\,\mathrm{W\,g^{-1}}$. Due to the large uncertainties for single point

correlative measurements, as discussed in Section 6.3.2, it is not possible to refine the range of sensitivities reported by this data. It is however worth noting that both datasets indicate that high altitude ice clouds within tropical storms are a major contributor to the observed LW CRF.

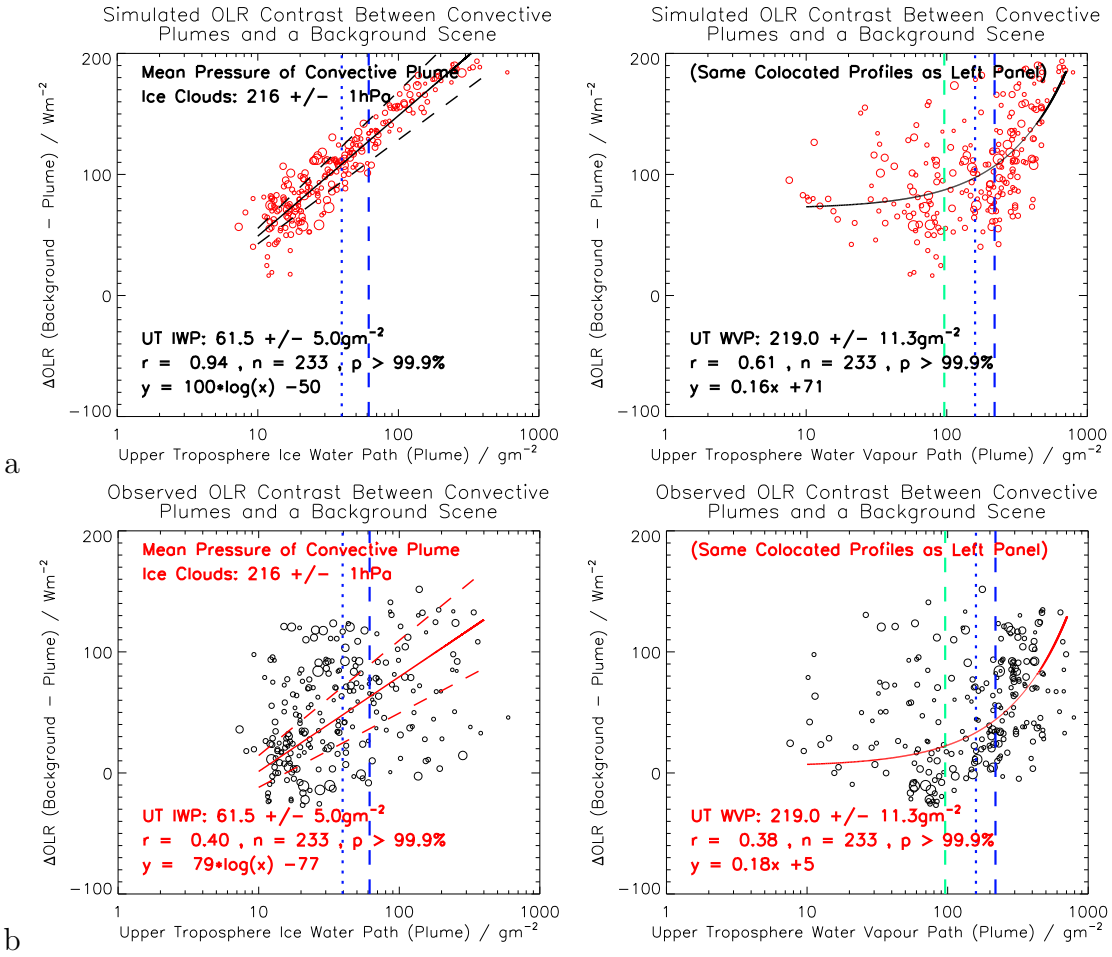

Figure 36: Correlation of Outgoing Longwave Radiation (OLR) suppression with Upper Troposphere (UT) cloud ice water path (IWP) and water vapour path (WVP). OLR difference is calculated in the same two tropical high cloud conditions as Figure 35 with reference to a simulated cloud-cleared "background" scene. Panels: (a) Simulated longwave Cloud Radiative Forcing (LW CRF) in $W\,m^{-2}$; (b) observed LW CRF at the same locations. Open circles indicate the correlative data points and are weighted by $1/\left(\sigma\left(F^{+}_{\mathrm{obs}}\right)^{2}+\sigma\left(F^{+}_{\mathrm{mod}}\right)^{2}\right)$. Red circles and the black least squares fit lines on panel (a) plots show the range of simulated contrasts in OLR using MLS (Aura) and ECMWF ERA-Interim data input into AER RRTM_LW. Black circles and red best-fits on panel (b) indicate the OLR contrast for the same locations using the CERES (Aqua) SSF data product (FM3). Left panel: Relationship of LW CRF to IWP at $261\,hPa > p > 82\,hPa$; (right) same profile data expressed in terms of WVP. The mean properties of the background, convective plume and anvil outflow scene-types are indicated by green dashed, blue dashed and dotted lines respectively.

LW CRF observation data reported in Figure 36(b) show a seemingly stochastic covariance with MLS IWP for individual high cloud cases, yet present an overall statistically significant (yet weak) positive correlation. In contrast, the modelled data for the same cloud profiles presented in Figure 36(a) indicate a strong positive relationship with IWP. The more scattered character of the observed data may reflect local uncertainties in the RRTM_LW parameterisation of tropical convective ice crystals by the Cloud Community Model (CCM) Version 3. Modelled OLR generated by the RRTM appear to be show a direct proportionality to $\log(IWP)$, with little or no sensitivity to changes in the size of particles. This may be because the plume data is characterised by a thick ice cloud column with a near-constant cloud-top pressure and temperature of the Tropical Tropopause Layer (TTL). To support this view, bulk property analysis reveals that the IWC weighted mean pressure indicates that the thickest region of this cloud is rather consistently centred at $216 \pm 1\,\mathrm{hPa}$ in the mid-troposphere. This indicates a rather uniform vertical scale of tropical plumes.

Another plausible cause of the apparent discrepancy between the random observed data and rather deterministic modelled data of Figure 36 is through intense tropical precipitation and thermal instabilities that are both characteristic features of deep convection. The resulting fall-out of ice crystals and consequential vaporisation and melting result in latent heat removal from the atmosphere. This provides the energy for descent in the location of free tropical convection. As ice particles descend they also generate a downward motion of air, which in combination with latent heat exchange fuels turbulent exchange. As a result of these local dynamics and diabatic heat exchange, crystals may not be at an equilibrium temperature with the surrounding environmental air-mass. The optical characteristics that describe the longwave absorption and emission may therefore behave in an unpredictable fashion in nature, but not in climate models.

Water Vapour Path and LW CRF Figure 36 show that the anvil-outflow scene-type is characterised by $10\,\mathrm{g\,m^{-2}} < WVP < 700\,\mathrm{g\,m^{-2}}$ and that WVP, as with $\log(IWP)$, is positively correlated to LW CRF. The notable difference is that the strength of this correlation is weaker ($r = 0.61$) with a lower sensitivity than for IWP comparisons with a gradient of $0.16\,\mathrm{W\,g^{-1}}$. The unpredictable nature of MLS water vapour detection in the presence of thick ice clouds means that uncertainties are large and cannot easily be quantified. The notable difference

with IWP is its linear rather than logarithmic relationship to LW CRF. The sensitivity in the rate of longwave cooling due to variability in water vapour mass in thick "tropical plumes" is therefore ~ 100 fold smaller than for ice water content. There is a general correlation between these data, although the data presents a large point-to-point variability between individual high cloud cases and its related uncertainty. The modelled OLR suppression in Figure 36(a) for WVP is much weaker than for IWP indicating that UT WV plays a much less important role in the contribution to longwave radiation budget in the presence of thick cloud. In opposition, this finding is not supported by direct observational data from CERES presented in Figure 36(b), or by other recent studies by Harries (2000), John et al. (2011) that indicate that UT moisture plays a key role in the observed OLR variability.

6.4.2 The Effect of Atmospheric Conditions on Longwave Forcing for a Proto-Anvil Outflow Scene

The proto-anvil detection scheme described in Section 6.2.1 identifies an adjacent high cloud scene-type adjacent to the plume profiles. The profile detection specifically states that the minimum IWC in the upper troposphere model layers ($7 < m < 14$) must contain ice free layers of $IWC < 0.03\,\mathrm{mg\,m^3}$, so a discontinuous upper troposphere cloud ice layer is present for all the anvil outflow data. Figure 37 present two different types of anvil outflow detections: one in the near-view and one at the far-view. Firstly it is worth noting that the far-view data (48 % of profiles) are affected by limb-viewing shadowing of the MLS received radiance at 240 GHz. This measurement error results in artificially lowered IWPs that will cause an over-sensitivity of IWC in both the observed and simulated LW CRF data.

Ice Water Path and LW CRF Analysis of the IWP data concurs with the view that thinner columns of ice clouds are present in the conditions associated with anvil outflow cirrus. Figure 37 indicates that this scene-type is characterised by $1\,\mathrm{g\,m^{-2}} < IWP < 400\,\mathrm{g\,m^{-2}}$. Notably, the data presents a positive correlation simulated between $\log(IWP)$ and $C_{\mathrm{LW}}(\mathrm{outflow})$ as for the plume data, although considering the large point-to-point uncertainties in measurements indicated in Section 6.3.2 it is rather difficult to refine their relative impact on the LW CRF. The Pearson's correlation coefficient that indicates the strength of the $\log(IWP)$

to LW CRF relationship is just $r = 0.44$ for the modelled anvil outflow data. This is significantly lower than for the convective plume data presented by Figure 36(a) that reflects higher measurement error and indicates a much lower confidence in the future feedback response of anvil outflow cirrus. In general, the AER model indicates a weaker sensitivity of LW CRF to anvil cirrus than for the plumes with a positive gradient of 17 to 28 $\mathrm{W\,g^{-1}}$. This finding is supported by direct observational data from CERES presented in Figure 37(b) that reports a cloud ice sensitivity of 19 to 34 $\mathrm{W\,g^{-1}}$.

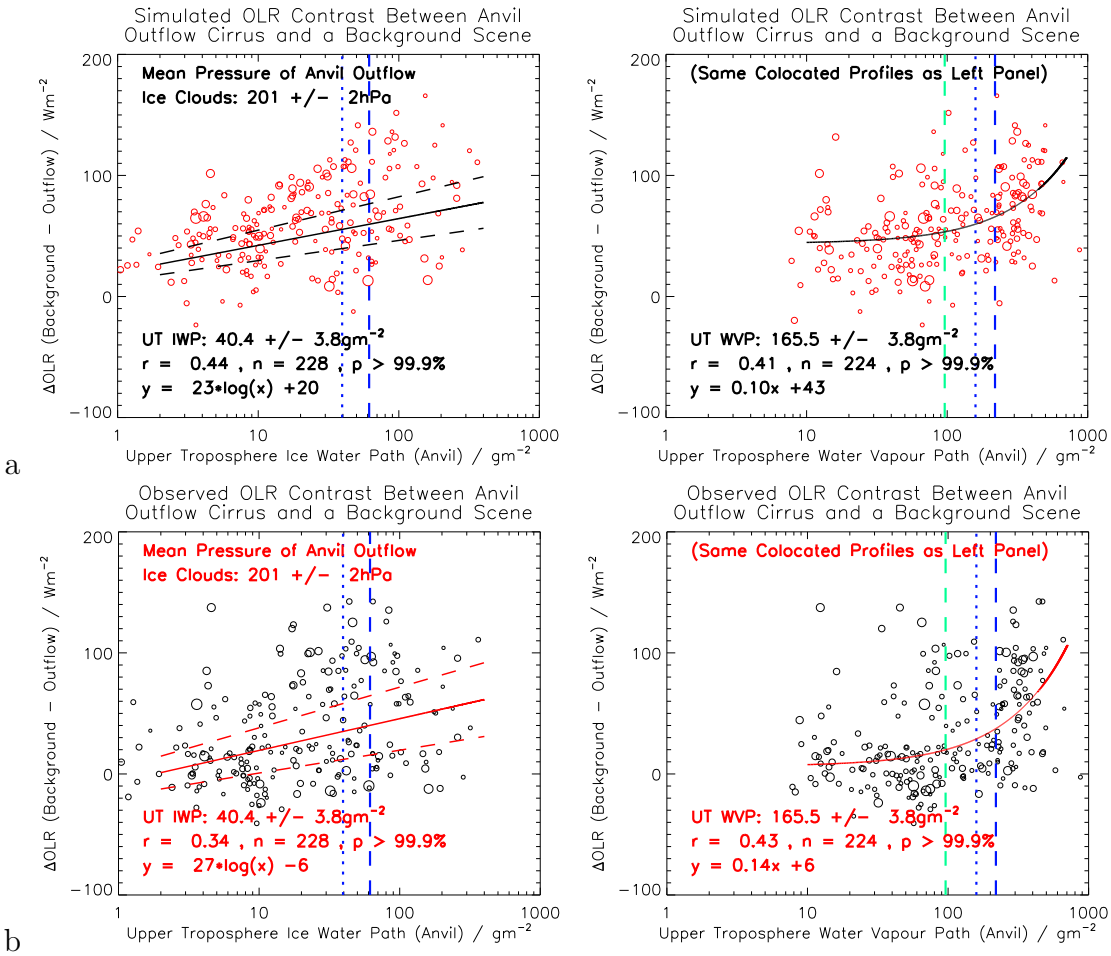

Figure 37: Same as Figure 36, but for convective anvil outflow cirrus scene-type identified using the proto-anvil detection method described in the text.

There are several fundamental differences in the character of the two high cloud scene-type data presented in Figure 37 that may cause the stochastic relationship. Firstly, it is noted that anvil cirrus is defined by a discontinuous cloud layer with ice at the top and often liquid water clouds below. The intermediate zone between these clouds is located in the mid-troposphere. As anvil

outflow cirrus is rarely often thin enough for thermal radiation to pass through, the longwave radiation leaving the upper cloud-top to space is most sensitive to the mixed-phase and low troposphere clouds. These properties and spatial distribution of these clouds is not as well specified in the model simulations as ice clouds. In addition, warm cloud data may not be temporally consistent with the clouds above due to a significant temporal off-set between MLS and ECMWF observations of up to 3 hours and partially uncoupled circulation features of the upper and lower clouds for anvil cirrus. The combination of these factors may account for much of the apparent random point-to-point scatter in the LW CRF data of Figure 37.

The weighted least-squared best fits of the correlative data in Figures 36 and 37 reinforce the view that significantly lower cloud ice sensitivities are found in the anvil outflow scene than for the convective plumes. This supports the view that the ice crystal properties of the two scene-types are fundamentally different. One plausible cause of this difference is that tropical anvil outflow cirrus is its closer proximity to the cloud-point tropical tropopause layer (TTL), where colder temperatures are often found. Ice clouds are on average located at pressures 15 ± 2 hPa lower in the anvil outflow than the convective plumes. The precision of this calculation and its significance within the reported error margin is achieved by averaging a large data sample of 233 profiles that eliminates local bias and sources of error that exist for individual profiles. In addition, whilst a 4 km vertical field-of-view is reported for the version 2 MLS IWC product e.g. Livesey et al. (2007), any systematic bias in cloud-top pressure is likely to be equivalent at each sensed pressure level for both scene-types data and cannot account for this discrepancy.

Water Vapour Path and LW CRF The WVP data presented in Figure 37 shows a similar bulk property in WVP and LW CRF sensitivities as Figure 36, with little distinction between the two data given the large variability between individual data points. There are two notable differences: smaller suppressions in OLR are found at the same WVP values in the presence of anvil outflow conditions than within the plumes; and secondly that lower mean WVPs are found in the anvil outflow conditions than for the plume data, as indicated by the blue dotted and dashed lines respectively. The first observation is likely to be a result of a stronger coincidence between UT WVP and IWP for tropical convection

than for anvil outflow cirrus. The second observation of a lower mean WVP is a direct consequence of lower absolute humidities outside of moist convection. Lower WV concentrations in the anvil outflow cirrus are also consistent with the higher characteristic altitude of this stratified cloud, extending outward from the convective anvil top rather than an icy column that extends into the mid-troposphere (as for the convective plume). Anvil cirrus clouds often form in lower temperatures that are more often found at these higher altitudes, which correspond to a lower water vapour saturation point with respect to ice.

6.4.3 Bulk Property Analysis in Different Scene-type Conditions

Figures 36 and 37 also indicate the bulk properties of each scene-type i.e. the average properties that characterise each set of conditions (scene-types). The vertical blue lines indicate that the mean IWP is approximately 50 % ($20 \pm 5\,\mathrm{g\,m^{-2}}$) higher in the conditions of plume scenes than for the proto-anvil outflow scene-type. The upper tropospheric absolute humidity is only 30 % lower in the presence of the anvil outflow, as expected given owing largely to the higher altitude outflow cirrus, with an absence of a cloudy associated with sub-saturated air that lies beneath it.

The background scene (green dashed line) contains the least water vapour that is noticeably drier, and it is this drier air that means that the scene is almost entirely cloud-less in the upper troposphere. Even though the background scene is non-convective defined by a near-zero IWC, the data indicates a relatively high point-to-point variability in IWP in the order of $0.3\,\mathrm{g\,m^{-2}}$, which reflects the MLS instrument measurement noise at the 240 GHz viewing frequency. A higher sensitivity to lower IWP values are required for subvisual and thin cirrus detection (e.g. Massie et al. (2011)), indicating the limitation of MLS detection to thicker anvil cirrus.

6.4.4 Uncertainties in Estimates of Longwave Energy Transfer

The data in this chapter show that the OLR is not affected solely by high clouds and that other factors play an important role in the RT of longwave radiation from the atmosphere to space. The atmospheric parameters or factors that strongly influence the RT simulated OLR include the following:

1. Cloud top height and spatial location - The vertical position of ice clouds

is critical in accurate calculations of the OLR by RT models. Uncertainties in the MLS detection of cloud-top pressure and cloud ice concentrations cause large uncertainties, since high clouds that are optically thick emit much less OLR than clouds of the same altitude that are optically thin. It is also essential that warm clouds are coincident in space and time with the overlying measurements, since uncertainties in the horizontal position of warm clouds input from the ECMWF can impose significant RT errors.

2. Cloudy-sky gas retrievals - The MLS data presented in Section 5.3.3 shows that middle and UT WV exhibits a great spatial variability that is often spatially coincident with tropical convection. Since upper tropospheric WV and other non-mixed greenhouse gases such as ozone are highly dynamic in the tropical troposphere, as indicated in Chapter 5, accurate retrievals that are spatially consistent with high cloud data are essential. In particular, cloud parameterisation calculations are highly dependent upon reliable MLS temperature retrieval that is particularly unreliable in the presence of thick high clouds. There are currently large errors associated with the cloud-clearance process for in the presence of thick cloud, such as for MLS ozone and temperature retrievals (Livesey et al. 2007).

3. Stratospheric intrusions - Exchange of moisture across the tropical tropopause layer could potential exert a strong greenhouse forcing in the presence of deep tropical convection. There is evidence from WV and ozone measurement data presented in Chapter 5 of significant anomalies aloft of tropical plumes in the UTLS, which can affect the representation and estimated cloud forcing in the presence of ice clouds.

4. Ice and water particle parameterisation - Particles with shorter effective radii are less absorbing in the infra-red than larger ice particles at the same mass concentration, in accordance with a $\log_{10}$(IWP) relationship (McFarquhar & Heymsfield 1998). The atmospheric conditions of the surrounding outflow cirrus are often characterised by smaller and irregularly shaped ice crystals (Wyser 1998, Iacono et al. 2000, Hong et al. 2009). The misrepresentation of different absorption properties in RT models that result from different particle size and shape spectra mean longwave RT simulations present large uncertainties in the presence of high clouds (Jensen et al. 2009).

5. Horizontal inhomogeneities along the limb view - IWC is reported by MLS as an average value that represents an extensive along-track distance. Unless the cloud is horizontally homogeneous in nature; the local IWC may deviate substantially from the mean along-track concentration. As a result, CERES OLR measurement may not be representative of the local scene viewed by MLS. For valid studies with MLS ice clouds must be sufficiently large, ideally with horizontal length-scales of $y > 150\,\text{km}$. To improve this analysis, future observations must therefore have a much better along-track sampling to better validate cloud parameterisation schemes for climate prediction.

6. MLS IWC measurement uncertainties - When the local IWC concentration is low, measurement uncertainties are highly influential on the OLR variability and quality of the RT calculations. Further MLS measurement errors are detailed in Section 6.2. In particular, some systematic biases exist in the data analysis for optically thin ice clouds where measurement noise presents negative IWC values from the V2 product that are not allowed inputs for the RRTM_LW.

7. RRTM_LW input errors - Further sources of error in LW RT arise from the cloudy-sky part of the RRTM_LW code, which neglects the effects of LW scattering. Its absence may produce small errors when examination of high cloud scenes, although the quality of the cloudy input often carries much larger uncertainties.

Sampling errors are associated with the limited period of study, which should ideally be extended to multiple days and seasons. Variability in high cloud properties operate on many different time-frames. In particular, the Asian monsoon is most pronounced in the autumn months and exerts a seasonal trend in calculations, with higher cloud fractions reported in Chapter 4. Several cycles introduce internal climate variability into the system and could affect the LW CRF calculations. In particular, an intraseasonal oscillation dominates the variability of high clouds in the tropical atmosphere that is known as the Madden Julian Oscillation (MJO). In addition, the El Niño Southern Oscillation (ENSO) in the tropical Pacific, the Meridional Overturning Circulation (MOC) in the Atlantic, and other natural variability in the climate system also play a role in the low latitude climate. During the period of study the positive phase of the ENSO dominated the

global climate system that is associated a more intense radiative cooling (Cess et al. 2001). The variability in the character of the tropical ocean impose a feedback on the sensitivity of OLR to changes in the cloud ice concentration (Larson & Hartmann 2003).

6.5 Discussion / Conclusions

In this chapter the longwave radiative forcing of high cloud are investigated using AER RRTM_LW simulations of OLR that are compared against direct CERES (Aqua) OLR observations. This study identifies two distinctly different scene-types. One set of high cloud data consists of thicker and continuous vertical columns of deep convection that are easily identified in the MLS measurement data, of 50 to 80 $\mathrm{W\,m^{-2}}$. A less well defined scene-type is identified that is called the proto-anvil outflow cirrus, which represents a higher altitude thinner cloud layers with CRF values of 30 to 60 $\mathrm{W\,m^{-2}}$. This analysis allows a better characterisation of tropical anvil cirrus, whose radiative properties and representation in climate models are currently a subject of particular uncertainty (Solomon et al. 2007). Some of the differences between high clouds are identified that may indicate how to best improve this level of confidence. The results of this study are broadly consistent with Hartmann & Wood (2008), who estimate that LW CRF equator-ward of 30° peaks around 50 $\mathrm{W\,m^{-2}}$ within strong ascent. The uncertainties in LW CRF (C_{LW}) calculations are however large, in the order of $\Delta\, C_{\mathrm{LW}} \pm 30\,\mathrm{W\,m^{-2}}$.

The relatively good consistency between simulations and measurements indicates that LW CRF of anvil outflow is comparatively easy to characterise due to the better sampling of this more extensive and laminar high cloud type. In contrast, the convective plume scene-type is characterised by relatively smaller length-scales of variable cloud-top pressure. Scene-type sampling differences are in part a consequence of the coarse horizontal field-of-view of MLS. In addition, the horizontally homogeneous structure of anvil cirrus increases the sensitivity of the MLS to low ice crystal concentrations that are typical of thin anvil cirrus. Interestingly, the anvil clouds data also reveal some contrasting properties that mark the transition between warm convection and the background scene, with characteristics that can be distinguished from the surroundings. Accurate representations of these thin high clouds in climate models may help account for

a steady rise in the OLR reputed by Rossow & Schiffer (1999), Wielicki et al. (2002) equator-ward of 20°, a finding that is not well verifiable through model simulations.

The main source of error involved in anvil outflow cirrus arises from a poorly specified lower to mid-troposphere composition and mixed phased clouds. In addition, the higher occurrence of anvil outflow detection ahead of a plume indicates that MLS shadowing of profiles in the far-view of thick clouds produces a low IWC bias. A finer horizontal sampling by space-borne instruments is also required to monitor the high spatial variability in cloud altitude, ice particle number density, ice layer thickness and scattered high cloud scenes. Several aspects of the data support the case for large uncertainties in the UT WVP measurement data in the presence of high clouds. In general, the data from this study indicate that improved greenhouse gas retrievals in the presence of cloud are essential for confirmation of several characteristics of high clouds.

The apparent strong positive correlation between $\log(IWP)$ and LW CRF, with a sensitivity value broadly consistent with observations, supports the view that high clouds are the main contributor to the rate of longwave cooling in the tropics. The stochastic nature of the observation data in contrast to simulations indicates that parameterisation issues may be especially important in the representation of high clouds. In contrast, UT WVP appear to present a less clear linear relationship to LW CRF with some inconsistencies between 200 and $1000\,\mathrm{g\,m^{-2}}$ (supported by observations) that indicate a higher sensitivities of LW CRFs at high WVPs. This observation in the data may be entirely attributable to measurement errors, such as a significant dry-bias in the Version 2 MLS data for thick ice clouds. Studies by Fueglistaler et al. (2009) indicate that discrepancies between water vapour measurements in the presence of the tropical tropopause layer substantially impede accurate climate modelling.

Further errors are associated with both the measured and simulated OLR that cause the large range of plausible LW CRFs. One source of error arises from the degradation of CERES OLR data to make it spatially consistent with MLS. At the 300 km length scale of each measurement point many high clouds are too small to be correctly resolved. Whilst the use of co-located comparisons enables valid comparisons, the horizontal resolution of measurements is essential for future cloud studies. This study indicates that MLS detections of several absorbing gases encounter large uncertainties and inaccuracies in the presence of high clouds;

therefore it is difficult to represent the absolute impact on the LW CRF. In addition, since there is a strong seasonal cycle in high cloud fraction, further studies using inter-annual and seasonal data may reveal striking differences in the low latitude LW CRF.

Uncertainties in the RT output of OLR could be reduced by incorporating accurate greenhouse gas retrievals in the presence of clouds, an area of atmospheric modelling that warrants further work. Since MLS WV retrieval presents a bias and unreliable data in the presence of thick cloud e.g. Livesey et al. (2007), a cloud-cleared scene that excludes thick ice cloud profiles is used as an alternative reference scene. Whilst this reference scene is cloud-cleared, climate feedback studies based on changes in cloud fraction alone are likely to lead to a slight over-estimate in climate sensitivity, i.e. the equilibrium change in the annual mean global surface temperature following a doubling of the atmospheric equivalent carbon dioxide concentration (Solomon et al. 2007). This is because satellite observations indicate that an increase in the tropical convective area coincides with a decrease in the surrounding upper tropospheric water vapour concentration (Lindzen et al. 2001, John et al. 2011). The clear-sky variability in water vapour concentration poses a larger forcing on climate than in the convective area, where thick ice clouds account for much of the observed suppression in OLR. Future LW CRF must therefore consider the non-local effect that convection poses on the radiation budget, especially the drying of neighbouring atmosphere.

The cloud parameterisation that characterises the ice particle shape and size spectra of ice clouds also poses another significant source of error. By using an updated version of RT model, with improved inputs for cloud optical properties, it is plausible that improvements could be made to this study to refine estimates of the LW CRFs for thin anvil outflow clouds. In addition to space-borne measurements a combination of in-situ balloon and aircraft data, a range of passive and active microwave and infra-red satellite instruments with different viewing geometries, and ground-based lidars are also essential to provide a near-complete representation of ice cloud properties (Buehler et al. 2007, Waliser et al. 2009). Currently, the fourth generation of NCAR's Community Climate Model described by Acker et al. (1996) adds further detail to ice cloud parameterisation, however the representation of cloud radiative properties remain uncertain in climate models (Solomon et al. 2007, Chapter 1.).

6.5.1 Evaluation of the Proto-Anvil Detection Scheme

The proto-anvil outflow detection scheme described in this study examines ice mass concentrations (IWC) and along-track gradients in low troposphere cloud to identify two contrasting scenes in the transition zone between deep convection and the surrounding ice-free atmosphere. This scheme could have been devised differently to identify two quite different high cloud scenes, yet the relative patterns of IWP and WVP sensitivities to LW CRF would be similar. The method in this chapter effectively divides the convective scene, which consists of the anvil outflow and plume, into equal divisions. This method provides an equal sample size for each high cloud scene-type and presents equivalent comparisons of upper tropospheric humidity and ice clouds. This is particularly important for investigating the relative effects of different atmospheric parameters in the presence of different high clouds on the future climate.

The contrasting radiative properties of the two high cloud scene types indicate that the cloud edge detection algorithm is identifying some desired bulk properties of anvil outflow compared to the convective plumes. This includes lower absolute humidities and ice water content, and a distinctly different pattern in the sensitivities of UT WV and IWP that is supported by observations. The findings are consistent with the view that anvil cirrus is characterised by a horizontally laminar ice layer, which is confined at the top of free tropical convection.

7 Conclusions

7.1 Technical Summary

Investigations in this thesis demonstrate how co-located cloud data from A-train instruments, whose measurement footprints cover the same locations at the same times, lead the way to improved comparisons of high cloud radiative properties that have previously been scarce. A validation study first confirms that Microwave Limb Sounder (MLS) on-board the Aura satellite views higher cloud tops where the CERES and MODIS (Aqua) instruments also view higher altitude clouds at the same locations. The study also shows a consistent pattern in high cloud distribution and fractional coverage from CERES, MODIS and MLS whilst noting that MLS may be more sensitive to thinner ice clouds. Whilst cloud-top heights provide a rough indication to cloud radiative properties, later investigations show that MLS offers a much deeper understanding of the role of high clouds in the rate of longwave cooling that can only be obtained from instruments that report information about a clouds interior. In particular, it is shown that the coincident footprints of A-train measurements that are undertaken from different satellite platforms offers particular promise in reporting reliable estimates of the seasonal high cloud fraction. Validation studies indicate that nadir-sensors report cloud-top heights that are consistent with MLS, yet their finer horizontal sampling produces gaps between measurements for scattered high cloud scenes. Overall, the data shows that limb sounding is more successful for detailed high cloud studies. This is because MLS provides a higher vertical resolution of thick tropospheric clouds than many infrared nadir-viewing sensors.

Detailed examinations of high cloud are undertaken later in the thesis, demonstrating that the MLS alone can provide a great deal of composition data including water vapour; the most abundant of the Earth's greenhouse gases, which is found in its highest concentrations within tropical storms. Whilst water vapour retrievals are a known source of error in the presence of thick clouds, the MLS alone provides adequate data to simulate much of the observed variability in the observed longwave energy budget. The most valuable feature of MLS is its diverse data product portfolio that describe much of the atmospheric composition of the mid- to upper troposphere. Its main pitfall is that its limb radiances are easily saturated in the moist and frequently cloudy low to mid-troposphere below. Later in this thesis it is shown how co-located liquid cloud data from the European

Center for Medium-range Weather Forecasts (ECMWF) is a used to improve our descriptions of the tropical atmosphere. The ECMWF ERA-interim data product provides further confidence that MLS is successful at detecting deep plumes of tropical cloud that extend from the planetary boundary layer up to the tropical tropopause. The combination of ECMWF data with MLS allows in particular permits more accurate simulations of the longwave energy budget, which can be used to better attribute the influence of high clouds to climate forcing. In addition, co-located ECMWF data enables deep convective profiles to be identified with better confidence.

Co-located analysis of simulated Outgoing Longwave Radiation (OLR) is achieved by the use of a radiative transfer model, which is fed with both MLS and ECMWF data. The chosen model simulates the broadband longwave emission and is a common choice for use in global climate models. Later studies in the thesis demonstrate that by direct comparisons of the modelled OLR with direct observational data from CERES that the longwave Cloud Radiative Forcing (CRF) can be refined in the conditions of two scene-types typical of tropical storms. The refinement of this parameter is only possible by direct validation against observations, as the modelled differences in the sensitivity of CRF to upper tropospheric ice and humidity are only valid when supported by observations of the same section of atmosphere. Direct observational data from CERES enables the quantification of uncertainties in climate forcing. The results again support the view that MLS provides a broadly accurate representation of the tropical atmosphere that reflects the main features of the observed atmosphere. The study also reveals some atmospheric conditions where MLS is least successful; noticeably with apparent dry artefacts and unreliable retrievals in the water vapour data.

Overall, early validation studies show that synergistic methods offer particular value for future climate studies, with each instrument sensitive to different high cloud properties; MODIS views low to middle troposphere clouds well and MLS only reporting data on ice clouds. Valid combination of these data with the wealth of other cloud products now available, must carefully consider the spatial resolution of each. This combination is usually limited by the instrument that offers the poorest horizontal resolution; the MLS instrument in the case of this study. Whilst value is generally added by the MLS, the quality of the cross-instrument comparisons in this thesis is significantly degraded by the rela-

tively poor along-track resolution of MLS and its narrow across-track sampling in contrast to nadir sensors.

Future synergistic datasets that describe clouds must add value or additional features to the existing cloud datasets from which it is composed. This would allow new datasets to be provided with a better specification of cloud properties for use in climate models at seasonal timescales and beyond. More detailed studies of cloud properties and processes would therefore be possible in the context of regional to global changes in atmospheric composition and Earth system processes. Comparisons of this type are particularly useful in refining cloud parameterisation schemes - the descriptions of cloud particle sizes and shapes. This thesis demonstrates this success by exploring the differences between the modelled and observed radiation budget data using coincident data.

Further details of specific thesis findings and their implications for climate uncertainty and prediction are discussed in Section 7.2. Section 7.3 then proceeds to discuss the current availability of alternative ice cloud products and whether their measurements offer consistency with MLS. Section 7.4 then presents a future vision of high cloud studies and the requirements for Earth Observation instrumentation to overcome present challenges.

7.2 Co-located Studies of Ice Clouds - Implications

In this thesis several components of the atmospheric composition and physical conditions are examined that contribute toward calculations of longwave energy budget in the presence of tropical ice clouds. Specifically, it is shown how close comparisons of MLS data with other spatially coincident measurements allow the high Cloud Radiative Forcing (CRF) to be refined. This is achieved using coincident measurements of OLR from CERES (Aqua) that report relatively low measurement errors and high stability (Spence et al. 2003). Overall, the study demonstrates how co-located measurements enhance descriptions of high cloud radiative properties and could be used to improve representations of cloud properties in response to climate change.

There are several different methods for estimating the longwave (LW) radiation budget (RB) in cloudy sky conditions. Chapter 3 shows that CTPs are subjective, with no robust method for their estimation, often with no definitive boundary between cloud layers and overlying clear sky. Instruments such

as MODIS therefore provides a much better opportunity to study the shortwave component of the radiation budget, since much of the solar radiation is scattered from the surfaces of low clouds and thicker ice clouds. In contrast, broadband instruments such as CERES offer no detailed information about high clouds. Inter-comparisons of MLS CTPs with CERES (Aqua) CTPs derived from brightness temperatures, reveals a weak positive correlation with a mean low altitude bias of $3 - 4\,\mathrm{km}$. The application of CERES is later proved invaluable; providing direct observational evidence of the longwave radiative forcing of tropical clouds.

Co-located studies of high clouds in Chapter 3 demonstrate a general consistency of MLS with both MODIS and CERES; whilst the uncertainties involved in the use of CTPs in climate models are much too high. Comparisons between nadir and limb-viewed measurements also show inconsistencies for scattered cloud scenes and differences in viewing geometry and horizontal resolutions. As a consequence, MLS data reports a low pressure CTP bias, with lower altitude clouds visible at nadir that are undetected across the limb. Despite this, data in Chapter 3 shows how complementary cloud properties; such as thermodynamic phase and cloud mask information from co-located MODIS data viewed at nadir, can be used in conjunction with MLS to determine horizontal homogeneity of cloud and therefore to allow focussed studies on thick tropical ice clouds. This kind of synergistic comparison is valuable to increase the validity of future cloud studies. Later work in Chapter 5 and 6 shows that many others variables account for the observed regional variability in the longwave radiation budget, rather than a cloud-top view on climate.

In Chapter 4 methods are developed to estimate the high cloud fraction and to present seasonal maps of its global distribution and occurrence frequency. These kinds of study are useful for inter-comparisons with other cloud measurements, since often direct comparison of cloud products is not possible due to differences spatial coverage and field of view. Valid A-train comparisons are undertaken by spatially averaging nadir-sensor data within each MLS measurement footprint. This process allows the quantification of cross-instrument differences in high cloud fraction. The data shows how by combining information from different instruments confidence can be greatly improved in the presence of high cloud and the seasonal distribution in its occurrence frequency. These studies find that large-scale regions of convective high clouds detected by the MLS are found infrequently outside the tropics. In addition, accurate and reliable data

on the global high cloud fraction in Southeast Asia, Central Africa and Central America may be critical in the future prediction of extreme rainfall events and regional forecasts for agriculture and management of water resources.

Coincident simulations and observations of OLR are examined Chapter 5. The correlative data shows that accurate specification of clouds and spatially coincident measurement are essential to correctly represent the radiation budget, as large uncertainties are often found in the presence of tropical high cloud. This is mainly due to large horizontal variability in the OLR at the location of deep convection. Largely as a result of the poor along-track view of MLS, individual profile level bias as large as $120\,\mathrm{W\,m^{-2}}$ are found in the presence of tropical convection. This is a major limitation for accurate calculation of cloud radiative properties and calls for a much better horizontal resolution of clouds future cloud-climate studies. In addition, whilst numerical weather data (from ECMWF) is shown to successfully supplement MLS data with information about low clouds, temporally coincident data is required. This could be provided through synergistic combination from other ice cloud sensors onboard the A-train constellation (discussed later in Section 7.3), which offer a unique set of measurements from satellites in the same orbit.

Whilst case studies cannot ascertain whether any ice water content anomalies can be assigned to thin outflow clouds, they present some anomalies in the data retrievals in the presence of clouds that are often missed with large-scale data analysis. Several LW radiative Heating Rate anomalies (HRs) in the order of $0.5\,\mathrm{K\,day^{-1}}$ are apparent from the analysis in Chapter 5 in the tropical tropopause layer (TTL). These features are thought to be associated with thin cirrus that is maintained by a balance between sedimentation and radiative driven lofting (Jensen et al. 2009). Correctly locating thin cirrus is important in climate studies, since comparisons with radiative budget data at the same locations can help refine estimates of the cirrus radiative forcing and feedback processes that present great uncertainty for climate predictions.

On a profile basis several characteristics of tropical high clouds were identified in Chapter 5, using two case studies to reassert findings in each case. Atmospheric composition data, comprising upper troposphere to lower stratosphere ozone and water vapour were studies for equatorial satellite passes within the warm and cold-pool regions of the Pacific. Noticeably, the data shows that higher absolute humidities in the mid-troposphere coincide with ice detections and high LW

heating rates (HRs) aloft of dense cloud. Rather than low to mid-tropospheric WV coinciding with higher absolute humidities of the TTL, several dry anomalies are detected in the case studies of Chapter 5. Whilst this data could indicate artefacts, it may also indicate that convective overshooting of moisture causes cross-tropopause exchange of moisture. To further support these findings it is imperative that water vapour retrievals are improved in the presence of thick cloud, which could only be achieved realistically by examining the spectral signature of ice clouds. These kinds of studies could be achieved by the use of a fine-resolution infra-red instrument, such as HIRDLS (Aura) that is discussed later in Section 7.3.1.

Ozone anomalies are also found above thick tropical ice clouds. These features may be associated with dynamic exchange across the tropopause, or indicate that high absolute humidities readily promote ozone depletion in convective zones. As the tropical convective zone may be expanding as the climate warms, accurate retrievals are essential to correctly represent the role of tropical convection in the chemical transport of ozone and the recovery of the ozone layer. This has direct implications for both human and plant life. Large uncertainties currently exist in MLS ozone retrievals above thick ice cloud that must be remedied. These limitations in the ozone data product for thick cloud currently inhibit the progression in the understanding of heterogeneous ozone chemistry the presence of tropical convective clouds and anvil outflow cirrus. To meet these scientific goals, future instrumentation must therefore be designed to allow accurate cloudy-sky retrievals of ozone at mid-troposphere to lower stratosphere altitudes.

A focussed study in Chapter 6 explores the sensitivity of longwave Cloud Radiative Forcing (LW CRF) to upper troposphere water vapour and ice water content in the conditions of two tropical scene types. A proto-anvil outflow detection scheme is devised to identify thick ice clouds that extend the troposphere. The success of this proto-anvil detection is supported by coincident observations, with deep plumes characterised by a mean LW CRF of 50 to 80 $\mathrm{W\,m^{-2}}$ and the anvil outflow by a significantly lower LW CRF of 30 to 60 $\mathrm{W\,m^{-2}}$. The analysis shows that the thicker anvil outflow cirrus is apparently well detected by MLS, with the radiative properties of convective plume scene limited by large uncertainties in the upper troposphere water vapour. The study emphasises the need for accurate humidity retrievals in the presence of thick cloud to correctly simulate the Earth's radiation budget.

Later in Chapter 6 it is shown ice particles of the anvil outflow form at slightly lower pressures, with a significantly lower sensitivity to cloud ice that is 15 to 40 % of the convective plume scene. The high point-to-point scatter in the data reflect the poor along-track resolution and narrow across-track view of MLS, whilst uncertainties in ice water content are too high to adequately refine LW CRF calculations. The coincidence of A-train measurements is invaluable in these estimates of cloud-climate uncertainty. Ideally future polar orbiting satellites are required with closely consecutive measurements to further advance the understanding of clouds and their representation in global climate models.

To add complexity, the mesoscale convective systems where tropical ice clouds form most frequently are associated with strong vertical motions and dynamical driven mixing. These turbulent tropical conditions are known to alter the number concentration of small crystals (Barahona & Nenes 2008, Ichkawa et al. 2012). In addition, heavy precipitation is frequently found in the vicinity of these storms alter the local latent and sensible heat budget. The consequence is that parameterisation schemes that describe tropical ice clouds are often invalid, particularly as large hydrometeors that form in turbulent conditions are not well specified. There is therefore a need for additional ice cloud properties to be reported by satellite instruments, such as their size and shape, which could be achieved by analysis of the radiance polarisation. These kind of cloud measurements are currently undertaken by the CALIOP sensor on CALIPSO, discussed in Section 7.3.2.

Refining LW RT simulations in radiative transfer models are also essential to understand the high cloud feedbacks. The findings in Chapter 6 are in support of a general "cold bias" in the presence of thick tropical cirrus, which may indicate that General Circulation Models (GCMs) overestimate the LW CRF. In addition, accurate representation of thin cirrus in climate models is required that covers a relatively large area of the Earth's surface. Thin cirrus may account for the observed steady rise in the tropical OLR that is not yet attributable by model simulations (Rossow & Schiffer 1999). The correct representation of cirrus is therefore of particular importance, since it exerts a relative strong warming effect on climate. An improved portfolio of anvil outflow cirrus measurements are also required to gain a better understanding of its maintenance and formation mechanisms, so future change in the distribution of cirrus can be better represented in models.

7.3 Present Studies of Ice Clouds

7.3.1 Consistency of MLS Cloud Ice with Other Limb Sounding Sensors

There are many other limb-sounding instruments currently in operation that are capable of monitoring ice clouds. Together these instruments provide complementary information on the same clouds, yet viewed by a set of differently designed instrumentation. Their antennas receive radiance data of varied frequency that is processed by different detection algorithms. In particular, the consistency of MLS cloud-ice detection is discussed in the context of cloud data products from two infra-red sounders that general offer a higher sensitivity to thin anvil cirrus. Onboard the NASA A-train there is one other satellite instrument that reports ice water content; the High Resolution Dynamic Limb Sounder (HIRDLS) on Aura (Gille et al. 2011). Another valuable IR limb sounder with a cirrus data product has been funded by the European Space Agency (ESA) and is located on the EnviSat "Environment Satellite". This instrument is known as the Michelson Interferometer for Passive Atmospheric Sounding (MIPAS).

Whilst ice clouds cause a broadband reduction in the longwave transmission, HIRDLS provides a detailed infrared spectral signature of ice clouds with a resolution of $0.025\,\mathrm{cm}^{-1}$. This information sheds light on the intricacies of ice cloud optical properties in radiative transfer models. The HIRDLS instrument also offers a similar vertical resolution as MLS of 3 km. The main distinction between HIRDLS and MLS (Aura) are their useful detection range for cloud ice that is determined by the saturation of received radiances. Both the HIRDLS and MLS ice water content products offer almost mutually exclusive data products. Whilst HIRDLS reports successful ice cloud detections of $IWC > 0.03\,\mathrm{mg\,m}^{-3}$ typically of high altitude thin cirrus, MLS detects ice clouds typically of $IWC > 0.3\,\mathrm{mg\,m}^{-3}$ found within thicker tropical ice clouds. HIRDLS IWC data is therefore particularly akin to synergistic combination with MLS, particularly as its housing on the same satellite ensures its measurements footprints are positioned at broadly the same locations and report data at the same times. Analysis of HIRDLS data by Massie et al. (2010), Sembhi et al. (2012) reveal that thin cirrus is distributed in the same general locations as detections of convective clouds by MLS and their respective products could be well combined.

A good cross-instrument consistency of MLS ice cloud detections is also found

with both the HIRDLS and MIPAS instruments. Notably, global maps of MIPAS (EnviSat) ice cloud data by Greenhough et al. (2005), Sembhi et al. (2012) presents similar seasonal distributions of tropical cirrus. The most comparable features of the MIPAS, HIRDLS and MLS data are characteristic peaks in the high cloud frequency occurrences over the Asian, Central African and Amazon regions. Further recent comparisons with the HIRDLS ice water content product by Sembhi et al. (2012) also reveal a similar peak occurrence frequency in high clouds as MLS of 50 to 80 %.

The notable difference between MLS cloud ice data and MIPAS cloud detections reported by Greenhough et al. (2005) is the detection of polar stratospheric clouds (PSCs) by MIPAS over the both poles during the respective hemisphere winter. These PSCs are composed of either water-based ice crystals or a through a combination of nitric acid (HNO_3) and water vapour and are not too thin to be viewed by the MLS that principally reports thicker ice clouds in the tropics. Recent work by Sembhi et al. (2012) also show that MIPAS is sensitive to smoke and pollution aerosol clouds, such as those released by intense Australian bush fires of 2009.

7.3.2 Consistency of MLS Cloud Ice with Nadir-Viewing Sensors

In addition to the MLS and HIRDLS, the NASA A-train payload also includes another detector that views ice clouds at a high vertical resolution. This instrument is an active visible to ultra-violet frequency nadir sensor and is known as the Cloud-Aerosol Lidar with Orthogonal Polarization (CALIOP) (Winker et al. 2006). Comprising part of the CALIPSO satellite payload, CALIOP provides a valuable insight into the vertical extent of clouds and aerosols (Massie et al. 2010, Sembhi et al. 2012). Complementary to the MLS, CALIOP also discriminates between ice clouds and water clouds by depolarization measurements. This feature allows the discrimination between non-spherical aerosol and ice particles. In contrast, the MLS ice cloud product is solely based on the spherical particle assumption (Livesey et al. 2007). MLS detections therefore lack sufficient detail on thin cirrus that is required to better calculate their radiative properties for improved representation in global climate models. CALIOP however can detect thin high altitude cirrus and aerosol that is invisible to microwave sensors, whilst is saturated by the thicker ice clouds viewed by MLS (Sembhi et al. 2012). In resemblance to MIPAS detections, a similar pattern in the seasonal high cloud

frequency occurrence is observed by CALIOP and MLS that again indicates the connection between thin anvil cirrus and tropical convection.

Closely twinned with CALIPSO in the A-train constellation, the CloudSat Cloud Profiling Radar (CPR) radar backscatter sensor offers a product that is sensitive to ice clouds of a similar thickness as the MLS instrument. In its favour, the nadir-viewing CPR receives information on most cloudy-sky scenes from the tops of cirrus to low level lower troposphere even for thick layers of tropical cloud. The CPR therefore provides a much better representation of extratropical cirrus (poleward of 30 degrees) that is not possible by MLS. The CPR also offers a higher along-track resolution than MLS, with approximately 10 times more profiles per day. The main advantage of MLS is its higher vertical resolution and sensitivity to lower ice water content values that comprise thin cirrus. In contrast, CloudSat detections are not so easily saturated and therefore report additional information on the larger snow and ice hydrometeor ice contained within high clouds. In spite of the shorter path-length of CloudSat Radar signal compared to the limb view, the infrared viewing frequency limits its detection to $IWC < 5\,\mathrm{mg\,m^3}$ (Waliser et al. 2009).

Recent work by Waliser et al. (2009), Wu et al. (2009) show that ice clouds are detected in broadly in the same regions by MLS and CloudSat CPR instruments, whilst at the altitude of greatest interception between the instruments ($p \sim 200\,\mathrm{hPa}$) the CPR on average views $\sim 50\,\%$ more ice water content. Future studies with liquid water content from CloudSat would add great value to future climate modelling studies; particularly as studies in this thesis required additional lower troposphere data from ECMWF that lacks the consistency offered by co-located A-train data.

7.4 Future Ice Cloud Studies and Final Remarks

Further co-located studies of high clouds are required to help improve descriptions of properties and processes and their representation in weather and General Circulation Models (GCMs). This study shows that RT simulations efforts are currently hampered by uncertainties in retrievals of greenhouse gases in the presence of clouds, such as upper tropospheric WV. Improved gaseous retrievals within cloudy-sky plumes will help increase confidence in cloud data that obtained using a range of different space-borne instruments. Whilst each cloud monitoring

instrument presents its own limitations, many different measurements techniques are needed to reduce the likelihood of bias. In addition, the unique instrument designs of space-borne instruments provide different clues about the properties of the same high clouds.

The CloudSat (radar) and CALIPSO CALIOP (lidar) instruments follow each other in close succession in the NASA A-train and are therefore highly valued for studies of clouds that are move and evolve over relatively short periods of time. The CloudSat CPR can be used to report data on both thick and thin clouds, whilst CALIPSO is sensitive to thinner high clouds and aerosols and with rapidly attenuated back-scatter induced by dense cloud particles (Chase et al. 2011). Due to their strikingly different view-point on the same clouds, the combination of their products would greatly increase confidence in cloud properties. Future simulations of the LW radiation budget would also be greatly improved by the better treatment of ice clouds using this data.

An extended study with many days of satellite data is generally required to help refine estimates of cloud-climate processes and the monthly to decadal variability in LW CRFs. More work using detailed cloud interior data is also required, which is now provided by many space-borne detections. Specifically, the climate community would benefit from studies that isolate several contrasting high cloud scene-types and characterise these scenes in terms of physical properties such as local scale dynamics, and also their chemical compositions. These parameters are not generally included in cloud parameterisation schemes, but are essential for more detailed studies of high clouds. Standard classifications of high clouds by Rossow & Schiffer (1999) include only optically thick and thin layers. These broad definitions encompass a large spectrum of clouds with different formation mechanisms, vertical layering and large and micro-scale processes. By improving the classification and identification of different cloud-types from space-born instruments, using a more improved scheme than described in this thesis, future cloud parameterisations could be undertaken on a scene-specific basis. This could be achieved by combining many Earth Observation data on cloud properties, physical conditions and atmospheric composition measurements.

The response of high cloud to climate change varies considerably between different GCMs, with the largest feedback response simulated over the tropics (Solomon et al. 2007). A much better horizontal sampling of high clouds are therefore required than MLS to refine calculations of the tropical LW CRF. Since

many high clouds reveal sharp horizontal contrasts in their properties, future studies are best resolved with nadir instruments, with supporting evidence from co-located MLS cloud data. The Ice Cloud Imager (ICI) concept microwave instrument provides an alternative future choice, with a comparable sensitivity to tropical ice clouds as MLS. ICI offers the main advantage of its conical scanning mode that provides a better horizontal resolution, which is invaluable for detailed studies of high clouds Buehler et al. (2007). ICI is a multi-spectral Microwave Imaging Radiometer that is expected to operate in a similar set of viewing frequencies as the MLS. It will form part of the MetOp-Second Generation (MetOp-SG) satellite payload and is jointly funded by the European Space Agency (ESA) and EUMETSAT (Alberti et al. 2012).

Since a basic cloud-edge analysis can isolate two distinct high cloud scene types, the JPL science team could incorporate a different parameterisation schemes to detect ice within the anvil outflow regions. The current version 3 of the MLS cloud detection is based on a spherical particle parameterisation. Although this representation functions well for deep convective plumes, it is generally less successful the ice crystals of anvil outflows that are characterised by irregular and much smaller ice particles (Stephens 1984, Fu et al. 1995, Iacono et al. 2000). The proto-anvil detection scheme developed in this study shows that future schemes could be implemented to provide a higher confidence on the locations where conditions are most favourable for thin cirrus formation.

Further work is needed to assess the sensitivity of LW RT to differences in the cloud particle shape and size distributions. In particular, location based (in-situ) measurement data has previously been successful in determining the properties of ice crystals, such as the Central Equatorial Pacific Experiment (CEPEX) (McFarquhar & Heymsfield 1997). Co-located comparisons of aerosols on cloud processes also warrant further work, and has been identified as a major source of uncertainty in anthropogenic climate change assessment and prediction (Solomon et al. 2007).

Future satellite missions must explore ice cloud properties for a range of different scene-types across the globe, particularly as every cloud-type has a unique set of properties and spatial coverage that exert a different forcing on the Earth's climate system. Space-borne detection of ice cloud offer much more detailed information than many other ground-based or in-situ sensors and should remain a priority for future data collection. Earth Observations now offer a great deal of

detail about the interior of clouds and offer a relatively inexpensive alternative to the extensive in-situ observations required for studies of a similar scale.

References

Acker, T., Buja, L., Rosinski, J. et al. (1996), *User's Guide to NCAR CCM3*, NCAR, Boulder, CO. NCAR/TN - 421+IA.

Ackerman, S., K.Strabala, P.Menzel et al. (1997), Discriminating Clear-sky from Cloud with MODIS: Algorithm Theoretical Basis Document MOD35, Technical Report, NASA Goddard Space Flight Center.

Alberti, G., Pica, G., Memoli, A. et al. (2012), TWO Microwave Imaging Radiometers for MetOp Second Generation, Technical Report, CNIT Tyrrhenian Workshop, Naples.

Allan, R. a. (2000), 'Evaluation of Simulated Clear-sky Longwave Radiation using Ground-based Observations', *J. Climate* **13**, 1951 – 1964.

Allan, R., Shine, K. & Slingo, A. (1999), 'The dependence of clear-sky Outgoing Longwave Radiation on Surface Temperature and Relative Humidity', *Q.J.R. Meteorol. Soc.* **125(558)**(2103).

Allen, J., Sherwood, S. & Norris, J. (2011), 'The Equilibrium Response to Idealized Thermal Forcings in a Comprehensive GCM: Implications for Recent Tropical Expansion', *Atmos. Chem. Phys.* **11**, 31643 – 31688.

Andrews, D. (2000), *Atmospheric Physics*, Cambridge University Press, Chapter 3. The Radiative-Transfer Equation.

Asrar, G., Kaye, J. & Morel, P. (2001), 'NASA Research Strategy for Earth System Science: Climate Component', *BAMS* **82**(7), 1309 – 1329.

Aumann, H., Chahine, M., Gautier, C. et al. (2003), 'AIRS/AMSU/HSB on the Aqua mission: Design, Science Objectives, Data Products, and Processing Systems', *IEEE Trans. Geosci. Remote Sensing* **41**(2).

Ayazi, R., Tassa, A., Wells, A. et al. (2012), The Growing use of GMES across Europe's Regions, Technical Report, NEREUS and European Space Agency.

Barahona, D. & Nenes, A. (2008), 'Parameterization of Cirrus Cloud Formation in Large-Scale Models: Homogeneous Nucleation', *J. Geophys. Res* **113**(D11211). doi:10.1029/2007JD009355.

Barath, F., Chavez, M. C., Cofield, R. E. et al. (1993), 'The Upper Atmosphere Research Satellite Microwave Limb Sounder Instrument', *98* **98**(D6), 10751 – 10762. doi:10.1029/93JD00798.

Bedka, K., Dworak, R., Brunner, J. et al. (2012), 'Validation of Satellite-based Objective Overshooting Cloud-top Detection Methods using CloudSat Cloud Profiling Radar Observations', *J. Appl. Meteor. Clim.* **51**(10), 1811 – 1822.

Benedetti, A., Stephens, G. L. & Haynes, J. M. (2003), 'Ice Cloud Microphysics Retrievals from Millimeter Radar and Visible Optical Depth Using an Estimation Theory Approach', *J. Geophys. Res.* **108**(D11). doi:10.1029/2002JD002693.

Boehm, M., Verlande, J. & Ackerman, T. (1999), 'On the Maintenance of High Tropical Cirrus', *J. Geophys. Res.* **104**, 24423 – 24433.

Borbas, E. & Ruston, B. (2011), The RTTOV UWiremis IR Land Surface Emissivity Module, Technical Report, EUMETSAT. Darmstadt, Germany.

Buehler, S., Jiménez, C., Evans, K. et al. (2007), 'A Concept for a Satellite Mission to Measure Cloud Ice Water Path, Ice Particle Size, and Cloud Altitude', *Q. J. R. Meteorol. Soc.* **133**(S2), 109 – 128.

Cao, C., Xu, H., Sullivan, J. et al. (2005), 'Intersatellite Radiance Biases for the High-resolution Infrared Radiation Sounders (HIRS) on Board NOAA-15, -16, and -17 from Simultaneous Nadir Observations', *J. Atmos. Oceanic Tech.* **22**(4), 381 – 395.

Cess, R., Wielicki, B., Zhou, X. et al. (2001), 'The Influence of the 1998 El Ninõ upon Cloud-Radiative Forcing over the Pacific Warm Pool', *J. Climate* **14**(9), 2129 – 2137.

Cetrone, J. & Houze, R. (2009), 'Anvil Clouds of Tropical Mesoscale Convective Systems in Monsoon regions', *Q.J.R. Meteorol. Soc.* **135**, 305 – 317.

Chaplin, M. (2011), Water Absorption Spectra, Technical Report, London South Bank University (LSBU), url: http://www.lsbu.ac.uk/water/vibrat.html.

Chase, J., Wu, D., Read, W. et al. (2011), 'The Role of Tropical Deep Convective Clouds on Temperature, Water Vapor, and Dehydration in the Tropical Tropopause Layer (TTL)', *Atmos. Chem. Phys.* **11**, 3811 – 3821.

Chen, J., Carlson, B., Genio, A. D. et al. (2002), 'Evidence for Strengthening of the Tropical General Circulation in the 1990s', *Science* **295**(838 - 841).

Clarke, G. (1973), *Statistics and Experimental Design*, Edward Arnold, Chapter 8: Other Tests of Significance, pp. 54 – 69.

Clough, S., Shephard, M., Mlawer, E. et al. (2005), 'Atmospheric Radiative Transfer Modeling: A Summary of the AER Codes', *Spectroscopy and Radiative Transfer* **91**, 223 – 244.

Cole, A. & Kantor, A. (1962), 'Tropical and Subtropical Atmospheres', *J. Appl. Meteorol.* **2**, 90 – 98.

Currey, C. & Green, R. (1998), 'Validation of the CERES Shortwave Measurements over Desert and Cloud Scenes', *Amer. Meteor. Soc.* **10th conference on atmospheric radiation**, 567 – 570.

Dalanoe, J. & Hogan, R. (2010), 'Combined CloudSat-CALIPSO-MODIS Retrievals of the Properties of Ice Clouds', *J. Geophys. Res.* **115**(D00H29).

Dee, D., Uppala, S., Simmons, A. et al. (2011), 'The ERA-Interim Reanalysis: Configuration and Performance of the Data Assimilation System', *Q.J.R. Meteorol. Soc.* **137**(656), 553 – 597.

Del Genio, A. (1996), 'A Prognostic Cloud Water Parameterization for Global Climate Models', *J. Climate* **9**, 270 – 304.

Dunbar, B. (2007), NASA - CALIPSO, Technical Report, NASA, url: http://www.nasa.gov/mission_pages/calipso/.

Ebbing, D. & Gammon, S. (1999), *General Chemistry: Sixth Edition*, Houghton Mifflin, Chapter 10.

Ebert, E. & Curry, J. (1992), 'A Parameterization of Ice Cloud Optical Properties for Climate Models', *J. Geophys. Res.* **97**(D4), 3831 – 3836.

Edwards, J., Havemann, S., Thelen, J. et al. (2007), 'A New Parametrization for the Radiative Properties of Ice Crystals: Comparison with Existing Schemes and Impact in a GCM', *Atm. Res.* **83**(1), 19 – 35.

Forster, P. & Shine, K. (1999), 'Stratospheric Water Vapour Changes as a Possible Contributor to Observed Stratospheric Cooling', *Geophys. Res. Lett.* **26**(21), 3309 – 3312.

Franklin, J. & Brown, O. (2007), 'Atlantic Hurricane Season of 2006', *Mon. Wea. Rev.* **136**, 1174 – 1200.

Frey, R., Baum, B., Menzel, W. et al. (1999), 'A Comparison of Cloud Top Heights Computed from Airborne Lidar and MAS Radiance Data Using CO_2 Slicing', *J. Geophys. Res.* **104(D20)**(24), 24547 – 24555.

Froidevaux, L., Livesey, N., Read, W. et al. (2006), 'Early Validation Analysis of Atmospheric Profiles from EOS MLS on the Aura Satellite', *IEEE Trans. Geosci. Remote Sensing* **44**(5), 1106 – 1121.

Fu, Q., Krueger, S. & Liou, K. (1995), 'Interactions of Radiation and Convection in Simulated Tropical Cloud Clusters', *JAS* **52**(9).

Fu, Q. & Liou, K. (1993), 'Parameterization of the Radiative Properties of Cirrus Clouds', *JAS* **50**(13), 2008 – 2025.

Fueglistaler, S., Dessler, A., Dunkerton, T. et al. (2009), 'Tropical Tropopause Layer', *Rev. Geophys.* **47**(RG1004), 1 – 31.

Gettelman, A., Kinnison, D., Dunkerton, T. et al. (2004), 'Impact of Monsoon Circulations on the Upper Troposphere and Lower Stratosphere', *J. Geophys. Res.* **109**(D22). doi:10.1029/2004JD004878.

Gille, J., Gray, L. et al. (2011), High Resolution Dynamics Limb Sounder Earth Observing System (EOS) Data Description and Quality Version 6 (V6), (HIRDLS Version 6.00.00), Technical Report, NASA / NERC.

Goddard Space Flight Center, ed. (Retrieved Jan 2012), *Stratospheric Ozone: An Electronic Textbook*, NASA, Chapter 6: Stratospheric Dynamics and the Transport of Ozone and Other Trace Gases.

Greenhough, J., Remedios, J., Sembhi, H. et al. (2005), 'Towards Cloud Detection and Cloud Frequency Distributions from MIPAS Infra-Red Observations', *ASR* **36**(5), 800 806.

Haag, W., Karcher, B., Strom, J. et al. (2003), 'Freezing Thresholds and Cirrus Cloud Formation Mechanisms Inferred from In-situ Measurements of Relative Humidity', *Atmos. Chem. Phys.* **3**, 1791 – 1806.

Hansen, J., Nazarenko, L., Ruedy, R. et al. (2005), 'Earth's Energy Imbalance: Confirmation and Implication', *Science* **308**, 1431 – 1435.

Harries, J. (1996), 'The Greenhouse Earth: A View from Space', *Q.J.R. Meteorol. Soc.* **122**, 799 – 818.

Harries, J. (1997), 'Atmospheric Radiation and Atmospheric Humidity', *Q.J.R. Meteorol. Soc.* **123**(544), 2173 – 2186.

Harries, J. (2000), 'Physics of the Earth's Radiative Energy Balance', *Contemporary Physics* **41**, 309 – 322.

Harries, J., Brindley, H., Sagoo, P. et al. (2001), 'Increases in Greenhouse Forcing Inferred from the Outgoing Longwave Radiation Spectra of the Earth in 1970 and 1997', *Nature* **410**(March).

Hartmann, D., Holton, J., Fu, Q. et al. (2001), 'The Heat Balance of the Tropical Tropopause, Cirrus, and Stratospheric Dehydration', *Geophys. Res. Lett.* **28**(10), 1969 – 1972.

Hartmann, D. & Larson, K. (2002), 'An Important Constraint on Tropical Cloud - Climate Feedback', *Geophys. Res. Lett.* **29**(20), 1951.

Hartmann, D., Moy, L., Fu, Q. et al. (2001), 'Tropical Convection and the Energy Balance at the Top of the Atmosphere', *J. Climate* **14**(24), 4495 – 4511.

Hartmann, D., Ockert-Bell, M., Michelsen, M. et al. (1992), 'The Effect of Cloud type on Earth's Energy Balance: Global Analysis', *J. Climate* **5**(11), 1281 – 1304.

Hartmann, D. & Wood, R. (2008), 'Dynamic Effects on the Tropical Cloud Radiative Forcing and Radiation Budget', *J. Climate* **21**, 2337 – 2351.

Held, I. & Soden, B. (2000), 'Water Vapor Feedback and Global Warming', *Annu. Rev. Energy Environ.* **25**, 441 – 475.

Heymsfield, A. (1984), 'A Parameterization of the Particle Size Spectrum of Ice Clouds in Terms of the Ambient Temperature and the Ice Water Content', *JAS* **41**(5), 846 – 855.

Heymsfield, A., Matrosov, S. & Baum, B. (2003), 'Ice Water Path - Optical Depth Relationships for Cirrus and Deep Stratiform Ice Cloud Layers', *J. Climate* **42**, 1369 – 1390.

Highwood, E. & Hoskins, B. (1998), 'The Tropical Tropopause', *Q.J.R. Meteorol. Soc.* **124**, 1579 – 1604.

Holton, J. (1995), 'Stratosphere-Troposphere Exchange', *Rev. Geophys.* **33**(4), 403 – 439.

Holton, J. & Gettelman, A. (2001), 'Horizontal Transport and the Dehydration of the Stratosphere', *Geophys. Res. Lett.* **28**(15), 2799 – 2802.

Hong, G., Yang, P. et al. (2009), 'Parameterization of Shortwave and Longwave Radiative Properties of Ice Clouds for use in Climate Models', *Journal of Climate* **22**, 6287 – 6312.

Iacono, M., Mlawer, E., Clough, S. et al. (2000), 'Impact of an Improved Longwave Radiation Model, RRTM, on the Energy Budget and Thermodynamic Properties of the NCAR Community Climate Model, CCM3', *J. Geophys. Res.* **105**(D11), 14873 – 14890.

Ichkawa, H., Masunaga, H., Tsushima, Y. et al. (2012), 'Reproducibility by Climate Models of Cloud Radiative Forcing Associated with Tropical Convection', *J. Climate* **25**(4), 1247 – 1262.

IPCC (2001), The IPCC TAR: The Scientific Basis, Technical Report, Cambridge, UK: Cambridge Univ. Press.

Jensen, E. (1999), 'High Humidities and Subvisible Cirrus Near the Tropical Tropopause', *Geophys. Res. Lett.* **26**(15), 2347 – 2350.

Jensen, E., Lawson, P., Baker, B. et al. (2009), 'On the Importance of Small Ice Crystals in Tropical Anvil Cirrus', *Atmos. Chem. and Phys.* **9**(15), 5519 – 5537.

Jensen, E., Pfister, L., Ackerman, A. et al. (2001), 'A Conceptual Model of the Dehydration of air due to Freeze-drying by Optically Thin, Laminar Cirrus rising slowly across the Tropical Tropopause', *J. Geophys. Res.* **106**(17), 237 – 252.

Jensen, E., Toon, O., Selkirk, H. et al. (1996), 'On the Formation and Persistence of Subvisible Cirrus Clouds near the Tropical Tropopause', *J. Geosphys. Res* **101**, 21361 – 21375.

John, V., Holl, G., Allan, R. et al. (2011), 'Clear-sky Biases in Satellite Infrared Estimates of Upper Tropospheric Humidity and its Trends', *J. Geophys. Res.* **116**(D14). doi: 10.1029/2010JD015355.

Kelly, A. (2007), Earth Observing System EOS Aura, Technical Report, Goddard Space Flight Center, NASA. url: http://aura.gsfc.nasa.gov/aurafeature102907.html.

Kelly, M. & Randall, D. (2001), 'A Two-box Model of Zonal Atmospheric Circulation in the Tropics', *Journal of Climate* **14**(19), 3944 – 3964.

King, M., Tsay, S., Platnick, S. et al. (1997), Cloud Retrieval Algorithms for MODIS: Optical Thickness, Effective Particle Radius, and Thermodynamic Phase, Technical Report Algorithm Theor. Basis Doc., NASA Goddard Space Flight Center.

Larson, K. & Hartmann, D. (1999), 'The Role of Clouds, Water Vapor, Circulation, and Boundary Layer Structure in the Sensitivity of the Tropical Climate', *J. Climate* **12**, 2359 – 2374.

Larson, K. & Hartmann, D. (2003), 'Interactions among Cloud, Water Vapor, Radiation, and Large-scale Circulation in the Tropical Climate. Part I: Sensitivity to Uniform Sea Surface Temperature Changes', *Journal of Climate* **16**(10), 1425 – 1455.

Lee, J., Yang, P., Dessler, A. et al. (2009), 'Distribution and Radiative Forcing of Tropical Thin Cirrus Clouds', *J. Climate* **66**(12), 3721 – 3731.

Lee, R. B., Barkstrom, B. R., Smith, G. L. et al. (1996), 'The Clouds and the Earth's Radiant Energy System (CERES) Sensors and Preflight Calibration Plans', *J. Atmos. Oceanic. Technol.* **13**(2), 300 – 313.

Levelt, P. & Noordhoek, R. (2002), OMI Algorithm Theoretical Basis Document, Technical Report, Royal Netherlands Meteorological Institute (KNMI).

Li, J.-L., Waliser, D., Jiang, J. et al. (2005), 'Comparisons of EOS MLS Cloud Ice Measurements with ECMWF Analyses and GCM Simulations: Initial Results', *Geophys. Res. Letts.* .

Lindzen, R., Chou, M. & Hou, A. (2001), 'Does the Earth Have an Adaptive Infrared Iris?', *J. Climate* **82**(3), 417 – 432.

Liou, K.-N. (1986), 'Influence of Cirrus Clouds on Weather and Climate Processes: A Global Perspective', *Mon. Wea. Rev.* **114**, 1167 – 1199.

Livesey, N. J. & Snyder, W. V. (2004), EOS MLS Retrieval Processes Algorithm Theoretical Basis, Technical Report D-16159, Jet Propulsion Laboratory.

Livesey, N., Read, W., Froidevaux, L. et al. (2003), 'The UARS Microwave Limb Sounder version 5 Dataset: Theory, Characterization and Validation', *J. Geophys. Res.* **108**(D13).

Livesey, N., Read, W., Lambert, A. et al. (2007), Version 2.2 level 2 Data Quality and Description Document, Technical Report, JPL CALTECH. Version 2.2x-1.0a.

Livesey, N., Snyder, W. & Read, W. (2006), 'Retrieval Algorithms for the EOS Microwave Limb Sounder (MLS)', *IEEE Trans. Geosci. Remote Sensing* **44**(5), 1144 – 1154.

Loeb, N., Kato, S., Loukachine, K. et al. (2007), 'Angular Distribution Models for Top-of-Atmosphere Radiative Flux Estimation from the Clouds and the Earth's Radiant Energy System Instrument on the Terra Satellite. Part II: Validation', *J. Atmos. Oceanic Technol.* **24**(564 - 584).

Loeb, N., Manalo-Smith, N., Kato, S. et al. (2003), 'Angular Distribution Models for Top-of-atmosphere Radiative Flux Estimation from the Clouds and the Earth's Radiative Energy System Instrument on the Tropical Rainfall Measuring Mission Satellite: Part I Methodology', *J. Appl. Meteor.* **42**, 240 – 265.

Loeb, N., Wielicki, B., Rose, F. et al. (2007), 'Variability in Global Top-of-atmosphere Shortwave Radiation between 2000 and 2005', *Geophys. Res. Lett* **34**(L03704).

Lohmann, U. & Roeckner, E. (1995), 'Influence of Cirrus Cloud Radiative Forcing on Climate and Climate Sensitivity in a General Circulation Model', *J. Geophys. Res.* **100**(D8), 16305 – 16323.

Loyola, D., Valks, P., Ruppert, T. et al. (2006), 'The 1997 El Ninõ impact on Clouds, Water Vapour, Aerosols and Reactive Trace Gases in the Troposphere, as Measured by the Global Ozone Monitoring Experiment', *Adv. GeoSci.* **6**, 267 – 272.

Lyman, J., Willis, J. & Johnson, G. (2006), 'Recent Cooling of the Upper Ocean', *Geophys. Res. Lett.* **33**(L18604), 1272 – 1282.

Manabe, S. & Wetherald, R. (1967), 'Thermal Equilibrium of the Atmosphere with a Given Distribution of Relative Humidity', *JAS* **24**(3), 241 – 259.

Massie, S., Gille, J., Craig, C. et al. (2010), 'HIRDLS and CALIPSO Observations of Tropical Cirrus', *J. Geophys. Res.* **15**(D00H11), doi:10.1029/2009JD012100.

Massie, S., Jiang, J. H. et al. (2011), HIRDLS: High Resolution Dynamics Limb Sounder, Earth Observing System (EOS), Ice Water Content (IWC) Document, Technical Report, CLAS / NCAR.

Maurellis, A. & Tennyson, J. (2003), 'The Climatic effects of Water Vapour', *Physics World* pp. 29 – 33.

McFarquhar, G. & Heymsfield, A. (1997), 'Parameterization of Tropical Cirrus Ice Crystal Size Distributions and Implications for Radiative Transfer: Results from CEPEX', *J. Climate* **54**(17), 2187 – 2200.

McFarquhar, G. & Heymsfield, A. (1998), 'The Definition and Significance of an Effective Radius for Ice Clouds', *J. Climate* **55**(11), 2039 – 2052.

McFarquhar, G., Heymsfield, A., Spinhime, J. et al. (2000), 'Thin and Subvisual Tropical Tropopause Cirrus: Observations and Radiative impacts', *J. Atmos. Sci.* **57**(12), 1841 – 1853.

Menzel, W. & Strabala, K. (2006), Cloud top Properties and Cloud Phase Algorithm Theoretical Basis Document, Technical Report, NASA Goddard Space Flight Center, url: http://modis-atmos.gsfc.nasa.gov/_docs/atbd_mod04.pdf.

Mie, G. (1908), 'Beiträge zur Optik trüber Medien, Speziell Kolloidaler Metallösungen', *Annalen der Physik* **25**, 377 – 445.

Nakaya, U. (1954), *Snow Crystals: Natural and Artificial*, Harvard University Press.

NOAA National Weather Service, W. F. O. (2010), A Comprehensive Glossary of Weather Terms for Storm Spotters, Technical Report, Technical Memorandum NWS SR - 145, url: http://www.srh.nasa.gov/.

Osterman, G. (2008), Earth Observing System (EOS) Tropospheric Emission Spectrometer (TES), Technical Report, Jet Propulsion Laboratory, CalTech.

Platnick, S., King, M. et al. (2003), 'The MODIS Cloud Products: Algorithms and Examples from Terra', *ITGRS* **41**(2).

Platt, C. (1989), 'The Role of Cloud Microphysics in High-cloud Feedback Effects on Climate Change', *Nature* **341**, 428 – 429.

Ramanathan, V. & Inamdar, A. (2006), *Frontiers of Climate Modeling: The Radiative Forcing due to Clouds and Water Vapor*, Cambridge University Press.

Ramaswamy, V. (2001), *IPCC 2001, Third Assessment Report (TAR): The Scientific Basis*, Intergovernmental Panel on Climate Change, Chapter 6. Radiative Forcing of Climate Change, pp. 349 – 416.

Randel, W., Wu, F. & Vomel, H. (2006), 'Decreases in Stratospheric Water Vapor after 2001: Links to Changes in the Tropical Tropopause and the Brewer-Dobson Circulation', *J. Geophys. Res.* **111**(D12312).

Read, W., Lambert, A., Bacmeister, J. et al. (2007), 'Aura Microwave Limb Sounder Upper Tropospheric and Lower Stratospheric H_2O and Relative Humidity with Respect to Ice Validation', *J. Geophys. Res.* **112**(D24S35), doi:10.1029/2007JD008752.

Reinecker, M., Suarez, M., Todling, R. et al. (2007), The GEOS-5 Data Assimilation System: A Documentation of GEOS-5.0, Technical Report, NASA. TM-104606, Technical Report Series on Global Modeling and Data Assimilation.

Rodgers, C. D. (2000), *Inverse Methods For Atmospheric Sounding: Theory and Practice*, World Scientific Publishing Co., Chapter Optimal Methods for Non-linear Inverse Problems.

Rolland, P., Liou, K., King, M. et al. (2000), 'Remote Sensing of Optical and Microphysical Properties of Cirrus Clouds Using Moderate-Resolution Imaging Spectroradiometer Channels: Methodology and Sensitivity to Physical Assumptions', *J. Geophys. Res.* **105**(D9), 11721 – 11738. doi: 10.1029/2000JD900028.

Rossow, W. & Schiffer, R. (1999), 'Advances in Understanding Clouds from ISCCP', *Bull. Amer. Meteor. Soc.* **80**, 2261 – 2288.

Rothman, L., Gordon, I. et al. (2009), 'The HITRAN 2008 Molecular Spectroscopic Database', *JQSRT* **110**, 533 – 572.

Samuelson, R. (1970), 'Non-local Thermodynamic Equilibrium in Cloudy Planetary Atmospheres', *J. Climate* .

Saunders, R., Brunel, P., English, S. et al. (2005), RTTOV8 - Science and Validation Report, NWP SAF, Met. Office.

Savtchenko, A., Kummerer, R., Smith, P. et al. (2008), 'A-Train Data Depot: Bringing Atmospheric Measurements Together', *IEEE Trans. Geosci. Remote Sensing* **46**(10), 2788 – 2795.

Seidel, D., Fu, Q., Randel, W. et al. (2008), 'Widening of the Tropical Belt in a Changing Climate', *Nature GeoScience* **1**(Jan.), 22 – 24.

Sembhi, H., Remedios, J. & Trent, T. (2012), 'MIPAS Detection of Cloud and Aerosol Particle Occurrence in the UTLS with Comparison to HIRDLS and CALIOP', *Atmos. Meas. Tech.* **5**(10), 2537 2553. doi:10.5194/amt-5-2537-2012.

Sherwood, S. & Dessler, A. (2001), 'A Model for Transport Across the Tropical Tropopause', *J. Atmos. Sci.* **58**, 765 – 779.

Smith, G. & Wielicki (2004), 'Clouds and Earth's Radiant Energy System: An Overview', *Advances in Space Research* **33**, 1125 – 1131.

Soden, B. (1997), 'Variations in the Tropical Greenhouse Effect During El Ninõ', *J. Climate* **10**, 1050 – 1055.

Soden, B., Jackson, D., Ramaswamy, V. et al. (2005), 'The Radiative Signature of Upper Tropospheric Moistening', *Science* **310**, 841 – 844.

Solomon, S., D. Qin, M. M., Z. Chen, M. M., Averyt, K., Tignor, M. & (eds.), H. M. (2007), IPCC, 2007: Climate Change 2007: The Physical Science Basis: Contribution of Working Group I to the Fourth Assessment, Technical Report, Cambridge University Press, Cambridge, United Kingdom and New York, NY, USA.

Spence, P., Priestley, K., Kizer, E. et al. (2003), 'Three-Channel Intercomparison and Direct Comparison On-orbit Stability Analyses as Applied to the CERES Instruments on the Terra and Aqua Satellites', *Proc. SPIE* **5151**, 307 – 317.

Stammes, K., Tasy, S., Wiscombe, W. et al. (1988), 'Numerically Stable Algorithm for Discrete-Ordinate-Method Radiative Transfer in Multiple Scattering and Emitting Layered Media', *Appl. Opt.* **27**, 2502 – 2509.

Stephens, G. (1984), 'The Parameterization of Radiation for Numerical Weather Prediction and Climate Models', *Mon. Wea. Rev* **112**, 826 – 867.

Stephens, G., Gabriel, P. & Partain, P. (2001), 'Parameterization of Atmospheric Radiative Transfer. Part I: Validity of Simple Models', *J. Atmos. Sci* **58**, 3391 – 3409.

Stephens, G. L., Vane, D. G., Boain, R. J. et al. (2002*a*), 'The CloudSat Mission and the A-train: A New Dimension of Space Based Observations of Clouds and Precipitation', *Bull. Amer. Meteor. Soc.* **83**, 1771 – 1790.

Stephens, G., Starr, D., Sassen, K. & Lynch, D., eds (2002), *Cirrus*, Vol. 498pp., Oxford University Press.

Stephens, G., Tsay, S.-C., Jr., P. S. et al. (1990), 'The Relevance of the Microphysical and Radiative Properties of Cirrus Clouds to Climate and Climate Feedback', *J. Atmos. Sci.* **47**, 1742 – 1754.

Stephens, G., Vane, D., Boain, R. et al. (2002*b*), 'The CloudSat Mission and the A-Train: A New Dimension of Space-Based Observations of Clouds and Precipitation', *Bull. Amer. Meteor. Soc.* **83**, 1771 – 1790.

Stevens, G., Wielicki, W. & Trepte, C. (2008), The Afternoon Constellation: Aqua, CALIPSO, CloudSat, PARASOL, Aura: The "A" train, Technical Report, NASA Goddard Space Flight Center, url: http://aura.gsfc.nasa.gov/images/project/A-train3.pdf.

Stevenson, D., Dentener, F., Schultz, M. et al. (2006), 'Multimodel Ensemble Simulations of Present-day and near-future Tropospheric Ozone', *J. Geophys. Res.* **111**(D08301).

Stith, J., Dye, J. & Bansemer, A. (2002), 'Microphysical Observations of Tropical Clouds', *J. Climate* **41**(2), 97 – 117.

Sun, D. & Lindzen, R. (1993), 'Distribution of Tropical Tropospheric Water Vapor', *J. Climate* **50**(12), 1643 – 1660.

Tompkins, A. & Craig, G. (1999), 'Sensitivity of Tropical Convection to Sea Surface Temperature in the Absence of Large-Scale Flow', *J. Climate* **12**(2), 462 – 476.

Trenberth, K. (1998), 'Atmospheric Moisture Residence Times and Cycling: Implications for Rainfall Rates and Climate Change', *Climatic Change* **39**(4), 667 – 694.

Trenberth, K., Fasullo, J. & Kiehl (2009), 'Earth's Global Energy Budget', *AMS* **90**(3), 311 – 324.

Trenberth, K. et al. (2002), 'Changes in Tropical Clouds and Radiation', *Science* **296**(5576), 2095.

Udelhofen, P. & Hartmann, D. (1995), 'Influence of Tropical Cloud Systems on the Relative Humidity in the Upper Troposphere', *100* **100**(D4), 7423 – 7440.

Waliser, D., Li, J.-L., Woods, C. et al. (2009), 'Cloud Ice: A Climate Model Challenge with Signs and Expectations of Progress', *J. Geophys. Res.* **114**(D00A21).

Waters, J., Froidevaux, L., Harwood, R. et al. (2006), 'The Earth Observing System Microwave Limb Sounder (EOS MLS) on the Aura Satellite', *IEEE Trans. Geosci. Remote Sensing* **44**(5), 1075 – 1092.

Wielicki, B. & Barkstom, B. (1997), Clouds and the Earth's Radiant Energy System (CERES), Technical Report, Atmospheric Sciences Division, NASA Langley Research Center.

Wielicki, B., Barkstrom, B., Harrison, E. et al. (1996), 'Clouds and the Earth's Radiant Energy System (CERES): An Earth Observing System Experiment', *Bull. Ameri. Meteor. Soc* **77**(853 - 868).

Wielicki, B. et al. (2002), 'Evidence for Large Decadal Variability in the Tropical Mean Radiative Energy Budget', *Science* .

Williams, K. & Webb, M. (2009), 'A Quantitative Performance Assessment of Cloud Regimes in Climate Models', *Clim. Dyn.* **33**(1), 141 – 157.

Winker, D., Hostetler, C., Vaughan, M. et al. (2006), CALIOP Algorithm Theoretical Basis Document, Part 1: CALIOP Instrument, and Algorithms Overview, Technical Report, NASA / LARC, url: http://www-calipso.larc.nasa.gov/resources/pdfs/PC-SCI-202.Part1_v2-Overview.pdf.

Winker, D. M., Pelon, J. & McCormick, M. P. (2002), 'The CALIPSO mission: Spaceborne Lidar for Observation of Aerosols and Clouds', *Proc. SPIE* **4893**, 1 – 11.

Wong, T., Wielicki, B. & III, R. L. (2005), 'Reexamination of the Observed Decadal Variability of the Earth Radiation Budget using Altitude-corrected ERBE/ERBS Nonscanner WFOV Data', *J. Climate* **19**, 4028 – 4040.

Wong, T., Young, D., Minnis, P. et al. (2000), Clouds and the Earth's Radiant Energy System (CERES): Validation Plan, Technical Report, Atmospheric Science Division: NASA Langley Research Center.

Wu, D., Austin, R., Deng, M. et al. (2009), 'Comparisons of Global Cloud Ice from MLS, CloudSat, and Correlative Data Sets', *J. Geophys. Res.* **114**(D11).

Wu, D. & Jiang, J. (2004), EOS MLS Algorithm Theoretical Basis for Cloud Measurements, Technical Report Version 1.0, JPL, CalTech.

Wu, D., Jiang, J. & Davis, C. (2006), 'EOS MLS Cloud Ice Measurements and Cloudy-sky Radiative Transfer Model', *IEEE Trans. Geosci. Remote Sensing* **44**(5), 1156 – 1165.

Wu, D., Jiang, J. & Read, W. (2008), 'Validation of the Aura MLS Cloud Ice Water Content (IWC) Measurements', *J. Geophys. Res.* **113**(D15S10).

Wyser, K. (1998), 'The Effective Radius in Ice Clouds', *J. Climate* **11**(7), 1793 – 1801.

Xiang, X. & Barnes, W. (2006), 'An Overview of MODIS Radiometric Calibration and Characterization', *Adv. Atmos. Sci* **23**(1), 69 – 79.